

**L and R mode electromagnetic instabilities in space plasmas having  
kappa velocity distributions**

by

**Farran Dominique Henning**

Submitted in fulfilment of the academic requirements for the degree of Doctor of Philosophy in the School of Chemistry and Physics, University of KwaZulu-Natal, Westville, December, 2014.

As the candidate's Supervisor I have approved this thesis for submission

Signed: .....

Name: .....

Date: .....

## Abstract

Space plasmas support a wide range of plasma wave modes. This thesis focuses on the L and R mode waves. In particular, a theoretical investigation of (i) the whistler wave, and (ii) the electromagnetic ion cyclotron (EMIC) wave, is performed. These are electromagnetic waves that propagate parallel to the ambient magnetic field. They exist in a diverse range of plasma conditions and, hence, there is a need to investigate their dispersive characteristics and growth rates under a variety of plasma parameters.

Setting this work apart from previous studies of the whistler and EMIC instabilities is the choice of particle velocity distribution. *In situ* measurements have shown that the kappa distribution provides the best fit to particle velocity distributions in a variety of space plasmas. Motivated by this, all particle species in this thesis shall have a velocity distribution modelled by the kappa or bi-kappa distribution. This allows for the overabundance of superthermal particles, which are ever present in space plasmas, to be taken into account. The electron thermal anisotropy driven parallel propagating whistler instability in the Saturnian magnetosphere, is investigated first. Motivated by observations, the hot and cool electron species are each modelled by a bi-kappa distribution with different index  $\kappa$ . A parameter survey, using parameter values for the Saturnian magnetosphere as a guide, is performed. It is found that the growth rate of the whistler instability is highly dependent on the spectral indices and temperature anisotropy of each electron species, as well as the plasma parallel beta value of the hot electrons.

Secondly, a study of the EMIC instability in the terrestrial magnetosphere for a variety of relative abundances of the ion species is performed. Here it is assumed that the hot ring current ions ( $\text{H}^+$ ,  $\text{He}^+$  and  $\text{O}^+$ ), cool ions of plasmaspheric origin ( $\text{H}^+$ ,  $\text{He}^+$  and  $\text{O}^+$ ), as well as the electrons, have particle velocity distributions modelled by the bi-kappa distribution. The plasmaspheric ion populations play a relatively minor role in governing the dispersive characteristics and growth rates of the branches of the EMIC instability. On the other hand, it is found that the EMIC instabilities are highly sensitive to the relative abundance of the ring current ions, especially the proton and helium branches.

## Preface

The work presented in this thesis was carried out by the author from January 2011 to December 2014, in the School of Chemistry and Physics, University of KwaZulu-Natal, Westville, under the supervision of Professor R. L. Mace.

These studies represent original work by the author and have not otherwise been submitted in any form for a degree or diploma to another tertiary institution. Where use was made of the works of others, it has been duly acknowledged in the text.

Signed: .....

## DECLARATION 1 - PLAGIARISM

I, Farran Dominique Henning, declare that

1. The research reported in this thesis, except where otherwise indicated, is my original research.
2. This thesis has not been submitted for any degree or examination at any other university.
3. This thesis does not contain other persons' data, pictures, graphs or other information, unless specifically acknowledged as being sourced from other persons.
4. This thesis does not contain other persons' writing, unless specifically acknowledged as being sourced from other researchers. Where other written sources have been quoted, then: (a) Their words have been re-written but the general information attributed to them has been referenced (b) Where their exact words have been used, then their writing has been placed in italics and inside quotation marks, and referenced.
5. This thesis does not contain text, graphics or tables copied and pasted from the Internet, unless specifically acknowledged, and the source being detailed in the thesis and in the References sections.

Signed: .....

## DECLARATION 2 - PUBLICATIONS

DETAILS OF CONTRIBUTION TO PUBLICATIONS that form part and/or include research presented in this thesis.

Publication 1: **Henning, F. D. and Mace, R. L. (2014), “Effects of ion abundances on electromagnetic ion cyclotron wave growth rate in the vicinity of the plasmopause”, *Physics of Plasmas*, 21(4):042905.** The analytical and numerical work, in the above paper, was done by the first author, F. D. Henning. Both authors (F. D. Henning and R. L. Mace) were deeply involved in the write up and interpretation of the results.

Publication 2: Paper in draft, intended for publication in *Physics of Plasmas*. **“Whistler instability driven by electron thermal anisotropy in a dual electron kappa plasma” by Henning, F. D. and Mace, R. L.** The analytical work, numerical work and interpretation of the results, in the above paper, have been done by the first author, F. D. Henning. Both authors (F. D. Henning and R. L. Mace) are currently involved in the write up of the draft.

Signed: .....



# Acknowledgements

I would like to thank Prof. R. L. Mace for his academic guidance and financial support. The National Research Foundation (NRF) is acknowledged for research support. Any opinion, findings and conclusions or recommendations expressed in this material are those of the authors and, therefore, the NRF does not accept any liability thereto.

I would also like to thank Dr. J. A. E. Stephenson and Dr. A. B. Collier for their encouragement and emotional support, especially during the write up of this thesis.

My daily interaction with my fellow post graduate students, especially Reginald Abdul and Sharmini Pillay, provided a positive and productive work environment.

To my family and friends, thank you for all your encouragement and for providing an unwavering support system.

To my parents, thank you for all that you have done for me, the sacrifices you have made to further my education and the support you have provided throughout my years of study.

To my husband and daughter, without both of you by my side this would have never been possible.



# Contents

<b>1</b>	<b>General introduction</b>	<b>1</b>
1.1	L and R mode waves . . . . .	2
1.2	Wave-particle interactions . . . . .	4
1.3	Kappa velocity distribution . . . . .	8
1.4	Thesis outline . . . . .	11
<b>2</b>	<b>Whistler mode instability</b>	<b>13</b>
2.1	Introduction . . . . .	14
2.2	Motivation and aim . . . . .	20
2.3	Model and basic equations . . . . .	23
2.4	Numerical results . . . . .	29
2.4.1	Variation of the spectral index of the hot electrons, $\kappa_h$ . . . . .	30
2.4.2	Variation of the spectral index of the cool electrons, $\kappa_c$ . . . . .	62
2.5	Discussion and conclusions . . . . .	83
<b>3</b>	<b>Electromagnetic ion cyclotron waves</b>	<b>89</b>
3.1	Introduction . . . . .	90
3.2	Motivation and aim . . . . .	97
3.3	Model and basic equations . . . . .	98
3.4	Numerical results . . . . .	102
3.5	Discussion and conclusions . . . . .	118

<b>4</b>	<b>General summary</b>	<b>123</b>
<b>A</b>	<b>Dispersion relation for parallel propagating L and R mode waves in a plasma with an arbitrary velocity distribution</b>	<b>129</b>
<b>B</b>	<b>Dispersion relation for parallel propagating L mode waves with an arbitrary number of kappa distributed plasma particle species</b>	<b>137</b>

# List of Figures

1.1	Normal cyclotron resonance between charged particles and circularly polarised electromagnetic waves. The top diagram gives a schematic illustration of a left hand circularly polarised wave interacting with a positive ion. The bottom diagram gives a schematic illustration of a right hand circularly polarised wave interacting with an electron. This figure is reproduced from <i>Tsurutani and Lakhina (1997)</i> . . . . .	7
1.2	Anomalous resonance between an ion and a right hand circularly polarised wave. This figure is reproduced from <i>Tsurutani and Lakhina (1997)</i> . . . . .	8
1.3	Plots of the kappa distribution for $\kappa = 1.6$ —, $\kappa = 2.0$ —, $\kappa = 3.0$ — and $\kappa = \infty$ — (the Maxwellian case). . . . .	9
2.1	Regions and plasma populations in Saturn's magnetosphere as derived from Voyager data ( <i>Sittler et al., 1983</i> ). . . . .	15

- 2.2 (Reproduced from *Schippers et al. (2008)*) Composite CAPS/ELS and MIMI/LEMMS (energy channels C0 - C7) spectral plots of electron intensities versus energy, observed at (top) 2200 UT ( $R = 9R_s$ , local time 18.32 h, latitude 0.23 degrees) and at (bottom) 0727 UT ( $R = 12.8R_s$ , local time 19.82 h, latitude 0.35 degrees) on days of 142 and 143 of year 2006 during Rev. 24, respectively. Original data are represented in black, *Schippers et al. (2008)* interpolated data is represented in red, and the results of the various models used by *Schippers et al. (2008)* are represented in blue. Left (a): Model with two Maxwellian distributions. Middle (b): Model with one Maxwellian and one kappa distribution. Right (c) Model with two kappa distributions. . . . 22
- 2.3 Whistler mode dispersion relation (top) and growth rate (middle) for a sequence of plasmas having different  $\kappa_h$  values, fixed temperature anisotropies corresponding to  $A_c = 0$ ,  $A_h = 0.1$  and all other parameters are as in Table 2.1. The bottom panel illustrates the dependence of  $k^*\rho_h$  on  $\kappa_h$  for a fixed  $\kappa_c$  by magnifying the middle panel around the values of  $k\rho_h$  where  $\gamma = 0$  (see text). . . . . 33
- 2.4 Whistler mode dispersion relation (top) and growth rate (middle) for a sequence of plasmas having different  $\kappa_h$  values, fixed temperature anisotropies corresponding to  $A_c = 0$ ,  $A_h = 0.2$  and all other parameters are as in Table 2.1. The bottom panel illustrates the dependence of  $k^*\rho_h$  on  $\kappa_h$  for a fixed  $\kappa_c$  by magnifying the middle panel around the values of  $k\rho_h$  where  $\gamma = 0$  (see text) . . . . . 35
- 2.5 Whistler mode dispersion relation (top) and growth rate (middle) for a sequence of plasmas having different  $\kappa_h$  values, fixed temperature anisotropies corresponding to  $A_c = 0$ ,  $A_h = 0.5$  and all other parameters are as in Table 2.1. The bottom panel illustrates the dependence of  $k^*\rho_h$  on  $\kappa_h$  for a fixed  $\kappa_c$  by magnifying the middle panel around the values of  $k\rho_h$  where  $\gamma = 0$  (see text). . . . . 37

2.6 Whistler mode dispersion relation for a sequence of plasmas having different  $\kappa_h$  values, fixed temperature anisotropies corresponding to  $A_c = A_h = 0.1$  and all other parameters are as in Table 2.1 (top panel). The bottom panel illustrates the dispersion relation zoomed in around the point of intersection (see main text). The dashed horizontal line represents  $\omega_h^* = \omega_c^* = 0.0909091|\Omega_e|$ . . . . . 41

2.7 Whistler mode growth rate for a sequence of plasmas having different  $\kappa_h$  values, fixed temperature anisotropies corresponding to  $A_c = A_h = 0.1$  and all other parameters are as in Table 2.1 (top panel). The bottom panel illustrates the dispersion relation zoomed in around the point where  $\gamma = 0$  for all curves (see main text). . . . . 42

2.8 Whistler mode dispersion relation for a sequence of plasmas having different  $\kappa_h$  values, fixed temperature anisotropies corresponding to  $A_c = A_h = 0.2$  and all other parameters are as in Table 2.1 (top panel). The bottom panel illustrates the dispersion relation zoomed in around the point of intersection (see main text). The dashed horizontal line represents  $\omega_h^* = \omega_c^* = 0.1666667|\Omega_e|$ . . . . . 43

2.9 Whistler mode growth rate for a sequence of plasmas having different  $\kappa_h$  values, fixed temperature anisotropies corresponding to  $A_c = A_h = 0.2$  and all other parameters are as in Table 2.1 (top panel). The bottom panel illustrates the dispersion relation zoomed in around the point where  $\gamma = 0$  for all curves (see main text). . . . . 44

2.10 Whistler mode dispersion relation for a sequence of plasmas having different  $\kappa_h$  values, fixed temperature anisotropies corresponding to  $A_c = A_h = 0.5$  and all other parameters are as in Table 2.1 (top panel). The bottom panel illustrates the dispersion relation zoomed in around the point of intersection (see main text). The dashed horizontal line represents  $\omega_h^* = \omega_c^* = 0.3333333|\Omega_e|$ . . . . . 46

- 2.11 Whistler mode growth rate for a sequence of plasmas having different  $\kappa_h$  values, fixed temperature anisotropies corresponding to  $A_c = A_h = 0.5$  and all other parameters are as in Table 2.1 (top panel). The bottom panel illustrates the dispersion relation zoomed in around the point where  $\gamma = 0$  for all curves (see main text). . . . . 47
- 2.12 Whistler mode dispersion relation (top) and growth rate (bottom) for a sequence of plasmas having different  $\kappa_h$  values, fixed temperature anisotropies corresponding to  $A_h = 0.1$ ,  $A_c = 0$  and hot electron temperature,  $T_h = 100$  eV. All other parameters are as in Table 2.1. . . . . 49
- 2.13 Whistler mode dispersion relation (top) and growth rate (bottom) for a sequence of plasmas having different  $\kappa_h$  values, fixed temperature anisotropies corresponding to  $A_h = 0.2$ ,  $A_c = 0$  and hot electron temperature,  $T_h = 100$  eV. All other parameters are as in Table 2.1. . . . . 51
- 2.14 Whistler mode dispersion relation (top) and growth rate (middle) for a sequence of plasmas having different  $\kappa_h$  values, fixed temperature anisotropies corresponding to  $A_h = 0.75$ ,  $A_c = 0$  and hot electron temperature,  $T_h = 100$  eV. All other parameters are as in Table 2.1. The bottom panel illustrates the dependence of  $k^* \rho_h$  on  $\kappa_h$  for a fixed  $\kappa_c$ . . . . . 53
- 2.15 Whistler mode dispersion relation (top) and growth rate (bottom) for a sequence of plasmas having different  $\kappa_h$  values, fixed temperature anisotropies corresponding to  $A_h = 1.0$ ,  $A_c = 0$  and hot electron temperature,  $T_h = 100$  eV. All other parameters are as in Table 2.1. . . . . 55
- 2.16 Whistler mode dispersion relation (top) and growth rate (bottom) for a sequence of plasmas having different  $\kappa_h$  values, fixed temperature anisotropies corresponding to  $A_c = A_h = 0.1$  and hot electron temperature,  $T_h = 100$ eV. All other parameters are as in Table 2.1. The dashed horizontal line represents  $\omega_h^* = \omega_c^* = 0.0909091|\Omega_e|$ . The middle panel illustrates the dispersion relation zoomed in around the point of intersection (see main text). . . . . 57

2.17 Whistler mode dispersion relation (top) and growth rate (bottom) for a sequence of plasmas having different  $\kappa_h$  values, fixed temperature anisotropies corresponding to  $A_c = A_h = 0.2$  and hot electron temperature,  $T_h = 100\text{eV}$ . All other parameters are as in Table 2.1. The dashed horizontal line represents  $\omega_h^* = \omega_c^* = 0.1666667|\Omega_e|$ . The middle panel illustrates the dispersion relation zoomed in around the point of intersection (see main text). . . . . 58

2.18 Whistler mode dispersion relation (top) and growth rate (bottom) for a sequence of plasmas having different  $\kappa_h$  values, fixed temperature anisotropies corresponding to  $A_c = A_h = 0.75$  and hot electron temperature,  $T_h = 100\text{ eV}$ . All other parameters are as in Table 2.1. The dashed horizontal line represents  $\omega_h^* = \omega_c^* = 0.42857|\Omega_e|$ . The middle panel illustrates the dispersion relation zoomed in around the point of intersection (see main text). . . . . 60

2.19 Whistler mode dispersion relation (top) and growth rate (bottom) for a sequence of plasmas having different  $\kappa_h$  values, fixed temperature anisotropies corresponding to  $A_c = A_h = 1.0$  and hot electron temperature,  $T_h = 100\text{eV}$ . All other parameters are as in Table 2.1. The dashed horizontal line represents  $\omega_h^* = \omega_c^* = 0.5|\Omega_e|$ . The middle panel illustrates the dispersion relation zoomed in around the point of intersection (see main text). . . . . 61

2.20 Whistler mode dispersion relation (top) and growth rate (bottom) for a sequence of plasmas having different  $\kappa_c$  values, fixed temperature anisotropies corresponding to  $A_c = 0.1, A_h = 0$  and all other parameters are as in Table 2.1. . . . . 63

2.21 Whistler mode dispersion relation (top) and growth rate (bottom) for a sequence of plasmas having different  $\kappa_c$  values, fixed temperature anisotropies corresponding to  $A_c = 0.5, A_h = 0$  and all other parameters are as in Table 2.1. . . . . 65

- 2.22 Whistler mode dispersion relation (top) and growth rate (bottom) for a sequence of plasmas having different  $\kappa_c$  values, fixed temperature anisotropies corresponding to  $A_c = 2.0$ ,  $A_h = 0$  and all other parameters are as in Table 2.1. . . . . 67
- 2.23 Whistler mode dispersion relation (top) and growth rate (middle) for a sequence of plasmas having different  $\kappa_c$  values, fixed temperature anisotropies corresponding to  $A_c = A_h = 0.1$  and all other parameters are as in Table 2.1. The dashed horizontal line represents  $\omega_h^* = \omega_c^* = 0.0909091|\Omega_e|$ . The bottom panel illustrates the growth rate zoomed in around the peak growth rates. . . . . 68
- 2.24 Whistler mode dispersion relation (top) and growth rate (middle) for a sequence of plasmas having different  $\kappa_c$  values, fixed temperature anisotropies corresponding to  $A_c = A_h = 0.5$  and all other parameters are as in Table 2.1. The dashed horizontal line represents  $\omega_h^* = \omega_c^* = 0.33333|\Omega_e|$ . The bottom panel illustrates the growth rate zoomed in around the peak growth rates. . . . . 70
- 2.25 Whistler mode dispersion relation (top) and growth rate (middle) for a sequence of plasmas having different  $\kappa_c$  values, fixed temperature anisotropies corresponding to  $A_c = A_h = 2.0$  and all other parameters are as in Table 2.1. The dashed horizontal line represents  $\omega_h^* = \omega_c^* = 0.666667|\Omega_e|$ . The bottom panel illustrates the growth rate zoomed in around the peak growth rates. . . . . 72
- 2.26 Whistler mode dispersion relation (top) and growth rate (bottom) for a sequence of plasmas having different  $\kappa_c$  values, fixed temperature anisotropies corresponding to  $A_h = 0$ ,  $A_c = 0.1$  and hot electron temperature,  $T_h = 100$  eV. All other parameters are as in Table 2.1. . . . . 74

2.27 Whistler mode dispersion relation (top) and growth rate (bottom) for a sequence of plasmas having different  $\kappa_c$  values, fixed temperature anisotropies corresponding to  $A_h = 0$ ,  $A_c = 0.5$  and hot electron temperature,  $T_h = 100$  eV. All other parameters are as in Table 2.1. . . . . 75

2.28 Whistler mode dispersion relation (top) and growth rate (bottom) for a sequence of plasmas having different  $\kappa_c$  values, fixed temperature anisotropies corresponding to  $A_h = 0$ ,  $A_c = 2.0$  and hot electron temperature,  $T_h = 100$  eV. All other parameters are as in Table 2.1. . . . . 77

2.29 Whistler mode dispersion relation (top) and growth rate (bottom) for a sequence of plasmas having different  $\kappa_c$  values, fixed temperature anisotropies corresponding to  $A_c = A_h = 0.1$  and hot electron temperature,  $T_h = 100$ eV. All other parameters are as in Table 2.1. The dashed horizontal line represents  $\omega_h^* = \omega_c^* = 0.0909091|\Omega_e|$ . . . . . 79

2.30 Whistler mode dispersion relation (top) and growth rate (bottom) for a sequence of plasmas having different  $\kappa_c$  values, fixed temperature anisotropies corresponding to  $A_c = A_h = 0.5$  and hot electron temperature,  $T_h = 100$ eV. All other parameters are as in Table 2.1. The dashed horizontal line represents  $\omega_h^* = \omega_c^* = 0.33333|\Omega_e|$ . . . . . 80

2.31 Whistler mode dispersion relation (top) and growth rate (bottom) for a sequence of plasmas having different  $\kappa_c$  values, fixed temperature anisotropies corresponding to  $A_c = A_h = 2.0$  and hot electron temperature,  $T_h = 100$ eV. All other parameters are as in Table 2.1. The dashed horizontal line represents  $\omega_h^* = \omega_c^* = 0.666667|\Omega_e|$ . . . . . 82

3.1 A schematic diagram of the terrestrial magnetosphere (*Daglis et al., 1999*). 91

3.2 The cyclotron motion and bounce motion of a charged particle along a geomagnetic field line (*Daglis et al., 1999*). . . . . 92

- 3.3 The cutoff frequencies for varying proton and oxygen ion relative abundances. The red line denotes the cutoff of the proton branch while the blue line denotes that of the helium branch. The dashed horizontal lines denote  $\omega_{\text{H}^+}^*/\Omega_{\text{H}^+}$  and  $\omega_{\text{He}^+}^*/\Omega_{\text{H}^+}$  for  $A_{\text{H}^+,h} = A_{\text{He}^+,h} = 1.0$ . The other fixed parameters are  $n_i = 25 \text{ cm}^{-3}$  and  $n_{\text{He}^+} = 2.25 \text{ cm}^{-3}(0.09 n_i)$ . The vertical lines labelled “A” and “B” represent the chosen parameters for an oxygen rich ring current (case 4) and a predominantly proton ring current (case 3), respectively, which will be used later. . . . . 105
- 3.4 The cutoff frequencies for varying proton and helium ion relative abundances. The red line denotes the cutoff frequency of the proton branch while the blue line denotes that of the helium branch. The dashed horizontal lines denote  $\omega_{\text{H}^+}^*/\Omega_{\text{H}^+}$  and  $\omega_{\text{He}^+}^*/\Omega_{\text{H}^+}$  for  $A_{\text{H}^+,h} = A_{\text{He}^+,h} = 1.0$ . Other fixed parameters are  $n_i = 25 \text{ cm}^{-3}$  and  $n_{\text{O}^+} = 1.25 \text{ cm}^{-3}$ . The vertical lines labelled “C” and “D” represent the chosen parameters for case 5 and case 6, respectively, which will be used later. . . . . 107
- 3.5 The EMIC waves branches (top panel) and their growth rates (bottom panel) shown for varying relative abundances of the plasmaspheric ions. The blue lines denote the numerical solutions to Equation (3.5) for case 1. The red lines denote numerical solutions to the same equation but with more typical plasmaspheric ion abundances, case 2. For the full set of parameters refer to Table 3.2. The horizontal dashed lines represent  $\omega_{\text{H}^+}^*/\Omega_{\text{H}^+}$  and  $\omega_{\text{He}^+}^*/\Omega_{\text{H}^+}$  as calculated by Equation (3.11). . . . . 110
- 3.6 The EMIC waves branches (top panel) and their growth (bottom panel) rates shown for varying relative abundance of the ring current ions. The red lines denote the numerical solutions to Equation (3.5) with a predominantly proton ring current, case 3. The blue lines denote solutions to the same equation but for an oxygen rich ring current, case 4. For the full set of parameters refer to Table 3.3. The horizontal dashed lines represent  $\omega_{\text{H}^+}^*/\Omega_{\text{H}^+}$  and  $\omega_{\text{He}^+}^*/\Omega_{\text{H}^+}$  as calculated by Equation (3.11). . . . . 114

- 3.7 The EMIC waves branches (top panel) and their growth rates (bottom panel) shown for varying relative abundance of the ring current ions. The red lines denote the numerical solutions to Equation (3.5) with parameters for case 5. The blue lines denote solutions to the same equation but for case 6. For the full set of parameters refer to Table 3.4. The horizontal dashed lines represent  $\omega_{\text{H}^+}^*/\Omega_{\text{H}^+}$  and  $\omega_{\text{He}^+}^*/\Omega_{\text{H}^+}$  as calculated by Equation (3.11). . 117



# List of Tables

2.1	Table of the baseline parameters used in the parameter survey. The subscripts, “h” and “c” correspond to hot and cool electron species, respectively, while “i” corresponds to the ion species. This data has been extracted by <i>Baluku et al. (2011)</i> from <i>Schippers et al. (2008)</i> for $13.1R_s$ . . . . .	29
3.1	The contribution of each ion species to the growth rate of each wave branch. Table adapted from <i>Mace et al. (2011)</i> . . . . .	101
3.2	Table of parameters chosen for Figure 3.5. . . . .	111
3.3	Table of parameters chosen for Figure 3.6. . . . .	115
3.4	Table of parameters chosen for Figure 3.7. . . . .	118



## Chapter 1

# General introduction

## 1.1 L and R mode waves

Space plasmas support a wide range of wave modes. The two modes that are of interest in this study are the left- and right-handed polarised electromagnetic waves, also known as the L and R mode, respectively (*Swanson, 2003*). In this introduction we shall briefly explore the theory of these two modes. A more detailed discussion of each mode will be carried out in the relevant chapters to follow.

Both the L and R modes are electromagnetic in nature and arise when we restrict our study to waves that propagate parallel to the magnetic field. The dispersion relation,  $D(k, \omega) = 0$ , of any plasma wave is important as it relates the wave number,  $k$ , of a wave to its frequency,  $\omega$ . The L and R modes have dispersion relations given by (*Gurnett and Bhattacharjee, 2005*, Eq. 9.3.33)

$$D(k_{\parallel}, \omega) = 1 - \frac{k_{\parallel}^2 c^2}{\omega^2} - \pi \sum_j \frac{\omega_{pj}^2}{\omega^2} \int_{-\infty}^{\infty} dv_{\parallel} \int_0^{\infty} dv_{\perp} v_{\perp}^2 \frac{1}{(k_{\parallel} v_{\parallel} - \omega \pm \Omega_j)} \cdot \left[ (\omega - k_{\parallel} v_{\parallel}) \frac{\partial f_{j0}}{\partial v_{\perp}} + k_{\parallel} v_{\perp} \frac{\partial f_{j0}}{\partial v_{\parallel}} \right] = 0 \quad \text{Im}(\omega) > 0, \quad (1.1)$$

where the choice of “ $+\Omega_j$ ” gives that of the L mode and the choice of “ $-\Omega_j$ ” gives that of the R mode. In Equation (1.1) the signed gyrofrequency for the  $j$ th species is given by  $\Omega_j = q_j B_0 / m_j$  and is characterised by mass  $m_j$  and charge  $q_j$  which may take positive or negative values. The plasma frequency  $\omega_{pj}$ , for the  $j$ th species is given by  $\omega_{pj} = (n_{0j} q_j^2 / \epsilon_0 m_j)^{1/2}$ , where  $n_{0j}$  is the equilibrium number density. The parameters  $v_{\perp}$  and  $v_{\parallel}$  are the perpendicular and parallel components of the velocity, respectively, and the function  $f_{j0}$  is the zeroth-order velocity distribution function of species  $j$ . Other parameters in Equation (1.1) are the parallel component of the wave number  $k_{\parallel}$ , where  $|k_{\parallel}| = k$ , since we are considering the case of parallel propagation with respect to the magnetic field,  $\mathbf{B}_0$ . The wave frequency,  $\omega$ , is complex and given by  $\omega = \omega_r + i\gamma$ . An outline of the derivation of the dispersion relations, Equation (1.1), is given in Appendix A.

The R mode waves which occur at frequencies below the electron gyrofrequency correspond to whistler waves. They are right hand circularly polarised, corresponding to the sense of electron gyration around the ambient magnetic field,  $\mathbf{B}_0$ . L mode waves that occur

at frequencies below the local proton gyrofrequency correspond to electromagnetic ion cyclotron (EMIC) waves. They are left hand circularly polarised, corresponding to the sense of ion gyration around  $\mathbf{B}_0$ . It is emphasised here that the polarisations in this study are expressed relative to the external (average) magnetic field as opposed to the frequently used convention of specifying polarisations with respect to the wave normal.

Whistler waves are among the most common naturally occurring waves found in the Earth's magnetosphere (*Storey, 1953; Helliwell, 1969; Gurnett et al., 1976; Scarf et al., 1984; Kennel et al., 1986*). They have also been detected in the magnetospheres of other planets, such as Jupiter (*Scarf et al., 1979; Gurnett et al., 1979; Kurth et al., 1985*), Neptune (*Gurnett et al., 1990*) and Saturn (*Gurnett et al., 2005; Akalin et al., 2006*). Their existence in a diverse range of plasma conditions reinforces the need to investigate their dispersive characteristics and growth rates for a variety of plasma parameters.

Whistler waves propagate above the proton gyrofrequency but below the electron gyrofrequency (*Helliwell, 1969*). *Kennel and Petschek (1966)* proposed the first comprehensive theory on how wave-particle interactions affect the dynamics of the Earth's magnetosphere. Since then, it has been generally accepted that whistler instabilities can lead to particle precipitation in the magnetosphere. Whistler waves play an important role in the acceleration and pitch angle scattering of radiation belt electrons (*Horne and Thorne, 1998; Shprits et al., 2006; Thorne, 2010*).

Electromagnetic ion cyclotron (EMIC) waves are generated in the equatorial region of the magnetosphere by wave-particle interactions with ring current ions (*Roux et al., 1982; Fraser et al., 2006, 2010*). They are frequently detected as Pc 1 and Pc 2 waves in ground based observations, which provides a well-understood identifier for these waves (*Anderson et al., 1992a; Fraser et al., 2006*). These pulsations were found to occur predominantly during the recovery phase (4-7 days after onset) of geomagnetic storms (*Wentworth, 1964*). *Jordanova et al. (2001)* investigated the excitation of EMIC waves in the equatorial plane during the pre-storm, main and recovery phases of the storm that occurred May 14-16, 1997. They found EMIC wave activity to be an important mechanism which contributes to proton precipitation from the ring current during geomagnetic storms. *Meredith et al.*

(2003) conducted a statistical survey of electron and proton minimum resonant energies. They concluded that EMIC waves play an important role in relativistic electron loss during storm conditions and may contribute to electron acceleration in the radiation belts.

## 1.2 Wave-particle interactions

Wave-particle interactions play a critical role in space plasma phenomena such as the formation of the magnetopause boundary layer, plasmaspheric hiss emissions, precipitation of particles causing auroras, etc. The resonant interaction between electromagnetic waves and particles has been studied extensively (*Kennel and Petschek, 1966; Lyons and Williams, 1984*). The interaction of low frequency waves with charged particles can transport energy from one region of the magnetosphere to another (*Tsurutani and Lakhina, 1997*). Such an example is how EMIC and whistler waves interact with Van Allen belt particles. This interaction can cause energetic protons and electrons to be scattered into the loss cone and, therefore, lead to ring current decay during the recovery phase of geomagnetic storms (*Tsurutani and Lakhina, 1997*). The loss cone is the set of angles in velocity space within which particles will precipitate. Particles with pitch angles (angle between the instantaneous particle velocity vector and the magnetic field vector) outside the loss cone will mirror and continue to be trapped (*Tsurutani and Lakhina, 1997*).

It is well known that the motion of charged particles in magnetic fields is a combination of circular motion around the field and translational motion along the field. A charged particle interacts strongly with a circularly polarised wave of frequency,  $\omega$ , and wave vector,  $\mathbf{k}$ , if its translational or guiding centre velocity produces the necessary Doppler shift to make the wave frequency in the guiding centre frame an integral multiple of its gyrofrequency. This is known as the cyclotron resonance interaction between the particles and waves and can be written as (*Tsurutani and Lakhina, 1997*),

$$\omega - \mathbf{k} \cdot \mathbf{v} = n\Omega. \quad (1.2)$$

In Equation (1.2),  $\omega$  is the wave angular frequency (with  $\omega > 0$ ),  $\mathbf{k}$  is the wave vector,  $\Omega$  and  $\mathbf{v}$  are the gyrofrequency and the velocity, respectively, of the particle in question and

$n$  is an integer.

The special case with  $n = 0$  in Equation (1.2) corresponds to the Landau resonance. At this resonance the particles do not see a rapid fluctuation in electric field of the wave, thus, they interact strongly. Those particles with velocities marginally less than the phase velocity of the wave,  $v_{ph}$ , will be accelerated up to the phase velocity by the wave electric field. Those particles with velocities slightly faster than  $v_{ph}$  will be decelerated down to  $v_{ph}$  (Tsurutani and Lakhina, 1997). If the number of slower particles is greater than the number of faster particles (in any interval around  $v_{ph}$ ), the average energy lost to the particles by the wave will be greater than that gained on average and, therefore, the wave will be damped (Tsurutani and Lakhina, 1997). This is known as Landau damping (Landau, 1946).

In the case of the L and R mode waves,  $n = \pm 1$ , Equation (1.2) becomes (Tsurutani and Lakhina, 1997),

$$\omega - k_{\parallel}v_{\parallel} = \pm\Omega. \quad (1.3)$$

where  $k_{\parallel}$  and  $v_{\parallel}$  are the parallel wave number and parallel velocity, respectively, due to the L and R modes being restricted to parallel propagation. The  $v_{\parallel}$  satisfying Equation (1.3) correspond to the poles in the integrand of Equation (1.1). The case of the L mode (“ $+\Omega$ ”) was discussed at length by Mace *et al.* (2011). They recognised that the pole,  $v_{\parallel}^{res}$ , in the integrand satisfies the phase locking condition (Mace *et al.*, 2011),

$$\omega - k_{\parallel}v_{\parallel}^{res} = \Omega. \quad (1.4)$$

Equation (1.4) gives the frequency,  $\omega$ , and wave number,  $k_{\parallel}$ , of a wave whose frequency in the particle guiding centre frame travelling at  $v_{\parallel}^{res}$  matches the particle’s own gyrofrequency. As such, the difference between the wave electric field phase and the particle gyrophase will remain fixed (phase locking) (Mace *et al.*, 2011). This allows particles whose parallel velocity,  $v_{\parallel}$ , lies close to  $v_{\parallel}^{res}$ , to have a strong interaction with the wave, depending on relative phase (Mace *et al.*, 2011). For the R mode the considerations are similar, but now it is electrons with  $\Omega < 0$  that interact with waves (normal resonance - see below). Since  $\Omega < 0$  in this case and we have selected the minus sign in Equation

(1.3), the condition for resonance can be written as  $\omega - k_{\parallel}v_{\parallel} = |\Omega|$ , which is discussed below and in Chapter 2.

There are two major types of resonances between particles and waves for  $n \neq 0$ : (i) normal resonances and (ii) anomalous resonances. Normal resonance between charged particles and waves is illustrated in Figure 1.1, reproduced from *Tsurutani and Lakhina (1997)*. For normal resonance, the waves and particles propagate toward each other (in opposite directions). Left hand circularly polarised waves interact with positive ions, whose gyromotion follows the left hand rule, as depicted in the top diagram of Figure 1.1. Electrons (whose gyromotion follows the right hand rule) interact with right hand circularly polarised waves as depicted in the bottom diagram of Figure 1.1. Consequently, the Doppler shift term ( $-\mathbf{k} \cdot \mathbf{v}$ ) is positive such that (*Tsurutani and Lakhina, 1997*),

$$\omega - k_{\parallel}v_{\parallel}^{res} = |\Omega|, \quad (1.5)$$

and the wave frequency is shifted up to the particle gyrofrequency,  $|\Omega|$ , i.e, the Doppler shifted frequency is positive for normal resonance irrespective of whether it is a left hand circularly polarised wave interacting with a positively charged ion or a right hand circularly polarised wave interacting with a negatively charged electron.

Anomalous resonance occurs when positive ions interact with right hand circularly polarised waves (as illustrated in Figure 1.2) and/or electrons interact with left hand circularly polarised waves. This kind of resonance occurs when the particle parallel velocity is considerably greater than the phase velocity of the wave and the particle “overtakes” the wave. In doing so, the Doppler shift produces a wave polarisation in the ion (electron) guiding centre frame of reference that is left (right) hand circularly polarised. By the resonance condition, Equation (1.3), the Doppler shift term is negative and, therefore, the Doppler shift term decreases the wave frequency to that of the negative of the gyrofrequency turning around the sense of polarisation (*Tsurutani and Lakhina, 1997*).

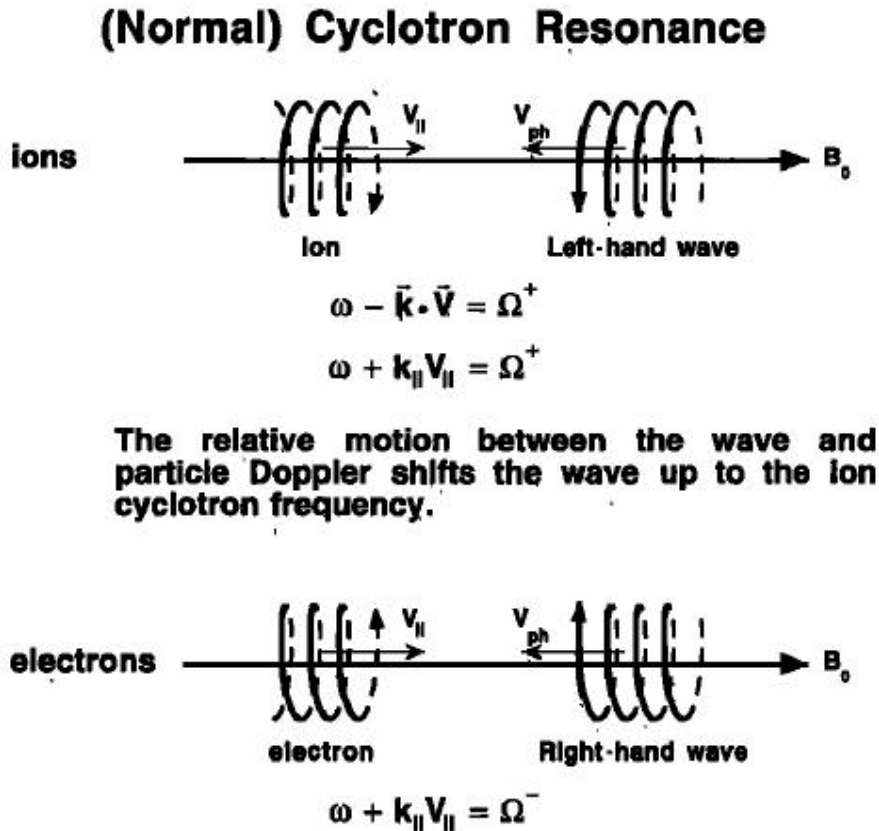


Figure 1.1: Normal cyclotron resonance between charged particles and circularly polarised electromagnetic waves. The top diagram gives a schematic illustration of a left hand circularly polarised wave interacting with a positive ion. The bottom diagram gives a schematic illustration of a right hand circularly polarised wave interacting with an electron. This figure is reproduced from *Tsurutani and Lakhina (1997)*.

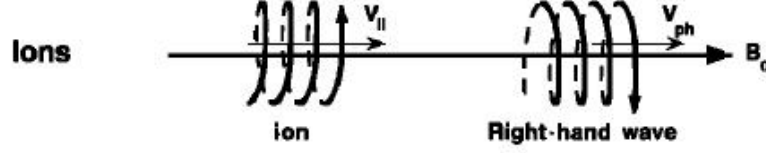


Figure 1.2: Anomalous resonance between an ion and a right hand circularly polarised wave. This figure is reproduced from *Tsurutani and Lakhina (1997)*.

### 1.3 Kappa velocity distribution

The Maxwellian distribution has long been the chosen particle distribution to model plasmas found in space, despite the fact that these space plasmas are frequently found to be far from equilibrium. *In situ* measurements of space plasmas by spacecraft have shown mounting evidence that velocity space distributions exhibit a non-Maxwellian form. The primary reason for this is because of an overabundance of superthermal particles which are distributed in energy, or momentum, according to a power law (*Christon et al., 1988; Maksimovic et al., 1997a; Schippers et al., 2008; Dialynas et al., 2009; Arridge et al., 2009*). The kappa distribution best describes the superthermal particle populations which are ever present in space plasmas (*Pierrard and Lazar, 2010*). It provides a good fit to particle velocity distributions in plasmas, as it has a power law superthermal tail and smoothly merges it with a Gaussian core.

*Vasyliunas (1968)* was the first to use the family of  $\kappa$  distributions while trying to fit OGO 1 and OGO 2 solar wind electron data. The isotropic kappa distribution (*Summers and Thorne, 1991*) is given by

$$f(\mathbf{v}) = (\pi\kappa\theta^2)^{-3/2} \frac{\Gamma(\kappa+1)}{\Gamma(\kappa-1/2)} \left(1 + \frac{\mathbf{v}^2}{\kappa\theta^2}\right)^{-(\kappa+1)}, \quad (1.6)$$

where the generalised thermal speed  $\theta$  is given by

$$\theta = \left[2 \left(\frac{\kappa - \frac{3}{2}}{\kappa}\right)\right]^{1/2} \left(\frac{T}{m}\right)^{1/2}. \quad (1.7)$$

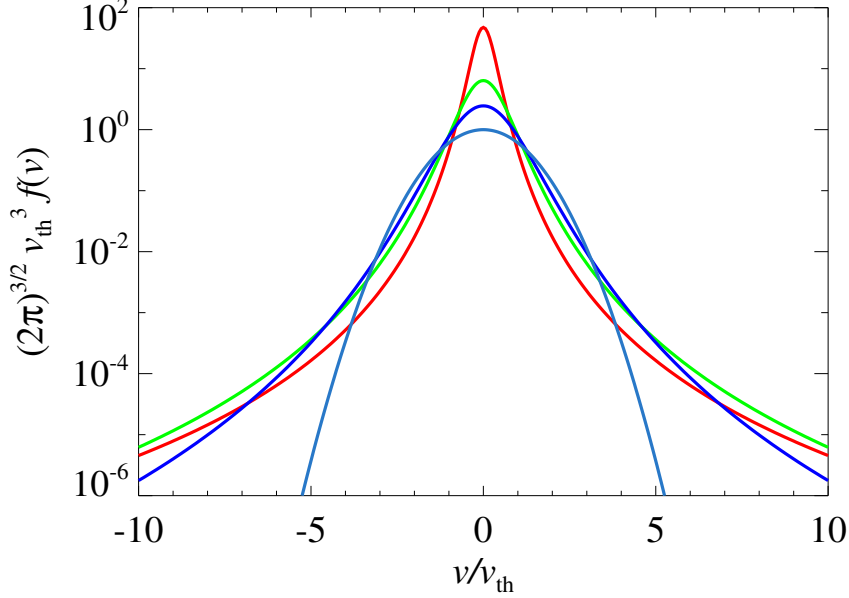


Figure 1.3: Plots of the kappa distribution for  $\kappa = 1.6$  —,  $\kappa = 2.0$  —,  $\kappa = 3.0$  — and  $\kappa = \infty$  — (the Maxwellian case).

Parameters in the above equations are the spectral index,  $\kappa$ , the gamma function,  $\Gamma$ , the kinetic temperature,  $T$ , and mass,  $m$ . It is important to note that  $\kappa > \frac{3}{2}$ , otherwise  $T$  diverges (*Summers and Thorne, 1991*). In the limit  $\kappa \rightarrow \infty$ , the kappa distribution function, Equation (1.6), reduces to a Maxwellian distribution (*Summers and Thorne, 1991*). In practical terms, however, quasi-Maxwellian behaviour can be attained for  $\kappa$  as low as 10 (*Hellberg and Mace, 2002*).

Over the years, the kappa distribution has gained popularity amongst researchers and has become, for many, the model of choice for velocity distributions of charged particle species in space plasmas. It has been shown to be the equilibrium velocity distribution for a plasma in a superthermal radiation field (*Hasegawa et al., 1985*). *Christon et al. (1988)* and *Christon et al. (1989)* showed that the electrons and the central plasma sheet ions can be well fitted by a kappa distribution. The kappa distribution has been shown to be a useful model for electrons and protons escaping from the solar corona (*Maksimovic*

*et al.*, 1997b). It has also been shown to be the best model for particle populations in the Saturnian magnetosphere (*Krimigis et al.*, 1983; *Schippers et al.*, 2008; *Arridge et al.*, 2009). In fact, *Schippers et al.* (2008) found that the electron velocity distribution functions in the Saturnian magnetosphere were best characterised by the sum of two kappa distributions. This idea was reinforced by *Arridge et al.* (2009) who used the sum of two kappa distributions as the electron distribution function in their study of Saturn's nightside and pre-dawn electron plasma sheet.

The kappa distribution has also been used in theoretical studies of plasma waves. *Summers and Thorne* (1991) derived a modified dispersion function based on the kappa distribution valid for integer values of  $\kappa$ . *Mace and Hellberg* (1995) extended this idea and generalised the dispersion function of *Summers and Thorne* (1991) to allow for arbitrary real values of  $\kappa$  by demonstrating its close relationship to the Gauss hypergeometric function. *Hellberg and Mace* (2002) suggested that in some cases, magnetised plasmas may have anisotropic power law distributions. Owing to this, they present the idea of a kappa-Maxwellian distribution, which has a one dimensional kappa distribution along a preferred direction in velocity space and a two dimensional Maxwellian distribution in the plane perpendicular to this direction. *Mace and Hellberg* (2009) showed the more general applicability of the plasma dispersion function,  $Z_{\kappa M}$ , introduced by *Hellberg and Mace* (2002) for plasmas having a kappa-Maxwellian distribution. *Mace* (2004) and *Henning et al.* (2011) used the kappa distribution as the electron particle velocity distribution for a study of electron Bernstein waves. *Henning et al.* (2011) used the kappa distribution to model both electron populations (hot and cool) and applied their model to conditions observed in the Saturnian magnetosphere.

Many mechanisms have been proposed to account for the origin of the superthermal tails of the velocity distributions and occurrence of the kappa distribution in space plasmas (*Pierrard and Lazar* (2010) and references therein). There is also theoretical justification for the use of the kappa distribution from the emerging field of non-extensive statistical mechanics. The introduction of a thermo-statistical theory based on non-extensive entropy provides a statistical mechanical basis for the existence of the kappa distribution (*Tsal-*

lis, 1988). *Leubner* (2002) showed that the kappa distribution arises as a consequence of the generalised entropy by non-extensive statistics. *Livadiotis and McComas* (2009) have shown the kappa distribution to be equivalent to the  $q$ -distribution function that results from the maximisation of the Tsallis entropy (*Pierrard and Lazar*, 2010) under the constraints of the canonical ensemble. The  $q$ -distribution has been applied to investigate plasmas with non-Maxwellian distributions in studies of the solar interior (*Du*, 2006), the solar wind (*Leubner and Voros*, 2005), ion acoustic waves (*Liu and Du*, 2008), and interplanetary space (*Leubner*, 2004), among others.

How Tsallis statistics underpins the theory of the kappa distribution was clearly discussed by *Livadiotis and McComas* (2009). They explained at length how the kappa distribution arises naturally from Tsallis statistical mechanics, essentially as the so-called escort probability function. This link between the kappa distribution and the non-extensive statistical mechanics of Tsallis provides a solid theoretical basis for the existence of the kappa distribution and raises its status above that of only a useful fit function.

## 1.4 Thesis outline

In the work to follow, we study instability of both the L and R mode waves under a variety of conditions. In both of the studies presented, we solve the dispersion relations for EMIC (L mode) and whistler waves (R mode) numerically and without approximation. We assume that the velocity distributions of all particle species is given by the bi-kappa distribution (*Summers and Thorne*, 1991) which is the kappa analogue of the bi-Maxwellian. Using the bi-kappa distribution allows for different temperatures perpendicular and parallel to  $\mathbf{B}_0$ .

Firstly, in Chapter 2, we investigate the parallel propagating whistler instability in the Saturnian magnetosphere, driven by temperature anisotropy in both the hot and cool electron species. *Schippers et al.* (2008) found that the electron velocity distribution functions in the Saturnian magnetosphere were best characterised by the sum of two kappa distributions. Therefore, we shall assume that the velocity distribution of both hot and cool electron species is that of the bi-kappa distribution. This chapter presents

results from a parameter survey of the dispersion relation and growth rate for different anisotropies, temperatures and spectral indices of the two electron components.

Next, in Chapter 3, we present the results from a study of the behaviour of EMIC wave dispersion relation and growth rate for a variety of relative abundances of the ion species.

Following the model of *Mace et al.* (2011), it is assumed that the hot ring current ions, cool ions of plasmaspheric origin, as well as the electrons, have particle velocity distributions modelled by the bi-kappa distribution. In this chapter, the effects of varying the relative ion abundances and how this influences wave growth and damping, are investigated.

Finally, in Chapter 4, we provide the general summary of the thesis.

## Chapter 2

# Whistler mode instability

## 2.1 Introduction

Saturn is a gas planet surrounded by nine rings and orbited by sixty-two known moons (*Gombosi and Hansen, 2005*). Saturn's magnetic field is mostly dipolar, with north and south poles at the end of a single magnetic axis (*Russell, 1993*). However, its magnetic field has also been found to have a weaker quadrupole, octupole and higher components (*Russell, 1993*).

A wealth of data has been sent back by the Cassini spacecraft about the Saturnian magnetosphere. It has been shown to be highly variable and influenced by the solar wind, sources of plasma within the planetary system, as well as the planet's rotation (*Gombosi and Hansen, 2005*). The Saturnian magnetosphere extends between 20 and 25 Saturnian radii ( $R_s \approx 60268\text{km}$ ) towards the Sun. The solar wind strongly affects the magnetic field by compressing it on the day side and drawing it out on the night side to form a long magnetotail (*Russell, 1993*). This magnetotail forms the channel through which solar plasma enters the inner magnetosphere (*Russell, 1993*).

The Saturnian magnetosphere can be divided into three main regions. Region 1, the inner magnetosphere, is found within 9-10  $R_s$ . Region 2 is a dynamic and extended plasmashet and is between 9-10  $R_s$  and 12-14  $R_s$ , depending on solar activity. The extension of the plasmashet is a consequence of the rapid rotation of Saturn ( $T = 10.2$  hours). Region 3 is found beyond 12-14  $R_s$  and forms the high-latitude magnetosphere (*Sittler et al., 1983*; *Gurnett et al., 2005*; *Young et al., 2005*; *André et al., 2008*). The positions of the boundaries that define these regions are largely dependent on solar activity and while these positions do not overlap, the position of these boundaries is variable. A schematic of the regions of the Saturnian magnetosphere and plasma populations derived from Voyager data is provided in Figure 2.1 (*Sittler et al., 1983*).

The primary source of plasma in Saturn's magnetosphere originates within the magnetosphere itself (*Gombosi and Hansen, 2005*). The moons (primarily Enceladus) and rings of Saturn provide a substantial amount of heavy ions making up the dense plasma of the inner magnetosphere. Neutral gas provided by the moons is ionised in the inner magnetosphere, loading the closed magnetic field lines with heavy ions (*Gombosi and Hansen,*

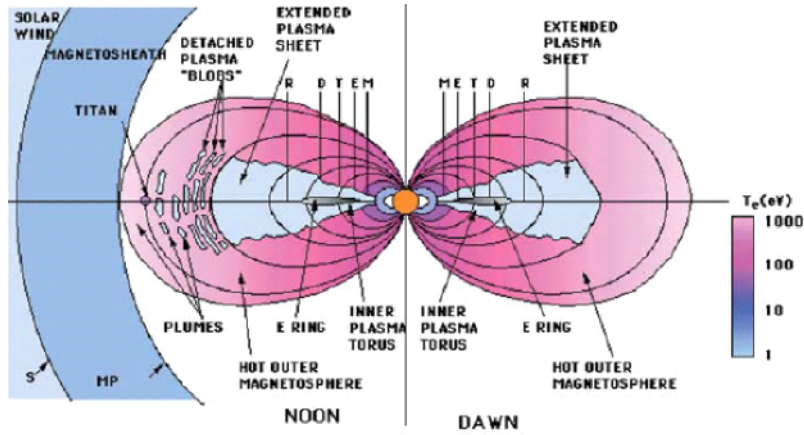


Figure 2.1: Regions and plasma populations in Saturn's magnetosphere as derived from Voyager data (*Sittler et al.*, 1983).

2005). The plasmashet region is composed of a mixture of both cool and hot plasma populations. This is a highly variable region with stretched magnetic field lines (*André et al.*, 2008). The outer magnetosphere has a quiet magnetic field, low plasma density and is strongly influenced by the solar wind (*André et al.*, 2008).

The area of the Saturnian magnetosphere which is of particular interest in this chapter is that of the plasmashet region, where both hot and cool electron populations are found. *Rymer et al.* (2007) performed phase space density analysis of electron measurements made by the Cassini CAPS instrument. They used this to investigate the sources of two different electron components. The two electron components of interest were the hot (1 - 100 keV) and cool (1 - 100 eV) electrons. *Rymer et al.* (2007) found that the source of the cool electrons exists within the boundaries of  $4 R_s$  and  $11 R_s$ . This source is most likely the neutral cloud (*Jurac and Richardson*, 2005). The hot electrons, on the other hand, originate in the outer magnetosphere and are transported radially inward via centrifugal interchange instability (*Hill*, 2006). The energy of the hot electrons tends to increase with a decrease in radial distance, which is consistent with invariant-conserving transport (*Rymer et al.*, 2007).

As previously discussed in Chapter 1, Section 1.1, whistler waves are electromagnetic waves

in a magnetised plasma which occur at frequencies below the electron cyclotron frequency. They are right hand circularly polarised (R mode), corresponding to the sense of electron gyration around the ambient magnetic field. The study of whistler waves in planetary magnetospheres is vital as they play a key role in many space plasma phenomena, such as the pitch-angle scattering and hence precipitation loss of trapped radiation belt electrons (*Kennel and Petschek, 1966; Scarf and Russell, 1976; Tsurutani and Lakhina, 1997; Xiao et al., 2009*). This was discussed in detail in Chapter 1, Section 1.2.

Whistler waves in the Saturnian magnetosphere have long been studied (*Gurnett et al., 1981; Scarf et al., 1982; Gurnett et al., 2005*). Voyager 1 encountered Saturn in November 1980 and provided the first opportunity to investigate plasma waves in the Saturnian magnetosphere. *Gurnett et al. (1981)* reported that whistler mode hiss and chorus emissions were observed. They found that the whistler mode emissions reached a maximum as Voyager 1 approached the equator. Voyager 2 was launched shortly after and was expected to supplement and extend the measurements from plasma wave phenomena of Voyager 1 (*Scarf et al., 1982*). *Scarf et al. (1982)* reported that Voyager 2 also detected whistler mode emissions in the Saturnian magnetosphere, complementing the findings of Voyager 1. Whistler mode emissions were also reported by *Gurnett et al. (2005)* using data from Cassini's first approach and its orbit of Saturn.

The magnetospheres of planets contain many sources of free energy able to produce plasma instabilities which lead to the emission of waves propagating in the whistler mode (*Singhal and Tripathi, 2006*). These instabilities usually arise due to anisotropic electron distributions, such as beams, rings, loss cones and temperature anisotropy. The source of free energy of interest in this study is that of electron temperature anisotropy,  $T_{\perp}/T_{\parallel} > 1$ , where  $T_{\perp}$  and  $T_{\parallel}$  are the perpendicular and parallel kinetic temperatures, respectively. The whistler instability driven by electron temperature anisotropy in a plasma has been studied extensively using both the Maxwellian (*Gary and Wang, 1996; Gary and Cairns, 1999; Quan-Ming et al., 2004; Gary et al., 2011, 2012*) and the kappa (*Mace, 1998; Xiao et al., 2006a,b; Singhal and Tripathi, 2006; Tripathi and Singhal, 2008; Mace and Sydora, 2010; Lazar et al., 2013*) distributions to model the electron velocity distributions.

*Mace* (1998) investigated the electron temperature anisotropy driven whistler instability in the vicinity of the Earth's foreshock. Taking note of the non-Maxwellian nature of the plasma in this region (*Gary*, 1981) and the presence of power law tails on the particle distributions (*Feldman et al.*, 1982), the bi-Lorentzian distribution was used as the particle velocity distribution. The investigation assumed a single electron component and a single proton component, each having the bi-Lorentzian as their statistical distribution in phase space. The conclusion was that when the electrons have a velocity distribution modelled by the bi-Lorentzian distribution, the instability growth rate far exceeds that predicted by the Maxwellian model with similar electron anisotropy.

*Xiao et al.* (2006a) investigated the parallel propagating whistler instability in a plasma using the fully relativistic kappa-loss-cone (KLC) distribution. They evaluated the growth rates of the whistler instability in a plasma composed of a dominant cold electron population, a small hot electron population and background neutralising ions. They compared the results using the KLC distribution to those obtained using the typical kappa distribution under various conditions. They found that the wave growth produced by the kappa distribution was less than that of the KLC distribution in the lower wave frequency range ( $\omega \lesssim 0.1\Omega_e$ ). This trend is reversed at higher wave frequencies. This is due to the KLC distribution having a higher fractional number of resonant electrons (responsible for wave growth) in the lower wave frequency case. The results show that the hot electrons play a dominant role in the whistler instability. They also concluded that the growth rates increase with an increase in thermal anisotropy, but the peak growth rate increased more rapidly for the kappa distribution than for the KLC distribution.

*Xiao et al.* (2006b) considered the whistler instability driven by electron temperature anisotropy. They used a bi-kappa distribution to model the energetic electrons in the presence of a cold plasma (cold isotropic electrons and cold protons). They investigated the instability threshold condition and how it is affected by both the spectral index  $\kappa$ , and the parallel electron beta value (the ratio of electron kinetic pressure to magnetic pressure). The instability threshold in this instance refers to the minimum anisotropy of electrons needed to drive the whistler wave instability. *Xiao et al.* (2006b) found that as the spectral

index is increased, the instability threshold condition for the kappa distribution decreases.

*Singhal and Tripathi* (2006) investigated parallel propagating whistler waves in a plasma composed of both hot and cool electron components. The cool electron component was represented by the Maxwellian distribution, while the hot electron component was given by the bi-Lorentzian distribution. The instability was driven by temperature anisotropy in the hot electrons, while the cool electrons were taken to be isotropic. This model was applied to the Saturnian magnetosphere and the effects on the temporal growth rate of varying the spectral index, temperature, temperature anisotropy and electron density of the hot electron species was investigated. It was found that the greatest electron density of the hot electrons investigated ( $n_h = 2.0\text{cm}^{-3}$ ) produced the broadest instability bandwidth (window of growing frequencies). When the hot electron temperature was increased, this resulted in an increase in growth rate and instability bandwidth. The results of *Singhal and Tripathi* (2006) also show that an increase in the anisotropy of the hot electrons results in an increase in the growth rate as well as an increase in the window of growing frequencies. As the anisotropy is increased, wave growth is observed at higher frequencies. The growth rate was shown to increase as the spectral index of the hot electrons was decreased. The bandwidth was found to increase as the spectral index decreased with wave growth seen at smaller frequencies for lower values of  $\kappa$ . While *Singhal and Tripathi* (2006) found their results were a good fit to observations made by Voyager and Cassini, they used parameters typically observed at low Saturnian radii ( $R = 2.2 - 6 R_s$ ), where the number density of the hot electron species is small ( $n_h = 0.001 - 0.007 n_e$ ).

*Tripathi and Singhal* (2008) studied the whistler instability using an anisotropic kappa loss cone (KLC) distribution and compared it to observations made by Voyager 2 in the outer planets of Uranus and Neptune. They considered a plasma where the cool (thermal) electrons and protons were represented by a Maxwellian distribution and the hot (superthermal) electrons and protons by the bi-kappa distribution (KLC distribution with  $l = 0$ ). They found that an increase in hot electron temperature resulted in a larger instability bandwidth at both Neptune and Uranus. An increase in hot electron anisotropy produced an increase in the window of growing frequencies with wave growth found at

higher frequencies for larger anisotropies. These results are similar to those of *Singhal and Tripathi* (2006) for the Saturnian magnetosphere. *Tripathi and Singhal* (2008) found that an increase in hot electron number density results in an increase in growth rate at both planets. However, an increase in hot electron number density gives a larger instability bandwidth at Uranus, while at Neptune there is no systematic change in bandwidth.

*Mace and Sydora* (2010) extended the work done by *Mace* (1998) by conducting a parameter survey of the parallel propagating whistler instability. Keeping their investigation confined to the single electron component case, they found that the growth rate of the instability is highly dependent on not only the spectral index,  $\kappa_e$ , but also the anisotropy and plasma parallel beta value of the electrons. They found that for small anisotropies, the harder the tail (the smaller the spectral index) on the electron velocity distribution, the larger the maximum growth rate. This trend is reversed at large temperature anisotropies. At intermediate anisotropies, there exists a particular  $\kappa_e$  which produces the maximum growth rate. The  $\kappa_e$  dependence of the peak maximum growth rate is in this case non-monotonic. Most importantly, *Mace and Sydora* (2010) found that there is a vital parallel electron beta dependence of the whistler instability. For a fixed value of the electron temperature anisotropy, the growth rate of the instability is strongly controlled by the parallel electron beta value. They found that the smaller the parallel electron beta value, the smaller the growth rate and vice versa. It is also the parallel electron beta value that governs at which intermediate value of the anisotropy the variation in peak growth rate becomes non-monotonic with an increase in  $\kappa_e$ .

*Lazar et al.* (2013) used the kappa distribution as the particle velocity distribution to investigate the threshold conditions for the whistler instability driven by temperature anisotropy for parameters typically found in the solar wind. They found that the instability threshold can be very sensitive to the spectral index and the effect of the superthermal electrons is dependent on both the temperature anisotropy and plasma beta value. The lowest thresholds were found to decrease with an increase in superthermal electrons at low anisotropies. At larger anisotropies, this trend is reversed and the presence of superthermal particles was found to suppress the growth rate and increase the threshold.

## 2.2 Motivation and aim

*Schippers et al.* (2008) analysed the radial distribution of electron populations in Saturn's magnetosphere using data collected by instruments on board the Cassini satellite. They used a forward modelling method to test different distribution functions which were compared to the observational data. Specifically, they tried three different distribution functions:

- (i) a Maxwellian distribution was used to model both cool (thermal) and hot (superthermal) electron species,
- (ii) a Maxwellian distribution was used to model the thermal electron population, while a kappa distribution was chosen to represent the superthermal electrons and
- (iii) separate kappa distributions were used to model each electron population.

The results of the various models are illustrated in Figure 2.2, reproduced from *Schippers et al.* (2008).

*Schippers et al.* (2008) found that when both electron species were modelled by a Maxwellian distribution, the model produced fluxes that were too low compared to the original data. This is clearly evident in Figure 2.2a. Additionally, it did not reproduce the tail distribution of the superthermal electron population. While using a Maxwellian distribution to model the thermal electrons and a kappa distribution for the superthermal electrons (Figure 2.2b) resolved the pitfalls of the dual Maxwellian model, the model only appeared to fit the data well at low radial distances. At larger radial distances the model was not accurate enough due to the broadening of the thermal peak. On the other hand, *Schippers et al.* (2008) found that the dual kappa distribution model (Figure 2.2c) always provided the best fit to the electron velocity distribution.

*Arridge et al.* (2009) reinforced the idea that in the Saturnian magnetosphere the electron components exhibit a distinctly non-thermal character that requires a weighted sum of two kappa distributions to properly model their velocity distribution. They used dual kappa distributions as the electron distribution functions in their study of Saturn's nightside and pre-dawn electron plasma sheet. The most common state of the nightside and pre-dawn electron plasma sheet is the quiescent state which has a steady electron temperature

of approximately 100 eV. In this state they found that in this region of the Saturnian magnetosphere the electron distribution functions were best characterised by the dual kappa distribution.

The aim of this chapter is to investigate the parallel propagating whistler instability in the Saturnian magnetosphere driven by temperature anisotropy in both the hot and cool electron species. Following the results of *Schippers et al.* (2008), we shall assume that the velocity distributions of both hot and cool electron species are that of the bi-kappa distribution. Using parameter values derived by *Schippers et al.* (2008) as a guide, this chapter presents results from a parameter survey of the dispersion relation and growth rate for different anisotropies, temperatures and spectral indices of the two electron components.

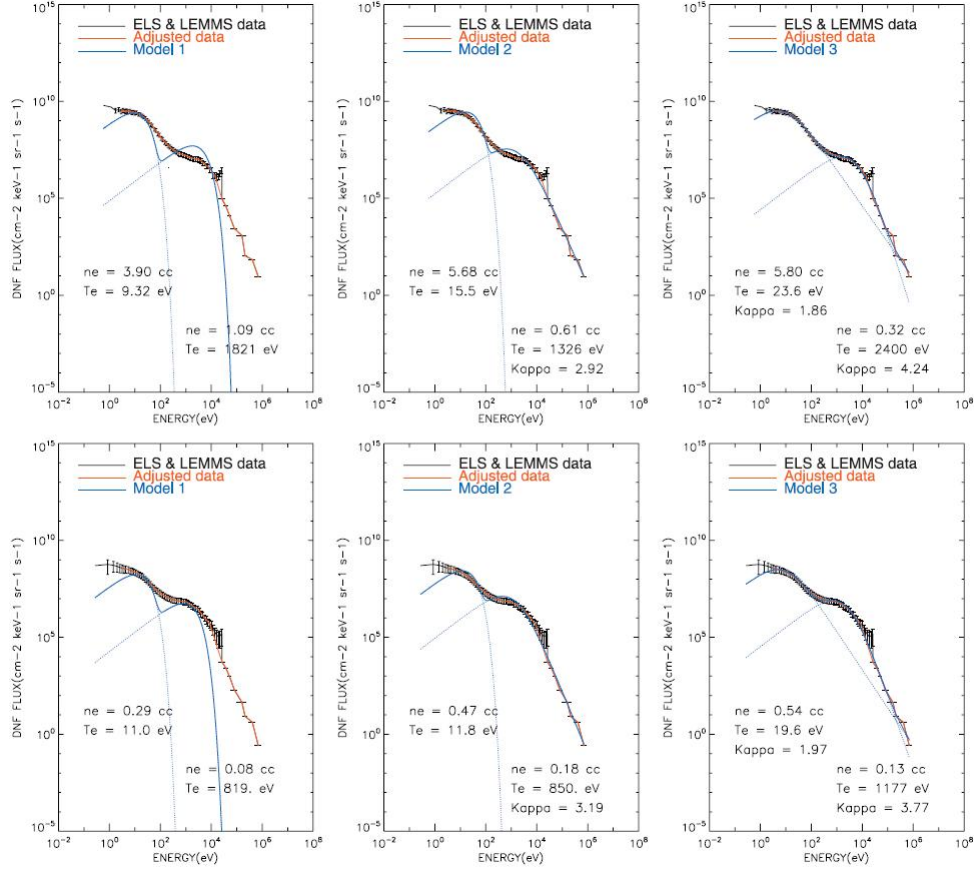


Figure 2.2: (Reproduced from *Schippers et al. (2008)*) Composite CAPS/ELS and MIMI/LEMMS (energy channels C0 - C7) spectral plots of electron intensities versus energy, observed at (top) 2200 UT ( $R = 9R_s$ , local time 18.32 h, latitude 0.23 degrees) and at (bottom) 0727 UT ( $R = 12.8R_s$ , local time 19.82 h, latitude 0.35 degrees) on days of 142 and 143 of year 2006 during Rev. 24, respectively. Original data are represented in black, *Schippers et al. (2008)* interpolated data is represented in red, and the results of the various models used by *Schippers et al. (2008)* are represented in blue. Left (a): Model with two Maxwellian distributions. Middle (b): Model with one Maxwellian and one kappa distribution. Right (c) Model with two kappa distributions.

## 2.3 Model and basic equations

The model and basic equations used in this chapter are similar to those used by *Mace and Sydora* (2010), in which the plasma is assumed to be uniform, collisionless and immersed in a uniform magnetic field,  $\mathbf{B}_0$ . Without loss of generality, the direction of  $\mathbf{B}_0$  is taken to be the  $z$ -axis of the Cartesian coordinate system. It is assumed that all particle species have a bi-kappa velocity distribution (*Summers and Thorne, 1991*),

$$f(v_{\perp}, v_{\parallel}) = \pi^{-3/2} \frac{1}{\theta_{\perp}^2 \theta_{\parallel}} \frac{\Gamma(\kappa + 1)}{\kappa^{3/2} \Gamma(\kappa - \frac{1}{2})} \left( 1 + \frac{v_{\perp}^2}{\kappa \theta_{\perp}^2} + \frac{v_{\parallel}^2}{\kappa \theta_{\parallel}^2} \right)^{-(\kappa+1)}, \quad (2.1)$$

where  $\kappa$  is the spectral index,  $\Gamma$  is the gamma function and  $v_{\perp}$  and  $v_{\parallel}$  are the perpendicular and parallel components of the velocity, respectively, with respect to  $\mathbf{B}_0$ . The parameters  $\theta_{\perp}$  and  $\theta_{\parallel}$  are generalised thermal speeds perpendicular and parallel to  $\mathbf{B}_0$ , respectively, and are related to the kinetic temperatures,  $T_{\perp}$  and  $T_{\parallel}$  via (*Summers and Thorne, 1991*),

$$\theta_{\perp} = \left[ 2 \left( \frac{\kappa - \frac{3}{2}}{\kappa} \right) \right]^{1/2} \left( \frac{T_{\perp}}{m} \right)^{1/2}, \quad (2.2)$$

$$\theta_{\parallel} = \left[ 2 \left( \frac{\kappa - \frac{3}{2}}{\kappa} \right) \right]^{1/2} \left( \frac{T_{\parallel}}{m} \right)^{1/2}. \quad (2.3)$$

The dispersion relation for parallel propagating R mode waves in a plasma with arbitrary velocity distribution,  $f_{j0}$ , is given by (*Gurnett and Bhattacharjee, 2005; Mace and Sydora, 2010*) (see Appendix A for the derivation)

$$\begin{aligned} \frac{k_{\parallel}^2 c^2}{\omega^2} = & 1 - \pi \sum_j \frac{\omega_{pj}^2}{\omega^2} \int_{-\infty}^{\infty} dv_{\parallel} \int_0^{\infty} dv_{\perp} v_{\perp}^2 \frac{1}{k_{\parallel} v_{\parallel} - \omega - \Omega_j} \\ & \cdot \left[ (\omega - k_{\parallel} v_{\parallel}) \frac{\partial f_{j0}}{\partial v_{\perp}} + k_{\parallel} v_{\perp} \frac{\partial f_{j0}}{\partial v_{\parallel}} \right] \quad (\text{Im } \omega > 0), \end{aligned} \quad (2.4)$$

where  $\Omega_j = q_j B_0 / m_j$  is the signed gyrofrequency, where  $q_j$  and  $m_j$  are the charge and mass of the  $j$ th component, respectively. The plasma frequency of the  $j$ th component is given by  $\omega_{pj} = (n_{0j} q_j^2 / \epsilon_0 m_j)^{1/2}$  with  $n_{0j}$  being the equilibrium number density. Other parameters are the parallel component of the wave number  $k_{\parallel}$ , where  $|k_{\parallel}| = k$  since we are

considering the case of parallel propagation with respect to  $\mathbf{B}_0$ , and the wave frequency,  $\omega$ , which is complex and given by  $\omega = \omega_r + i\gamma$ .

In Equation (2.4) it is observed that there is a pole in the integrand. This has been discussed for the L mode wave case in Chapter 1, Section 1.2. The same principles apply to R mode waves whose underlying microphysics of wave-particle interactions is similar. The pole in the integrand at  $v_{\parallel} = v_{\parallel j}^{res}$ , corresponds to the cyclotron resonance condition (*Mace et al.*, 2011)

$$\omega - k_{\parallel} v_{\parallel j}^{res} = -\Omega_j. \quad (2.5)$$

Equation (2.5) indicates that a particle in the distribution whose parallel velocity,  $v_{\parallel}$ , lies close to  $v_{\parallel j}^{res}$  can have a strong interaction with the wave, allowing for momentum and energy exchange between them (*Mace et al.*, 2011; *Tsurutani and Lakhina*, 1997).

We seek to obtain the dispersion relation for parallel propagating electromagnetic R mode waves in a plasma where the velocity distribution for each plasma species,  $j$ , is given by the bi-kappa distribution, Equation (2.1). The derivatives of Equation (2.1) with respect to  $v_{\parallel}$  and  $v_{\perp}$  are

$$\frac{\partial f}{\partial v_{\parallel}} = -\pi^{-3/2} \frac{2}{\theta_{\perp}^2 \theta_{\parallel}^3} \frac{\Gamma(\kappa + 2)}{\kappa^{5/2} \Gamma(\kappa - \frac{1}{2})} v_{\parallel} \left( 1 + \frac{v_{\perp}^2}{\kappa \theta_{\perp}^2} + \frac{v_{\parallel}^2}{\kappa \theta_{\parallel}^2} \right)^{-(\kappa+2)}, \quad (2.6)$$

and

$$\frac{\partial f}{\partial v_{\perp}} = -\pi^{-3/2} \frac{2}{\theta_{\perp}^4 \theta_{\parallel}} \frac{\Gamma(\kappa + 2)}{\kappa^{5/2} \Gamma(\kappa - \frac{1}{2})} v_{\perp} \left( 1 + \frac{v_{\perp}^2}{\kappa \theta_{\perp}^2} + \frac{v_{\parallel}^2}{\kappa \theta_{\parallel}^2} \right)^{-(\kappa+2)}, \quad (2.7)$$

respectively. Substituting Equations (2.6) and (2.7) into Equation (2.4) yields,

$$\begin{aligned} \frac{k_{\parallel}^2 c^2}{\omega^2} &= 1 + \sum_j \pi^{-1/2} \frac{2}{\theta_{\perp j}^2 \theta_{\parallel j}} \frac{\Gamma(\kappa_j + 2)}{\kappa_j^{5/2} \Gamma(\kappa_j - \frac{1}{2})} \frac{\omega_{pj}^2}{\omega^2} \int_{-\infty}^{\infty} \frac{dv_{\parallel}}{k_{\parallel} v_{\parallel} - \omega - \Omega_j} \\ &\cdot \left[ \frac{\omega}{\theta_{\perp j}^2} + \left( \frac{1}{\theta_{\parallel j}^2} - \frac{1}{\theta_{\perp j}^2} \right) k_{\parallel} v_{\parallel} \right] \int_0^{\infty} dv_{\perp} v_{\perp}^3 \left( 1 + \frac{v_{\perp}^2}{\kappa_j \theta_{\perp j}^2} + \frac{v_{\parallel}^2}{\kappa_j \theta_{\parallel j}^2} \right)^{-(\kappa+2)}. \end{aligned} \quad (2.8)$$

Using standard integrals (*Gradshteyn and Ryzhik*, 2000) to evaluate Equation (2.8) (see Appendix B for a full derivation), we arrive at the dispersion relation for parallel propagating electromagnetic R mode waves in a plasma where the velocity distribution for each

plasma species,  $j$ , is given by the bi-kappa distribution (*Mace and Sydora, 2010*)

$$\frac{k^2 c^2}{\omega^2} = 1 + \sum_j \frac{\omega_{pj}^2}{\omega^2} \left\{ A_j + \left[ A_j \left( \frac{\omega + \Omega_j}{k\theta_{\parallel j}} \right) + \frac{\omega}{k\theta_{\parallel j}} \right] U_{\kappa_j} \left( \frac{\omega + \Omega_j}{k\theta_{\parallel j}} \right) \right\}, \quad (2.9)$$

where  $k = |k_{\parallel}|$ . The function  $U_{\kappa}$  is the dispersion plasma function (*Mace and Hellberg, 2009*) defined in terms of the Gauss hypergeometric function  ${}_2F_1$  by

$$U_{\kappa}(\zeta) = i \frac{(\kappa - \frac{1}{2})}{\kappa^{3/2}} {}_2F_1 \left[ 1, 2\kappa; \kappa + 1; \frac{1}{2} \left( 1 - \frac{\zeta}{i\kappa^{1/2}} \right) \right]. \quad (2.10)$$

The thermal anisotropy of particle species  $j$  is defined by

$$A_j = \frac{\theta_{\perp j}^2}{\theta_{\parallel j}^2} - 1 = \frac{T_{\perp j}}{T_{\parallel j}} - 1. \quad (2.11)$$

*Mace and Sydora (2010)* derived an estimate of the growth rate of the whistler instability in an electron-ion plasma. Using the same procedure we can extend it to the dual electron case. We begin by making the assumption that (*Mace and Sydora, 2010*)

$$\left| \frac{\omega + \Omega_j}{k\theta_{\parallel j}} \right| \gg 1, \quad (2.12)$$

for each species  $j$ . This allows for the asymptotic expansion of the dispersion plasma function  $U_{\kappa}$  such that (*Mace and Sydora, 2010*),

$$\begin{aligned} U_{\kappa}(\zeta) &= \pi^{1/2} \frac{\Gamma(\kappa)}{\kappa^{1/2} \Gamma(\kappa - 1/2)} \left( 1 + \frac{\zeta^2}{\kappa} \right)^{-\kappa} (i - \tan \kappa \pi) \\ &\quad - \frac{1}{\zeta} - \frac{1}{2} \left( \frac{\kappa}{\kappa - 3/2} \right) \frac{1}{\zeta^3} + \dots \end{aligned} \quad (2.13)$$

Substituting the first three terms of Equation (2.13) with  $\zeta = (\omega + \Omega_j)/(k\theta_{\parallel j})$  into Equation (2.9) yields

$$\begin{aligned} \frac{k^2 c^2}{\omega^2} &= 1 + \sum_j \frac{\omega_{pj}^2}{\omega^2} \left\{ A_j + \left[ A_j \left( \frac{\omega + \Omega_j}{k\theta_{\parallel j}} \right) + \frac{\omega}{k\theta_{\parallel j}} \right] \right. \\ &\quad \cdot \left[ i\pi^{1/2} \frac{\Gamma(\kappa_j)}{\kappa_j^{1/2} \Gamma(\kappa_j - 1/2)} \left( 1 + \frac{1}{\kappa_j} \left( \frac{\omega + \Omega_j}{k\theta_{\parallel j}} \right)^2 \right)^{-\kappa_j} \right. \\ &\quad \left. \left. - \frac{k\theta_{\parallel j}}{\omega + \Omega_j} - \frac{1}{2} \left( \frac{\kappa_j}{\kappa_j - 3/2} \right) \frac{(k\theta_{\parallel j})^3}{(\omega + \Omega_j)^3} \right] \right\}. \end{aligned} \quad (2.14)$$

It is noted that for tractability purposes we have ignored the small term proportional to  $\tan \kappa\pi$  in Equation (2.14). For cases where  $\kappa$  is a non-integer, it only gives rise to a small additional term in the real part, and vanishes identically when  $\kappa$  is an integer. Expanding the brackets in Equation (2.14) yields,

$$\begin{aligned}
\frac{k^2 c^2}{\omega^2} &= 1 + \sum_j \frac{\omega_{pj}^2}{\omega^2} \left\{ -\frac{1}{2} \left( \frac{\kappa_j}{\kappa_j - 3/2} \right) \frac{A_j(k\theta_{\parallel j})^2}{(\omega + \Omega_j)^2} - \frac{\omega}{\omega + \Omega_j} - \frac{1}{2} \left( \frac{\kappa_j}{\kappa_j - 3/2} \right) \frac{(k\theta_{\parallel j})^2 \omega}{(\omega + \Omega_j)^3} \right\} \\
&+ i\pi^{1/2} \sum_j \frac{\omega_{pj}^2}{\omega^2} \frac{\Gamma(\kappa_j)}{\kappa_j^{1/2} \Gamma(\kappa_j - 1/2)} \left[ A_j \left( \frac{\omega + \Omega_j}{k\theta_{\parallel j}} \right) + \frac{\omega}{k\theta_{\parallel j}} \right] \left[ 1 + \frac{1}{\kappa_j} \left( \frac{\omega + \Omega_j}{k\theta_{\parallel j}} \right)^2 \right]^{-\kappa_j} \\
&= 1 - \sum_j \frac{\omega_{pj}^2}{\omega(\omega + \Omega_j)} \left\{ 1 + \frac{1}{2} \left( \frac{\kappa_j}{\kappa_j - 3/2} \right) \frac{A_j(k\theta_{\parallel j})^2}{\omega(\omega + \Omega_j)} + \frac{1}{2} \left( \frac{\kappa_j}{\kappa_j - 3/2} \right) \frac{(k\theta_{\parallel j})^2}{(\omega + \Omega_j)^2} \right\} \\
&+ i\pi^{1/2} \sum_j \frac{\omega_{pj}^2}{\omega^2} \frac{\Gamma(\kappa_j)}{\kappa_j^{1/2} \Gamma(\kappa_j - 1/2)} \left[ A_j \left( \frac{\omega + \Omega_j}{k\theta_{\parallel j}} \right) + \frac{\omega}{k\theta_{\parallel j}} \right] \left[ 1 + \frac{1}{\kappa_j} \left( \frac{\omega + \Omega_j}{k\theta_{\parallel j}} \right)^2 \right]^{-\kappa_j}.
\end{aligned} \tag{2.15}$$

Simplifying Equation (2.15) we arrive at the approximate dispersion relation (*Mace and Sydora, 2010*),

$$\begin{aligned}
\frac{k^2 c^2}{\omega^2} &= 1 - \sum_j \frac{\omega_{pj}^2}{\omega(\omega + \Omega_j)} \left\{ 1 + \frac{1}{2} \left( \frac{\kappa_j}{\kappa_j - 3/2} \right) \frac{k^2 \theta_{\parallel j}^2}{\omega(\omega + \Omega_j)^2} [A_j(\omega + \Omega_j) + \omega] \right\} \\
&+ i\pi^{1/2} \sum_j \frac{\omega_{pj}^2}{\omega^2} \frac{\Gamma(\kappa_j)}{\kappa_j^{1/2} \Gamma(\kappa_j - 1/2)} \left[ A_j \left( \frac{\omega + \Omega_j}{k\theta_{\parallel j}} \right) + \frac{\omega}{k\theta_{\parallel j}} \right] \left[ 1 + \frac{1}{\kappa_j} \left( \frac{\omega + \Omega_j}{k\theta_{\parallel j}} \right)^2 \right]^{-\kappa_j}.
\end{aligned} \tag{2.16}$$

*Mace and Sydora (2010)* noted an interesting phenomenon in Equation (2.16), which we repeat here. If we substitute  $\theta_{\parallel j}$  as defined in Equation (2.3) into Equation (2.16) it is observed that all  $\kappa_j$  dependence vanishes in the real part. This is due to the chosen order of expansion of  $U_\kappa$  (Equation (2.13)) and effectively shows that the  $\kappa_j$  dependence in the real part of the dispersion relation only enters at higher orders (*Mace and Sydora, 2010*). Specialising Equation (2.16) to a plasma composed of ions “i”, hot electrons “h”, and cool

electrons “c”, gives,

$$\begin{aligned} \frac{k^2 c^2}{\omega^2} = & 1 - \frac{\omega_{ph}^2}{\omega(\omega - |\Omega_e|)} - \frac{\omega_{pc}^2}{\omega(\omega - |\Omega_e|)} - \frac{\omega_{pi}^2}{\omega(\omega + \Omega_i)} \\ & + i\pi^{1/2} \sum_{j=h,c} \frac{\omega_{pj}^2}{\omega^2} \frac{\Gamma(\kappa_j)}{\kappa_j^{1/2} \Gamma(\kappa_j - 1/2)} \left[ A_j \left( \frac{\omega - |\Omega_e|}{k\theta_{\parallel j}} \right) + \frac{\omega}{k\theta_{\parallel j}} \right] \left[ 1 + \frac{1}{\kappa_j} \left( \frac{\omega - |\Omega_e|}{k\theta_{\parallel j}} \right)^2 \right]^{-\kappa_j}, \end{aligned} \quad (2.17)$$

where we have ignored the thermal effects in the real part of Equation (2.17) for tractability reasons. We emphasise that the sum over particle species  $j$  in the imaginary term of Equation (2.17) is only over hot “h”, and cool “c”, electron species. The small ion damping term has been ignored due to its negligible contribution compared to that of the electron terms.

To find weakly damped/growing solutions to Equation (2.17), let  $\omega = \omega_r + i\gamma$ , where  $|\gamma| \ll \omega_r$  is assumed. Using the usual method (*Krall and Trivelpiece*, 1986, p. 389) of performing a Taylor expansion about some real frequency  $\omega = \omega_r$  ( $\gamma = 0$ ) of both the real and imaginary parts of Equation (2.17) and ignoring terms  $O(\gamma^2)$  and higher yields

$$\begin{aligned} \frac{k^2 c^2}{\omega_r^2} = & 1 - \frac{\omega_{ph}^2}{\omega_r(\omega_r - |\Omega_e|)} - \frac{\omega_{pc}^2}{\omega_r(\omega_r - |\Omega_e|)} - \frac{\omega_{pi}^2}{\omega_r(\omega_r + \Omega_i)} \\ & + i \frac{\gamma}{\omega_r} \left[ 2 \frac{k^2 c^2}{\omega_r^2} + \omega_{ph}^2 \frac{(2\omega_r - |\Omega_e|)}{\omega_r(\omega_r - |\Omega_e|)^2} + \omega_{pc}^2 \frac{(2\omega_r - |\Omega_e|)}{\omega_r(\omega_r - |\Omega_e|)^2} + \omega_{pi}^2 \frac{(2\omega_r + \Omega_i)}{\omega_r(\omega_r + \Omega_i)^2} \right] \\ & + i\pi^{1/2} \sum_{j=h,c} \frac{\Gamma(\kappa_j)}{\kappa_j^{1/2} \Gamma(\kappa_j - 1/2)} \frac{\omega_{pj}^2}{\omega_r^2} \left[ A_j \left( \frac{\omega_r - |\Omega_e|}{k\theta_{\parallel j}} \right) + \frac{\omega_r}{k\theta_{\parallel j}} \right] \left[ 1 + \frac{1}{\kappa_j} \left( \frac{\omega_r - |\Omega_e|}{k\theta_{\parallel j}} \right)^2 \right]^{-\kappa_j}. \end{aligned} \quad (2.18)$$

Solving for the real part of Equation (2.18) we arrive at

$$\frac{k^2 c^2}{\omega_r^2} = 1 - \frac{\omega_{ph}^2}{\omega_r(\omega_r - |\Omega_e|)} - \frac{\omega_{pc}^2}{\omega_r(\omega_r - |\Omega_e|)} - \frac{\omega_{pi}^2}{\omega_r(\omega_r + \Omega_i)}, \quad (2.19)$$

while the imaginary part of Equation (2.18) yields an expression for the growth/damping rate,  $\gamma$ , such that

$$\begin{aligned} \frac{\gamma}{\omega_r} = & -\pi^{1/2} \sum_{j=h,c} \frac{\Gamma(\kappa_j)}{\kappa_j^{1/2} \Gamma(\kappa_j - 1/2)} \frac{\omega_{pj}^2}{\omega_r^2} \frac{1}{R(\omega_r)} \left[ A_j \left( \frac{\omega_r - |\Omega_e|}{k\theta_{\parallel j}} \right) + \frac{\omega_r}{k\theta_{\parallel j}} \right] \\ & \cdot \left[ 1 + \frac{1}{\kappa_j} \left( \frac{\omega_r - |\Omega_e|}{k\theta_{\parallel j}} \right)^2 \right]^{-\kappa_j}. \end{aligned} \quad (2.20)$$

This expression for the growth rate, Equation (2.20), is similar to that derived by *Mace and Sydora* (2010) with the exception being that here we have the sum over two electron species rather than the single electron species case considered by *Mace and Sydora* (2010). The function  $R(\omega_r)$  is defined analogously to that of *Mace and Sydora* (2010) as

$$R(\omega_r) = 2 \frac{k^2 c^2}{\omega_r^2} + \omega_{ph}^2 \frac{(2\omega_r - |\Omega_e|)}{\omega_r(\omega_r - |\Omega_e|)^2} + \omega_{pc}^2 \frac{(2\omega_r - |\Omega_e|)}{\omega_r(\omega_r - |\Omega_e|)^2} + \omega_{pi}^2 \frac{(2\omega_r + \Omega_i)}{\omega_r(\omega_r + \Omega_i)^2}, \quad (2.21)$$

and is identical to their form, upon noting that  $\omega_{pe}^2 = \omega_{ph}^2 + \omega_{pc}^2$ . Equation (2.21) can be simplified by eliminating  $k^2 c^2 / \omega_r^2$  using Equation (2.19) and, therefore [cf. *Mace and Sydora* (2010)],

$$R(\omega_r) = 2 + \frac{\omega_{ph}^2 |\Omega_e|}{\omega_r(\omega_r - |\Omega_e|)^2} + \frac{\omega_{pc}^2 |\Omega_e|}{\omega_r(\omega_r - |\Omega_e|)^2} - \frac{\omega_{pi}^2 \Omega_i}{\omega_r(\omega_r + \Omega_i)^2}. \quad (2.22)$$

The expression for the growth rate, Equation (2.20), provides great insight into the instability criteria. In Equation (2.20) it is evident that the contribution to the growth rate of an electron species  $j$  with thermal anisotropy  $A_j$  will be zero for frequencies  $\omega_r$  satisfying (*Mace and Sydora*, 2010)

$$A_j (\omega_r - |\Omega_e|) + \omega_r = 0. \quad (2.23)$$

This, in turn, implies that the electron species  $j$  will make a positive contribution to the growth rate when

$$A_j (\omega_r - |\Omega_e|) + \omega_r < 0, \quad (2.24)$$

or synonymously, when [cf. *Mace and Sydora* (2010)]

$$\omega_r < \frac{A_j}{A_j + 1} |\Omega_e| \equiv \omega_j^*. \quad (2.25)$$

Conversely, for  $\omega_r > \omega_j^*$  the electron species  $j$  produces cyclotron damping and the overall growth rate of the wave at such frequencies is reduced.

Table 2.1: Table of the baseline parameters used in the parameter survey. The subscripts, “h” and “c” correspond to hot and cool electron species, respectively, while “i” corresponds to the ion species. This data has been extracted by *Baluku et al. (2011)* from *Schippers et al. (2008)* for  $13.1R_s$ .

	$T$ (eV)	$n_0$ ( $\text{cm}^{-3}$ )	$\kappa$
h	1000	0.18	4.0
c	10.2	0.21	2.1
i	0.102	0.39	5.0

## 2.4 Numerical results

In this section the numerical solutions to Equation (2.9) without approximations, for a plasma composed of two electron species with disparate temperatures and a single, singly charged ion species (proton) is presented. The aim of this section is to provide a parameter survey of the whistler instability driven by electron thermal anisotropy within the environment of the Saturnian magnetosphere. For this purpose, baseline parameter values as presented in Table 2.1 are used. The electron parameters in Table 2.1 were extracted from the Saturnian magnetospheric electron model of *Schippers et al. (2008)* by *Baluku et al. (2011)*. These parameter values are indicative of those found in the vicinity of  $13.1R_s$  where  $B_0 = 9.412$  nT in the standard dipolar model (*Baumjohann and Treumann, 1996*). The ion parameters in Table 2.1 are representative only, and are characteristic of the isotropic ion parameters typically seen in space plasmas (*Christon et al., 1988, 1989*). The objective is to account for the innate temporal variability of a dynamic system such as the Saturnian magnetosphere, giving rise to variations in spectral indices, electron anisotropies and temperatures.

An important parameter governing the whistler instability is the parallel electron beta value of each electron species  $j$ . It is given by (*Mace and Sydora, 2010*),

$$\beta_{\parallel j} = \frac{n_{0j} T_{\parallel j}}{B_0^2 / (2\mu_0)} = 2 \frac{\omega_{pj}^2 / \Omega_e^2}{c^2 / v_{th\parallel j}^2}. \quad (2.26)$$

From Equation (2.26) it can be seen that this value is dependent on both the number

density and temperature of the electron species for a given magnetic field strength,  $B_0$ . Attention should also be drawn to the fact that all parallel wave numbers  $k = |k_{\parallel}|$ , in the figures to follow, are normalised with respect to the inverse of the hot electron thermal gyroradius,  $\rho_h = v_{th\parallel h}/|\Omega_e|$ . The wave frequency,  $\omega$ , has been normalised with respect to the electron gyrofrequency,  $|\Omega_e|$ .

### 2.4.1 Variation of the spectral index of the hot electrons, $\kappa_h$

In this section the effects of varying the spectral index of the hot electrons on the parallel whistler instability are investigated for various anisotropies of both electron species and two different  $\beta_{\parallel h}$  values.

#### Variation of $\kappa_h$ with $\beta_{\parallel h} = 0.816992$ and $\beta_{\parallel c} = 0.00972221$

The parameters in this section are as in Table 2.1 with  $B_0 = 9.412$  nT and, therefore,  $\beta_{\parallel h} = 0.816992$  and  $\beta_{\parallel c} = 0.00972221$ . The parameter survey begins with an investigation into the effects of varying the spectral index of the hot electrons with a variety of  $A_h$  values and with  $A_c = 0$ . Figure 2.3 illustrates the dispersion relation  $\omega_r(k)$  and growth rate  $\gamma(k)$  curves for a sequence of plasmas with different  $\kappa_h$  values and fixed  $A_h = 0.1$  and  $A_c = 0$ . The real part of the dispersion relation (top panel) shows very little dependence on  $\kappa_h$  at small and intermediate wave numbers ( $k\rho_h \lesssim 0.7$ ). The  $\kappa_h$  dependence is enhanced as the wave number is increased with a significant difference in dispersive characteristics emerging beyond  $k\rho_h \approx 0.7$ . Over the interval  $0.7 \lesssim k\rho_h \lesssim 1.0$ , we notice that an increase in  $\kappa_h$  produces an increase in frequency.

The middle panel of Figure 2.3 illustrates the growth rate curves of the instability. It is noted here that in the figures to follow only the values of the growth rate,  $\gamma$ , corresponding to instability are illustrated as this study is focused on the variability of wave growth. Whether the instability will experience growth (or be cyclotron damped) depends on the contribution to the growth rate provided by each electron species. To investigate this further we follow the approach of *Mace and Sydora* (2010). Specialising Equation (2.20) to a plasma composed of hot electrons with anisotropy  $A_h$ , and cool electrons with  $A_c = 0$ ,

gives

$$\begin{aligned} \frac{\gamma}{\omega_r} = & -\pi^{1/2} \frac{\Gamma(\kappa_h)}{\kappa_h^{1/2} \Gamma(\kappa_h - 1/2)} \frac{\omega_{ph}^2}{\omega_r^2} \frac{1}{R(\omega_r)} \left[ A_h \left( \frac{\omega_r - |\Omega_e|}{k\theta_{\parallel h}} \right) + \frac{\omega_r}{k\theta_{\parallel h}} \right] \\ & \times \left[ 1 + \frac{1}{\kappa_h} \left( \frac{\omega_r - |\Omega_e|}{k\theta_{\parallel h}} \right)^2 \right]^{-\kappa_h} \\ & - \pi^{1/2} \frac{\Gamma(\kappa_c)}{\kappa_c^{1/2} \Gamma(\kappa_c - 1/2)} \frac{\omega_{pc}^2}{\omega_r^2} \frac{1}{R(\omega_r)} \left[ \frac{\omega_r}{k\theta_{\parallel c}} \right] \left[ 1 + \frac{1}{\kappa_c} \left( \frac{\omega_r - |\Omega_e|}{k\theta_{\parallel c}} \right)^2 \right]^{-\kappa_c}. \end{aligned} \quad (2.27)$$

From Equation (2.27) it is evident that for the chosen anisotropies, the cool electrons will always produce cyclotron damping since they are isotropic and, therefore, the second term is always negative. The hot electrons on the other hand, will contribute positively to the growth rate when [cf. *Mace and Sydora (2010)*]

$$A_h (\omega_r - |\Omega_e|) + \omega_r < 0, \quad (2.28)$$

i.e., for all frequencies satisfying

$$\omega_r < \frac{A_h}{A_h + 1} |\Omega_e| = \omega_h^*. \quad (2.29)$$

For the case with  $A_h = 0.1$ , according to Equation (2.29) the hot electrons will make a positive contribution to the growth rate for all frequencies satisfying  $\omega_r < \omega_h^* = 0.0909091|\Omega_e|$ . For a plasma composed of hot anisotropic electrons and cool electrons with  $A_c = 0$ , the instability will experience growth as long as the positive contribution provided by the hot electrons in Equation (2.27) is greater in magnitude than the magnitude of the second term in that equation, responsible for cool electron cyclotron damping. This is only possible for frequencies  $\omega_r < \omega_h^*$ , otherwise both electron species are a source of cyclotron damping.

In all cases investigated in Figure 2.3, increasing the spectral index of the hot electrons with  $A_h = 0.1$  and  $A_c = 0$ , resulted in a decrease in the window of growing wave numbers, i.e., the greater  $\kappa_h$ , the smaller the instability bandwidth. This is illustrated in the middle panel of Figure 2.3. An interesting phenomenon is observed at small wave numbers ( $k\rho_h \lesssim 0.1$ ). In this region, an increase in  $\kappa_h$  results in a monotonic decrease in the growth rate. This relates to an earlier discussion in Chapter 1, Section 1.2. When the spectral

index is small there are more superthermal particles in the tail of the particle velocity distribution. Owing to this, there are more particles with parallel velocities,  $v_{\parallel}$ , large enough to induce the Doppler shift required for cyclotron resonance at these small wave numbers (Mace *et al.*, 2011). The more particles that participate in this cyclotron resonance process, the greater the contribution to the growth rate. As the spectral index is increased the probability of these wave-particle interactions occurring is decreased, therefore, wave growth is suppressed.

In the middle panel of Figure 2.3, it is seen that with the exception of the case where  $\kappa_h = 1.6$ , an increase in  $\kappa_h$  results in a monotonic decrease in the peak growth rate with the peak maximum growth rate corresponding to the case  $\kappa_h = 2.0$ . In the case of the curve representing  $\kappa_h = 1.6$ , the peak growth rate lies below the curve corresponding to  $\kappa_h = 4.0$  but above the case where  $\kappa_h = 20.0$ .

In their investigation of the single electron species case Mace and Sydora (2010) determined that there exists a single frequency and wave number at which all electron thermal effects and all  $\kappa$  dependency, vanish. This point is seen graphically as a common point of intersection in the plots of the real part of the dispersion relation and the wave number corresponding to this frequency defines the upper bound of the interval of growing wave numbers. This does not apply to the two electron species case when  $A_h \neq A_c$  as there is no single point at which  $\gamma = 0$  for all curves. This is illustrated in the bottom panel of Figure 2.3. From Equation (2.27) it is evident that the wave number at which  $\gamma = 0$  ( $k^* \rho_h$ ) is dependent on both  $\kappa_c$  and  $\kappa_h$ . It is at this point ( $k^* \rho_h$ ) that the negative contribution from the cool electron term in Equation (2.27) equals in magnitude the magnitude of the positive contribution provided by the hot electrons. The bottom panel of Figure 2.3 illustrates the dependence of  $k^* \rho_h$  on  $\kappa_h$  for a fixed  $\kappa_c = 2.1$ . To interpret this figure we note that the values of  $k^* \rho_h$  are those where the growth rate curve  $\gamma/|\Omega_e|$  passes through zero. For  $A_h = 0.1$ ,  $A_c = 0$  the wave number at which  $\gamma = 0$ ,  $k^* \rho_h$ , is greatest for  $\kappa_h = 3.0$ . For  $\kappa_h < 3.0$  there is a monotonic increase in  $k^* \rho_h$  with an increase in  $\kappa_h$ . For  $\kappa_h > 3.0$  this monotonic trend is reversed, i.e., an increase in  $\kappa_h$  results in a decrease in  $k^* \rho_h$ .

Figure 2.4 is similar to Figure 2.3 except that here the anisotropy of the hot electrons has

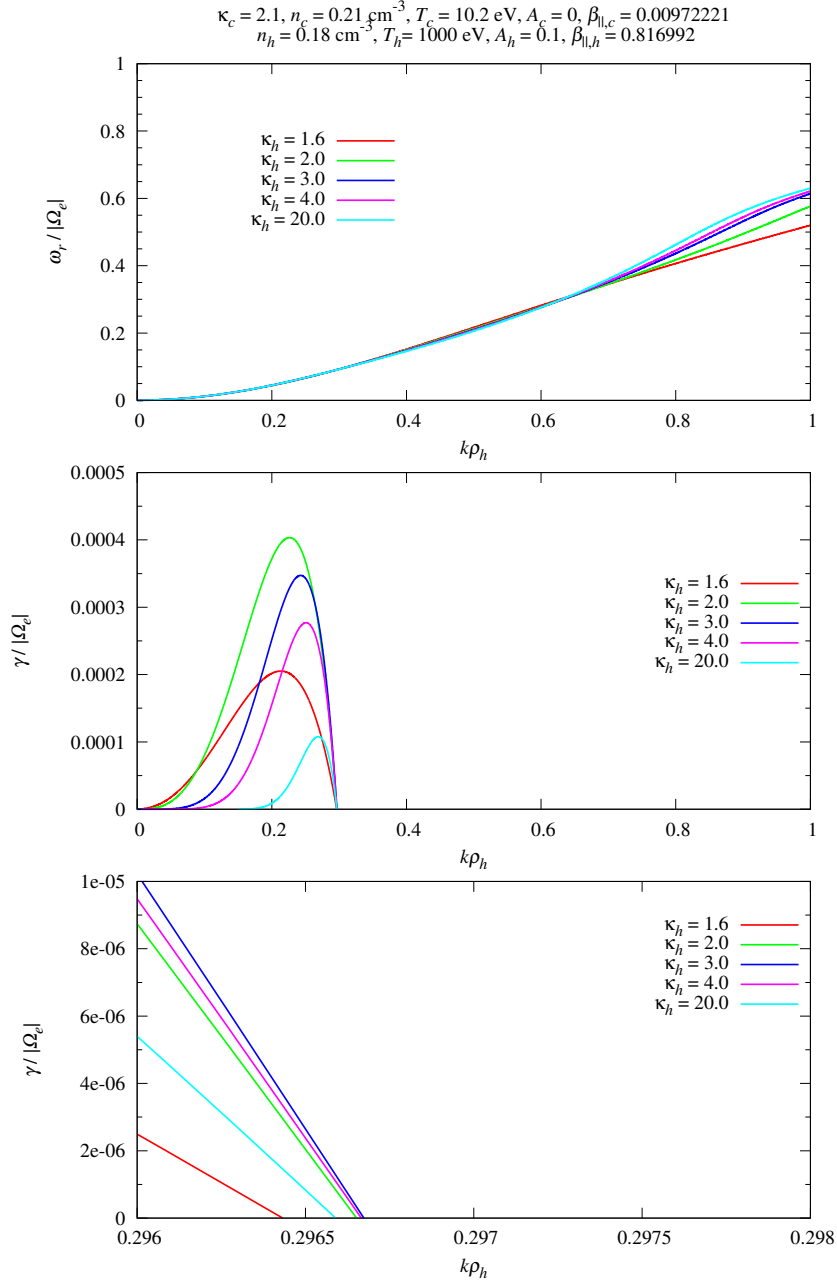


Figure 2.3: Whistler mode dispersion relation (top) and growth rate (middle) for a sequence of plasmas having different  $\kappa_h$  values, fixed temperature anisotropies corresponding to  $A_c = 0, A_h = 0.1$  and all other parameters are as in Table 2.1. The bottom panel illustrates the dependence of  $k^* \rho_h$  on  $\kappa_h$  for a fixed  $\kappa_c$  by magnifying the middle panel around the values of  $k\rho_h$  where  $\gamma = 0$  (see text).

been increased so that  $A_h = 0.2$ . The  $\kappa_h$  dependence of the real part of the dispersion relation has not been greatly affected by the increase in anisotropy of the hot electrons. The dependence of the real frequency on  $\kappa_h$  is again only seen at large wave numbers,  $0.7 \lesssim k\rho_h \lesssim 1.0$ , with an increase in  $\kappa_h$  producing an increase in frequency over this range. At smaller wave numbers,  $k\rho_h \lesssim 0.7$ , there is no significant difference between the curves for different values of  $\kappa_h$  within graphical accuracy.

The growth rate on the other hand has been significantly altered by an increase in  $A_h$ . In the middle panel of Figure 2.4 it is observed that the peak maximum growth rate corresponds to  $\kappa_h = 4.0$  rather than  $\kappa_h = 2.0$  as was seen in the case where  $A_h = 0.1$ . For  $A_h = 0.2$ , plasmas with  $\kappa_h < 4.0$  will experience a monotonic increase in peak growth rate with an increase in  $\kappa_h$ . For cases where  $\kappa_h > 4.0$ , the maximum growth rate monotonically decreases with an increase in  $\kappa_h$ .

At this level of anisotropy, the hot electrons will contribute positively to the growth rate for all frequencies  $\omega_r < \omega_h^* = 0.16667|\Omega_e|$  corresponding to  $A_h = 0.2$ . The cool electrons remain a source of damping. The instability will have a resultant positive growth rate as long as (i)  $\omega_r < \omega_h^*$  and (ii) the positive contribution provided by the hot electrons is greater than the damping term from the cool electrons, as mentioned before.

The dependency on  $\kappa_h$  of the wave number at which  $\gamma = 0$ ,  $k^*\rho_h$ , is monotonic for the case  $A_h = 0.2$ ,  $A_c = 0$ . An increase in  $\kappa_h$  results in an increase in  $k^*\rho_h$  as seen in the bottom panel of Figure 2.4. However, the differences between each case are small and do not affect the overall trend with regard to the window of growing wave numbers, which is dominated by the growth rate behaviour at small wave numbers,  $k\rho_h \lesssim 0.1$ . In all cases of  $\kappa_h$  investigated, an increase in the spectral index of the hot electrons results in a decrease in the instability bandwidth. As explained previously, this is because as the spectral index of the hot electrons is increased, the probability of cyclotron resonance of the particles at small wave numbers ( $k\rho_h \lesssim 0.1$ ) is decreased.

Figure 2.5 shows the dispersion relation and growth rate for the case where  $A_h = 0.5$  ( $A_c = 0$ ). At this level of hot electron anisotropy, a variation in the spectral index of the hot electrons results in a more significant change in the real part of the dispersion relation. For

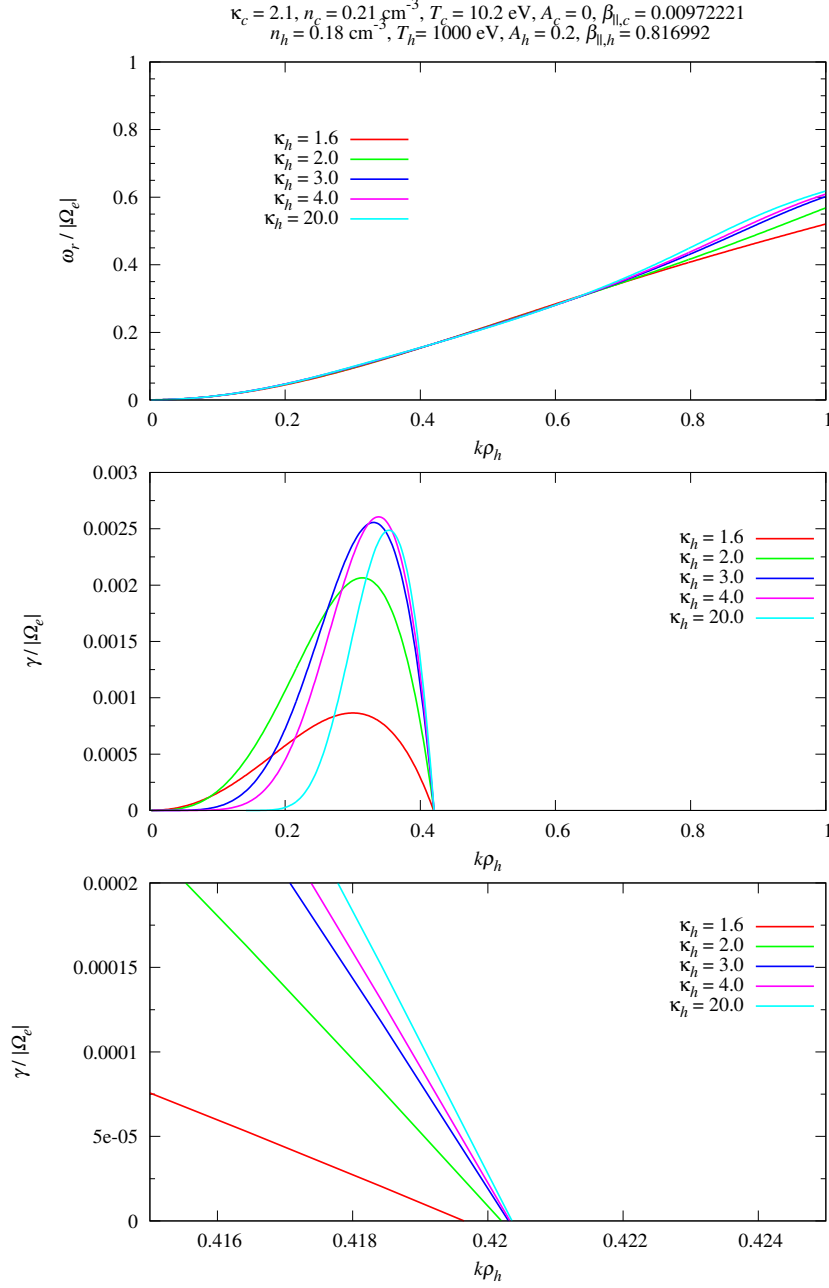


Figure 2.4: Whistler mode dispersion relation (top) and growth rate (middle) for a sequence of plasmas having different  $\kappa_h$  values, fixed temperature anisotropies corresponding to  $A_c = 0, A_h = 0.2$  and all other parameters are as in Table 2.1. The bottom panel illustrates the dependence of  $k^* \rho_h$  on  $\kappa_h$  for a fixed  $\kappa_c$  by magnifying the middle panel around the values of  $k\rho_h$  where  $\gamma = 0$  (see text).

wave numbers in the range  $k\rho_h \lesssim 0.6$ , the curves show a greater  $\kappa_h$  dependency than in the previous two cases ( $A_h = 0.1$ ,  $A_h = 0.2$ ). In the wave number range  $0.6 \lesssim k\rho_h \lesssim 0.8$  this dependency lessens but then increases again at larger wave numbers ( $0.8 \lesssim k\rho_h \lesssim 1.0$ ) with an increase in  $\kappa_h$  producing an increase in frequency at most wave numbers investigated. For this value of the anisotropy of the hot electrons ( $A_h = 0.5$ ), an increase in their spectral index results in a monotonic increase in the maximum growth rate, with peak maximum growth rate corresponding to  $\kappa_h = 20.0$  (quasi-Maxwellian). This is clearly illustrated in the middle panel of Figure 2.5. This trend is opposite to that seen in Figure 2.3 for the  $A_h = 0.1$  case.

The hot electrons contribute positively to the growth rate for all frequencies below  $\omega_r = \omega_h^* = 0.33333|\Omega_e|$  for the chosen value of  $A_h$ . The cool electrons on the other hand, remain a constant source of cyclotron damping. For  $A_h = 0.5$ , an increase in  $\kappa_h$  results in a monotonic increase in  $k^*\rho_h$  (bottom panel). As in the previous cases ( $A_h = 0.1$ ,  $A_h = 0.2$ ) an increase in  $\kappa_h$  results in a decrease in the window of growing wave numbers.

Figures 2.6 - 2.11 address the question of varying the cool and hot electron anisotropies in unison. In these figures the two electron species differ in most characteristics but have equal thermal anisotropy.

Figure 2.6 illustrates the whistler mode dispersion relation for a sequence of plasmas having different  $\kappa_h$  values, fixed temperature anisotropies corresponding to  $A_c = A_h = 0.1$  and all other parameters are as in Table 2.1. Figure 2.7 illustrates the whistler mode growth rate curves for the same set of parameters.

In Figure 2.6 (top panel), it is observed that varying the spectral index of the hot electrons has very little effect on the dispersion curves at small and intermediate wave numbers ( $k\rho_h \lesssim 0.65$ ). As the wave number is increased so is the  $\kappa_h$  dependence of the curves, with a significant difference emerging at larger wave numbers ( $0.65 \lesssim k\rho_h \lesssim 1.0$ ). At these larger wave numbers, an increase in  $\kappa_h$  produces an increase in frequency.

As previously mentioned, in the investigation of the single electron species case considered by *Mace and Sydora (2010)*, they determined that there exists a single frequency and wave number at which all electron thermal effects and all  $\kappa$  dependency, vanish. This point is

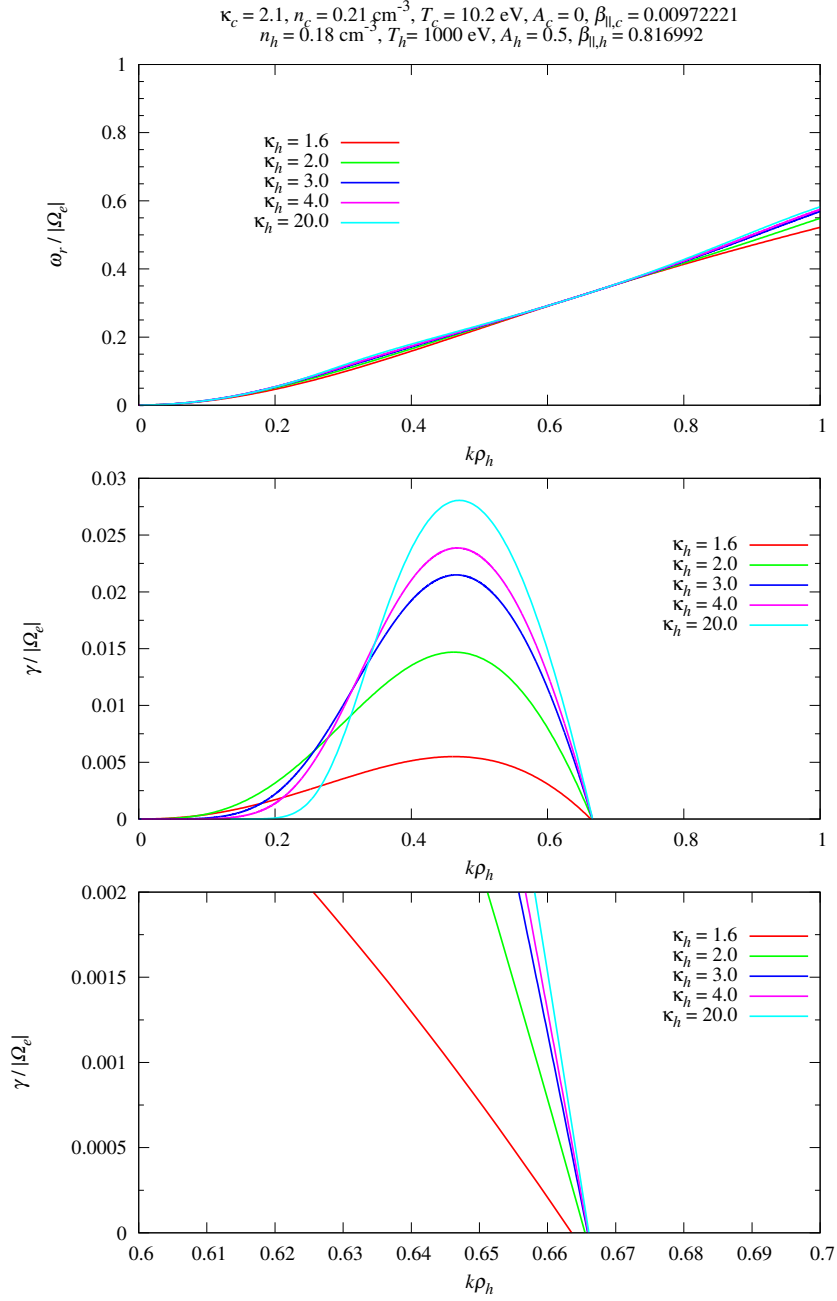


Figure 2.5: Whistler mode dispersion relation (top) and growth rate (middle) for a sequence of plasmas having different  $\kappa_h$  values, fixed temperature anisotropies corresponding to  $A_c = 0, A_h = 0.5$  and all other parameters are as in Table 2.1. The bottom panel illustrates the dependence of  $k^* \rho_h$  on  $\kappa_h$  for a fixed  $\kappa_c$  by magnifying the middle panel around the values of  $k\rho_h$  where  $\gamma = 0$  (see text).

seen graphically as a common point of intersection in the plots of the real part of the dispersion relation. In addition, they found that the wave number of this point defines the upper bound of the interval of growing wave numbers. This point of intersection is also present in the two electron species case for the special case when  $A_h = A_c$ . On closer examination (lower panel of Figure 2.6), it is found that there exists a common point of intersection of all the curves at  $\omega_r = \omega_h^* = 0.0909091|\Omega_e|$  (horizontal dashed line).

To determine the frequency at which the intersection occurs in the case of two electron species, in a manner similar to *Mace and Sydora (2010)*, an asymptotic expansion of the ion term is performed, leaving all other terms in the dispersion relation, Equation (2.9), in their original form

$$\begin{aligned} \frac{k^2 c^2}{\omega^2} = & 1 + \frac{\omega_{ph}^2}{\omega^2} \left\{ A_h + \left[ A_h \left( \frac{\omega - |\Omega_e|}{k\theta_{\parallel h}} \right) + \frac{\omega}{k\theta_{\parallel h}} \right] U_{\kappa_h} \left( \frac{\omega - |\Omega_e|}{k\theta_{\parallel h}} \right) \right\} \\ & + \frac{\omega_{pc}^2}{\omega^2} \left\{ A_c + \left[ A_c \left( \frac{\omega - |\Omega_e|}{k\theta_{\parallel c}} \right) + \frac{\omega}{k\theta_{\parallel c}} \right] U_{\kappa_c} \left( \frac{\omega - |\Omega_e|}{k\theta_{\parallel c}} \right) \right\} \\ & - \frac{\omega_{pi}^2}{\omega(\omega + \omega_{ci})}. \end{aligned} \quad (2.30)$$

From Equation (2.30) it is evident that, for all thermal effects of both electron species to vanish, both  $A_h(\omega - |\Omega_e|) + \omega = 0$  and  $A_c(\omega - |\Omega_e|) + \omega = 0$  need to be satisfied. The solutions to these equations with  $\omega = \omega_r + i\gamma$  are

$$\omega_r = \left( \frac{A_h}{A_h + 1} \right) |\Omega_e| = \omega_h^* \quad \gamma = 0 \quad (2.31)$$

and

$$\omega_r = \left( \frac{A_c}{A_c + 1} \right) |\Omega_e| = \omega_c^* \quad \gamma = 0, \quad (2.32)$$

respectively. From the above equations it is evident that if  $A_h = A_c$  the solutions to both Equations (2.31) and (2.32) will be the same. Thus, thermal effects of both electron species will vanish at the same frequency.

The wave number at which this frequency (where all thermal effects vanish) occurs can be estimated by substituting the conditions  $A_h(\omega - |\Omega_e|) + \omega = 0$  and  $A_c(\omega - |\Omega_e|) + \omega = 0$  into Equation (2.30) and letting  $A_h = A_c = A_e$  so that Equations (2.31) and (2.32) become

$$\omega_r = \frac{A_e}{(A_e + 1)} |\Omega_e| \quad \gamma = 0. \quad (2.33)$$

Substituting Equation (2.33) into Equation (2.30), the wave number at which all thermal effects of both electron species vanish can be approximated by [cf. *Mace and Sydora* (2010)]

$$k^2 c^2 = \left( \frac{A_e}{A_e + 1} \right)^2 |\Omega_e|^2 + \omega_{ph}^2 A_e + \omega_{pc}^2 A_e - \frac{A_e \omega_{pi}^2 |\Omega_e|}{A_e |\Omega_e| + (A_e + 1) \omega_{ci}}. \quad (2.34)$$

This is precisely the result obtained by *Mace and Sydora* (2010) upon noting that  $\omega_{pe}^2 = \omega_{ph}^2 + \omega_{pc}^2$ . The above equations for  $\omega$  (Equation (2.33)) and  $k$  (Equation (2.34)) are independent of the spectral index of both electron species. Therefore, the equations give a common point through which all parallel whistler mode dispersion curves must pass, irrespective of the spectral index or any other thermal effects. Since the imaginary part of this point has  $\gamma = 0$  (see Equation (2.31) and (2.32)) it corresponds to the upper limit of wave growth, both in terms of  $\omega_r$  and in terms of  $k$ . At this wave number all curves will have  $\gamma = 0$  irrespective of the value of the spectral index.

Applying this concept to the current case with  $A_h = A_c = 0.1$ , there now exists a single frequency (and wave number) in the dispersion curves at which all thermal effects and  $\kappa$  dependency of both electron species vanish. This is illustrated in detail in the bottom panel of Figure 2.6, where it is clearly evident that there is a single point of intersection of all the curves at the frequency corresponding to  $\omega_r = \omega_h^*$  (dashed horizontal line). In the growth rate curves, a sharp cutoff of the growth rate is seen at a value of  $k$  corresponding to  $\omega_r = \omega_h^* = 0.0909091|\Omega_e|$ . All wave growth is confined below this frequency. This is clearly evident in the bottom panel of Figure 2.7, which shows the growth rate curves corresponding to Figure 2.6.

The top panel of Figure 2.7 illustrates the  $\kappa_h$  dependence of the growth rate of the parallel whistler instability for the chosen anisotropy of  $A_h = A_c = 0.1$ . With the exception of the curve corresponding to  $\kappa_h = 1.6$ , an increase in  $\kappa_h$  results in a monotonic decrease in the peak growth rates with a peak maximum growth rate corresponding to the case where  $\kappa_h = 2.0$ . The case  $\kappa_h = 1.6$  has a peak growth rate which lies below the curve  $\kappa_h = 4.0$  but above  $\kappa_h = 20.0$ .

In all cases investigated in Figure 2.7, increasing the spectral index of the hot electrons resulted in a decrease in the window of growing wave numbers. At small wave numbers

( $k\rho_h \lesssim 0.1$ ), an increase in  $\kappa_h$  results in a monotonic decrease in the growth rate. As explained previously, this is because at low values of  $\kappa_h$  there are more tail electrons with large enough parallel velocities for cyclotron resonance (leading to wave amplification) at smaller wave numbers than in the higher  $\kappa_h$  cases. Therefore, the greater  $\kappa_h$ , the smaller the instability bandwidth.

Figures 2.8 and 2.9 are similar to Figures 2.6 and 2.7 but in this case the anisotropy of the electrons has been increased to  $A_h = A_c = 0.2$ . The top panel of Figure 2.8 illustrates the real part of the dispersion relation and like Figure 2.6, varying  $\kappa_h$  has very little effect at small and intermediate wave numbers ( $k\rho_h \lesssim 0.65$ ). However, the  $\kappa_h$  dependence of the dispersion curves becomes more prominent as it moves toward larger wave numbers. An increase in  $\kappa_h$  results in an increase in frequency in the range  $0.65 \lesssim k\rho_h \lesssim 1.0$ . The frequency at which the  $\kappa$  dependency of both electron species vanishes and the curves intersect is illustrated in the bottom panel of Figure 2.8 and found to occur at  $\omega_r = \omega_h^* = \omega_c^* = 0.16667|\Omega_e|$  (horizontal dashed line) for  $A_h = A_c = 0.2$ .

The growth rate has been altered significantly by an increase in  $A_h$  and is illustrated in the top panel of Figure 2.9. The peak maximum growth rate corresponds to  $\kappa_h = 4.0$ . For  $A_h = A_c = 0.2$ , plasmas with  $\kappa_h < 4.0$  will experience a monotonic increase in peak growth rate with an increase in  $\kappa_h$ . For cases where  $\kappa_h > 4.0$ , the maximum growth rate of each case monotonically decreases with an increase in  $\kappa_h$ . In all cases of  $\kappa_h$  investigated, an increase in the spectral index of the hot electrons results in a decrease in the instability bandwidth.

At the wave number corresponding to the frequency at which all thermal effects of both electron species vanish, it is found that  $\gamma = 0$  for all curves irrespective of their value of  $\kappa_h$  or  $\kappa_c$ . As previously explained, this is due to the anisotropies of both electron species being equal and, therefore,  $\omega_h^* = \omega_c^*$ . This results in a single value of the wave number below which all wave growth is confined and is shown in the bottom panel of Figure 2.9.

Figures 2.10 and 2.11 show the dispersion relation and growth rate for the case where  $A_h = A_c = 0.5$ , respectively. In the top panel of Figure 2.10, it is observed that a variation in  $\kappa_h$  results in a more significant change in the real part of the dispersion

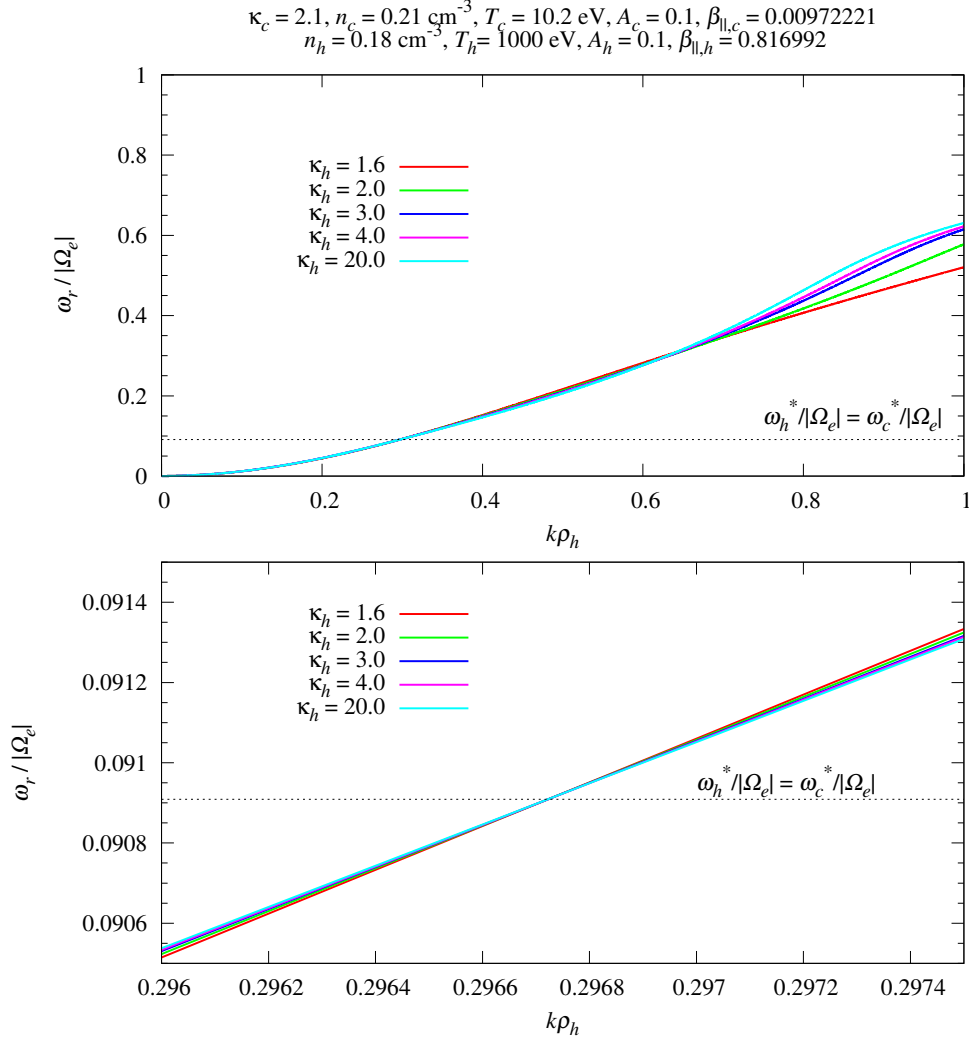


Figure 2.6: Whistler mode dispersion relation for a sequence of plasmas having different  $\kappa_h$  values, fixed temperature anisotropies corresponding to  $A_c = A_h = 0.1$  and all other parameters are as in Table 2.1 (top panel). The bottom panel illustrates the dispersion relation zoomed in around the point of intersection (see main text). The dashed horizontal line represents  $\omega_h^* = \omega_c^* = 0.0909091|\Omega_e|$ .

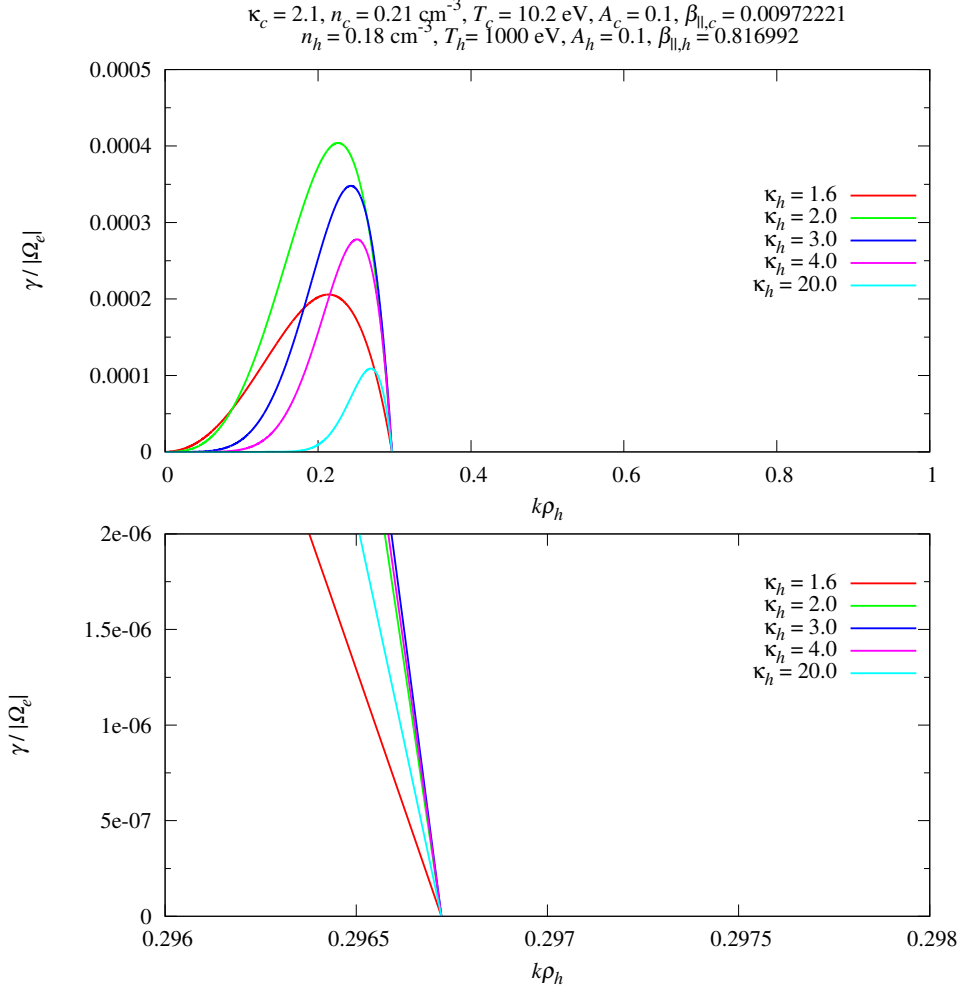


Figure 2.7: Whistler mode growth rate for a sequence of plasmas having different  $\kappa_h$  values, fixed temperature anisotropies corresponding to  $A_c = A_h = 0.1$  and all other parameters are as in Table 2.1 (top panel). The bottom panel illustrates the dispersion relation zoomed in around the point where  $\gamma = 0$  for all curves (see main text).

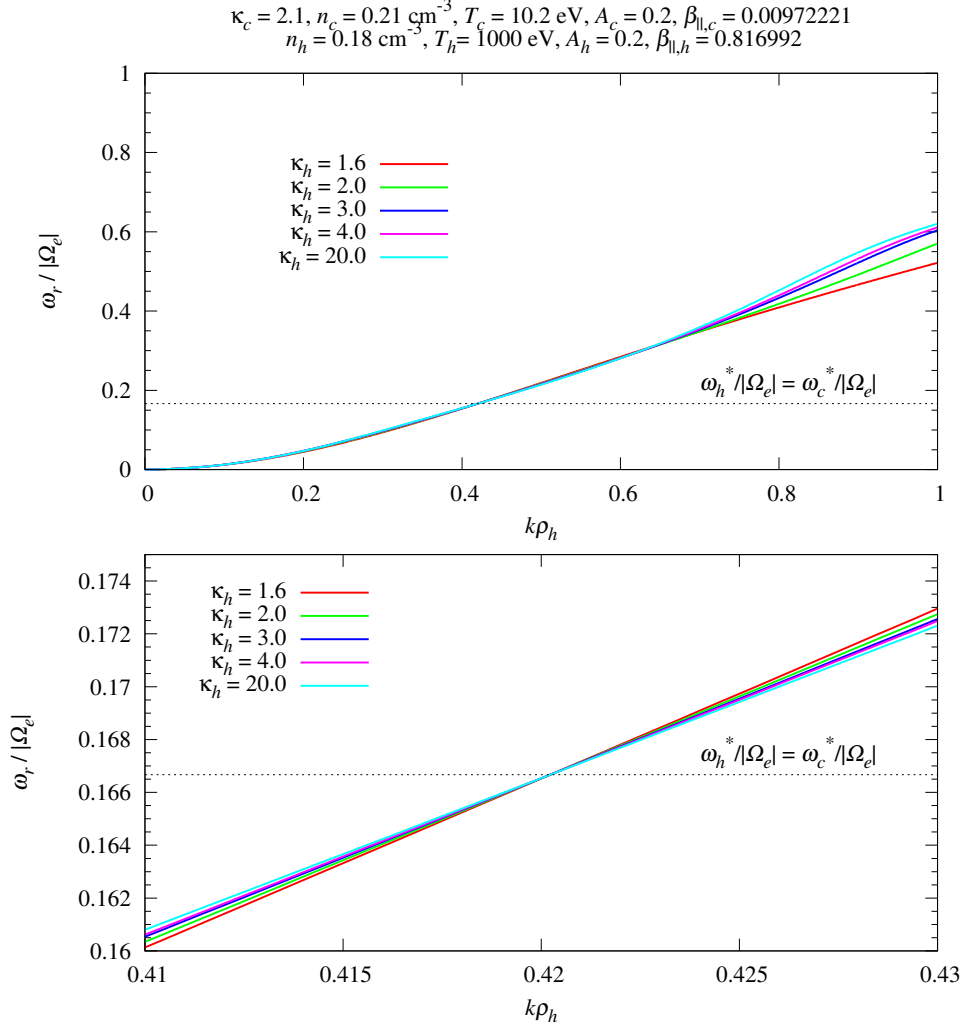


Figure 2.8: Whistler mode dispersion relation for a sequence of plasmas having different  $\kappa_h$  values, fixed temperature anisotropies corresponding to  $A_c = A_h = 0.2$  and all other parameters are as in Table 2.1 (top panel). The bottom panel illustrates the dispersion relation zoomed in around the point of intersection (see main text). The dashed horizontal line represents  $\omega_h^* = \omega_c^* = 0.1666667|\Omega_e|$ .

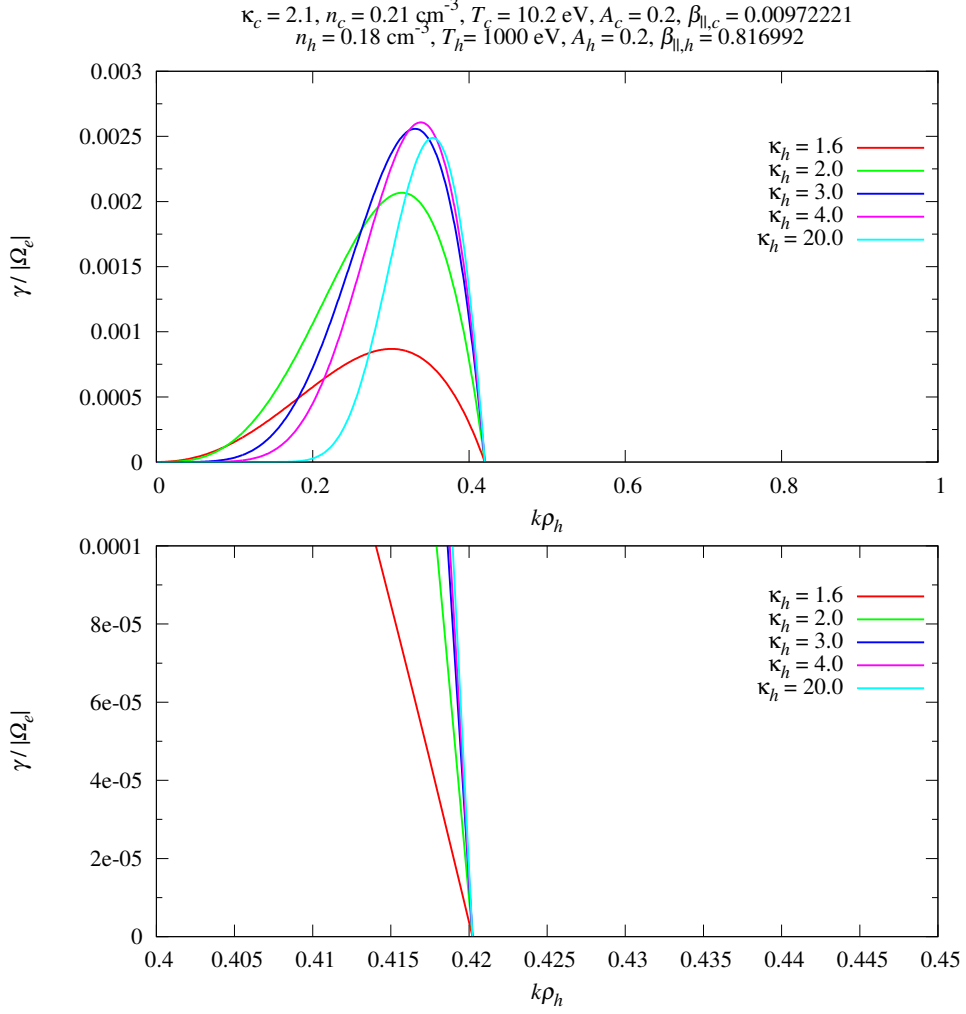


Figure 2.9: Whistler mode growth rate for a sequence of plasmas having different  $\kappa_h$  values, fixed temperature anisotropies corresponding to  $A_c = A_h = 0.2$  and all other parameters are as in Table 2.1 (top panel). The bottom panel illustrates the dispersion relation zoomed in around the point where  $\gamma = 0$  for all curves (see main text).

relation at small and intermediate wave numbers ( $k\rho_h \lesssim 0.65$ ) than in previous cases with smaller anisotropies ( $A = 0.1$  and  $A = 0.2$ ). At most of the intermediate to large wave numbers ( $0.2 \lesssim k\rho_h \lesssim 1.0$ ) a larger value of  $\kappa_h$  will produce a higher frequency. The exception to this being the point at which all thermal effects and  $\kappa$  dependence vanishes at  $\omega_r = \omega_h^* = \omega_c^* = 0.33333|\Omega_e|$  (horizontal dashed line). This is shown in the bottom panel of Figure 2.10.

The growth rate is illustrated in Figure 2.11. It is observed that the growth rate is greatly affected by the increase in anisotropy of both electron species. For  $A_h = A_c = 0.5$ , an increase in  $\kappa_h$  results in a monotonic increase in the maximum growth rate with peak maximum growth rate corresponding to the quasi-Maxwellian case ( $\kappa_h = 20.0$ ). This is shown in the top panel of Figure 2.11. This trend is opposite to that seen in Figure 2.7 for the  $A_h = A_c = 0.1$  case. Since  $A_h = A_c$ ,  $\omega_h^* = \omega_c^*$  and hence, there is a single value of  $k$  (corresponding to  $\omega_h^* = \omega_c^*$ ) at which  $\gamma = 0$  for all values of  $\kappa_h$  investigated. This is illustrated in the bottom panel of Figure 2.11. As is expected, an increase in  $\kappa_h$  results in a decrease in the window of growing wave numbers.

#### Variation of $\kappa_h$ with $\beta_{\parallel h} = 0.0816992$ and $\beta_{\parallel c} = 0.00972221$

The parameters in this section are similar to that of the previous section (as in Table 2.1) except that here the hot electron temperature has been lowered from  $T_h = 1000$  eV to  $T_h = 100$  eV. This change in hot electron temperature, results in a change in plasma parallel beta value of the hot electrons such that  $\beta_{\parallel h}$  has decreased from  $\beta_{\parallel h} = 0.816992$  to  $\beta_{\parallel h} = 0.0816992$ . The parameter  $\beta_{\parallel c}$  is unchanged as  $T_c$  has remained constant as per Table 2.1. How the lowering of  $\beta_{\parallel h}$  affects the effects of varying the spectral index of the hot electrons in a sequence of plasmas will be investigated in Figures 2.12 - 2.19. This will be done firstly, in a sequence of plasmas with varying  $A_h$  and  $A_c = 0$  and secondly, for the a sequence of plasmas with  $A_h = A_c$ .

Figure 2.12 illustrates the dispersion relation and growth rate for a sequence of plasmas with different  $\kappa_h$  values and fixed  $A_h = 0.1$ ,  $A_c = 0$ . The real part of the dispersion relation (top panel) shows very little dependence on  $\kappa_h$  at small wave numbers ( $k\rho_h \lesssim 0.2$ ). The

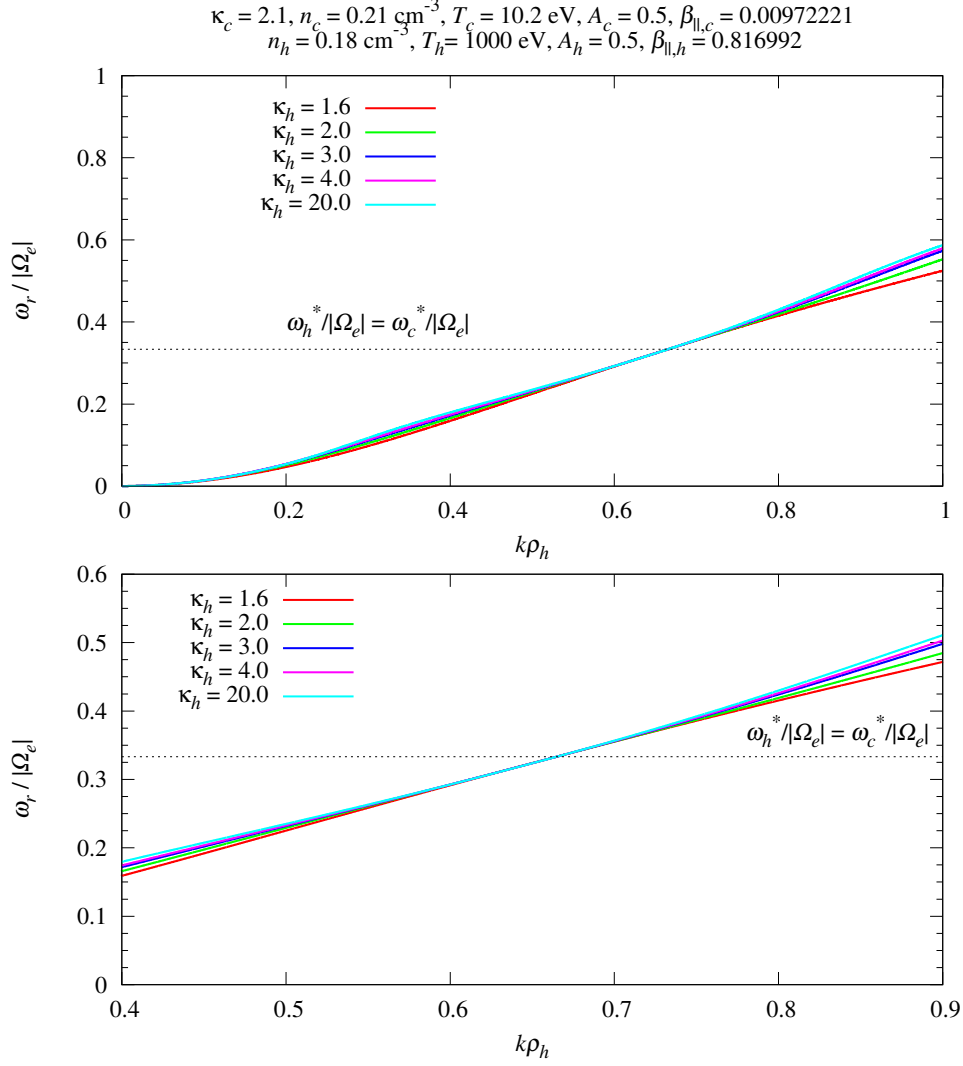


Figure 2.10: Whistler mode dispersion relation for a sequence of plasmas having different  $\kappa_h$  values, fixed temperature anisotropies corresponding to  $A_c = A_h = 0.5$  and all other parameters are as in Table 2.1 (top panel). The bottom panel illustrates the dispersion relation zoomed in around the point of intersection (see main text). The dashed horizontal line represents  $\omega_h^* = \omega_c^* = 0.3333333|\Omega_e|$ .

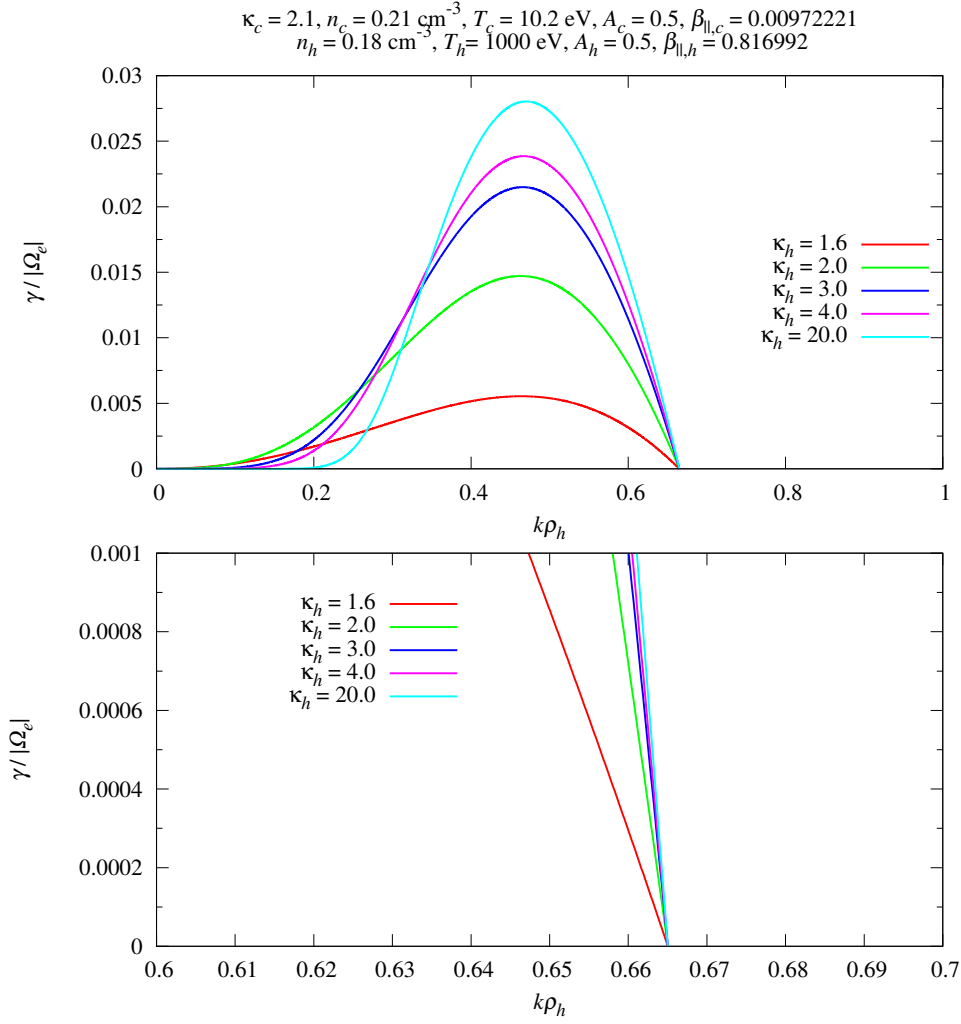


Figure 2.11: Whistler mode growth rate for a sequence of plasmas having different  $\kappa_h$  values, fixed temperature anisotropies corresponding to  $A_c = A_h = 0.5$  and all other parameters are as in Table 2.1 (top panel). The bottom panel illustrates the dispersion relation zoomed in around the point where  $\gamma = 0$  for all curves (see main text).

$\kappa_h$  dependence is enhanced as the wave number is increased with a significant difference in dispersive characteristics emerging at larger wave numbers ( $k\rho_h \gtrsim 0.2$ ). At intermediate wave numbers ( $0.2 \lesssim k\rho_h \lesssim 0.375$ ) an increase in  $\kappa_h$  produces lower frequencies. However, this trend is reversed at larger wave numbers ( $0.375 \lesssim k\rho_h \lesssim 0.5$ ) with an increase in  $\kappa_h$  producing higher frequencies in this range. For this chosen anisotropy of the hot electrons, the frequency below which the hot electrons will make a positive contribution to the growth rate is  $\omega_r = \omega_h^* = 0.0909091|\Omega_e|$ . The cool electrons will always provide a source of damping, as discussed previously, since they are taken to be isotropic.

The growth rate is illustrated in the bottom panel of Figure 2.12. It is observed that there is a monotonic decrease in peak growth rate with an increase in  $\kappa_h$ . The peak maximum growth rate corresponds to the case where  $\kappa_h = 1.6$ . The cases  $\kappa_h = 4.0$  and  $\kappa_h = 20.0$  show no growth over the entire range of wave numbers investigated. This implies that in all cases where  $\kappa_h \geq 4.0$ , the damping term provided by the cool electrons will always be greater in magnitude than the magnitude of the positive contribution provided by the anisotropic hot electrons.

Since  $A_h \neq A_c$ , there is no single value of  $k$  where  $\gamma = 0$  for all spectral indices. The wave number at which  $\gamma = 0$ ,  $k^*\rho_h$ , is dependent on the spectral index of both electron species. For a fixed spectral index of the cool electrons,  $\kappa_c = 2.1$ , the curve with the greatest value of  $k^*\rho_h$  is found for the case where  $\kappa_h = 2.0$ , this is then followed by the curves representing the cases  $\kappa_h = 1.6$  and  $\kappa_h = 3.0$ , respectively. In all cases investigated in Figure 2.12, increasing the spectral index of the hot electrons resulted in an overall decrease in the window of growing wave numbers, i.e., the greater  $\kappa_h$ , the smaller the instability bandwidth due to fewer resonant electrons at smaller wave numbers ( $k\rho_h \lesssim 0.1$ ).

Figure 2.13 is similar to Figure 2.12 except that here the anisotropy of the hot electrons has been increased to  $A_h = 0.2$ . The  $\kappa_h$  dependence of the real part of the dispersion relation (top panel) has not been greatly affected by the increase in anisotropy of the hot electrons. Any dependence is again only seen at intermediate to larger wave numbers ( $0.2 \lesssim k\rho_h \lesssim 0.5$ ).

An increase in  $\kappa_h$  results in lower frequencies for intermediate wave numbers ( $0.2 \lesssim k\rho_h \lesssim$

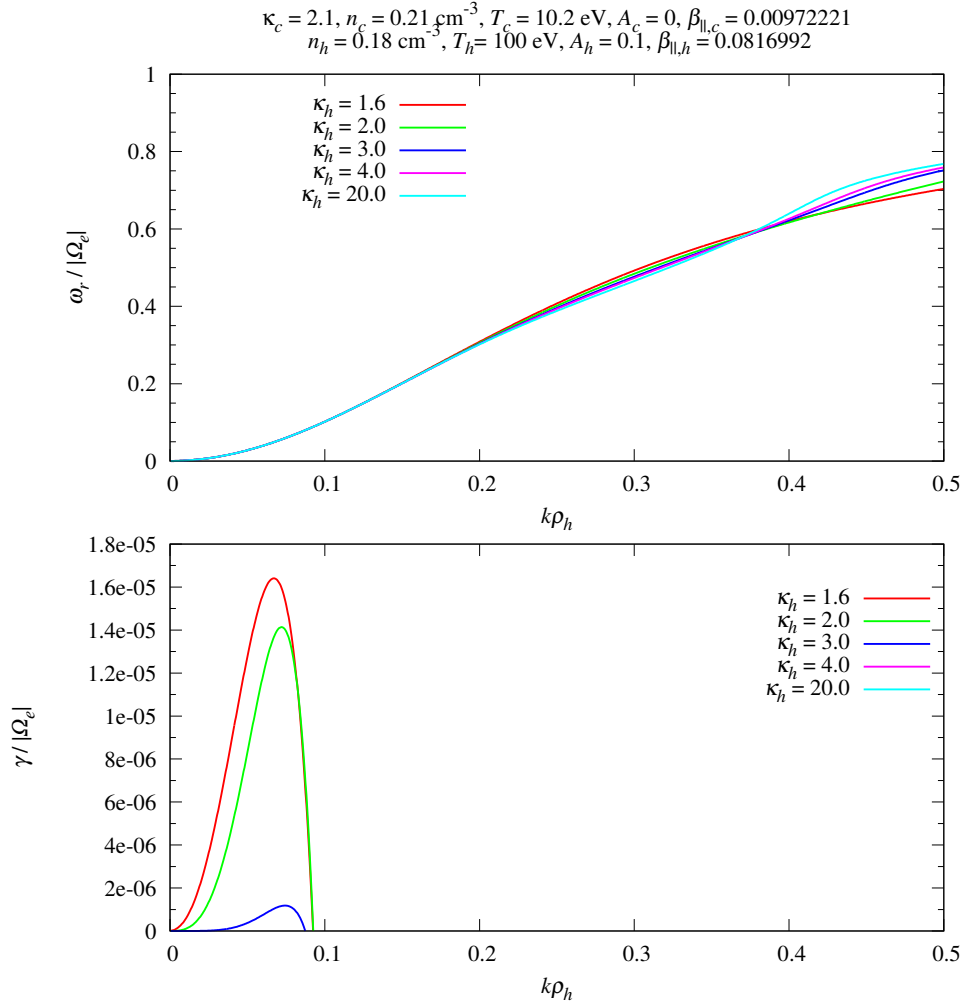


Figure 2.12: Whistler mode dispersion relation (top) and growth rate (bottom) for a sequence of plasmas having different  $\kappa_h$  values, fixed temperature anisotropies corresponding to  $A_h = 0.1$ ,  $A_c = 0$  and hot electron temperature,  $T_h = 100 \text{ eV}$ . All other parameters are as in Table 2.1.

0.375), while the reverse is observed at large wave numbers ( $0.375 \lesssim k\rho_h \lesssim 0.5$ ). This overall trend is similar to that seen in Figure 2.12.

The growth rate (bottom panel) has been significantly altered by an increase in  $A_h$ . Here the peak maximum growth rate corresponds to  $\kappa_h = 2.0$  rather than  $\kappa_h = 1.6$ , as was the case for Figure 2.12, where  $A_h = 0.1$ . For  $A_h = 0.2$ , plasmas with  $\kappa_h < 2.0$  will experience a monotonic increase in peak growth rate with an increase in  $\kappa_h$ . For cases where  $\kappa_h > 2.0$ , the maximum growth rate of each case monotonically decreases with an increase in  $\kappa_h$ . In Figure 2.12 ( $A_h = 0.1$ ) it was illustrated that  $\gamma < 0$  (no growth) for all wave numbers investigated in the case  $\kappa_h = 4.0$ . An increase in hot electron anisotropy from  $A_h = 0.1$  to  $A_h = 0.2$  is sufficient to allow for a range of wave numbers over which  $\gamma > 0$  for the case  $\kappa_h = 4.0$ . However, there is still no overall positive contribution to the growth rate for the case  $\kappa_h = 20.0$ , i.e., the cyclotron damping of the cool electrons is always greater in magnitude than the magnitude of the positive contribution provided by the hot electrons for the case  $\kappa_h = 20.0$ .

The hot electrons will provide a positive contribution to the growth rate at all frequencies below  $\omega_r = \omega_h^* = 0.16667|\Omega_e|$  corresponding to  $A_h = 0.2$ . The wave number at which this positive contribution to the growth rate equals, in magnitude, the damping term provided by the cool electrons is dependent on  $\kappa_h$  for a fixed  $\kappa_c$ . This dependency of the wave number at which  $\gamma = 0$ ,  $k^*\rho_h$ , is non-monotonic for the case  $A_h = 0.2$ . The maximum value of  $k^*\rho_h$  corresponds to the case where  $\kappa_h = 2.0$ . For cases where  $\kappa_h > 2.0$ , an increase in  $\kappa_h$  results in a monotonic decrease in  $k^*\rho_h$  as seen in the bottom panel of Figure 2.13. For cases where  $\kappa_h < 2.0$ , an increase in  $\kappa_h$  results in a monotonic increase in  $k^*\rho_h$ . In all cases of  $\kappa_h$  investigated in Figure 2.13, an increase in the spectral index of the hot electrons results in an overall decrease in the instability bandwidth.

Figure 2.14 shows the dispersion relation and growth rate curves for the case where  $A_h = 0.75$ ,  $A_c = 0$ . Due to the chosen anisotropy of the hot electrons,  $\omega_h^* = 0.42857|\Omega_e|$  and, therefore, the hot electrons will make a positive contribution to the growth rate for all frequencies below  $\omega_h^*$ . The dispersion curves (top panel) are not significantly affected by the variation in the spectral index of the hot electrons at small and intermediate wave

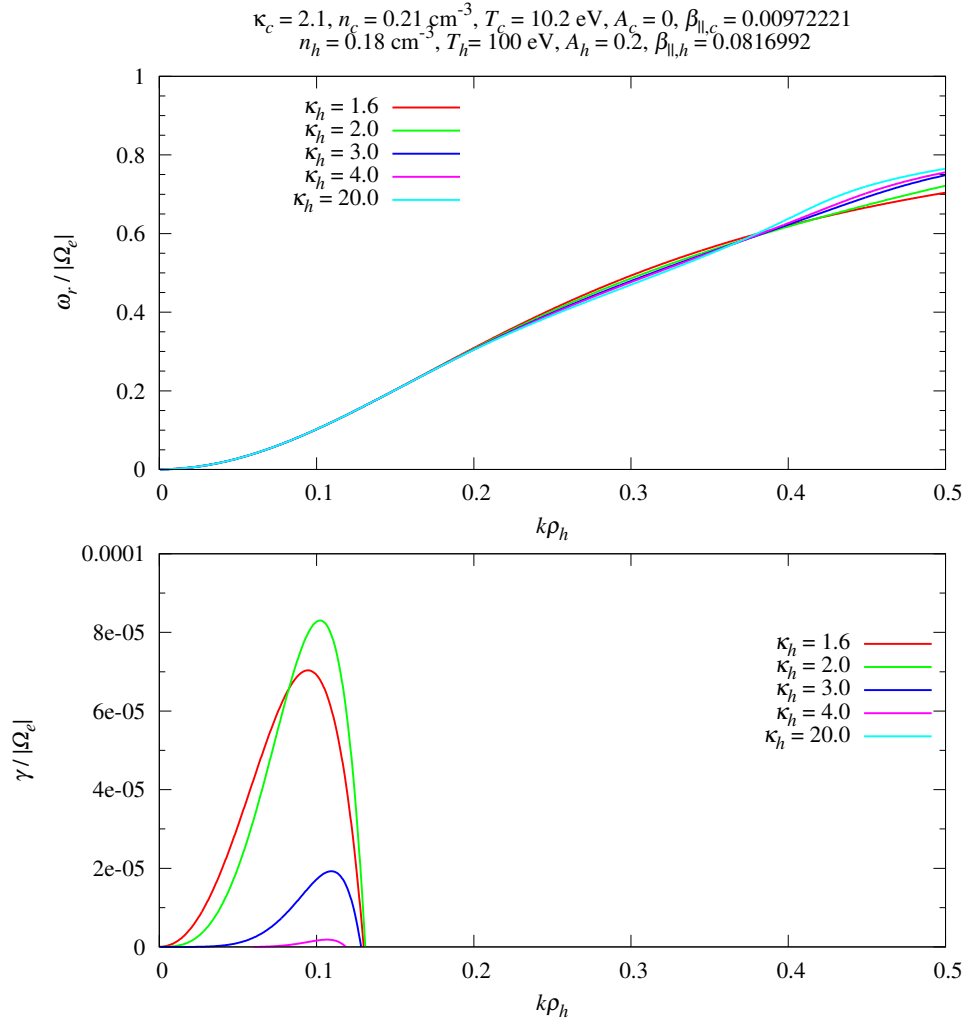


Figure 2.13: Whistler mode dispersion relation (top) and growth rate (bottom) for a sequence of plasmas having different  $\kappa_h$  values, fixed temperature anisotropies corresponding to  $A_h = 0.2$ ,  $A_c = 0$  and hot electron temperature,  $T_h = 100 \text{ eV}$ . All other parameters are as in Table 2.1.

numbers ( $k\rho_h \lesssim 0.4$ ). The  $\kappa_h$  dependency of the curves only becomes more prominent at larger wave numbers ( $0.4 \lesssim k\rho_h \lesssim 0.5$ ). In this range, an increase in  $\kappa_h$  results in an increase in frequency.

The growth rates for the case where  $A_c = 0$ ,  $A_h = 0.75$  (middle panel) are markedly different to the previous cases investigated with lower hot electron anisotropies. For  $A_h = 0.75$ , the peak maximum growth rate corresponds to  $\kappa_h = 3.0$ . Plasmas with  $\kappa_h < 3.0$  will experience a monotonic increase in peak growth rate with an increase in  $\kappa_h$ . For cases where  $\kappa_h > 3.0$ , the maximum growth rate of each case monotonically decreases with an increase in  $\kappa_h$ . This case with  $A_h = 0.75$ , differs significantly from those previously looked at (Figures 2.12 and 2.13) as in this instance, all curves have a range of wave numbers where  $\gamma > 0$ .

An increase in the spectral index of the hot electrons results in an overall decrease in the window of growing wave numbers for all cases investigated in Figure 2.14 (middle panel). This is because it is only for low values of  $\kappa_h$  that there are statistically more tail electrons with parallel velocities large enough to be Doppler shifted up to the cyclotron frequency at small wave numbers ( $k\rho_h \lesssim 0.1$ ). Unlike the previous cases (Figures 2.12 and 2.13), the dependency of the wave number at which  $\gamma = 0$ ,  $k^*\rho_h$ , is monotonic for  $A_h = 0.75$ . An increase in  $\kappa_h$  results in a monotonic increase in  $k^*\rho_h$  for all  $\kappa_h$  values studied and is clearly illustrated in the bottom panel.

Figure 2.15 shows the case where  $A_h = 1.0$  ( $A_c = 0$ ). The dispersion relation curves are illustrated in the top panel while the growth rates are depicted in the bottom panel. At this level of hot electron anisotropy, a variation in the spectral index of the hot electrons results in very little change in the real part of the dispersion relation than previously seen with smaller anisotropies. The most notable difference emerges at large wave numbers ( $0.4 \lesssim k\rho_h \lesssim 0.5$ ) where an increase in  $\kappa_h$  results in an increase in frequency. The frequency below which the hot electrons make a positive contribution to the growth rate is  $\omega_r = \omega_h^* = 0.5|\Omega_e|$ , while the cool electrons provide a source of cyclotron damping for all frequencies.

For this value of the anisotropy of the hot electrons it is evident from the bottom panel of

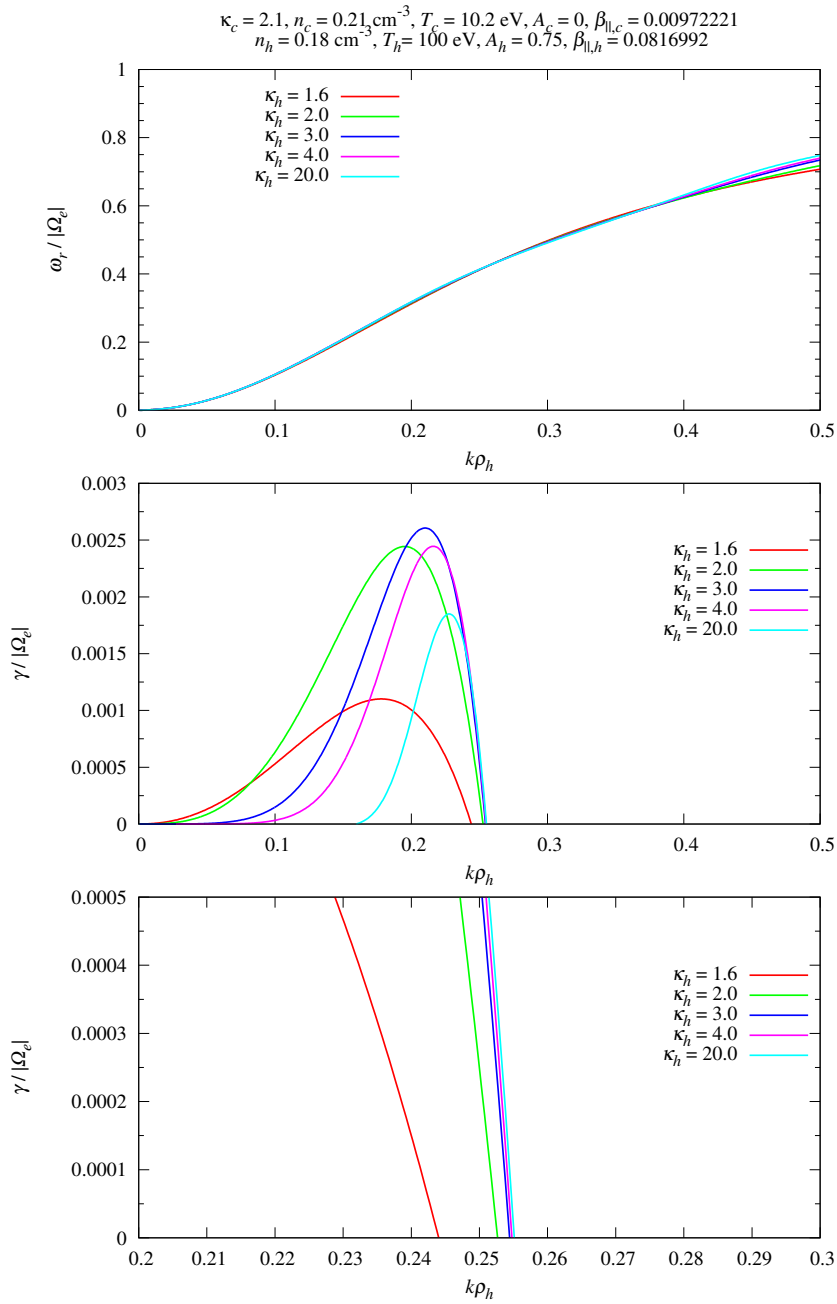


Figure 2.14: Whistler mode dispersion relation (top) and growth rate (middle) for a sequence of plasmas having different  $\kappa_h$  values, fixed temperature anisotropies corresponding to  $A_h = 0.75$ ,  $A_c = 0$  and hot electron temperature,  $T_h = 100 \text{ eV}$ . All other parameters are as in Table 2.1. The bottom panel illustrates the dependence of  $k^* \rho_h$  on  $\kappa_h$  for a fixed  $\kappa_c$ .

Figure 2.15 that an increase in  $\kappa_h$  results in a monotonic increase in the maximum growth rate with peak maximum growth rate corresponding to  $\kappa_h = 20.0$  (quasi-Maxwellian) . This trend is opposite to that seen in Figure 2.12 with  $A_h = 0.1$ . An increase in  $\kappa_h$  results in a decrease in the window of growing wave numbers. For the case with  $A_h = 1.0$  and  $A_c = 0$ , an increase in  $\kappa_h$  results in a monotonic increase in  $k^* \rho_h$ .

The effects of varying the spectral index of the hot electron species with  $\beta_{\parallel h} = 0.0816992$  and the anisotropies of both electron species being equal, i.e.,  $A_h = A_c$ , is investigated in Figures 2.16 - 2.19. Figure 2.16 illustrates the whistler mode dispersion relation and growth rate for a sequence of plasmas having different  $\kappa_h$  values, fixed temperature anisotropies corresponding to  $A_c = A_h = 0.1$ , hot electron temperature  $T_h = 100$  eV and all other parameters are as in Table 2.1. In the real part of the dispersion relation (top panel), varying the spectral index of the hot electrons has very little effect on the dispersion curves at small wave numbers ( $k\rho_h \lesssim 0.2$ ). As the wave number is increased so is the  $\kappa_h$  dependence of the curves. At intermediate wave numbers ( $0.2 \lesssim k\rho_h \lesssim 0.375$ ) an increase in  $\kappa_h$  results in a decrease in frequency. However, this trend is reversed at larger wave numbers ( $0.375 \lesssim k\rho_h \lesssim 0.5$ ) with an increase in  $\kappa_h$  producing higher frequencies in this range. The frequency at which all thermal effects of both electron species vanish is found to be  $\omega_r = \omega_h^* = \omega_c^* = 0.0909091|\Omega_e|$  since  $A_h = A_c = 0.1$ . This is illustrated in the middle panel of Figure 2.16. The vanishing of the  $\kappa$  dependence of the curves is not clearly notable as a variation of  $\kappa_h$  has little consequence at small wave numbers,  $k\rho_h \lesssim 0.2$  .

The wave number corresponding to the point at which all thermal effects of both electron species vanish in the real dispersion relation clearly defines an upper boundary of the interval of growing wave number in the growth rate curves (bottom panel). In the case with  $A_h = A_c = 0.1$ , a sharp cutoff of the growth rate at a value of  $k$  corresponding to  $\omega_h^* = \omega_c^* = 0.0909091|\Omega_e|$  is observed. All wave growth is confined below this value. This is clearly evident in the bottom panel of Figure 2.16.

The bottom panel of Figure 2.16 clearly depicts the  $\kappa_h$  dependence of the growth rate of the parallel whistler instability for the chosen anisotropy of  $A_h = A_c = 0.1$ . An increase in  $\kappa_h$  results in a monotonic decrease in the peak growth rates with a peak maximum growth

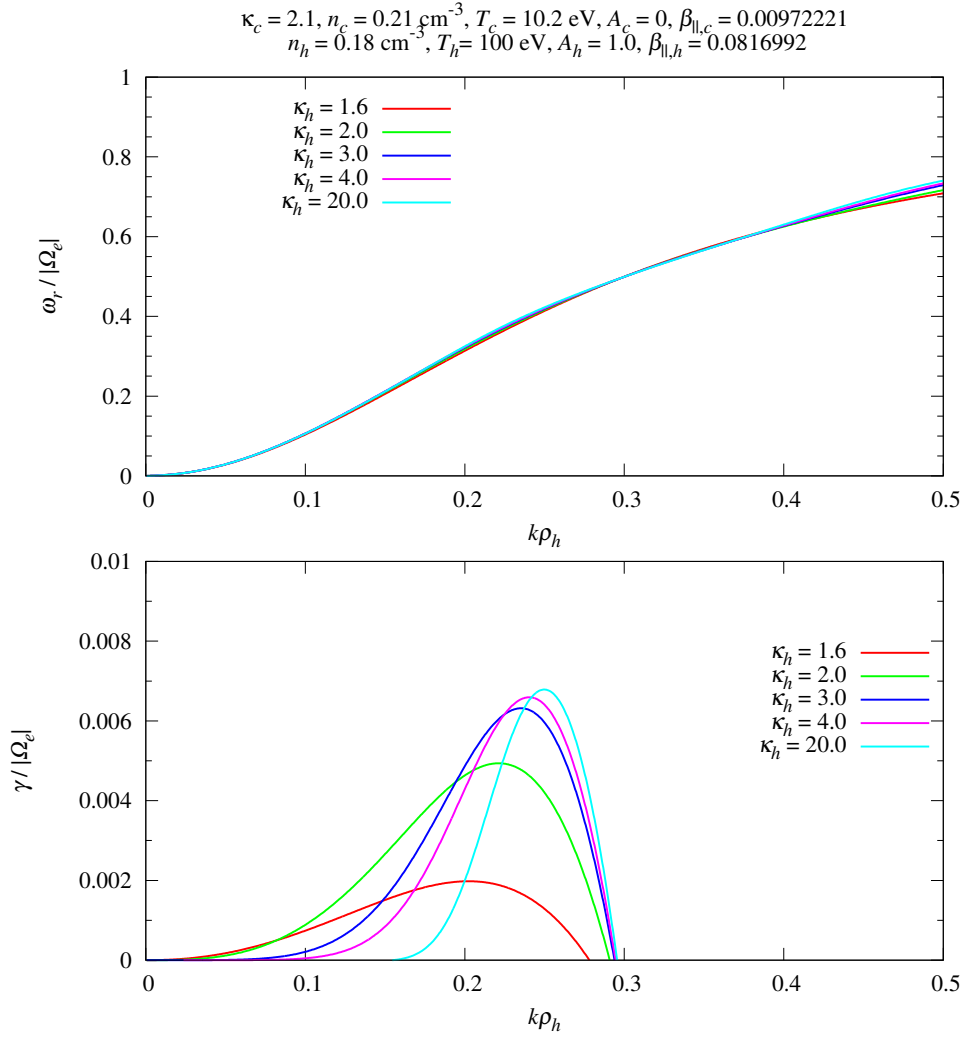


Figure 2.15: Whistler mode dispersion relation (top) and growth rate (bottom) for a sequence of plasmas having different  $\kappa_h$  values, fixed temperature anisotropies corresponding to  $A_h = 1.0$ ,  $A_c = 0$  and hot electron temperature,  $T_h = 100 \text{ eV}$ . All other parameters are as in Table 2.1.

rate corresponding to the case where  $\kappa_h = 1.6$ . In all cases of  $\kappa_h$  investigated in Figure 2.16, increasing the spectral index of the hot electrons resulted in a decrease in the window of growing wave numbers, i.e., the greater  $\kappa_h$ , the smaller the instability bandwidth due to fewer resonant electrons at small wave numbers  $k\rho_h \lesssim 0.1$ .

Figure 2.17 is similar to Figure 2.16 but the anisotropy of both electron species has been increased from  $A_h = A_c = 0.1$  to  $A_h = A_c = 0.2$ . The top panel illustrates the real part of the dispersion relation. Varying the spectral index of the hot electrons has very little effect at small wave numbers ( $k\rho_h \lesssim 0.2$ ), however, as the wave number is increased so is the  $\kappa_h$  dependence. At intermediate wave numbers ( $0.2 \lesssim k\rho_h \lesssim 0.375$ ) an increase in  $\kappa_h$  results in a decrease in frequency, while at large wave numbers ( $0.375 \lesssim k\rho_h \lesssim 0.5$ ) an increase in  $\kappa_h$  produces higher frequencies.

The frequency at which all  $\kappa$  dependency vanishes and the curves intersect is found to be  $\omega_r = \omega_h^* = \omega_c^* = 0.16667|\Omega_e|$  (horizontal dashed line) corresponding to  $A_h = A_c = 0.2$ . This is clearly depicted in the middle panel of Figure 2.17. At the wave number corresponding to this frequency, it is found that  $\gamma = 0$ , for all curves (bottom panel). This wave number is independent of both  $\kappa_h$  and  $\kappa_c$ . As previously explained, this is due to the anisotropies of both electron species being equal.

The growth rate (bottom panel) has been notably modified by an increase in  $A_h$ . The peak maximum growth rate corresponds to  $\kappa_h = 2.0$ , rather than  $\kappa_h = 1.6$ , as was seen in the case where  $A_h = 0.1$ . For  $A_h = 0.2$ , plasmas with  $\kappa_h < 2.0$  will experience a monotonic increase in peak growth rate with an increase in  $\kappa_h$ . For cases where  $\kappa_h > 2.0$ , the maximum growth rate of each case monotonically decreases with an increase in  $\kappa_h$ . In all cases of  $\kappa_h$  investigated, an increase in the spectral index of the hot electrons results in a decrease in the instability bandwidth.

Figure 2.18 shows the dispersion relation and growth rate for the case where  $A_h = A_c = 0.75$ . In the real part of the dispersion relation (top panel), at this level of electron anisotropy, the effects of varying the spectral index of the hot electrons are only seen at larger wave numbers ( $0.4 \lesssim k\rho_h \lesssim 0.5$ ). At small and intermediate wave numbers ( $k\rho_h \lesssim 0.4$ ) there is no noteworthy change in dispersive characteristics, while at large

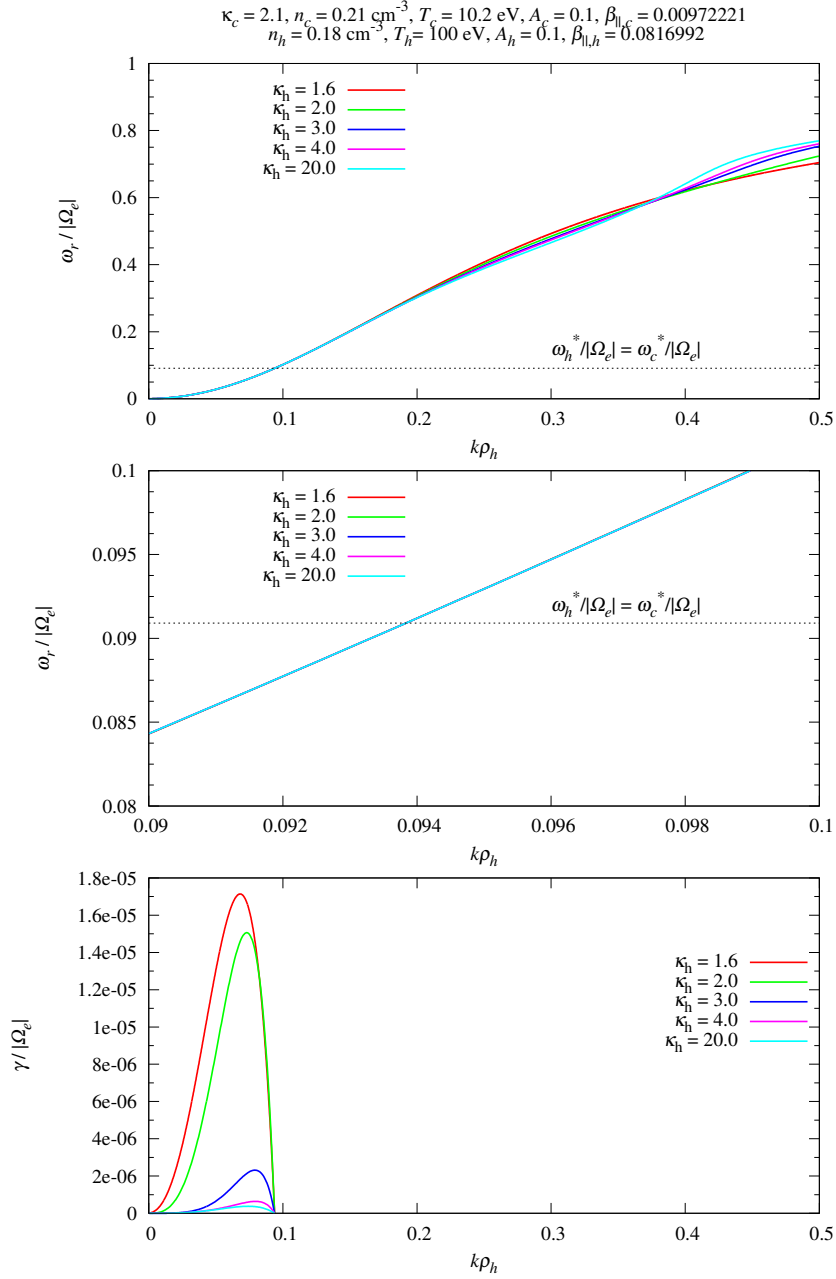


Figure 2.16: Whistler mode dispersion relation (top) and growth rate (bottom) for a sequence of plasmas having different  $\kappa_h$  values, fixed temperature anisotropies corresponding to  $A_c = A_h = 0.1$  and hot electron temperature,  $T_h = 100 \text{ eV}$ . All other parameters are as in Table 2.1. The dashed horizontal line represents  $\omega_h^* = \omega_c^* = 0.0909091|\Omega_e|$ . The middle panel illustrates the dispersion relation zoomed in around the point of intersection (see main text).

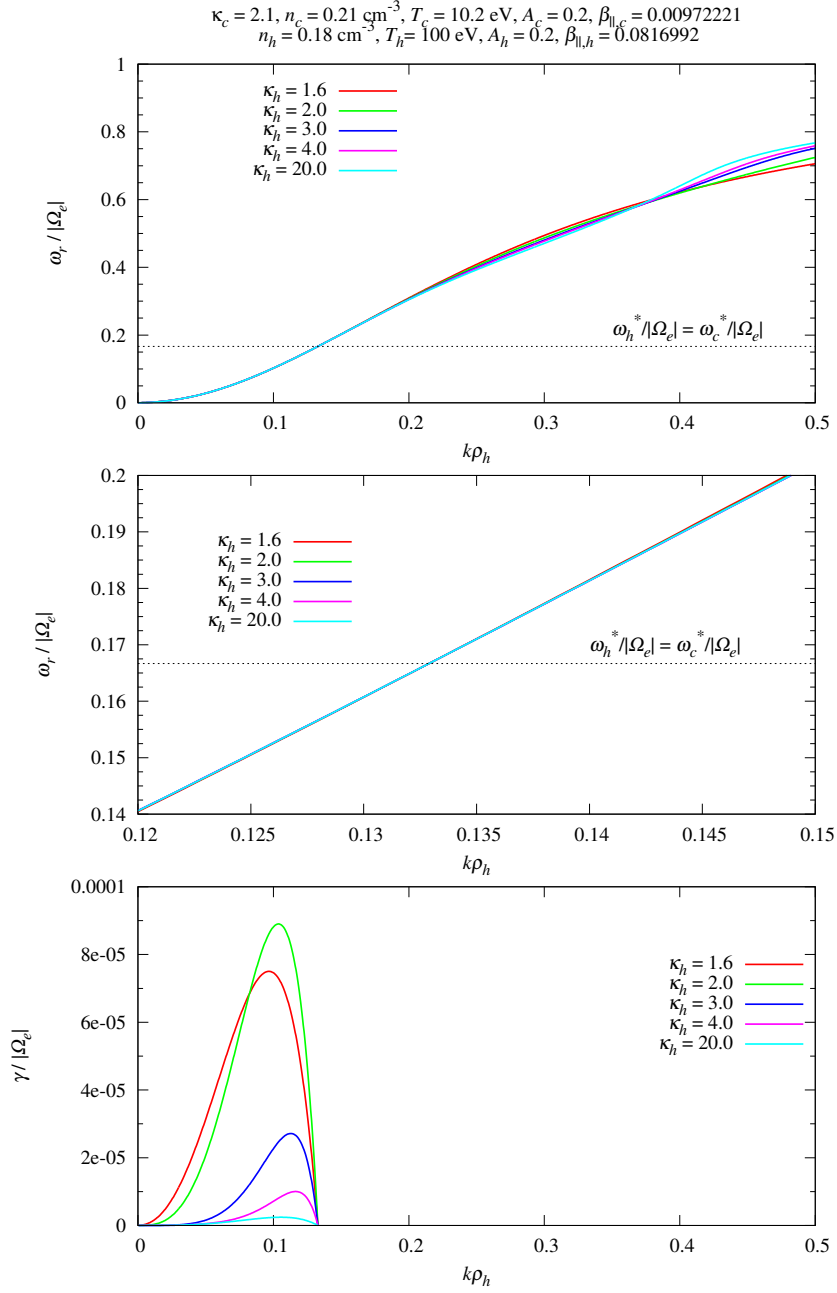


Figure 2.17: Whistler mode dispersion relation (top) and growth rate (bottom) for a sequence of plasmas having different  $\kappa_h$  values, fixed temperature anisotropies corresponding to  $A_c = A_h = 0.2$  and hot electron temperature,  $T_h = 100 \text{ eV}$ . All other parameters are as in Table 2.1. The dashed horizontal line represents  $\omega_h^* = \omega_c^* = 0.1666667|\Omega_e|$ . The middle panel illustrates the dispersion relation zoomed in around the point of intersection (see main text).

wave numbers the variation is clearly evident. In this range,  $0.4 \lesssim k\rho_h \lesssim 0.5$ , an increase in  $\kappa_h$  results in higher frequencies. The frequency at which all the curves intersect and the  $\kappa$  dependence vanishes is  $\omega_r = \omega_h^* = \omega_c^* = 0.42857|\Omega_e|$  for  $A_h = 0.75$ . This is clearly illustrated in the middle panel of Figure 2.18.

The growth rate (bottom panel) is greatly affected by the increase in anisotropy of both electron species. The peak maximum growth rate for this anisotropy corresponds to the case where  $\kappa_h = 3.0$ . Plasmas with  $\kappa_h < 3.0$  will experience a monotonic increase in peak growth rate with an increase in  $\kappa_h$ . For cases where  $\kappa_h > 3.0$ , the maximum growth rate of each case monotonically decreases with an increase in  $\kappa_h$ . An increase in  $\kappa_h$  results in a decrease in the window of growing wave numbers. Since  $A_h = A_c$ ,  $\omega_h^* = \omega_c^*$ , thus, there is a single value of  $k$  (corresponding to  $\omega_r = 0.42857|\Omega_e|$ ) at which  $\gamma = 0$ .

Figure 2.19 shows the case where  $A_h = A_c = 1.0$ . At this level of electron anisotropy, a variation in  $\kappa_h$  results in very little variation in the real part of the dispersion relation (top panel) compared to that observed with small anisotropies (Figures 2.16 and 2.17). Only at larger wave numbers ( $0.4 \lesssim k\rho_h \lesssim 0.5$ ) are the effects of varying  $\kappa_h$  observed. In this region, an increase in  $\kappa_h$  results in higher frequencies. The frequency below which both electron species make a positive contribution to the growth rate is  $\omega_r = \omega_h^* = \omega_c^* = 0.5|\Omega_e|$  for the chosen value of  $A_h = A_c = 1.0$ . This corresponds to the point at which all  $\kappa$  dependence vanishes and is illustrated in the middle panel of Figure 2.19.

For this value of both hot and cool electron anisotropy, an increase in  $\kappa_h$  results in a monotonic increase in the maximum growth rate with peak maximum growth rate corresponding to  $\kappa_h = 20.0$  (quasi-Maxwellian). This trend is opposite to that seen in Figure 2.16 with  $A_h = 0.1$  and illustrated in the bottom panel of Figure 2.19. An increase in  $\kappa_h$  results in a decrease in the window of growing wave numbers due to the decrease in the number of tail electrons with great enough parallel velocities to result in cyclotron resonance at small wave numbers ( $k\rho_h \lesssim 0.1$ ). Since  $A_h = A_c$  and  $\omega_h^* = \omega_c^*$ , there is a single value of  $k$  (corresponding to  $\omega_h^* = \omega_c^* = 0.5|\Omega_e|$ ) setting an upper bound, below which all wave growth is confined.

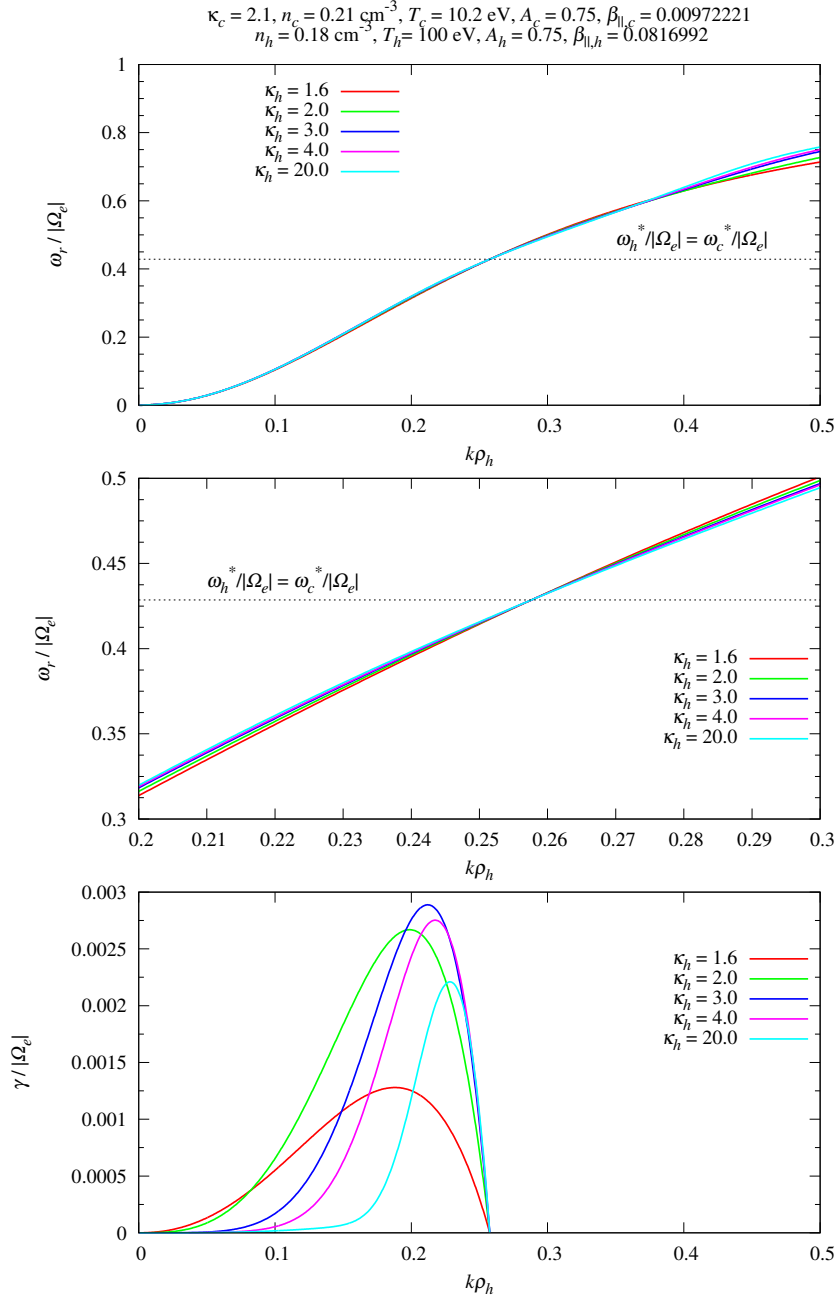


Figure 2.18: Whistler mode dispersion relation (top) and growth rate (bottom) for a sequence of plasmas having different  $\kappa_h$  values, fixed temperature anisotropies corresponding to  $A_c = A_h = 0.75$  and hot electron temperature,  $T_h = 100 \text{ eV}$ . All other parameters are as in Table 2.1. The dashed horizontal line represents  $\omega_h^* = \omega_c^* = 0.42857|\Omega_e|$ . The middle panel illustrates the dispersion relation zoomed in around the point of intersection (see main text).

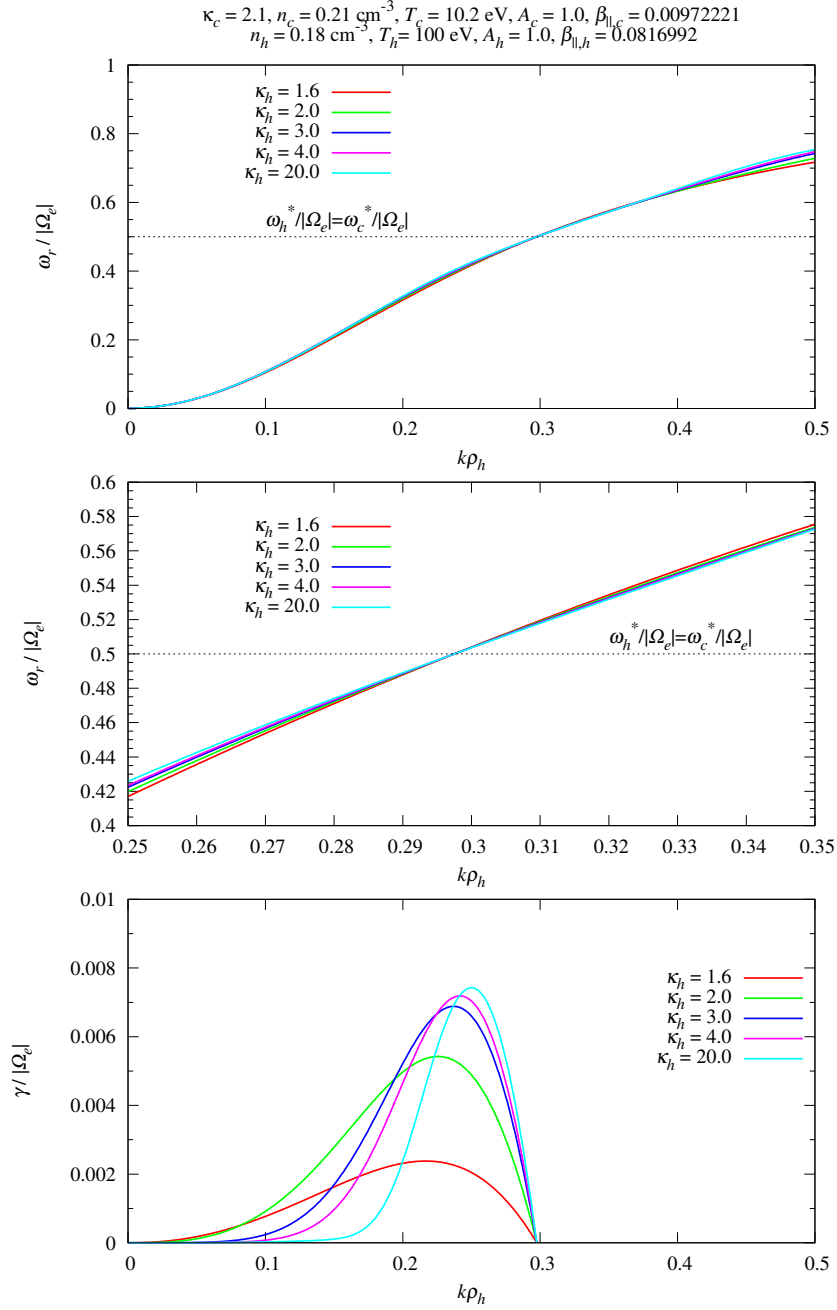


Figure 2.19: Whistler mode dispersion relation (top) and growth rate (bottom) for a sequence of plasmas having different  $\kappa_h$  values, fixed temperature anisotropies corresponding to  $A_c = A_h = 1.0$  and hot electron temperature,  $T_h = 100 \text{ eV}$ . All other parameters are as in Table 2.1. The dashed horizontal line represents  $\omega_h^* = \omega_c^* = 0.5|\Omega_e|$ . The middle panel illustrates the dispersion relation zoomed in around the point of intersection (see main text).

### 2.4.2 Variation of the spectral index of the cool electrons, $\kappa_c$

In this section the effects of varying the spectral index of the cool electrons on the parallel whistler instability are investigated for various anisotropies of both electron species and two different  $\beta_{\parallel h}$  values.

#### Variation of $\kappa_c$ with $\beta_{\parallel h} = 0.816992$ and $\beta_{\parallel c} = 0.00972221$

The parameters in this section are as in Table 2.1 with  $B_0 = 9.412\text{nT}$ , thus,  $\beta_{\parallel h} = 0.816992$  and  $\beta_{\parallel c} = 0.00972221$ . The effects of varying the spectral index of the cool electrons with a variety of  $A_c$  values and  $A_h = 0$  is investigated in Figures 2.20 - 2.22. Figure 2.20 illustrates the case for  $A_c = 0.1$ ,  $A_h = 0$ . For this chosen anisotropy of the cool electrons,  $\omega_c^* = 0.0909091|\Omega_e|$  and, therefore, the cool electrons will make a positive contribution to the growth rate for all frequencies  $\omega_r < \omega_c^*$ . The hot electrons on the other hand, have  $A_h = 0$  and hence, will always provide a negative contribution to the growth rate for all frequencies  $\omega_r > 0$  since  $\omega_h^* = 0$ . The dispersion curves, illustrated in the top panel of Figure 2.20, are not significantly affected by the variation of  $\kappa_c$  at small or intermediate wave numbers ( $k\rho_h \lesssim 0.9$ ). The  $\kappa_c$  dependency of the curves is only seen as  $k\rho_h$  approaches 1.0 with an increase in  $\kappa_c$  resulting in a negligible decrease in frequency in this range.

For  $A_c = 0.1$ ,  $A_h = 0$  the lowest value of the spectral index of the cool electrons,  $\kappa_c = 1.6$ , produces the greatest peak maximum growth rate and the broadest spectrum of wave numbers for which there is a positive growth rate. This is clearly illustrated in the bottom panel of Figure 2.20. The only other value of  $\kappa_c$  that results in a positive growth rate is for the case  $\kappa_c = 2.0$ . For all other values of  $\kappa_c$ , the positive contribution to the growth rate of cool electrons is not great enough to overcome the damping effects of the hot electrons and, thus,  $\gamma < 0$ . Since  $A_h \neq A_c$ , the wave number at which  $\gamma = 0$ ,  $k^*\rho_h$ , is variable and dependent on  $\kappa_c$  for a fixed value of  $\kappa_h = 4.0$ . An increase in  $\kappa_c$  results in a monotonic decrease in  $k^*\rho_h$  for our chosen parameter set in Figure 2.20

Figure 2.21 is similar to Figure 2.20, except in this case  $A_c = 0.5$ . The dispersion curves, illustrated in the top panel of Figure 2.21, show very little  $\kappa_c$  dependency at small or intermediate wave numbers ( $k\rho_h \lesssim 0.9$ ). The effects of varying  $\kappa_c$  are only seen at large

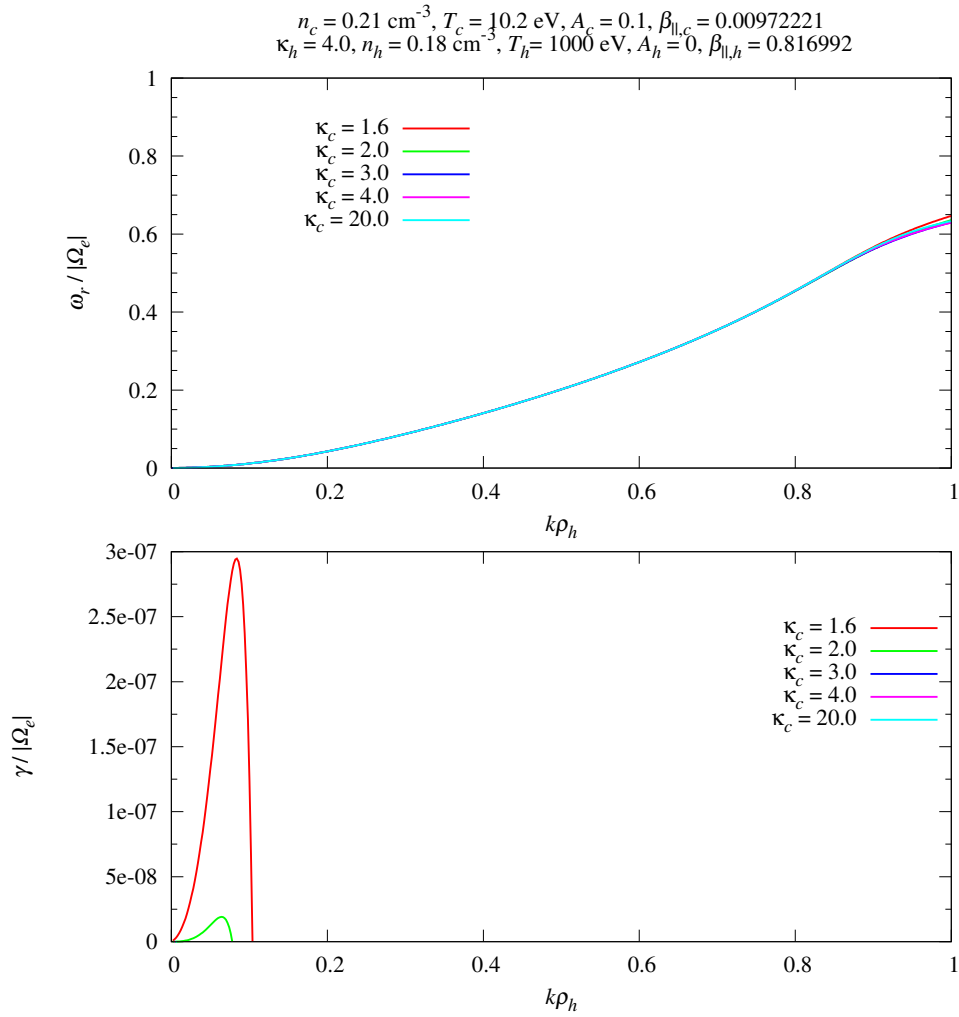


Figure 2.20: Whistler mode dispersion relation (top) and growth rate (bottom) for a sequence of plasmas having different  $\kappa_c$  values, fixed temperature anisotropies corresponding to  $A_c = 0.1$ ,  $A_h = 0$  and all other parameters are as in Table 2.1.

wave numbers with an increase in  $\kappa_c$  resulting in a minor decrease in frequency in the range  $0.9 \lesssim k\rho_h \lesssim 1.0$ . Since  $A_c = 0.5$ , the cool electrons will make a positive contribution to the growth rate for all frequencies below  $\omega_c^* = 0.33333|\Omega_e|$ . The hot electrons remain a source of damping for all frequencies.

In the bottom panel of Figure 2.21, it is clearly evident that the cases  $\kappa_c = 1.6$  and  $2.0$  produce a positive growth rate for a range of wave numbers. For the case  $\kappa_c = 3.0$ , there is a range of wave numbers where  $\gamma > 0$ , however, it is of the order of  $10^{-14}$ . This is not illustrated in Figure 2.21 but the fact that  $\kappa_c = 3.0$  does produce a range of wave numbers with a positive growth rate must be duly noted. The peak maximum growth rate corresponds to  $\kappa_c = 1.6$ . An increase in  $\kappa_c$  results in a monotonic decrease in peak growth rate. The dependence of  $k^*\rho_h$  on the spectral index of the cool electrons is monotonic, with an increase in  $\kappa_c$  resulting in a decrease in  $k^*\rho_h$ .

Figure 2.22 illustrates the effect of varying the spectral index of the cool electrons for the case where  $A_c = 2.0$ ,  $A_h = 0$ . In the top panel, the effects of varying  $\kappa_c$  are only seen as  $k\rho_h$  approaches 1.0 in the real part of the dispersion relation. For  $A_c = 2.0$ ,  $A_h = 0$ , an increase in  $\kappa_c$  results in a marginal increase in frequency in the range  $0.9 \lesssim k\rho_h \lesssim 1.0$ . The cool electrons will make a positive contribution to the growth rate for a considerably wider range of frequencies than in the previous cases ( $A_c = 0.1$  and  $A_c = 0.5$ ) since  $\omega_c^* = 0.666667|\Omega_e|$  for  $A_c = 2.0$ .

In the bottom panel we observe that at this level of anisotropy, the case with  $\kappa_c = 1.6$  produces the greatest peak maximum growth rate. This is followed by the case where  $\kappa_c = 2.0$ . For the case  $\kappa_c = 3.0$ , there is a small range of wave numbers that produce a positive growth rate, however, this is only of the order  $10^{-12}$ . For all other values of  $\kappa_c$ ,  $\gamma < 0$  for the entire range of wave numbers investigated. An increase in  $\kappa_c$  results in a monotonic decrease in  $k^*\rho_h$  as it did in the previous case for  $A_c = 0.1$  and  $0.5$ .

In Figures 2.20 - 2.22, it is clearly illustrated how at small wave numbers ( $k\rho_h \lesssim 0.2$ ) a decrease in spectral index of the cool electrons results in statistically more tail electrons with parallel velocities great enough to induce the Doppler shift required for cyclotron resonance. It is owing to this that at small wave numbers ( $k\rho_h \lesssim 0.2$ ) a decrease in  $\kappa_c$

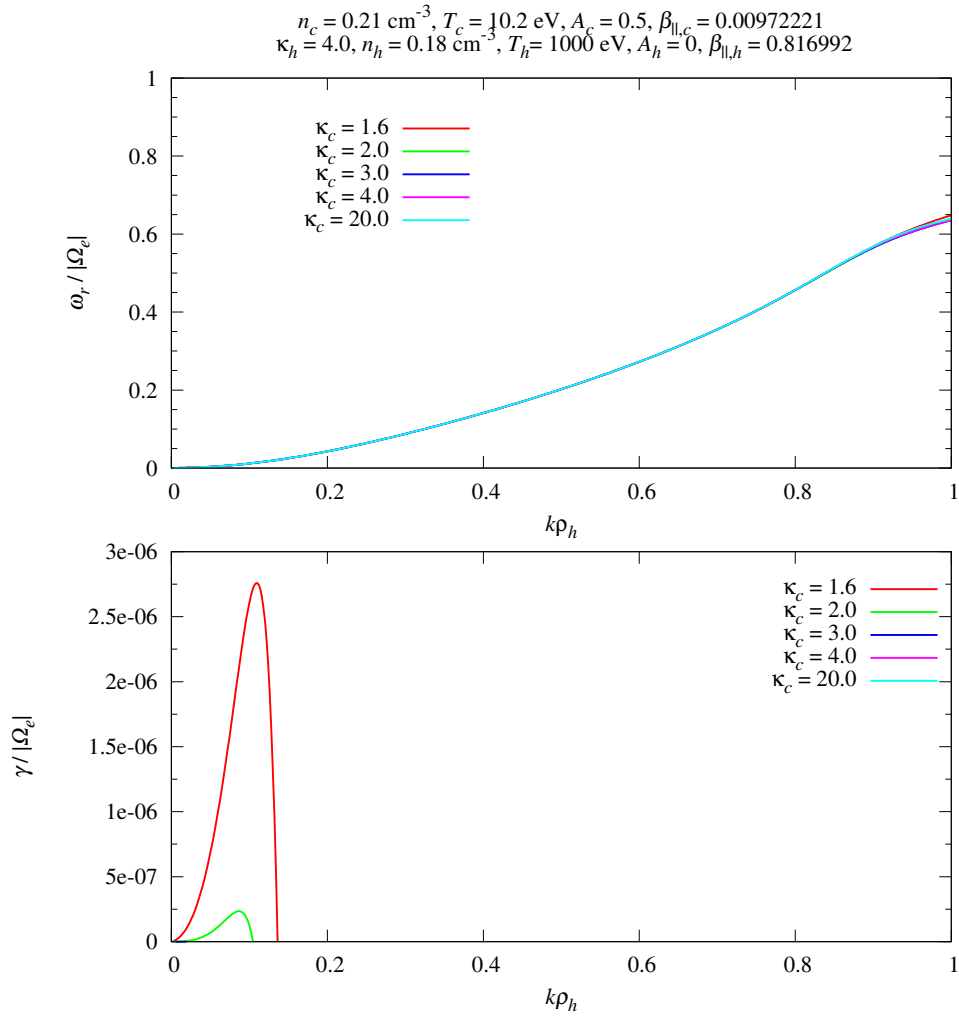


Figure 2.21: Whistler mode dispersion relation (top) and growth rate (bottom) for a sequence of plasmas having different  $\kappa_c$  values, fixed temperature anisotropies corresponding to  $A_c = 0.5$ ,  $A_h = 0$  and all other parameters are as in Table 2.1.

always results in a monotonic increase in growth rate.

The effects of varying the spectral index of the cool electron species with the anisotropies of both electron species being equal, i.e.,  $A_h = A_c$ , is investigated in the Figures 2.23 - 2.25 to follow. Figure 2.23 illustrates the whistler mode dispersion relation and growth rate for a sequence of plasmas having different  $\kappa_c$  values, fixed temperature anisotropies corresponding to  $A_c = A_h = 0.1$  and all other parameters are as in Table 2.1.

In the real part of the dispersion relation (top panel), varying the spectral index of the cool electrons has very little effect on the dispersion curves with a slight dependency only emerging as  $k\rho_h$  approaches 1.0. In this region, an increase in  $\kappa_c$  results in a decrease in frequency. Because  $A_h = A_c$ ,  $\omega_h^* = \omega_c^*$ , thus, there exists a single frequency at which all thermal effects of both electron species vanish. This is seen in the dispersion curves as a common point of intersection at  $\omega_r = \omega_h^* = \omega_c^* = 0.0909091|\Omega_e|$  (horizontal dashed line) for  $A_h = A_c = 0.1$ . The wave number corresponding to this point also defines an upper boundary of the interval of growing wave numbers. For  $A_h = A_c = 0.1$ , we see a sharp cutoff of the growth rate at a value of  $k$ , corresponding to  $\omega_h^* = \omega_c^* = 0.0909091|\Omega_e|$ , below which all wave growth is confined. This is clearly evident in the middle panel of Figure 2.23.

The middle panel of Figure 2.23 illustrates the  $\kappa_c$  dependence of the growth rate of the parallel whistler instability for the chosen anisotropy of  $A_h = A_c = 0.1$ . It initially appears as if the growth rate is not affected by a variation in  $\kappa_c$ . However, if we examine the curves more closely (bottom panel), it is evident that the peak growth rates are dependent on  $\kappa_c$ . The peak maximum growth rate corresponds to the case  $\kappa_h = 1.6$ . The peak growth rate decreases monotonically with an increase in  $\kappa_c$ .

Figure 2.24 shows the case for  $A_c = A_h = 0.5$  with all other parameters as in Figure 2.23. Similar to the previous case ( $A_h = A_c = 0.1$ ), there is no marked difference in dispersion curves at most wave numbers investigated. However, there is a marginal  $\kappa_c$  dependency which is seen at large wave numbers ( $0.9 \lesssim k\rho_h \lesssim 1.0$ ). In this range an increase in  $\kappa_c$  results in a marginal decrease in frequency. Since  $A_h = A_c = 0.5$ ,  $\omega_h^* = \omega_c^* = 0.33333|\Omega_e|$ , defining the frequency at which all thermal effects and  $\kappa$  dependency vanishes for both

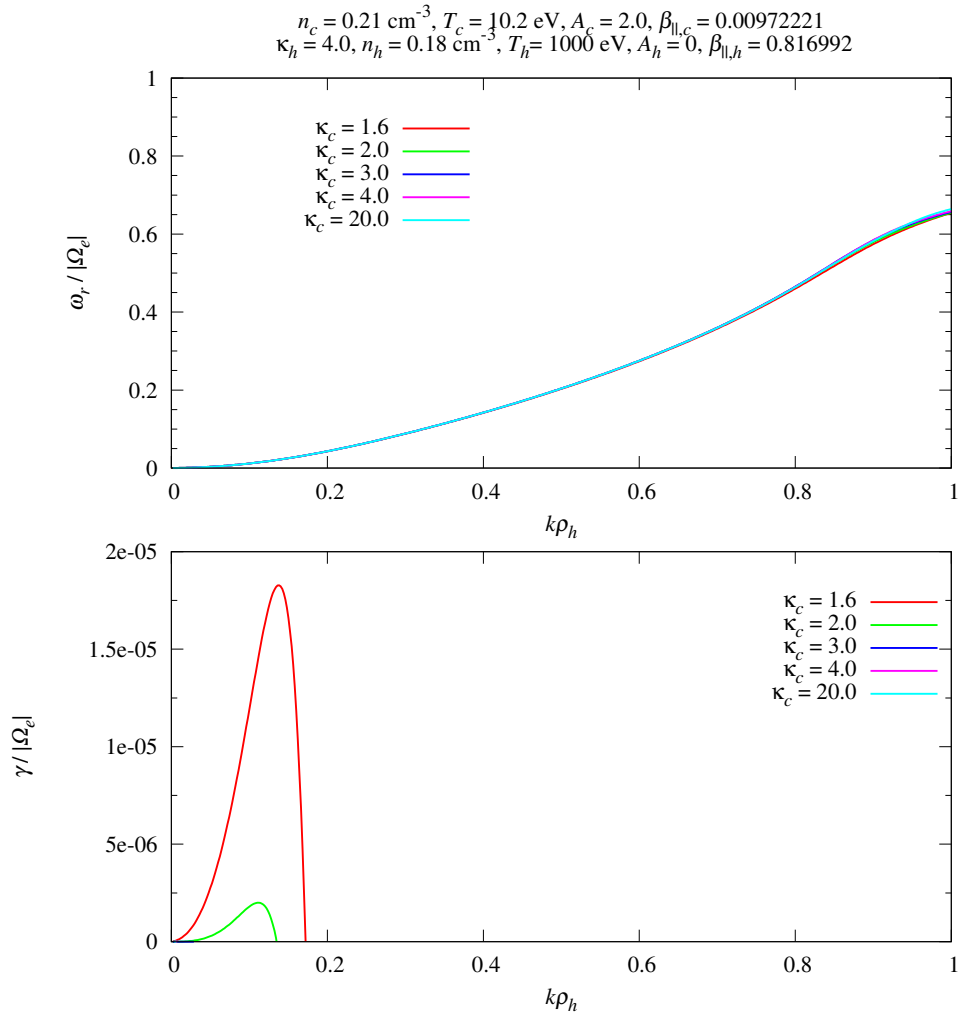


Figure 2.22: Whistler mode dispersion relation (top) and growth rate (bottom) for a sequence of plasmas having different  $\kappa_c$  values, fixed temperature anisotropies corresponding to  $A_c = 2.0$ ,  $A_h = 0$  and all other parameters are as in Table 2.1.

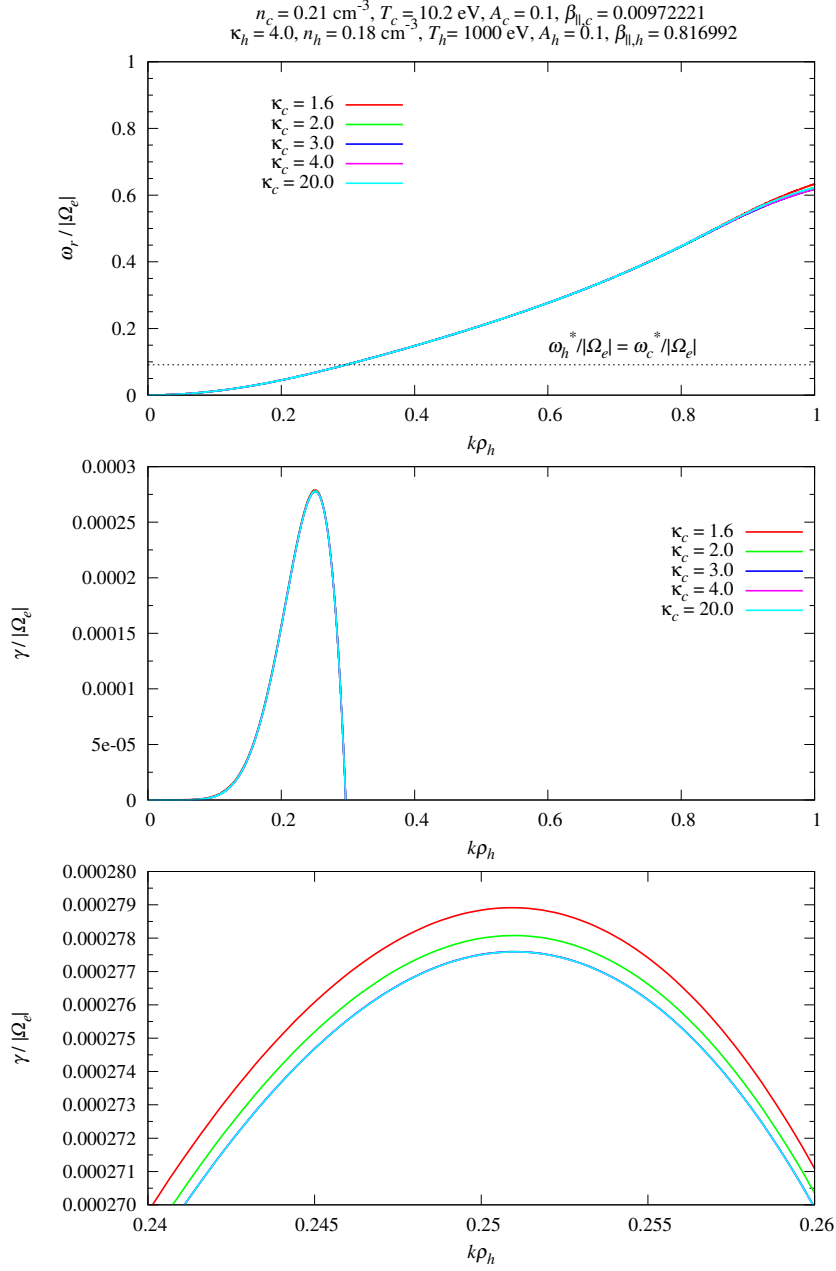


Figure 2.23: Whistler mode dispersion relation (top) and growth rate (middle) for a sequence of plasmas having different  $\kappa_c$  values, fixed temperature anisotropies corresponding to  $A_c = A_h = 0.1$  and all other parameters are as in Table 2.1. The dashed horizontal line represents  $\omega_h^* = \omega_c^* = 0.0909091|\Omega_e|$ . The bottom panel illustrates the growth rate zoomed in around the peak growth rates.

electron species. This is represented by the horizontal dashed line in the top panel of Figure 2.24. This point of intersection also defines the frequency below which both electron species contribute positively to the growth rate and in turn creates an upper boundary of the interval of growing wave numbers (middle panel).

The  $\kappa_c$  dependence of the growth rate is illustrated in the middle panel of Figure 2.24. Very little variation in the growth rate curves is seen (within graphical accuracy) for the range of cool electron spectral indices investigated. The  $\kappa_c$  dependency of the peak growth rate is best illustrated in the bottom panel, where it is evident that an increase in spectral index of the cool electrons results in a monotonic decrease in peak growth rate. The maximum peak growth rate corresponds to  $\kappa_c = 1.6$ .

Figure 2.25 illustrates the whistler mode dispersion relation and growth rate for a sequence of plasmas having different  $\kappa_c$  values and fixed temperature anisotropies corresponding to  $A_c = A_h = 2.0$ . This dramatic increase in anisotropy of both electron species has resulted in a decidedly broader spectrum of wave numbers for which there is a positive growth rate. This is due to the frequency  $\omega_h^* = \omega_c^* = 0.666667|\Omega_e|$  corresponding to a larger wave number than the previous cases ( $A = 0.1$  and  $A = 0.5$ ). Owing to this, we explore the  $\kappa_c$  dependency of the dispersion curves and growth rate over a larger range of wave numbers than that explored previously (Figures 2.23 and 2.24).

In the real part of the dispersion relation (top panel), we see very little  $\kappa_c$  dependence of the curves for  $k\rho_h \lesssim 1.3$ , thereafter, the dependence increases. At large wave numbers ( $1.3 \lesssim k\rho_h \lesssim 2.0$ ) an increase in  $\kappa_c$  results in a decrease in frequency. At the frequency  $\omega_h^* = \omega_c^* = 0.666667|\Omega_e|$  (horizontal dashed line) all thermal effects and  $\kappa$  dependency vanishes for both electron species, resulting in a common point of intersection for all curves.

The middle panel illustrates the growth rate curves. The sharp cutoff in growth rate is clearly evident at the wave number corresponding to  $\omega_h^* = \omega_c^* = 0.666667|\Omega_e|$ . At small wave numbers ( $k\rho_h \lesssim 0.5$ ) there is no significant difference in the growth rate curves with a variation in  $\kappa_c$ . However, as the wave number is increased so is the  $\kappa_c$  dependency. At larger wave numbers ( $k\rho_h \gtrsim 0.5$ ) an increase in  $\kappa_c$  results in a decrease in growth rate.

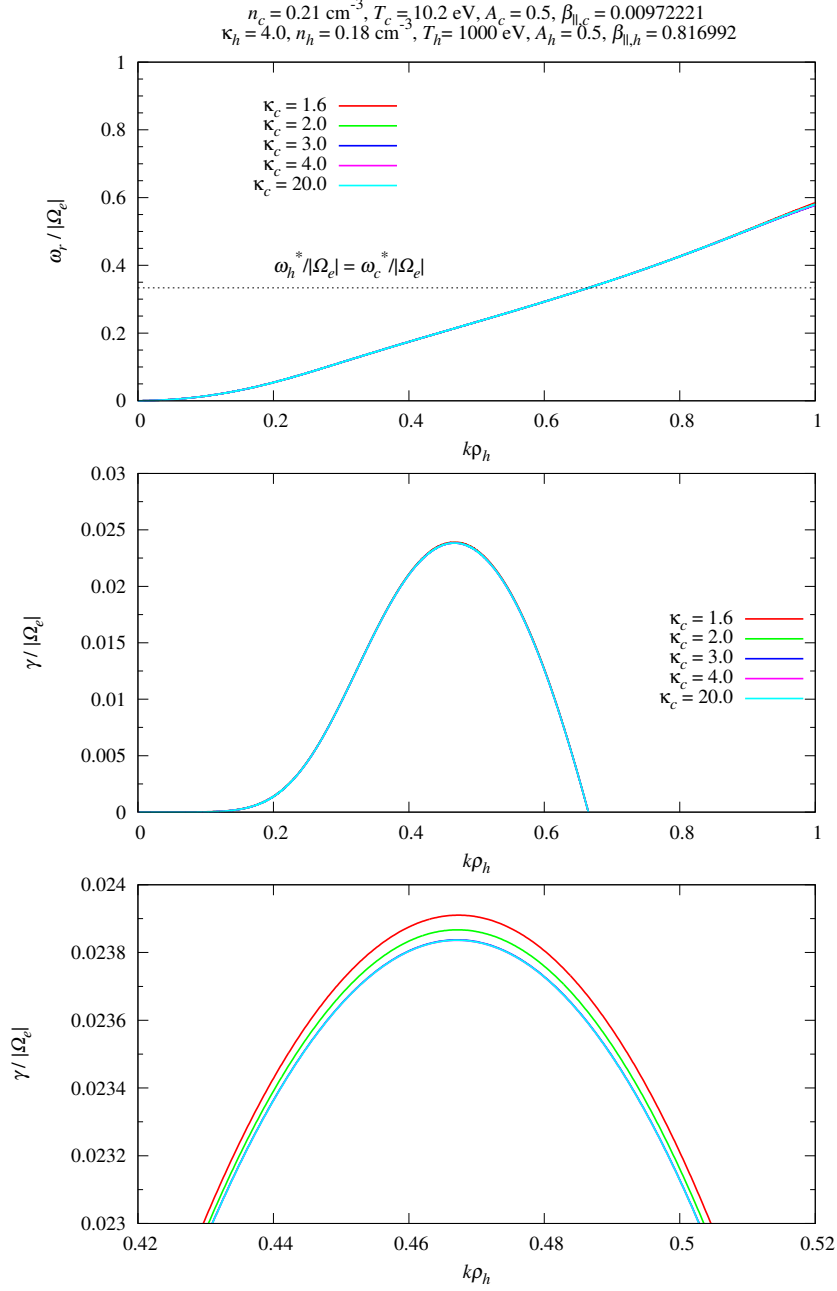


Figure 2.24: Whistler mode dispersion relation (top) and growth rate (middle) for a sequence of plasmas having different  $\kappa_c$  values, fixed temperature anisotropies corresponding to  $A_c = A_h = 0.5$  and all other parameters are as in Table 2.1. The dashed horizontal line represents  $\omega_h^* = \omega_c^* = 0.33333|\Omega_e|$ . The bottom panel illustrates the growth rate zoomed in around the peak growth rates.

The bottom panel of Figure 2.16 illustrates the  $\kappa_c$  dependence of the peak growth rate of the parallel whistler instability for the chosen electron anisotropy of  $A_h = A_c = 2.0$ . An increase in  $\kappa_c$  results in a monotonic decrease in the peak growth rates with a peak maximum growth rate corresponding to the case where  $\kappa_h = 1.6$ .

**Variation of  $\kappa_c$  with  $\beta_{\parallel h} = 0.0816992$  and  $\beta_{\parallel c} = 0.00972221$**

The parameters in this section are similar to that of the previous section (as in Table 2.1), except that here the hot electron temperature has been lowered from  $T_h = 1000$  eV to  $T_h = 100$  eV. This change in hot electron temperature results in a change in plasma parallel beta value of the hot electrons such that  $\beta_{\parallel h} = 0.0816992$  ( $\beta_{\parallel c}$  remains unchanged). How the lowering of  $\beta_{\parallel h}$  affects the effects of varying of  $\kappa_c$  firstly in a sequence of plasmas with varying  $A_c$  and  $A_h = 0$  and then in a sequence of plasmas with  $A_h = A_c$ , will be investigated in the figures to follow.

Figure 2.26 illustrates the dispersion relation  $\omega_r(k)$  and growth rate  $\gamma(k)$  curves for a sequence of plasmas with different  $\kappa_c$  values and fixed  $A_c = 0.1$ ,  $A_h = 0$ . The real part of the dispersion relation (top panel) shows very little dependence on  $\kappa_c$  at small and intermediate wave numbers ( $k\rho_h \lesssim 0.4$ ). The  $\kappa_c$  dependence is enhanced as the wave number is increased with a significant difference in dispersive characteristics emerging in the range ( $0.4 \lesssim k\rho_h \lesssim 0.5$ ). In this range, an increase in  $\kappa_c$  produces a decrease in frequency.

In all cases of  $\kappa_c$  investigated in Figure 2.26, increasing the spectral index of the cool electrons with  $A_c = 0.1$  and  $A_h = 0$ , resulted in a decrease in the window of growing wave numbers, i.e., the greater  $\kappa_c$ , the smaller the instability bandwidth. In the bottom panel of Figure 2.26, it is seen that at small wave numbers ( $k\rho_h \lesssim 0.1$ ) an increase in  $\kappa_c$  results in a monotonic decrease in the growth rate. As previously discussed, this is because as the spectral index is increased the probability of the particles participating in the cyclotron resonance process is decreased and wave growth is suppressed. The dependence of  $k^*\rho_h$  on  $\kappa_c$  for a fixed  $\kappa_h = 4.0$  is also illustrated here. For  $A_c = 0.1$ ,  $A_h = 0$  the wave number at which  $\gamma = 0$ ,  $k^*\rho_h$ , is greatest for  $\kappa_c = 1.6$ . An increase in  $\kappa_c$  results in a monotonic

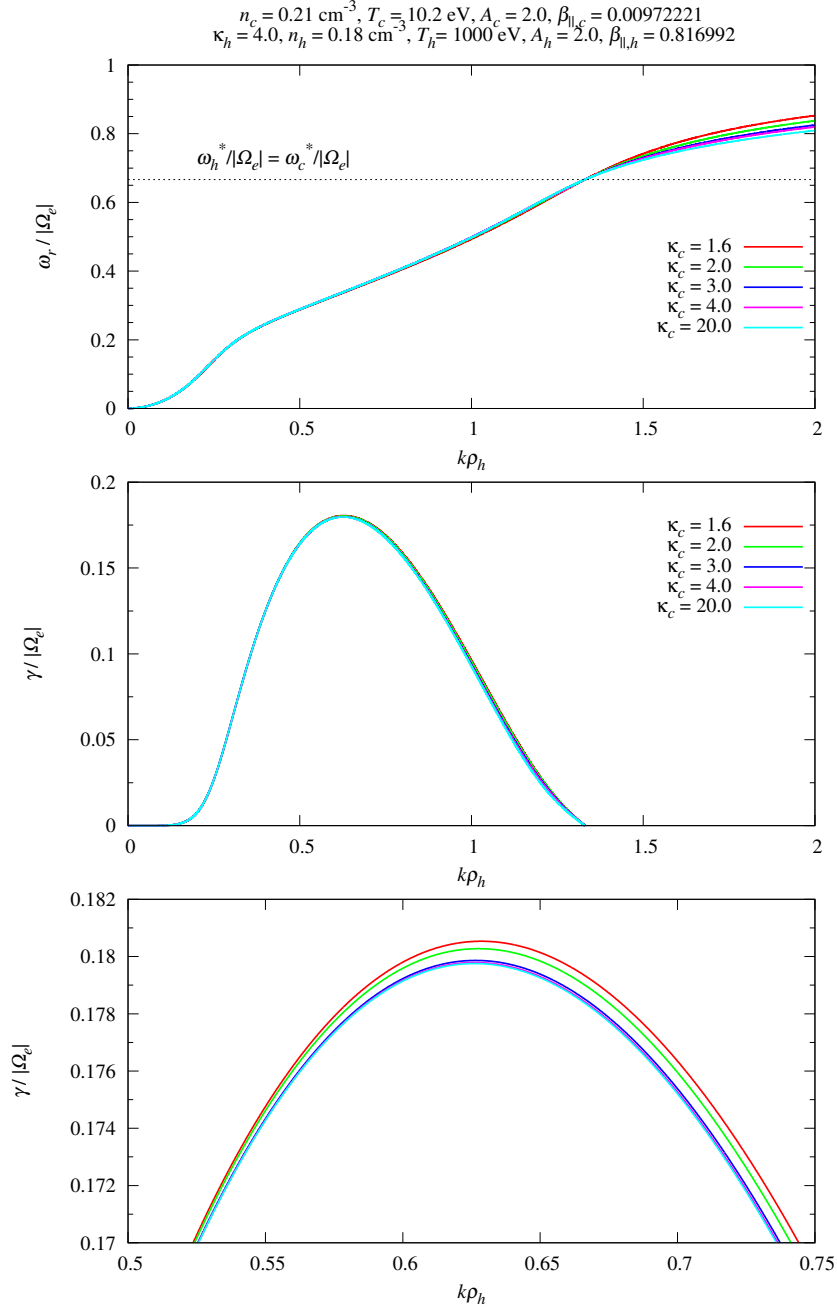


Figure 2.25: Whistler mode dispersion relation (top) and growth rate (middle) for a sequence of plasmas having different  $\kappa_c$  values, fixed temperature anisotropies corresponding to  $A_c = A_h = 2.0$  and all other parameters are as in Table 2.1. The dashed horizontal line represents  $\omega_h^* = \omega_c^* = 0.666667|\Omega_e|$ . The bottom panel illustrates the growth rate zoomed in around the peak growth rates.

decrease in  $k^* \rho_h$ .

In the bottom panel of Figure 2.26, we observe that an increase in  $\kappa_c$  results in a monotonic decrease in the peak growth rate with the peak maximum growth rate corresponding to  $\kappa_c = 1.6$ . Although there exists a range of wave numbers where  $\gamma > 0$  for the case  $\kappa_c = 3.0$ , this is not within graphical accuracy and is found to be of the order of  $10^{-11}$ . The cool electrons contribute positively to the growth rate for all frequencies below  $\omega_c^* = 0.0909091|\Omega_e|$  for the chosen value of  $A_c$ . The hot electrons on the other hand, are a constant source of cyclotron damping.

Figure 2.27 is similar to Figure 2.26 but in this case the anisotropy of the cool electrons has been increased from  $A_c = 0.1$  to  $A_c = 0.5$ . The real part of the dispersion relation (top panel) shows very little dependence on  $\kappa_c$  at small and intermediate wave numbers ( $k\rho_h \lesssim 0.4$ ). At larger wave numbers ( $0.4 \lesssim k\rho_h \lesssim 0.5$ ) the  $\kappa_c$  dependence is more pronounced with an increase in  $\kappa_c$  resulting in a decrease in frequency in this range. The cool electrons contribute positively to the growth rate for all frequencies below  $\omega_r = \omega_c^* = 0.33333|\Omega_e|$ .

In the bottom panel of Figure 2.27, we observe that an increase in  $\kappa_c$  results in a monotonic decrease in the peak growth rate with the peak maximum growth rate corresponding to  $\kappa_c = 1.6$ . For the case  $\kappa_c = 3.0$ , there exists a range of wave numbers where  $\gamma > 0$ . However, this is not within graphical accuracy and is found to be of the order of  $10^{-9}$ . All other values of  $\kappa_c$  investigated contribute negatively to the growth rate for all wave numbers considered.

The bottom panel of Figure 2.27 clearly illustrates how an increase in  $\kappa_c$  results in a decrease in the window of growing wave numbers due to fewer resonant electrons at small wave numbers ( $k\rho_h \lesssim 0.15$ ). The dependence of  $k^* \rho_h$  on  $\kappa_c$  for a fixed  $\kappa_h = 4.0$ , is clearly shown. An increase in  $\kappa_c$  results in a monotonic decrease in  $k^* \rho_h$ .

Figure 2.28 shows the dispersion relation and growth rate for the case where  $A_c = 2.0$  ( $A_c = 0$ ). At this level of cool electron anisotropy, a variation in  $\kappa_c$  results in an interesting phenomenon in the real part of the dispersion relation. At small and intermediate wave numbers ( $k\rho_h \lesssim 0.35$ ) the curves show little  $\kappa_c$  dependency, as was seen in the previous two cases ( $A_c = 0.1, A_c = 0.5$ ). However, unlike the previous two cases, here we witness a

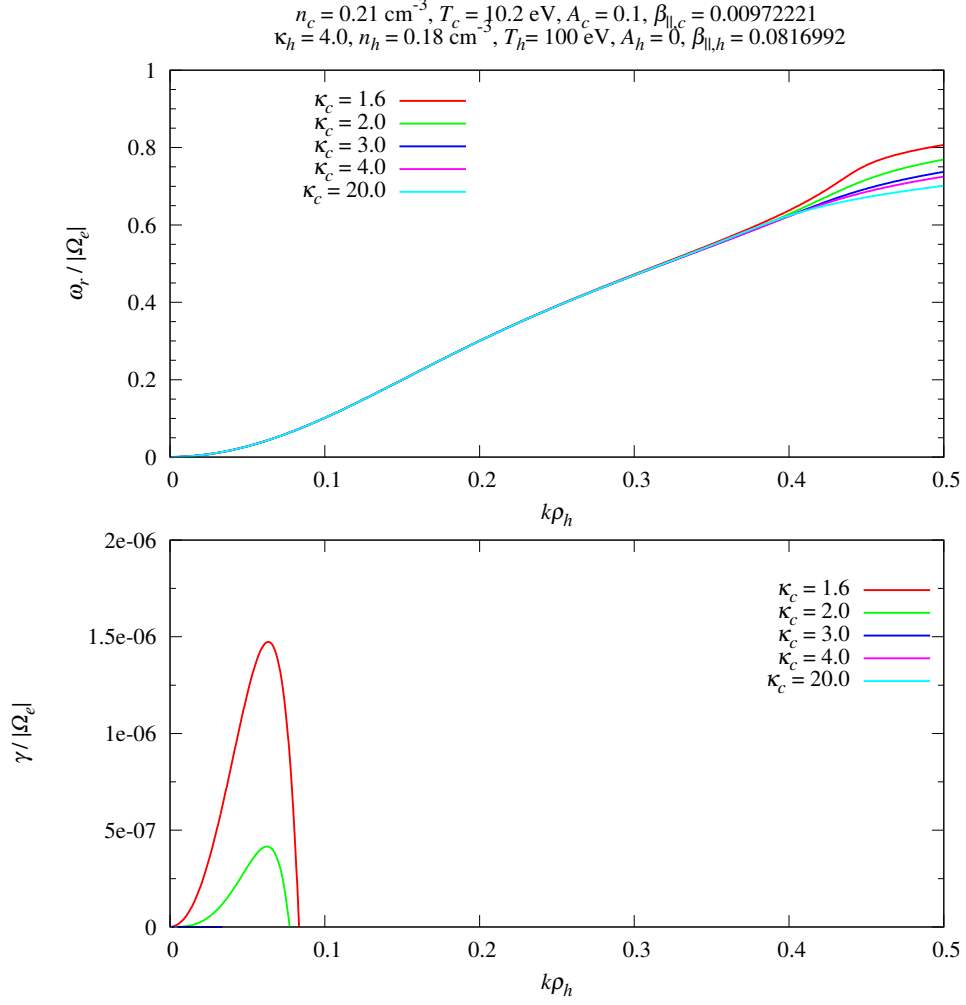


Figure 2.26: Whistler mode dispersion relation (top) and growth rate (bottom) for a sequence of plasmas having different  $\kappa_c$  values, fixed temperature anisotropies corresponding to  $A_h = 0$ ,  $A_c = 0.1$  and hot electron temperature,  $T_h = 100 \text{ eV}$ . All other parameters are as in Table 2.1.

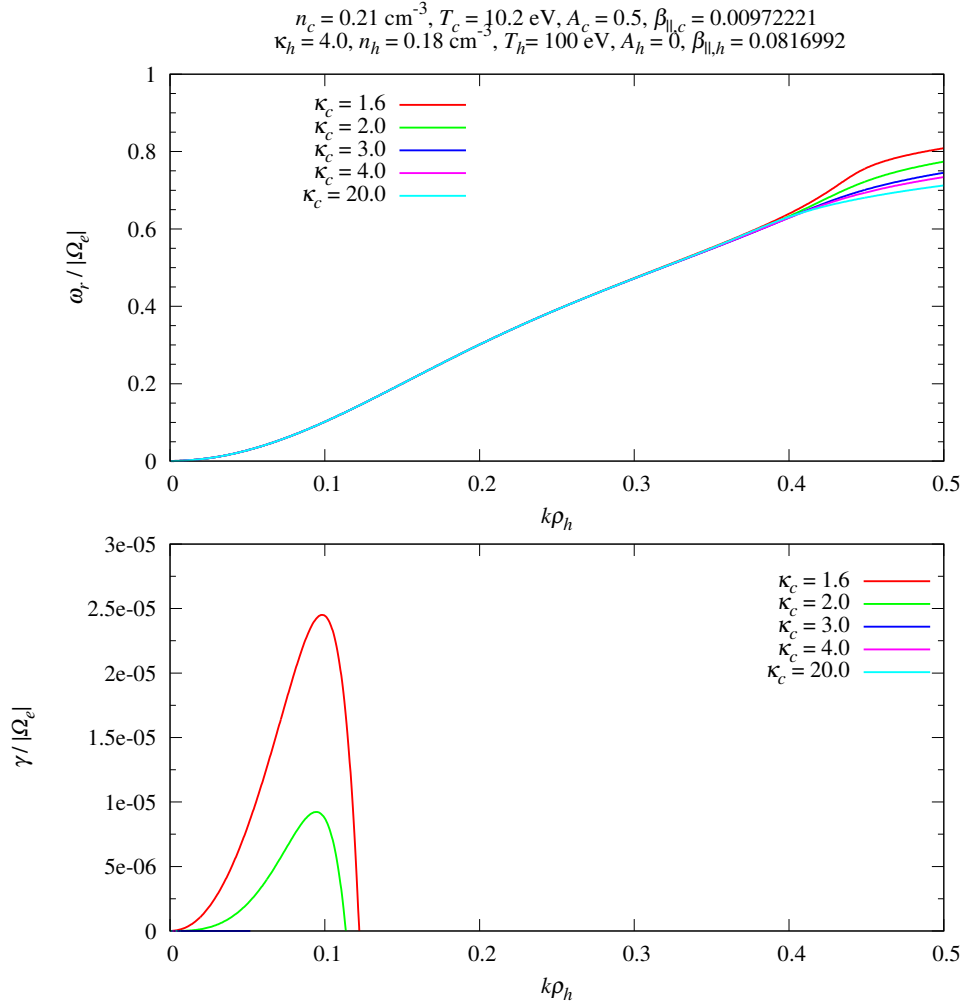


Figure 2.27: Whistler mode dispersion relation (top) and growth rate (bottom) for a sequence of plasmas having different  $\kappa_c$  values, fixed temperature anisotropies corresponding to  $A_h = 0$ ,  $A_c = 0.5$  and hot electron temperature,  $T_h = 100 \text{ eV}$ . All other parameters are as in Table 2.1.

cross over in trend. At  $k\rho_h \approx 0.4$  an increase in  $\kappa_c$  produces an increase in frequency. As  $k\rho_h$  is increased to  $k\rho_h = 0.5$  a reverse in the trend is observed.

For this value of the anisotropy of the cool electrons, an increase in spectral index of the cool electrons results in a monotonic decrease in the maximum growth rate with peak maximum growth rate corresponding to  $\kappa_c = 1.6$ . This is clearly illustrated in the bottom panel of Figure 2.28. The case  $\kappa_c = 3.0$  does experience a positive growth rate but it is of the order  $10^{-8}$  and hence, not within graphical accuracy. The dependence of  $k^*\rho_h$  on  $\kappa_c$ , is clearly demonstrated in the bottom panel, with an increase in  $\kappa_c$  resulting in a monotonic decrease in  $k^*\rho_h$ . In all cases investigated in Figure 2.28, increasing the spectral index of the cool electrons with  $A_c = 2.0$  and  $A_h = 0$ , resulted in a decrease in the window of growing wave numbers. The cool electrons contribute positively to the growth rate for all frequencies below  $\omega_c^* = 0.666667|\Omega_e|$ . The hot electrons remain a constant source of cyclotron damping.

Figures 2.29 - 2.31 address the question of varying the cool and hot electron anisotropies in unison. In these figures the two electron species differ in most characteristics but have equal thermal anisotropy. Figure 2.29 illustrates the whistler mode dispersion relation and growth rate for the case where  $A_c = A_h = 0.1$ . In the real part of the dispersion relation (top panel), varying the spectral index of the cool electrons has very little effect on the dispersion curves at small and intermediate wave numbers ( $k\rho_h \lesssim 0.35$ ). As the wave number is increased so is the  $\kappa_c$  dependence of the curves. More significant differences in dispersion curves emerge at large wave numbers ( $0.35 \lesssim k\rho_h \lesssim 0.5$ ). In this range, an increase in  $\kappa_c$  results in a decrease in frequency. There is a common point of intersection at  $\omega_r = \omega_h^* = \omega_c^* = 0.0909091|\Omega_e|$  (dashed line in top panel) signifying a single frequency at which all thermal effects of both electron species vanish.

The bottom panel of Figure 2.29 illustrates the  $\kappa_c$  dependence of the growth rate of the parallel whistler instability for the chosen anisotropy of  $A_h = A_c = 0.1$ . An increase in  $\kappa_c$  results in a monotonic decrease in the peak growth rate with a peak maximum growth rate corresponding to the case where  $\kappa_h = 1.6$ . Increasing the spectral index of the cool electrons resulted in a decrease in the window of growing wave numbers for all cases

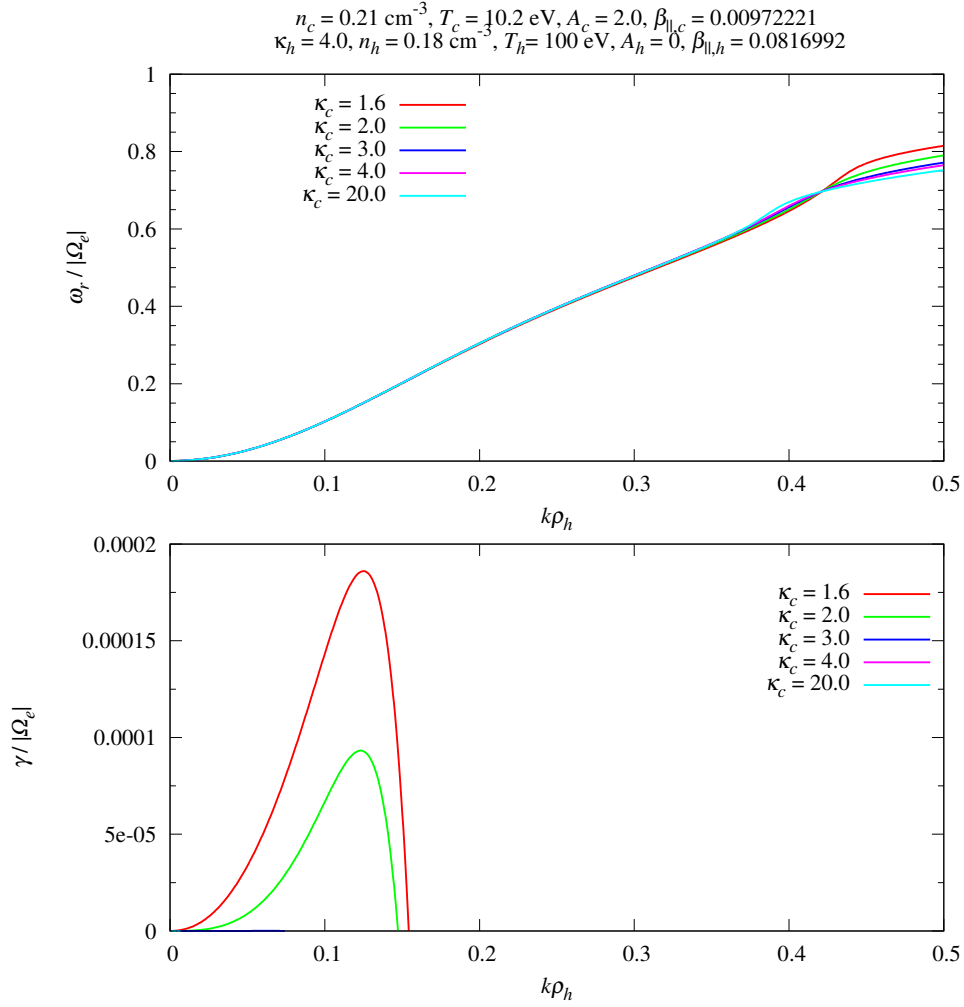


Figure 2.28: Whistler mode dispersion relation (top) and growth rate (bottom) for a sequence of plasmas having different  $\kappa_c$  values, fixed temperature anisotropies corresponding to  $A_h = 0$ ,  $A_c = 2.0$  and hot electron temperature,  $T_h = 100 \text{ eV}$ . All other parameters are as in Table 2.1.

investigated in Figure 2.29, i.e., the greater  $\kappa_c$ , the smaller the instability bandwidth.

The wave number corresponding to the point of intersection in the dispersion relation curves defines an upper boundary of the interval of growing wave numbers due to the fact that  $A_h = A_c$ . In this case with  $A_h = A_c = 0.1$ , we observe a sharp cutoff of the growth rate at a value of  $k$  corresponding to  $\omega_r = \omega_h^* = \omega_c^* = 0.0909091|\Omega_e|$  in the bottom panel of Figure 2.29. Both electron species will make a positive contribution to the growth rate for all wave numbers below this.

Figure 2.30 is similar to Figure 2.29 except in this case the anisotropy of the electrons has been increased from  $A_h = A_c = 0.1$  to  $A_h = A_c = 0.5$ . The top panel illustrates the real part of the dispersion relation. Varying the spectral index of the cool electrons has very little effect at small and intermediate wave numbers ( $k\rho_h \lesssim 0.35$ ), however, as the wave number is increased so is the  $\kappa_c$  dependence. An increase in  $\kappa_c$  results in a decrease in frequency in the range  $0.35 \lesssim k\rho_h \lesssim 0.5$ .

The frequency at which all  $\kappa$  dependency vanishes and the curves intersect is found to be  $\omega_r = \omega_h^* = \omega_c^* = 0.33333|\Omega_e|$  (dashed line in top panel). At the wave number corresponding to this frequency, we find that  $\gamma = 0$  for all curves irrespective of the value of  $\kappa_c$  ( $\kappa_h$  is fixed). As previously explained, this is due to the anisotropies of both electron species being equal.

The peak maximum growth rate corresponds to  $\kappa_h = 1.6$ . An increase in  $\kappa_c$  results in a monotonic decrease in the peak growth rates. In all cases of  $\kappa_c$  investigated in Figure 2.30, an increase in the spectral index of the cool electrons results in a decrease in the instability bandwidth. This is due to an increase in  $\kappa_c$  resulting in a decrease in growth rate at small wave numbers ( $k\rho_h \lesssim 0.15$ ) owing to there being fewer tail electrons with  $v_{\parallel}$  large enough to induce the Doppler shift required for cyclotron resonance.

Figure 2.31 illustrates the whistler mode dispersion relation and growth rate for a sequence of plasmas having different  $\kappa_c$  values and fixed temperature anisotropies corresponding to  $A_c = A_h = 2.0$ . In the real part of the dispersion relation (top panel), we see very little  $\kappa_c$  dependence of the curves. The effects of varying  $\kappa_c$  are only seen as  $k\rho_h$  approaches 0.5. As  $k\rho_h$  approaches 0.5, an increase in cool electron spectral index results in a decrease

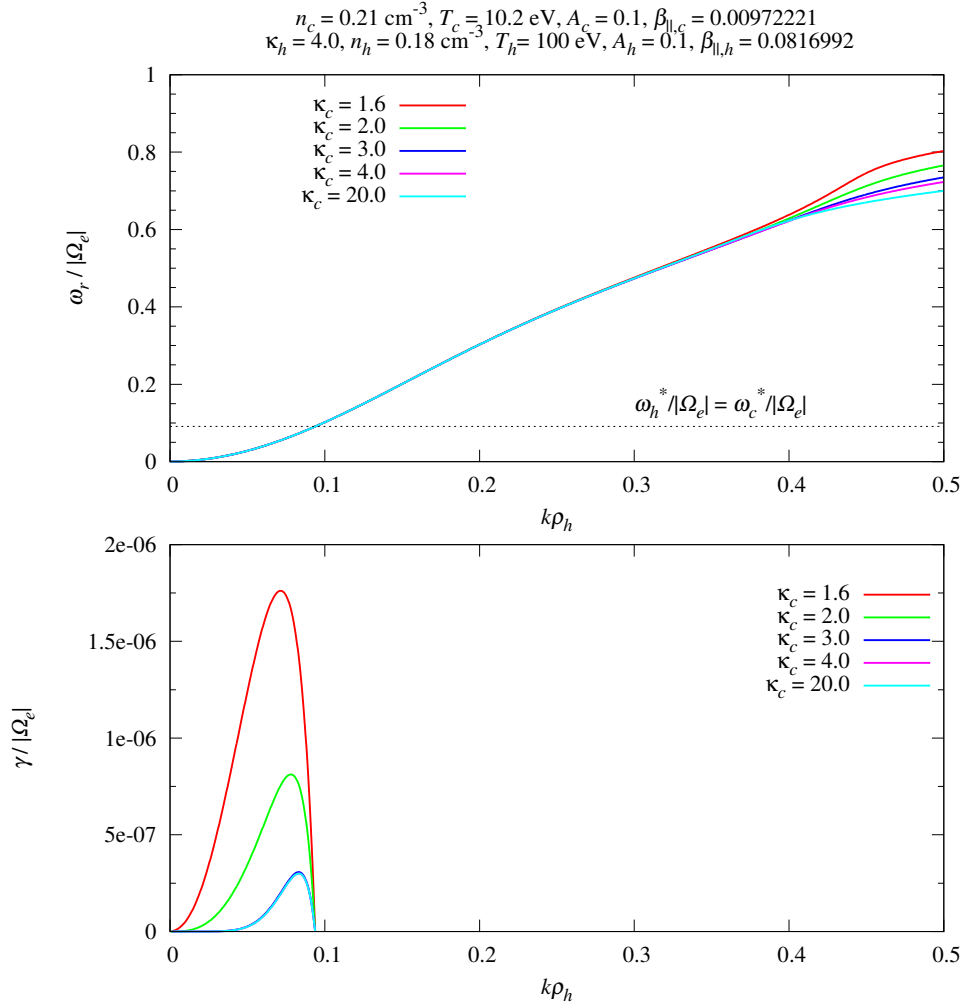


Figure 2.29: Whistler mode dispersion relation (top) and growth rate (bottom) for a sequence of plasmas having different  $\kappa_c$  values, fixed temperature anisotropies corresponding to  $A_c = A_h = 0.1$  and hot electron temperature,  $T_h = 100 \text{ eV}$ . All other parameters are as in Table 2.1. The dashed horizontal line represents  $\omega_h^* = \omega_c^* = 0.0909091|\Omega_e|$ .

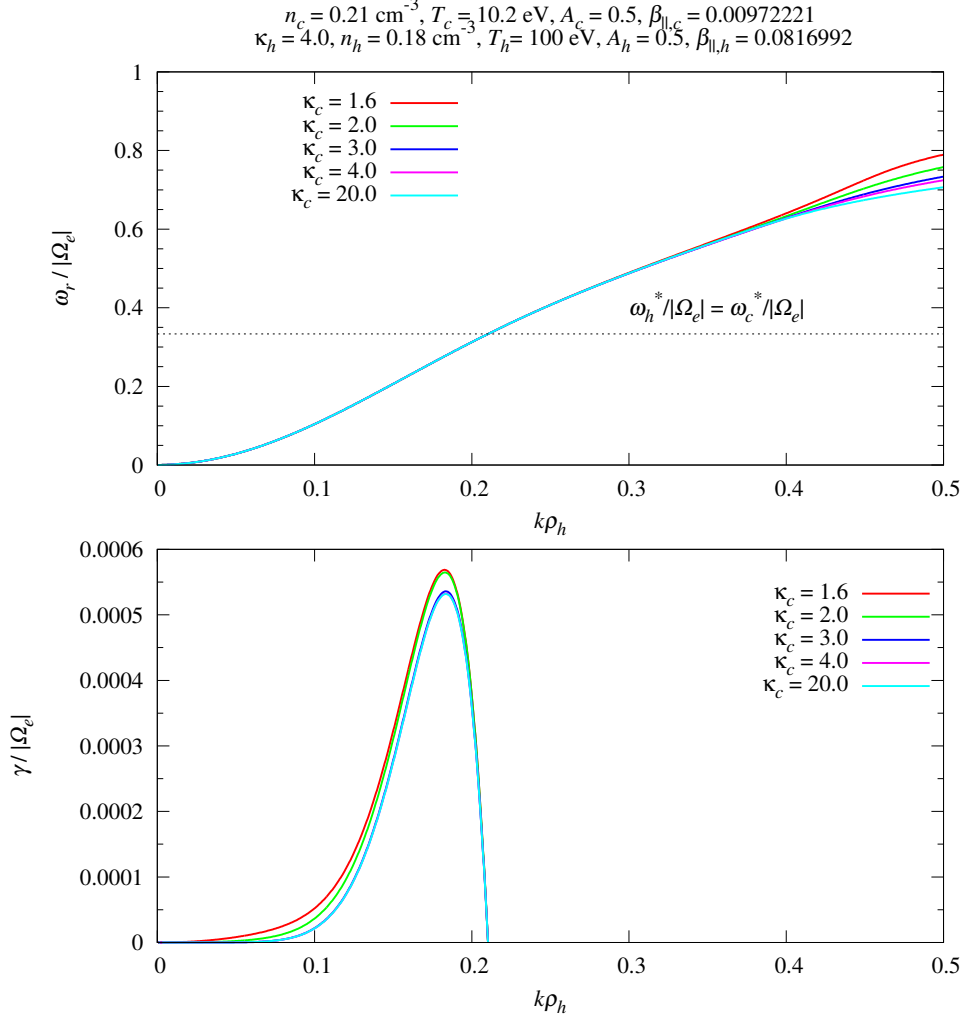


Figure 2.30: Whistler mode dispersion relation (top) and growth rate (bottom) for a sequence of plasmas having different  $\kappa_c$  values, fixed temperature anisotropies corresponding to  $A_c = A_h = 0.5$  and hot electron temperature,  $T_h = 100 \text{ eV}$ . All other parameters are as in Table 2.1. The dashed horizontal line represents  $\omega_h^* = \omega_c^* = 0.33333|\Omega_e|$ .

in frequency. At the frequency  $\omega_r = \omega_h^* = \omega_c^* = 0.666667|\Omega_e|$  all thermal effects and  $\kappa$  dependency of both electron species vanishes. This frequency is illustrated by the dashed line in the top panel of Figure 2.31.

The bottom panel illustrates the growth rate curves. The sharp cutoff in growth rate is clearly observed at the wave number corresponding to  $\omega_r = \omega_h^* = \omega_c^* = 0.666667|\Omega_e|$ . At small wave numbers ( $k\rho_h \lesssim 0.2$ ) the growth rates are less affected by a change in  $\kappa_c$  (compared to Figures 2.29 and 2.30), however, as the wave number is increased so is the  $\kappa_c$  dependency. For this chosen set of parameters, an increase in  $\kappa_c$  results in a monotonic decrease in the peak growth rates with a peak maximum growth rate corresponding to the case where  $\kappa_c = 2.0$ . The case  $\kappa_c = 1.6$  is the exception to this trend having a peak growth rate that lies between  $\kappa_c = 2.0$  and  $\kappa_c = 3.0$ .

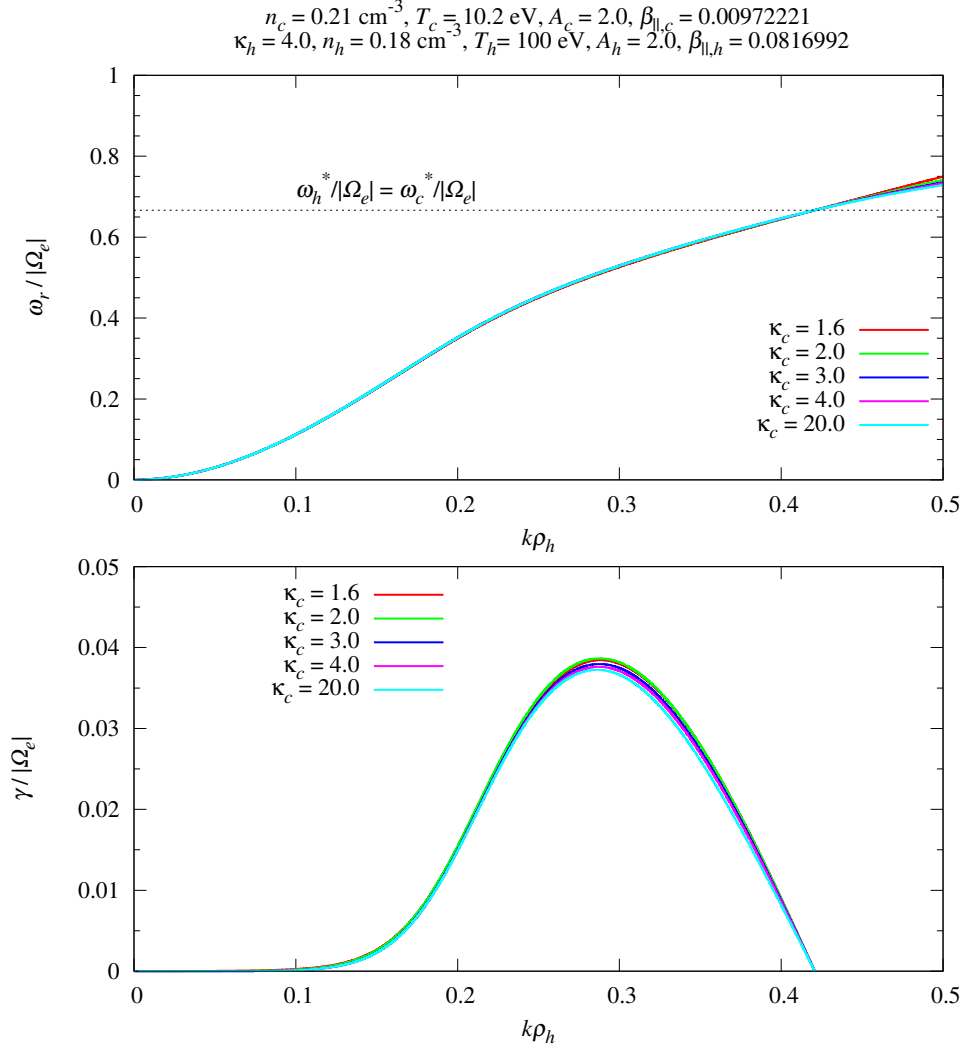


Figure 2.31: Whistler mode dispersion relation (top) and growth rate (bottom) for a sequence of plasmas having different  $\kappa_c$  values, fixed temperature anisotropies corresponding to  $A_c = A_h = 2.0$  and hot electron temperature,  $T_h = 100 \text{ eV}$ . All other parameters are as in Table 2.1. The dashed horizontal line represents  $\omega_h^* = \omega_c^* = 0.666667|\Omega_e|$ .

## 2.5 Discussion and conclusions

This chapter has presented a parameter survey of the parallel propagating whistler instability driven by temperature anisotropy in both the hot and cool electron species, for a plasma in which the velocity distribution of each plasma species is modelled by the bi-kappa distribution. The dispersion relation, Equation (2.9), was solved numerically for different anisotropies, temperatures and spectral indices of the two electron components using parameter values derived by *Schippers et al.* (2008) for the Saturnian magnetosphere as a guide. This was done to account for the innate temporal variability of a dynamic magnetosphere such as that of Saturn.

The effects of varying the spectral index of the hot electrons,  $\kappa_h$ , with a variety of hot electron temperature anisotropy values,  $A_h$ , and fixed cool electron temperature anisotropy  $A_c = 0$  at hot electron plasma parallel beta values,  $\beta_{\parallel h}$ , close to unity are evident in Figures 2.3 - 2.5. These figures revealed that the real part of the dispersion relation becomes increasingly dependent on  $\kappa_h$  as the value of  $A_h$  is increased from 0.1 to 0.5. In all cases of  $A_h$  investigated, the dependency of the dispersion curves on the spectral index of the hot electrons,  $\kappa_h$ , is clearly evident at large wave numbers ( $0.8 \lesssim k\rho_h \lesssim 1.0$ ). As  $A_h$  is increased, the dependency of the dispersion curves on  $\kappa_h$  becomes visible at smaller wave numbers ( $k\rho_h \lesssim 0.8$ ). The variation of the spectral index of the cool electrons,  $\kappa_c$ , with a variety of cool electron temperature anisotropy,  $A_c$ , values and  $A_h = 0$  for the same  $\beta_{\parallel h}$  value (Figures 2.20 - 2.22), revealed a very different trend. For all cases of  $A_c$  investigated, the real part of the dispersion relation showed very little  $\kappa_c$  dependence for all  $k\rho_h \lesssim 1.0$ . Only as  $k\rho_h$  approached 1.0 did a marginal  $\kappa_c$  dependency emerge.

For hot electron parallel beta values,  $\beta_{\parallel h} \ll 1$ , the effects of varying  $\kappa_h$  with a variety of  $A_h$  values and  $A_c = 0$  is markedly different to the  $\beta_{\parallel h} \approx 1$  case. At small anisotropies ( $A_h = 0.1$  and  $A_h = 0.2$ ), a variation in  $\kappa_h$  results in a distinct difference in dispersion curves at intermediate and large wave numbers ( $0.2 \lesssim k\rho_h \lesssim 0.5$ ) as illustrated in Figures 2.12 and 2.13. At larger anisotropies ( $A_h = 0.75$  and  $A_h = 1.0$ ), the  $\kappa_h$  dependence of the curves is only seen at large wave numbers ( $0.4 \lesssim k\rho_h \lesssim 0.5$ ) as observed in Figures 2.14 - 2.15. The dependency of the dispersion curves on a variation of  $\kappa_c$  with a variety of  $A_c$

values and  $A_h = 0$  for  $\beta_{\parallel h} \ll 1$  is only evident at large wave numbers ( $0.4 \lesssim k\rho_h \lesssim 0.5$ ), for all values of  $A_c$  investigated as observed in Figures 2.26 - 2.28. However, the trend of the curves is significantly dependent on  $A_c$ . At  $A_c = 0.1$  and  $0.5$  the trend is monotonic over the range  $0.4 \lesssim k\rho_h \lesssim 0.5$ , with an increase in  $\kappa_c$  resulting in a decrease in frequency. When  $A_c = 2.0$ , the trend is non-monotonic. At  $k\rho_h \approx 0.4$ , an increase in  $\kappa_c$  results in an increase in frequency. This trend is then reversed as  $k\rho_h$  increases, with an increase in  $\kappa_c$  resulting in a decrease in frequency as  $k\rho_h$  approaches  $0.5$ .

We defined a parameter  $k^*\rho_h$  (in Section 2.4) as the wave number at which the growth rate,  $\gamma$ , vanishes for plasmas where the temperature anisotropy of the hot electrons is not equal to that of the cool electrons, i.e.,  $A_h \neq A_c$ . At this point the wave number at which the positive contribution provided by one electron species equals, in magnitude, the negative contribution provided by the other. This parameter arises because we have  $A_h \neq A_c$  and, therefore, there is no single wave number, independent of  $\kappa$ , at which the growth rate vanishes for all curves. For the cases  $A_c = 0$  at  $\beta_{\parallel h}$  close to unity (Figures 2.3 - 2.5), the dependency of  $k^*\rho_h$  on  $\kappa_h$  is non-monotonic at very low values of  $A_h$  ( $A_h = 0.1$ ). As  $A_h$  is increased the dependency becomes monotonic with an increase in  $\kappa_h$  resulting in an increase in  $k^*\rho_h$  for  $A_h = 0.5$ . For  $A_h = 0$  with  $\beta_{\parallel h}$  close to unity (Figures 2.20 - 2.22), an increase in  $\kappa_c$  results in a monotonic decrease in  $k^*\rho_h$  for all cool electron anisotropies investigated.

For values of  $\beta_{\parallel h} \ll 1$  and  $A_c = 0$  (Figures 2.12 - 2.15), the variation of  $k^*\rho_h$  with  $\kappa_h$  is non-monotonic for small anisotropies ( $A_h = 0.1$  and  $0.2$ ). The largest value of  $k^*\rho_h$  is found for the case where  $\kappa_h = 2.0$ . For  $\kappa_h < 2.0$  an increase in  $\kappa_h$  results in an increase in  $k^*\rho_h$ . For  $\kappa_h > 2.0$  an increase in  $\kappa_h$  results in a decrease in  $k^*\rho_h$ . For larger anisotropies ( $A_h = 0.75$  and  $A_h = 1.0$ ), there is a monotonic increase in  $k^*\rho_h$  with an increase in  $\kappa_h$ . For  $A_h = 0$  with  $\beta_{\parallel h} \ll 1$  (Figures 2.26 - 2.28), an increase in  $\kappa_c$  results in a monotonic decrease in  $k^*\rho_h$  for all cool electron anisotropies investigated.

For the cases  $A_c = 0$  at  $\beta_{\parallel h}$  close to unity (Figures 2.3 - 2.5), the peak growth rates are highly dependent on both  $A_h$  and  $\kappa_h$ . At the lowest anisotropy ( $A_h = 0.1$ ), an increase in  $\kappa_h$  results in a monotonic decrease in peak growth rate (with the exception being for case

close to the theoretical minimum). As the anisotropy of the hot electrons is increased, this trend is gradually reversed with a peak maximum growth rate corresponding to the quasi-Maxwellian case for the largest anisotropy ( $A_h = 0.5$ ). For  $A_h = 0$  at  $\beta_{\parallel h}$  close to unity (Figures 2.20 - 2.22), in all cases of  $A_c$  investigated, the maximum peak frequency always corresponded to the case where  $\kappa_c = 1.6$ . This was followed by  $\kappa_c = 2.0$ . There was no overall positive contribution to the growth rate for higher values of  $\kappa_c$  investigated. For  $\beta_{\parallel h} \ll 1$  and  $A_c = 0$  (Figures 2.12 - 2.15), an increase in  $\kappa_h$  results in a monotonic decrease in peak growth rate for the lowest anisotropy ( $A_h = 0.1$ ). This trend is gradually reversed as  $A_h$  increases. At the largest anisotropy ( $A_h = 1.0$ ), the peak maximum growth rate corresponds to  $\kappa_h = 20.0$ . For  $\beta_{\parallel h} \ll 1$  and  $A_h = 0$  (Figures 2.26 - 2.28), an increase in  $\kappa_c$  results in a monotonic decrease in the peak growth rate with the peak maximum growth rate corresponding to  $\kappa_c = 1.6$ . This is followed by the case with  $\kappa_c = 2.0$ . Although there exists a range of wave numbers where  $\gamma > 0$  for the cases where  $\kappa_c = 3.0$ , this is not within graphical accuracy. For  $\kappa_c > 3.0$ , no wave growth is observed for all wave numbers investigated.

When  $A_h = A_c$ , there exists a single frequency at which all thermal effects of both electron species vanish. The wave number corresponding to this frequency sets an upper boundary below which all wave growth is confined, i.e., there exists a single value of  $k$  at which all curves will have  $\gamma = 0$  irrespective of the spectral indices. During our investigation of the effects of varying  $\kappa_h$  with  $A_h = A_c$  and  $\beta_{\parallel h}$  close to unity (Figures 2.6 - 2.11), it was found that increasing the anisotropy of both electron species results in the real part of the dispersion relation becoming increasingly dependent on  $\kappa_h$  at smaller wave numbers ( $k\rho_h \lesssim 0.4$ ). At values of  $\beta_{\parallel h} \ll 1$  (Figures 2.16 - 2.19), the reverse is true. The real part of the dispersion relation curves become decreasingly dependent on  $\kappa_h$  as  $A_h$  and  $A_c$  are increased with significant differences between dispersion curves only emerging in the range  $0.4 \lesssim k\rho_h \lesssim 0.5$  when  $A_h = A_c = 1.0$ .

In our investigation of the effects of varying  $\kappa_c$  with  $A_h = A_c$  and  $\beta_{\parallel h} \approx 1$  (Figures 2.23 - 2.25), it was found that as the anisotropy of both electron species was increased, the dependency of the real part of the dispersion relation on  $\kappa_c$  was only seen at large wave

numbers ( $k\rho_h \gtrsim 1.0$ ). For  $\beta_{\parallel h} \ll 1$  (Figures 2.29 - 2.31), as  $A_c$  and  $A_h$  increase, the effects of varying  $\kappa_c$  decreases at larger wave numbers ( $0.4 \lesssim k\rho_h \lesssim 0.5$ ) with hardly any variation in dispersion curves observed in this range for  $A_h = A_c = 2.0$ .

For the case  $A_h = A_c$ , the peak growth rates are highly dependent on  $\kappa_h$  for both  $\beta_{\parallel h} \ll 1$  and  $\beta_{\parallel h} \approx 1$ . For  $\beta_{\parallel h} \approx 1$  (Figures 2.6 - 2.11), at low anisotropies ( $A_h = A_c = 0.1$ ) there is a monotonic decrease in peak growth rate (with the exception being for  $\kappa_h = 1.6$ ) with an increase in  $\kappa_h$ . This trend is reversed as the anisotropy of the hot electrons is increased with a peak maximum growth rate corresponding to the quasi-Maxwellian case for large anisotropies ( $A_h = A_c = 0.5$ ). This trend also holds true for the case  $\beta_{\parallel h} \ll 1$  (Figures 2.16 - 2.19). An increase in  $\kappa_h$  results in a monotonic decrease in peak growth rate at small anisotropies ( $A_h = A_c = 0.1$ ) with a reverse in trend observed at large anisotropies ( $A_h = A_c = 1.0$ ). However, the range of anisotropies over which the aforementioned trend is seen depends on the value of  $\beta_{\parallel h}$ . In other words, for a fixed value of  $\beta_{\parallel h}$  there exists a range of anisotropies for which an increase in  $\kappa_h$  results in a decrease in peak growth rate. The size of this interval depends on  $\beta_{\parallel h}$ . The smaller the value of  $\beta_{\parallel h}$  the larger the interval. At a critical value of  $A_h$  and  $A_c$  (which is again dependent on  $\beta_{\parallel h}$ ) the reverse is observed and an increase in  $\kappa_h$  results in an increase in peak growth rate.

When investigating the  $\kappa_c$  dependence of the growth rate with  $A_h = A_c$ , it was found that for  $\beta_{\parallel h} \approx 1$  (Figures 2.23 - 2.25), an increase in  $\kappa_c$  results in a monotonic decrease in peak growth rate with peak maximum growth rate corresponding to  $\kappa_c = 1.6$  for all electron anisotropies investigated. This trend in peak growth rate holds true even for electron anisotropy of both species as high as 2.0.

For  $\beta_{\parallel h} \ll 1$  (Figures 2.29 - 2.31), an increase in  $\kappa_c$  results in a monotonic decrease in peak growth rate at the smallest anisotropy investigated,  $A_h = A_c = 0.1$ . This trend continues for the case  $A_h = A_c = 0.5$ . As the anisotropy is increased, this trend slowly starts to reverse. However, even at anisotropies as high as  $A_h = A_c = 2.0$ , a complete reversal in trend is not seen. For this electron anisotropy ( $A_h = A_c = 2.0$ ), the peak maximum growth rate corresponds to the case  $\kappa_c = 2.0$ .

An increase in the spectral index of the hot or cool electron species will always result

in a decrease in the window of growing wave numbers. This was evident in all of the cases investigated in this parameter survey. This is due to a phenomenon that occurs at small wave numbers. In this region, a small spectral index implies that there are more superthermal particles in the tail of the particle velocity distribution. Owing to this, there are more tail electrons at small wave numbers with parallel velocities,  $v_{\parallel}$ , large enough to induce the Doppler shift required for cyclotron resonance, in accordance with Equation (2.5) (*Mace et al.*, 2011). The more particles that participate in this cyclotron resonance process, the greater the contribution to the growth rate, leading to wave amplification. As the spectral index of either species is increased, the probability of these wave-particle interactions occurring is decreased and, therefore, so is the window of growing wave numbers (*Mace et al.*, 2011).

It is also important to note that in all cases investigated, an increase in  $\beta_{\parallel h}$  resulted in an increase in peak growth rate as well as an increase in the window of growing wave numbers for a fixed value of anisotropy of both electron species. As  $\beta_{\parallel h}$  is decreased a much larger anisotropy of the electron species is needed to produce significant wave growth. This is expected, as the particle pressure is considerably less than the magnetic pressure for small  $\beta_{\parallel h}$ , thus, the magnetic field produces a stabilising effect (*Mace and Sydora*, 2010).

In all cases investigated, an increase in anisotropy of an electron species always resulted in an increase in peak growth rate for a fixed spectral index of both electrons. An increase in anisotropy always resulted in a larger window of growing wave numbers and frequencies due to the condition for wave growth Equation (2.25).



## Chapter 3

# Electromagnetic ion cyclotron waves

The results of this chapter are summarised in the paper, **Henning, F. D. and Mace, R. L. (2014), “Effects of ion abundances on electromagnetic ion cyclotron wave growth rate in the vicinity of the plasmopause”, *Physics of Plasmas*, 21(4):042905.**

### 3.1 Introduction

Electromagnetic ion cyclotron (EMIC) waves are naturally occurring plasma emissions commonly observed in the Earth’s magnetosphere (*Anderson et al.*, 1992b,a; *Erlandson and Ukhorskiy*, 2001; *Fraser and Nguyen*, 2001). They occur at frequencies below the local proton gyrofrequency and are left hand circularly polarised (L mode), corresponding to the sense of ion gyration, when propagating parallel to the ambient magnetic field,  $\mathbf{B}_0$ . They play an important role in the overall dynamics of Earth’s magnetosphere as they contribute to the loss and energisation of magnetospheric particles due to their resonant interaction with ions and relativistic electrons by altering their pitch angles and energies (*Summers and Thorne*, 2003; *Albert and Bortnik*, 2009; *Xiao et al.*, 2011, 2012, 2013). This was previously discussed in greater detail in Chapter 1, Sections 1.1 and 1.2.

EMIC waves are predominantly excited in the vicinity of the plasmopause where the thermally anisotropic ring current and the cool plasmaspheric plasmas overlap (*Thorne and Horne*, 1997). The ring current is one of the main sources of free energy for the excitation of electromagnetic ion cyclotron waves in the terrestrial magnetosphere. It is a toroidally shaped electric current which flows westward around the Earth. It has variable density and is found at geocentric distances of between 2 and 9 Earth radii ( $R_E$ ) (*Daglis et al.*, 1999) (see Figure 3.1). Geomagnetically trapped particles gyrate around the ambient magnetic field as a result of the Lorentz force. However, these particles are also subject to drift motions due to the gradient and curvature of the magnetic field (*Baumjohann and Treumann*, 1996). The gradient drift motion, the curvature drift motion and gyration are the three basic motions of charged particles in the presence of an inhomogeneous magnetic field (*Daglis et al.*, 1999) (see Figure 3.2). These give rise to an azimuthal drift with electrons moving eastward and most ions moving westward resulting in a net charge

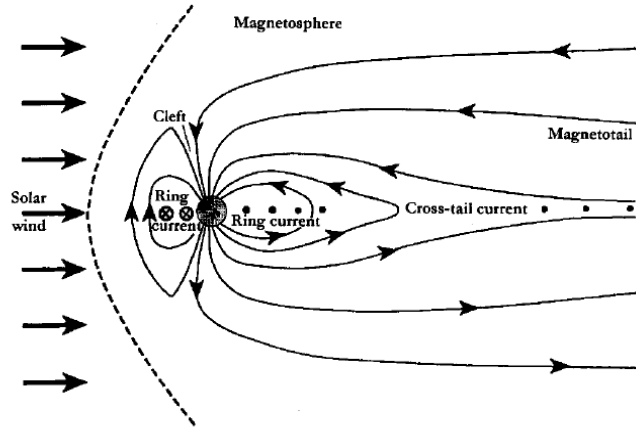


Figure 3.1: A schematic diagram of the terrestrial magnetosphere (*Daglis et al.*, 1999).

transport.

The ring current has a permanent existence due to the natural properties of charged particles in the geospace environment. However, its intensity is highly variable (*Daglis et al.*, 1999). During magnetic storms, for instance, its intensity is increased. These increases in the ring current intensity are responsible for global decreases in the Earth's surface magnetic field (*Baker and Daglis*, 2001). Such a global decrease in the surface magnetic field strength is the defining feature of geomagnetic storms. Intense geomagnetic storms can have adverse effects on technology systems such as navigation satellites, telecommunication cables and power grids (*Daglis et al.*, 1999).

The terrestrial ring current is enhanced by the injection of plasma sheet ions into the inner magnetosphere during magnetic storms (*Kavanagh et al.*, 1968; *Ejiri*, 1978; *Williams*, 1983; *Wolf et al.*, 1998; *Nosé et al.*, 2005). An enhanced dawn-dusk electric field convects, via  $\mathbf{E} \times \mathbf{B}$  drift, the plasma sheet particles towards Earth on the night side of the Earth's magnetosphere (*Williams*, 1983). These convecting ions experience both betatron and Fermi acceleration as they are transported to low altitudes to form the ring current (*Williams*, 1983). As pointed out by *Mace et al.* (2011), since the plasma sheet ions are a direct source of the ring current plasma (*Jordanova et al.*, 2003; *Nosé et al.*, 2005; *Lavraud*

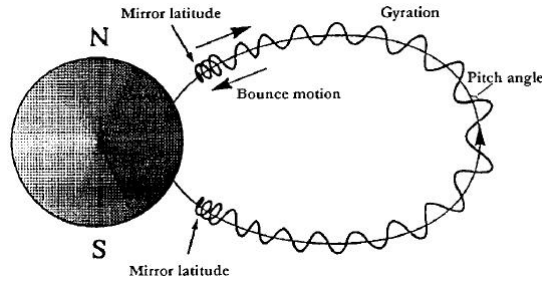


Figure 3.2: The cyclotron motion and bounce motion of a charged particle along a geomagnetic field line (*Daglis et al.*, 1999).

and Jordanova, 2007), the two plasma systems share many of the same characteristics, such as ion composition and energy density. The plasma sheet ions have been shown to have velocity distributions that exhibit power law tails (*Ipavich and Scholer*, 1983; *Ipavich et al.*, 1985) and have previously been well fitted by a kappa distribution function under a wide variety of geomagnetic conditions (*Christon et al.*, 1989, 1991). Owing to this, it is expected that the velocity distribution of the ring current ions would also be best modelled by the kappa distribution (*Mace et al.*, 2011). In fact, due to the acceleration mechanisms previously mentioned, it is possible that the power law tails of the ring current ions may be enhanced as they convect inward (*Mace et al.*, 2011).

Electromagnetic ion cyclotron waves driven by thermally anisotropic ions having velocity distributions that exhibit power law tails have been previously studied (*Xue et al.*, 1996a,b; *Chaston et al.*, 1997; *Vega et al.*, 1998; *Xiao et al.*, 2007; *Mace et al.*, 2011; *Zhou et al.*, 2013a,b). *Xue et al.* (1996a) examined the dispersive properties and growth rate of oblique EMIC waves for conditions in the Earth's outer magnetosphere ( $L = 7$ ) with the energetic particle distribution being that of the Lorentzian distribution. They found that, for the real part of the wave frequency, there is little discrepancy between the Maxwellian case and that of the Lorentzian. However, the growth and damping rates of each are significantly different. For small wave normal angles to the ambient magnetic field, the growth and damping rates were larger for the Maxwellian distribution case than its Lorentzian

counter part. For large wave normal angles, the growth and damping rates are relatively small in both cases. They found that the largest wave growth rate (temporal), for both distributions, was observed for parallel propagation.

*Xue et al.* (1996b) investigated the growth rate of field-aligned EMIC waves in the terrestrial magnetosphere. They used a bi-kappa velocity distribution to model the energetic ring current ions and compared their results to those obtained with its bi-Maxwellian counterpart. They explored the sensitivity of the growth rate to various plasma parameters that are typical of the outer magnetosphere. Their results showed an increase in convective growth rate in the outer magnetosphere ( $L \geq 5$ ) that maximised near the magnetopause ( $L \approx 9$ ). The most significant increase was seen in the bands above and below the helium gyrofrequency ( $\Omega_{\text{He}^+}$ ). In this instance bands refers to the range of frequencies. The band above  $\Omega_{\text{He}^+}$  is the frequency range  $\Omega_{\text{He}^+} < \omega_r < \Omega_{\text{H}^+}$ , while below refers to the frequency range  $\Omega_{\text{O}^+} < \omega_r < \Omega_{\text{He}^+}$ . The oxygen ions are a minor species whose presence only has a modest effect on the growth rate and, thus, *Xue et al.* (1996b) chose to confine the majority of their study to a plasma composed exclusively of protons and helium ions.

When investigating the effects that varying the spectral index,  $\kappa$ , would have on the wave convective growth rate, *Xue et al.* (1996b) observed that as the value of  $\kappa$  decreased, so did the peak growth rate. As pointed out by *Mace et al.* (2011), this result is due to their choice of plasma beta value being relatively high ( $\beta \approx 1$ ), as it is in the outer magnetosphere. Other parameters investigated were the anisotropy, density and temperature of the energetic protons, the ambient plasma density, and the concentration and temperature of the thermal helium ions. The results of *Xue et al.* (1996b) show that as the anisotropy of the energetic protons is increased, so are the peak growth rates in both the bands above and below  $\Omega_{\text{He}^+}$ . As the number density of the energetic protons is increased, so is the peak growth rate in both bands above and below  $\Omega_{\text{He}^+}$ . The same trend is seen for the investigation into the temperature variation.

An increase in concentration of the helium ions decreases the peak growth rate in the band above  $\Omega_{\text{He}^+}$ , while growth in the lower band ( $\Omega_{\text{O}^+} < \omega_r < \Omega_{\text{He}^+}$ ) is relatively insensitive to helium concentration. An increase in the temperature of the helium ions decreases the

peak growth rate in both bands above and below  $\Omega_{\text{He}^+}$ . For all of these investigations, *Xue et al.* (1996b) compared numerical results obtained using a bi-kappa particle distribution to model the energetic ring current ions to similar results using a bi-Maxwellian distribution. They concluded that the use of the Maxwellian distribution to describe the energetic ring current ions overestimates the peak convective growth rates in all cases. During their investigation of the effects of varying the ambient plasma density, they observed that for high densities ( $n_e \geq 10\text{cm}^{-3}$ ) there is a comparable convective gain both above and below  $\Omega_{\text{He}^+}$ . However, when looking at peak growth rates in the band above  $\Omega_{\text{He}^+}$ , they found that an increase in density results in a decrease in the peak growth rate, while in the band below  $\Omega_{\text{He}^+}$  the reverse is true.

*Chaston et al.* (1997) derived the electromagnetic dispersion relation for parallel propagation from the linearised Vlasov equation for both the bi-kappa distribution and a crescent shaped distribution (given by the generalised distribution function presented in *Gary and Sinha* (1989)). They examined the effects that both these distributions have on electromagnetic instabilities driven by the proton temperature anisotropy and relative drift between components in a plasma. Their study focused on the plasma sheet and the plasma sheet boundary layer regions. They investigated the effects of varying the spectral index,  $\kappa$ . It was found that a decrease in  $\kappa$  resulted in a decrease in the peak frequency growth rate and an increase in the frequency range over which the instability occurs. These results are consistent with those found by *Xue et al.* (1996b) in regions where they too use a relatively high value of plasma beta,  $\beta$ .

*Vega et al.* (1998) studied the L mode in electromagnetic proton-cyclotron waves in plasmas modelled by a Lorentzian distribution function. They considered a plasma consisting of only energetic anisotropic protons and an isotropic cool proton component both having bi-kappa velocity distributions. Their investigation revealed that the convective growth rate showed a significant dependence on the spectral index of the hot proton species,  $\kappa$ . The maximum growth rate was found to always decrease, or increase until  $\kappa$  reached some optimum value and then increased, or decreased, depending on both the thermal anisotropy of the hot protons and the cool proton concentration. Like *Xue et al.* (1996b), they too

showed that the maximum growth rates decrease with a decrease in the thermal anisotropy of the hot protons. *Vega et al.* (1998) showed that the influence of a high energy tail on the amplification and generation of electromagnetic proton-cyclotron waves depends on both the cool proton population as well as the values of thermal anisotropies. The temporal and convective growth rates can be larger than, equal to or smaller than those of Maxwellian plasmas, depending on the cool proton concentration and the anisotropy of the hot proton distribution.

*Xiao et al.* (2007) examined the EMIC instability driven by the thermal anisotropy ( $T_{\perp}/T_{\parallel} > 1$ ) of superthermal protons modelled with a typical kappa distribution in a cool multi-species plasma composed of electrons,  $H^+$ ,  $He^+$  and  $O^+$ . They derived a representation of the superthermal proton instability threshold condition associated with the kappa distribution under the marginal stability condition (*Xiao et al.*, 2007, Equation (10)). They found that as the spectral index  $\kappa$ , increased, the instability threshold condition generally decreased, tending to the lowest limiting values of the bi-Maxwellian model. This lead them to the conclusion that the bi-Maxwellian model overestimates the maximum growth rate.

*Zhou et al.* (2013a) used THEMIS simultaneous measurements of fields and particle velocity distributions to model some EMIC wave events observed in the outer magnetosphere ( $L \sim 6 - 7$ ). They fitted the observed overall ion velocity distributions with (i) a sum of bi-Maxwellian distributions and (ii) a sum of bi-kappa distributions, fixing  $\kappa = 2$  for each. They show that the bi-kappa fits are more consistent with the measured particle velocity distributions than the corresponding bi-Maxwellian ones. They were able to determine the path-integrated wave gain by ray tracing, using the EMIC growth rate in the small approximation limit,  $|\gamma|/\omega_r \ll 1$ . It was found that the smaller growth rate predicted by the Vlasov theory using the bi-kappa distribution produced wave gains that were more consistent with those measured, while those predicted by the bi-Maxwellian distribution tended to overestimate this value.

*Zhou et al.* (2013b) use similar techniques to *Zhou et al.* (2013a) to analyse an electron heating event observed by THEMIS. The heating event was analysed in terms of Landau

damping of oblique EMIC waves in the outer magnetosphere. Their results suggest that the frequencies of EMIC waves in the  $\text{He}^+$  branch produced by ion thermal anisotropy correlate well with the expected regions of strong Landau damping by cool electrons for the event considered. *Zhou et al.* (2013b) argue that this gives rise to an efficient transfer of energy from EMIC waves to the electrons and as a result could in turn provide a mechanism responsible for stable auroral red arcs.

All of the above mentioned works (*Xue et al.*, 1996a,b; *Chaston et al.*, 1997; *Vega et al.*, 1998; *Xiao et al.*, 2007; *Zhou et al.*, 2013a,b) consider EMIC waves in the outer magnetosphere ( $L \geq 6$ ). In this region the parallel plasma beta is high, with the bi-kappa model yielding smaller growth rates than the bi-Maxwellian one (*Mace et al.*, 2011). As the above mentioned references (*Zhou et al.* (2013a) and *Zhou et al.* (2013b)) illustrated, the resulting diminished rate of growth is more consistent with wave measurements in this region than growth rates predicted by bi-Maxwellian theory.

On the other hand, *Mace et al.* (2011) investigated the EMIC instability driven by hot ring current ions having velocity distributions that exhibit thermal anisotropy and power law tails of varying hardness for parameters consistent with the inner magnetosphere. They used a model whereby both the cool plasmaspheric ions as well as the hot ring current ions have velocity distributions that are modelled by the bi-kappa distribution. This investigation differed from those previously mentioned as it focused on the region of the magnetosphere in the vicinity of  $L = 4$ , i.e., the inner magnetosphere, where plasma beta values are smaller. They assumed an ion composition of cool protons, cool helium ions and cool oxygen ions provided by the plasmasphere and hot protons, hot helium ions and hot oxygen ions provided by the ring current.

Their investigation illustrated the effects of a ring current composed solely of energetic protons. In this case they found that all branches of the EMIC wave are destabilised, with the peak maximum growth rate corresponding to waves on the helium branch and the smallest corresponding to waves on the oxygen branch. In their investigation of the effects that the spectral index of the ring current protons has on the growth rates, they found that in both the proton and helium branches, an increase in the spectral index

resulted in a decrease in peak growth rate for all values of kappa besides  $\kappa = 1.6$ . In the oxygen branch, they found that there is a threshold value of kappa for which waves on the branch will be destabilised. These results were used as a reference case to compare with the results for a multi-species ring current.

*Mace et al.* (2011) then turned their attention to a plasma with ion composition of cool protons, cool helium ions and cool oxygen ions provided by the plasmasphere and hot protons, hot helium ions and hot oxygen ions provided by the ring current. For the parameters chosen, their results show that only the oxygen branch is destabilised and that the choice of spectral index for the ring current ions affects the peak maximum growth rate of this branch. They found that an increase in the spectral index decreased the peak growth rate. Their further investigations used a proton-rich ring current. In the case of the proton-rich ring current they found that the helium branch can be destabilised when  $\kappa = 1.6$  but is otherwise damped. The oxygen branch, on the other hand, continues to be the only branch that is destabilised.

*Mace et al.* (2011) concluded that in this region of the magnetosphere ( $L = 4$ ), the presence of power law tails on the ring current ions resulted in an increase in the growth rate of the EMIC instability, when compared to that of a bi-Maxwellian model, for the majority of cases investigated. In particular, it was found that the smaller the spectral index (the harder the tail) of the kappa distribution, the larger the maximum growth rate of the instability.

## 3.2 Motivation and aim

The main motivation for the work presented in this chapter was provided by the investigation of *Mace et al.* (2011). The model of *Mace et al.* (2011) was based on a previous bi-Maxwellian model of *Kozyra et al.* (1984). It considered groups of ion species from two sources, namely the hot anisotropic ring current and the cool plasmasphere. *Mace et al.* (2011) took the relative abundances of the cool plasmaspheric proton, helium and oxygen ion species to be 65%, 30% and 5%, respectively, similar to those of *Kozyra et al.* (1984). Although these abundances are possible in the vicinity of the plasmopause, they are not

typical. A more accurate representation of the plasmaspheric ion abundances would be  $\sim 80\%$  protons,  $10\% - 20\%$  helium ions and  $1\% - 5\%$  oxygen ions (*Young et al.*, 1977; *Xue et al.*, 1996a; *Craven et al.*, 1997). For the anisotropic ring current ion species, *Mace et al.* (2011) used equal number densities of protons, helium and oxygen ions, as used by *Kozyra et al.* (1984), which is not a typical representation of the ring current ions.

While the number densities of the plasmaspheric and ring current ion species used by *Mace et al.* (2011) are plausible, they do not span the full range of observed parameters. As previously discussed, the ring current is highly variable and largely dependent on solar activity (*Daglis et al.*, 1999). Consequently, the abundances of the ionic species can differ markedly from storm to storm. During some magnetic storms, for example, the abundance of energetic  $O^+$  ions of ionospheric origin increases dramatically, resulting in the EMIC wave growth being suppressed or its occurrence being confined to frequencies below the oxygen gyrofrequency (*Thorne and Horne*, 1997; *Daglis et al.*, 1998, 1999; *Nosé et al.*, 2005).

Motivated by the work of *Mace et al.* (2011), this chapter presents results from a study of the behaviour of EMIC wave growth rate for a variety of relative abundances of the ion species. Following *Mace et al.* (2011), it is assumed that the hot ring current ions, cool ions of plasmaspheric origin, as well as the electrons, have particle velocity distributions modelled by the bi-kappa distribution. However, the effects of varying the relative ion abundances and how this influences wave growth and damping, are addressed more completely.

### 3.3 Model and basic equations

The model used here is the same as that used by *Mace et al.* (2011), in which the plasma is assumed to be uniform, collisionless and immersed in a uniform magnetic field,  $\mathbf{B}_0$ . Without loss of generality, the direction of  $\mathbf{B}_0$  is taken to be along the  $z$ -axis of our Cartesian coordinate system. Following *Mace et al.* (2011), it is assumed that all particle species have a bi-kappa velocity distribution (*Summers and Thorne*, 1991),

$$f(v_{\perp}, v_{\parallel}) = \pi^{-3/2} \frac{1}{\theta_{\perp}^2 \theta_{\parallel}} \frac{\Gamma(\kappa + 1)}{\kappa^{3/2} \Gamma(\kappa - \frac{1}{2})} \left( 1 + \frac{v_{\perp}^2}{\kappa \theta_{\perp}^2} + \frac{v_{\parallel}^2}{\kappa \theta_{\parallel}^2} \right)^{-(\kappa+1)}, \quad (3.1)$$

where  $\kappa$  is the spectral index,  $\Gamma$  is the gamma function and  $v_{\perp}$  and  $v_{\parallel}$  are the perpendicular and parallel components of the velocity, respectively, relative to  $\mathbf{B}_0$ . The parameters  $\theta_{\perp}$  and  $\theta_{\parallel}$  are generalised thermal speeds perpendicular and parallel to  $\mathbf{B}_0$ , respectively, and are related to the kinetic temperatures,  $T_{\perp}$  and  $T_{\parallel}$  via (*Summers and Thorne, 1991*),

$$\theta_{\perp} = \left[ 2 \left( \frac{\kappa - \frac{3}{2}}{\kappa} \right) \right]^{1/2} \left( \frac{T_{\perp}}{m} \right)^{1/2}, \quad (3.2)$$

$$\theta_{\parallel} = \left[ 2 \left( \frac{\kappa - \frac{3}{2}}{\kappa} \right) \right]^{1/2} \left( \frac{T_{\parallel}}{m} \right)^{1/2}. \quad (3.3)$$

The dispersion relation for parallel propagating L mode waves in a plasma with arbitrary velocity distribution,  $f_{j0}$ , is given by (*Gurnett et al., 2005*) (see Appendix A for an outline of the derivation),

$$\begin{aligned} \frac{k_{\parallel}^2 c^2}{\omega^2} = & 1 - \pi \sum_j \frac{\omega_{pj}^2}{\omega^2} \int_{-\infty}^{\infty} dv_{\parallel} \int_0^{\infty} dv_{\perp} v_{\perp}^2 \frac{1}{k_{\parallel} v_{\parallel} - \omega + \Omega_j} \\ & \cdot \left[ (\omega - k_{\parallel} v_{\parallel}) \frac{\partial f_{j0}}{\partial v_{\perp}} + k_{\parallel} v_{\perp} \frac{\partial f_{j0}}{\partial v_{\parallel}} \right] \quad \text{Im}(\omega) > 0. \end{aligned} \quad (3.4)$$

In the above equation,  $\Omega_j = q_j B_0 / m_j$  is the signed gyrofrequency, where  $q_j$  and  $m_j$  are the charge and mass of the  $j$ th component, respectively. The plasma frequency of the  $j$ th component is given by  $\omega_{pj} = (n_{0j} q_j^2 / \epsilon_0 m_j)^{1/2}$  with  $n_{0j}$  being the equilibrium number density. Other parameters are the parallel component of the wave number  $k_{\parallel}$ , where  $|k_{\parallel}| = k$  since we are considering the case of parallel propagation with respect to  $\mathbf{B}_0$ , and the wave frequency,  $\omega$ , which is complex and given by  $\omega = \omega_r + i\gamma$ .

Substituting Equation (3.1) into Equation (3.4) yields the dispersion relation for parallel-propagating electromagnetic L mode waves in a plasma with a bi-kappa distribution (*Mace et al., 2011*) (see Appendix B for full derivation),

$$\frac{k^2 c^2}{\omega^2} = 1 + \sum_j \frac{\omega_{pj}^2}{\omega^2} \left\{ A_j + \left[ A_j \left( \frac{\omega - \Omega_j}{k \theta_{\parallel j}} \right) + \frac{\omega}{k \theta_{\parallel j}} \right] U_{\kappa j} \left( \frac{\omega - \Omega_j}{k \theta_{\parallel j}} \right) \right\}, \quad (3.5)$$

where  $k = |k_{\parallel}|$ . The function  $U_{\kappa}$  is the plasma dispersion function for a plasma with a kappa distribution (*Mace and Hellberg, 2009*), defined in terms of the Gauss hypergeometric function  ${}_2F_1$  by

$$U_{\kappa}(\zeta) = i \frac{(\kappa - \frac{1}{2})}{\kappa^{3/2}} {}_2F_1 \left[ 1, 2\kappa; \kappa + 1; \frac{1}{2} \left( 1 - \frac{\zeta}{i\kappa^{1/2}} \right) \right], \quad (3.6)$$

and the thermal anisotropy of particle species  $j$  is defined by

$$A_j = \frac{\theta_{\perp j}^2}{\theta_{\parallel j}^2} - 1 = \frac{T_{\perp j}}{T_{\parallel j}} - 1. \quad (3.7)$$

Assuming  $|\gamma| \ll \omega_r$  and ignoring the thermal effects in the real part of the dispersion relation, such that (*Mace et al., 2011*)

$$\frac{k^2 c^2}{\omega_r^2} = 1 - \sum_j \frac{\omega_{pj}^2}{\omega_r(\omega_r - \Omega_j)}, \quad (3.8)$$

*Mace et al.* (2011) derived an estimate of the growth rate of the EMIC instability,

$$\begin{aligned} \frac{\gamma}{\omega_r} = & -\pi^{1/2} \sum_j \frac{\Gamma(\kappa_j)}{\kappa_j^{1/2} \Gamma(\kappa_j - 1/2)} \frac{\omega_{pj}^2}{\omega_r^2} \frac{1}{R(\omega_r)} \left[ A_j \left( \frac{\omega_r - \Omega_j}{k\theta_{\parallel j}} \right) + \frac{\omega_r}{k\theta_{\parallel j}} \right] \\ & \cdot \left[ 1 + \frac{1}{\kappa_j} \left( \frac{\omega_r - \Omega_j}{k\theta_{\parallel j}} \right)^2 \right]^{-\kappa_j} \end{aligned} \quad (3.9)$$

where (*Mace et al., 2011*)

$$R(\omega_r) = 2 + \frac{1}{\omega_r} \sum_j \frac{\omega_{pj}^2 \Omega_j}{(\omega_r - \Omega_j)^2}. \quad (3.10)$$

The above expression for the growth rate, Equation (3.9), provides great insight into the instability criteria of each wave branch and determines the role that each ion species will play in either damping or contributing to positive growth of each wave branch. Using this estimate it was shown that an ion species  $j$ , with thermal anisotropy  $A_j$ , will make a positive contribution to wave growth only for those frequencies  $\omega_r$  satisfying (*Mace et al., 2011*)

$$\omega_r < \frac{A_j}{A_j + 1} \Omega_j \equiv \omega_j^*. \quad (3.11)$$

For a fixed positive  $A_j$ , this inequality sets the maximum wave frequency for which species  $j$  will provide a positive contribution to wave growth. Conversely, for  $\omega_r > \omega_j^*$ , the species

Table 3.1: The contribution of each ion species to the growth rate of each wave branch. Table adapted from *Mace et al. (2011)*.

Ion Species	Proton Branch	Helium Branch	Oxygen Branch
H <sup>+</sup>	+/-	+/-	+/-
He <sup>+</sup>	-	+/-	+/-
O <sup>+</sup>	-	-	+/-

$j$  produces cyclotron damping and the overall growth rate of the wave at such frequencies is reduced. In particular, regardless of the value of  $A_j$ , for wave frequencies above the gyrofrequency of species  $j$ , it is observed from Equation (3.11) that species  $j$  necessarily provides a damping contribution. The possible contribution of an ion species to the growth rate in our model have been tabulated in Table 3.1 (adapted from *Mace et al. (2011)*) for ease of reference.

For our choice of plasma composition, the approximate dispersion relation for EMIC waves, Equation (3.8), can be written as (*Mace et al., 2011*)

$$\frac{k^2 c^2}{\omega_r^2} = 1 - \frac{\omega_{pH^+}^2}{\omega_r(\omega_r - \Omega_{H^+})} - \frac{\omega_{pHe^+}^2}{\omega_r(\omega_r - \Omega_{He^+})} - \frac{\omega_{pO^+}^2}{\omega_r(\omega_r - \Omega_{O^+})} - \frac{\omega_{pe}^2}{\omega_r(\omega_r + |\Omega_e|)}, \quad (3.12)$$

where

$$\omega_{pj}^2 = \omega_{pj,c}^2 + \omega_{pj,h}^2,$$

is the square of the total plasma frequency of an ion species (calculated using both cool, “c”, and hot, “h”, components) and the index  $j$  can be any one of H<sup>+</sup>, He<sup>+</sup> or O<sup>+</sup>. The resonances ( $k \rightarrow \infty$ ) at the ion gyrofrequencies are plainly evident in Equation (3.12). The cutoff frequencies must be numerically determined by solving Equation (3.12) for  $\omega_r$  in the limit as  $k \rightarrow 0$ . It is obvious from Equation (3.12) that these cutoff frequencies are strongly dependent on the plasma frequencies and, hence, the number densities of the ion components (*Mace et al., 2011*).

### 3.4 Numerical results

The EMIC wave dispersion relation in a multi-ion species plasma is composed of a single branch for each ion species. Each branch is bound by a cutoff frequency at small wave numbers and a resonant frequency at large wave numbers. The exception to this is the lowest frequency branch, which connects with the Alfvén mode.

The gyrofrequency of an ion species,  $\Omega_j$ , determines the resonant frequency below which the wave branch of species  $j$  is confined at large wave numbers. This resonant frequency depends largely on the ambient magnetic field strength,  $B_0$ , which remains relatively constant for a given region of the magnetosphere. In the current investigation, the magnetic field strength has been set to represent the region of the magnetosphere in the vicinity of  $L = 4$ , which gives  $B_0 = 487.66\text{nT}$  in the standard dipolar model (*Baumjohann and Treumann, 1996*).

The cutoff frequency, defining the lower boundary of the wave branch, is quite variable. It depends largely on the number densities of the ion species (*Kozyra et al., 1984; Mace et al., 2011*) through Equation (3.12) with  $k \rightarrow 0$ . In the region of the magnetosphere representing  $L = 4$ , the number density of each ion species can vary dramatically depending on geomagnetic conditions. The position of the cutoff frequency of a wave branch relative to  $\omega_j^*$  (Equation (3.11)) determines whether or not there exists a range of frequencies for which species  $j$  contributes positively to the growth rate of the wave branch (*Mace et al., 2011*). Bearing in mind condition (3.11), it follows that the position of a cutoff frequency relative to the  $\omega_j^*$  is an important determinant of wave growth and indicates that the relative ion abundances (or number densities) play an important role in governing the growth/damping of a particular EMIC branch (*Mace et al., 2011*).

To investigate how the cutoff frequencies of the proton and helium branches vary with ion species abundances, we solve Equation (3.12) numerically for  $\omega_r$  in the limit  $k \rightarrow 0$ . Although the temperature of the ion species and their thermal anisotropies do not enter into the equations at the level of approximation of Equation (3.12), they are important for the calculation of  $\omega_j^*$ . For the current investigation we shall set the anisotropy of the hot ions ( $T = 10\text{ keV}$ ) to  $A_{i,h} = 1.0$  and  $A_{i,c} = 0$  (isotropic) for the cool ion species

( $T = 10$  eV). Since all cool ion species are isotropic,  $\omega_{j,c}^* = 0$  such that,  $\omega_r > \omega_{j,c}^*$  for all frequencies investigated. This implies that all cool ion species will be a constant source of cyclotron damping to all wave branches considered.

Figure 3.3 shows how the proton branch cutoff frequency (red line) and the helium branch cutoff frequency (blue line) vary with proton ( $n_{\text{H}^+}/n_i$ ) and oxygen ( $n_{\text{O}^+}/n_i$ ) relative ion abundances. The frequencies  $\omega_{\text{H}^+}^*$  and  $\omega_{\text{He}^+}^*$ , calculated by Equation (3.11) using  $A_{\text{H}^+,h} = A_{\text{He}^+,h} = 1.0$  are found such that  $\omega_{\text{H}^+}^* = 0.5 \Omega_{\text{H}^+}$  and  $\omega_{\text{He}^+}^* = 0.125 \Omega_{\text{H}^+}$ . These are illustrated by the dashed, horizontal lines in Figure 3.3. The total number density of the ions (sum of number densities of all ion species) and the total number density of the helium ions (hot and cool) have been kept constant at  $n_i = 25 \text{ cm}^{-3}$  and  $n_{\text{He}^+} = 2.25 \text{ cm}^{-3}$  ( $n_{\text{He}^+} = 0.09 n_i$ ), respectively. These values were chosen to coincide with the numerical investigation of the dispersion relation, Equation (3.5), which will be used later.

From Figure 3.3 we deduce that the hot anisotropic protons will only contribute positively to the growth rate of the proton branch of the EMIC instability if the total (hot plus cool) proton number density  $n_{\text{H}^+}$  is greater than  $0.575 n_i$  (red line). This is because it is only for this range that the cutoff frequency lies below the line representing  $\omega_{\text{H}^+}^*$ . Therefore, it is only for this range of number densities that there will exist a range of frequencies where  $\omega_r < \omega_{\text{H}^+}^*$ . All other ion species will be a constant source of damping of the proton branch for all number densities investigated here since  $\omega_r > \omega_{\text{He}^+}^* > \omega_{\text{O}^+}^*$ .

If  $n_{\text{H}^+} < 0.575 n_i$  then the hot ring current protons are a source of cyclotron damping of the proton branch, as are all the other ion species. For  $n_{\text{H}^+} < 0.575 n_i$ , the cutoff frequency lies above  $\omega_{\text{H}^+}^*$ , so  $\omega_r > \omega_{\text{H}^+}^*$  and, therefore, the protons are a source of damping in the proton branch. In fact, for this range of number densities  $\omega_r > \omega_{\text{H}^+}^* > \omega_{\text{He}^+}^* > \omega_{\text{O}^+}^*$ , and as a result, all ion species are a source of cyclotron damping for this branch (see Table 3.1). In other words, the proton branch of the EMIC instability is necessarily damped when  $n_{\text{H}^+} < 0.575 n_i$ .

The blue line in Figure 3.3 denoting that the helium branch cutoff frequency always lies below  $\omega_{\text{H}^+}^*$  irrespective of the ion abundances of the proton or oxygen ions. Consequently, the hot anisotropic ring current protons will always provide a positive contribution to the

growth rate of the helium branch. On the other hand we observe that the helium ions will contribute positively to the growth rate of the helium branch only when the total proton number density  $n_{\text{H}^+}$ , exceeds  $0.81 n_i$ . This implies that both the hot anisotropic protons and helium ions make a positive contribution to the growth rate of the helium branch for this range of proton ion abundances.

When  $n_{\text{H}^+} < 0.81 n_i$ , the cutoff frequency of the helium branch exceeds  $\omega_{\text{He}^+}^*$  and, therefore, the helium ions are a source of damping of the helium branch. Since the helium branch cutoff frequency always exceeds  $\omega_{\text{O}^+}^*$  (for all values of  $n_{\text{H}^+}$  and  $n_{\text{O}^+}$ ), the ring current oxygen ions will always be a source of damping of the helium branch (see Table 3.1). In other words, for  $n_{\text{H}^+} < 0.81 n_i$  both the helium and oxygen ions (both hot and cool species) are a source of damping of the helium branch as  $\omega_r > \omega_{\text{He}^+}^* > \omega_{\text{O}^+}^*$ .

It follows then that the question as to whether the helium EMIC branch is growing or damped depends on whether (i) in the case where  $n_{\text{H}^+} > 0.81 n_i$ , the positive contributions to the growth rate provided by the protons and helium ions exceeds in magnitude the magnitude of the negative contribution provided by the oxygen ions, or (ii) in the case where  $n_{\text{H}^+} < 0.81 n_i$ , the positive contribution to the growth rate provided by the protons exceeds in magnitude the magnitude of the negative contributions provided by the helium and oxygen ions.

Figure 3.4 illustrates, in a format similar to Figure 3.3, how the cutoff frequencies of the proton (red line) and helium (blue line) EMIC wave branches vary with the relative ion abundance of the protons and helium ions. In the case presented in Figure 3.4, the total number density of the oxygen ions has been kept constant at  $n_{\text{O}^+} = 1.25 \text{ cm}^{-3}$  (or  $n_{\text{O}^+} = 0.05 n_i$ ). The total number density of the ions,  $n_i$ , has been kept constant with  $n_i = 25 \text{ cm}^{-3}$ . The anisotropies of the hot protons and helium ions have been set such that  $A_{\text{H}^+,h} = A_{\text{He}^+,h} = 1.0$  as in Figure 3.3. By Equation (3.11) this gives  $\omega_{\text{H}^+}^* = 0.5 \Omega_{\text{H}^+}$  and  $\omega_{\text{He}^+}^* = 0.125 \Omega_{\text{H}^+}$ . These are illustrated by the dashed, horizontal lines in Figure 3.4. The red line in Figure 3.4, denoting the proton branch cutoff frequency, shows that the hot anisotropic protons will only contribute positively to the growth rate of the proton branch of the EMIC instability if the total proton number density  $n_{\text{H}^+}$ , is greater than  $0.655 n_i$ .

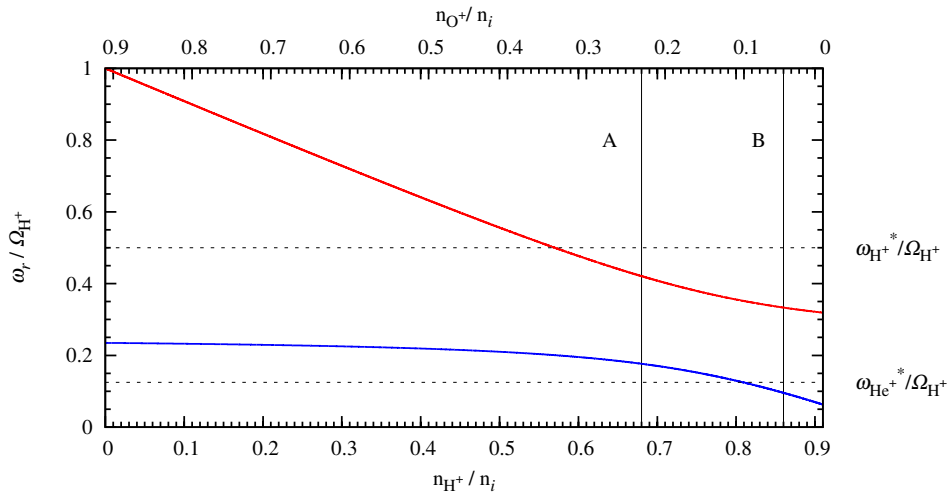


Figure 3.3: The cutoff frequencies for varying proton and oxygen ion relative abundances. The red line denotes the cutoff of the proton branch while the blue line denotes that of the helium branch. The dashed horizontal lines denote  $\omega_{H^+}^* / \Omega_{H^+}$  and  $\omega_{He^+}^* / \Omega_{H^+}$  for  $A_{H^+,h} = A_{He^+,h} = 1.0$ . The other fixed parameters are  $n_i = 25 \text{ cm}^{-3}$  and  $n_{He^+} = 2.25 \text{ cm}^{-3} (0.09 n_i)$ . The vertical lines labelled “A” and “B” represent the chosen parameters for an oxygen rich ring current (case 4) and a predominantly proton ring current (case 3), respectively, which will be used later.

It is only for this range of number densities that the cutoff frequency lies below the line representing  $\omega_{\text{H}^+}^*$ . All other ions are a source of damping of the proton branch since the proton cutoff frequency lies above  $\omega_{\text{He}^+}^*$  and  $\omega_{\text{O}^+}^*$  for all number densities investigated.

On the other hand, when  $n_{\text{H}^+} < 0.655 n_i$ , the hot ring current protons are a source of cyclotron damping of the proton branch. For this range of number densities the cutoff frequency lies above the line representing  $\omega_{\text{H}^+}^*$ , therefore, there will be no range of frequencies for which  $\omega_r < \omega_{\text{H}^+}^*$ . In fact, for this range of number densities, all ions will be a source of damping of the proton branch and the branch will be necessarily damped since  $\omega_r > \omega_{\text{H}^+}^* > \omega_{\text{He}^+}^* > \omega_{\text{O}^+}^*$ .

Figure 3.4 illustrates that the helium branch cutoff frequency (blue line) always lies below both  $\omega_{\text{H}^+}^*$  and  $\omega_{\text{He}^+}^*$  for the chosen anisotropies of the hot proton and helium ions. Therefore, the hot anisotropic ring current protons and helium ions will provide a positive contribution to the growth rate of the helium branch for all number densities investigated. The helium branch cutoff frequencies exceed the oxygen ion gyrofrequency (the maximum value of  $\omega_{\text{O}^+}^*$ ) for all cases considered, thus, the oxygen ions are a source of damping of the helium branch. However, the relatively small number density of the oxygen ions ( $n_{\text{O}^+} = 0.05 n_i$ ), ensures a minor damping contribution from them. This negative contribution is unlikely to exceed in magnitude the magnitude of the positive contributions to the growth rate provided by the hot ring current protons and helium ions. Although the cutoff frequency of the helium branch is less than  $\omega_{\text{He}^+}^*$  for all values of  $n_{\text{H}^+}/n_i$ , Figure 3.4 shows that a decrease in the relative abundance of the helium ions results in an increase in the cutoff frequency of the helium branch.

Figures 3.3 and 3.4 provide great insight into how the cutoff frequencies are affected by a variation in proton, helium and oxygen ion abundances. They also highlight the importance of the position of the cutoff frequency of each wave branch relative to  $\omega_j^*$ . Below we proceed with a numerical investigation of the dispersion relation, Equation (3.5). The wave number in Equation (3.5) is normalised with respect to the reciprocal of the thermal gyroradius of the cool protons,  $\rho_{\text{H}^+,c}$ , defined by  $\rho_{\text{H}^+,c} = v_{\text{H}^+,c,\parallel}/\Omega_{\text{H}^+}$ , where  $v_{\text{H}^+,c,\parallel} = (T_{\text{H}^+,c,\parallel}/m_{\text{H}^+})^{1/2}$  is their parallel thermal speed. The frequency,  $\omega$ , is normalised

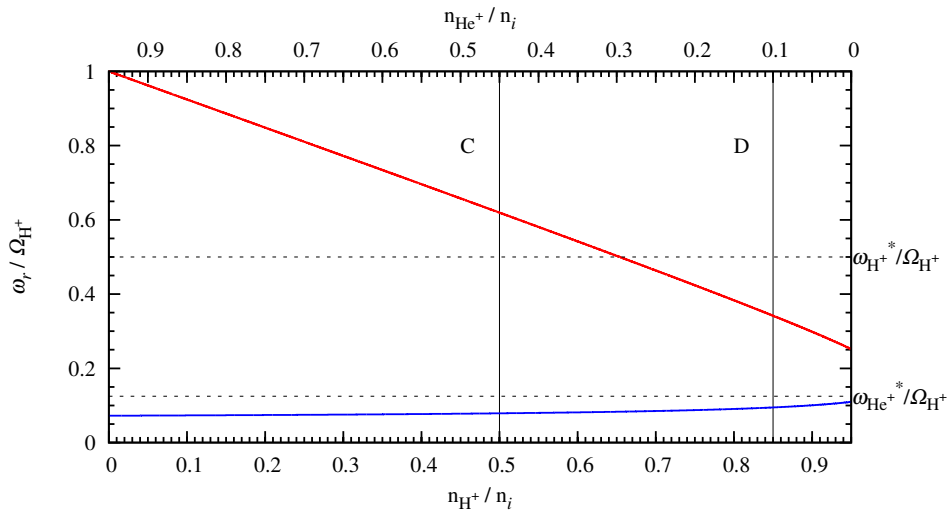


Figure 3.4: The cutoff frequencies for varying proton and helium ion relative abundances. The red line denotes the cutoff frequency of the proton branch while the blue line denotes that of the helium branch. The dashed horizontal lines denote  $\omega_{H^+}^* / \Omega_{H^+}$  and  $\omega_{He^+}^* / \Omega_{H^+}$  for  $A_{H^+,h} = A_{He^+,h} = 1.0$ . Other fixed parameters are  $n_i = 25 \text{ cm}^{-3}$  and  $n_{O^+} = 1.25 \text{ cm}^{-3}$ . The vertical lines labelled “C” and “D” represent the chosen parameters for case 5 and case 6, respectively, which will be used later.

with respect to the gyrofrequency of the protons,  $\Omega_{\text{H}^+}$ . The normalised dispersion relation is solved numerically, without approximation.

Figure 3.5 illustrates the dispersion relation (top panel) and growth rate (bottom panel) of each EMIC wave branch for the parameters of case 1 and case 2, given in Table 3.2. The ring current ion abundances are fixed and equal in both cases investigated. Figure 3.5 illustrates how a variation in the cool ion number density affects the dispersive characteristics and growth rate of each wave branch. Case 1 (blue line) represents the parameters as used in *Mace et al.* (2011). The red line denotes case 2 where more typical cool ion number densities have been used.

A change in cool ion number density has a significant effect on the dispersion relation of both the proton and helium EMIC wave branches. The most important feature of Figure 3.5 is the difference in cutoff frequencies of each branch, brought about by the number density changes. The proton branch cutoff frequency has decreased from  $\approx 0.628 \Omega_{\text{H}^+}$ , for the parameters chosen by *Mace et al.* (2011) (case 1), to  $\approx 0.576 \Omega_{\text{H}^+}$  in the case of more typical plasmaspheric ion number densities (case 2). This decrease in cutoff frequency can be attributed to the increase in total proton number density from  $11.5 \text{ cm}^{-3}$ , in case 1, to  $13.0 \text{ cm}^{-3}$ , in case 2. This is in agreement with earlier findings presented in Figure 3.3 and Figure 3.4. The latter figures illustrate how an increase in total proton number density will result in a decrease in the cutoff frequency of the proton branch.

The growth rate of the proton branch is absent from the bottom panel of Figure 3.5 because there is no range of wave numbers for which  $\gamma > 0$  in either case, i.e., the proton branch is damped for both case 1 and case 2. This is expected since  $\omega_r > \omega_{\text{H}^+}^* > \omega_{\text{He}^+}^* > \omega_{\text{O}^+}^*$  in both cases investigated. Because of these inequalities, all ion species (hot and cool) will contribute negatively to the growth rate resulting in overall cyclotron damping of the proton branch.

For the helium branch, the change in plasmaspheric ion number densities have resulted in a small increase in the cutoff frequency from  $\approx 0.131 \Omega_{\text{H}^+}$  in case 1 (blue line) to  $\approx 0.138 \Omega_{\text{H}^+}$  in case 2 (red line). This is consistent with the results illustrated in Figure 3.4. Figure 3.4 demonstrates how a decrease in the total number density of the helium ions results in

only a marginal increase in the cutoff frequency of the helium branch. In this instance, the cool helium ion number density has decreased from  $8 \text{ cm}^{-3}$  in case 1 to  $6.5 \text{ cm}^{-3}$  in case 2, leading to a decrease in total helium ion number density and results in a minor increase in the cutoff frequency.

In both case 1 and case 2 the helium branch has  $\omega_r < \omega_{\text{H}^+}^*$ . Therefore, the hot anisotropic ring current protons will provide a positive contribution to the growth rate for all wave numbers investigated. In the helium branch, the cutoff frequencies are above  $\omega_{\text{He}^+}^*$  and  $\omega_{\text{O}^+}^*$  in both cases 1 and 2 and, therefore, both the helium and oxygen ions contribute negatively to the growth rate. In the bottom panel of Figure 3.5, illustrating the growth rate of each branch, it is seen for both case 1 and case 2 that  $\gamma < 0$  for all wave numbers investigated for the helium branch. This is because the sum of the negative contributions to the growth rate provided by the helium and oxygen ions is greater in magnitude than the magnitude of the positive contribution provided by the hot ring current protons.

Altering the cool ion number densities to more typically observed values has not had a great effect on the dispersion relation curves of the oxygen branch (see upper panel of Figure 3.5). The oxygen branch has no cutoff frequency and, therefore, it is relatively insensitive to ion composition. With reference to the lower panel of Figure 3.5, we observe that the oxygen branch is the only branch that has a positive wave growth rate ( $\gamma > 0$ ). This is as expected since it is also the only branch that satisfies the condition  $\omega_r < \omega_{\text{O}^+}^* < \omega_{\text{He}^+}^* < \omega_{\text{H}^+}^*$ , thus, all hot anisotropic ions make a positive contribution to the overall growth rate. However, we do note that the change in plasmaspheric ion abundances to more typical values resulted in a very minor decrease in peak growth rate of the oxygen branch even though the relative abundance of the oxygen ions remained constant.

The results derived from Figure 3.5 suggest that the plasmaspheric (cool) ions play a relatively minor role in governing the dispersive characteristics and determining wave growth of the branches of the EMIC instability. Owing to this, we proceed with an investigation into the effects of varying the relative ion abundances of the hot anisotropic ring current ions on the dispersion relation and growth rate of each EMIC wave branch. To investigate these effects, we begin with a comparison of the dispersion relation and

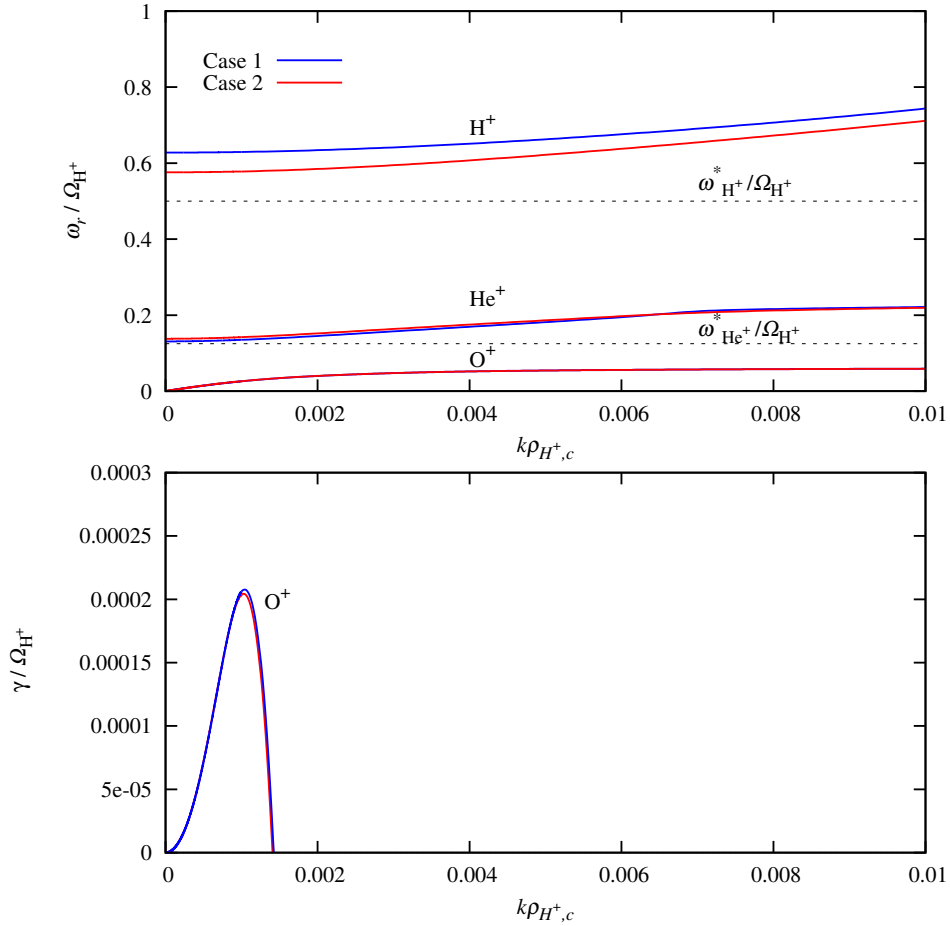


Figure 3.5: The EMIC waves branches (top panel) and their growth rates (bottom panel) shown for varying relative abundances of the plasmaspheric ions. The blue lines denote the numerical solutions to Equation (3.5) for case 1. The red lines denote numerical solutions to the same equation but with more typical plasmaspheric ion abundances, case 2. For the full set of parameters refer to Table 3.2. The horizontal dashed lines represent  $\omega_{H^+}^* / \Omega_{H^+}$  and  $\omega_{He^+}^* / \Omega_{H^+}$  as calculated by Equation (3.11).

Table 3.2: Table of parameters chosen for Figure 3.5.

Species	$n$ ( $\text{cm}^{-3}$ )		$T_{\parallel}$ (eV)	$A = T_{\perp}/T_{\parallel} - 1$	$\kappa$
	case 1	case 2			
$n_{\text{H}^+,c}$	6.5	8	10	0	3
$n_{\text{He}^+,c}$	3	1.5	10	0	3
$n_{\text{O}^+,c}$	0.5	0.5	10	0	3
$n_{\text{H}^+,h}$	5	5	$10^4$	1	2
$n_{\text{He}^+,h}$	5	5	$10^4$	1	2
$n_{\text{O}^+,h}$	5	5	$10^4$	1	2
$n_e$	25	25	10	0	3

growth rates between a ring current composed of 90% protons, 5% helium ions and 5% oxygen ions (case 3 in Table 3.3) and that of a ring current with 60% protons, 5% helium ions and 35% oxygen ions (case 4 in Table 3.3). These parameter choices correspond to the lines labelled “B” and “A”, respectively, in Figure 3.3. The plasmaspheric ion number densities have been kept constant at typically observed values (see Table 3.3 for a full set of parameters).

With reference to the top panel of Figure 3.6, we observe that in case 3, for a ring current composed of predominantly protons (red lines), the proton branch is confined to the frequencies  $0.332 \Omega_{\text{H}^+} < \omega_r < \Omega_{\text{H}^+}$ . For case 4, the oxygen rich ring current (blue lines), the frequency range is  $0.42 \Omega_{\text{H}^+} < \omega_r < \Omega_{\text{H}^+}$ . For the chosen hot proton anisotropy  $A_{\text{H}^+,h} = 1.0$ ,  $\omega_{\text{H}^+}^* = 0.5 \Omega_{\text{H}^+}$ , the cutoff frequencies, in both cases, lie below  $\omega_{\text{H}^+}^*$  and hence, in both cases, there exists a range of frequencies where the condition  $\omega_r < \omega_{\text{H}^+}^*$  holds true. For such frequencies, the hot protons will contribute positively to the growth rate of the proton branch. The helium and oxygen ring current ions both provide a source of damping of the proton branch, since  $\omega_r > \omega_{\text{He}^+}^* > \omega_{\text{O}^+}^*$ . However, it is clearly evident in the bottom panel of Figure 3.6, that there exists a range of wave numbers where  $\gamma > 0$  for both cases 3 and 4. For these wave numbers the magnitude of the positive contribution to the growth rate provided by the ring current protons is greater than the magnitude of the

negative contributions of the other ion species; therefore, the proton branch is destabilised.

Although the proton branch is destabilised in both cases 3 and 4, we note that the growth rate is far greater in magnitude and over a broader range of wave numbers for case 3 than that of case 4. This is due to the former having more energetic protons (90%) than that of the latter (60%). These results are, of course, consistent with the findings in Figure 3.3. Comparing lines “A” (case 4) and “B” (case 3) in Figure 3.3, it is seen how an increase in the total number density of the protons (from  $0.68 n_i$  in “A” to  $0.86 n_i$  in “B”) lowers the cutoff frequency of the proton branch and hence, increases the frequency range over which there will be a positive growth rate contribution by the hot proton component. The change in ion abundances also affects the wave numbers at which the instabilities occur in the proton branch. A positive growth rate is seen at smaller wave numbers in the case of the oxygen rich ring current (case 4),  $0.002 \lesssim k\rho_{H^+,c} \lesssim 0.004$ , than that of the predominantly proton ring current case (case 3),  $0.0045 \lesssim k\rho_{H^+,c} \lesssim 0.0075$ .

For case 3, the predominantly proton ring current (red line), the helium branch has a cutoff at  $\omega_r = 0.095 \Omega_{H^+}$  (see upper panel). This is as predicted by the vertical line “B” in Figure 3.3, for the parameters in case 3. The cutoff frequency is well below  $\omega_{He^+}^*$ , so the condition for the ring current helium ions to make a positive contribution to the growth rate of the helium branch,  $\omega_r < \omega_{He^+}^* = 0.125 \Omega_{H^+}$ , is satisfied over a broad range of  $\omega_r$ . Therefore, there exists a range of frequencies for which the hot anisotropic helium ions make a positive contribution to the growth rate of the helium branch. This range of frequencies is illustrated in the top panel of Figure 3.6. As discussed before for the anisotropy considered, the hot ring current protons will always provide a positive contribution to the growth rate of the helium branch since  $\omega_r < \omega_{H^+}^*$ , and, therefore, for this range of frequencies, both the ring current protons and helium ions will contribute positively to the growth rate. The oxygen ions are a constant source of cyclotron damping of the helium branch since  $\omega_r > \omega_{O^+}^*$ . However, there is a range of wave numbers where the positive contribution provided by the ring current protons and helium ions is greater in magnitude than the magnitude of the negative contribution provided by the ring current oxygen ions (and all cool ion species). Therefore, the helium branch is destabilised for

case 3. This is illustrated in the bottom panel of Figure 3.6.

For the case of the oxygen rich ring current, case 4, the helium branch has a cutoff frequency at  $\omega_r = 0.1756 \Omega_{\text{H}^+}$  as predicted by the vertical line “A” in Figure 3.3 and evident in the top panel of Figure 3.6 (blue lines). This is larger than the cutoff frequency in case 3 due to the increase in the total number density of the oxygen ions (see Table 3.3). A positive contribution to the growth rate of the helium branch is provided by the ring current protons since  $\omega_r < \omega_{\text{H}^+}^*$ . However, its cutoff frequency is above both  $\omega_{\text{He}^+}^*$  and  $\omega_{\text{O}^+}^*$ , resulting in the ring current helium and oxygen ions being a source of cyclotron damping of the helium branch in this case. The total negative contribution to the growth rate is greater in magnitude than the magnitude of the positive contribution of the hot ring current protons resulting in the wave being damped for all wave numbers investigated.

The oxygen branch, as mentioned previously, has no cutoff frequency and satisfies  $\omega_r < \omega_{\text{O}^+}^* < \omega_{\text{He}^+}^* < \omega_{\text{H}^+}^*$  in both cases 3 and 4. This results in a range of wave numbers with a positive growth rate ( $\gamma > 0$ ) in both cases as all ring current ion species contribute positively to the growth rate of the oxygen branch. However, the bottom panel of Figure 3.6 shows that the frequency range over which there is a positive contribution to the growth rate is greater for the oxygen rich ring current (case 4) and occurs over a larger range of wave numbers than that of the predominantly proton case (case 3). This is due to the relative abundance of the ring current oxygen ions being greater in case 4 ( $n_{\text{O}^+,h} = 5.25 \text{ cm}^{-3}$ ) than in case 3 ( $n_{\text{O}^+,h} = 0.75 \text{ cm}^{-3}$ ) and, thus, the magnitude of their positive contribution to the growth rate of the oxygen branch is greater.

Figure 3.7 illustrates how an alternative relative abundance parameter choice (see Table 3.4) for the ring current ions influences the dispersion relation and growth rates of each EMIC wave branch. Parameters for the cool plasmaspheric plasma and electron components are kept constant and the same as those in Figure 3.6 (see Table 3.4 for a full set of parameters). To investigate the effects of the relative abundances of the hot ring current ions on the dispersion curves and growth rates of the EMIC wave branches, we compare how they are affected by a ring current composed of 30% protons, 65% helium ions and 5% oxygen ions (case 5) to that of a ring current with 88.3% protons, 6.7% helium ions

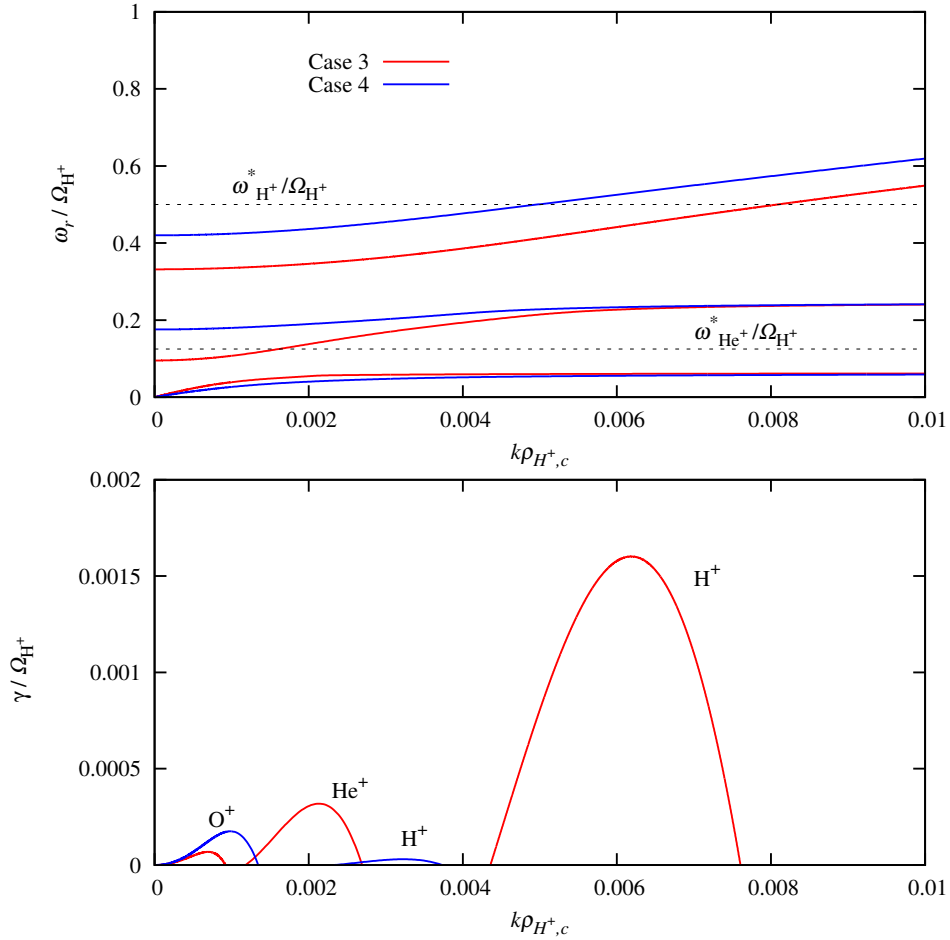


Figure 3.6: The EMIC waves branches (top panel) and their growth (bottom panel) rates shown for varying relative abundance of the ring current ions. The red lines denote the numerical solutions to Equation (3.5) with a predominantly proton ring current, case 3. The blue lines denote solutions to the same equation but for an oxygen rich ring current, case 4. For the full set of parameters refer to Table 3.3. The horizontal dashed lines represent  $\omega_{H^+}^* / \Omega_{H^+}$  and  $\omega_{He^+}^* / \Omega_{H^+}$  as calculated by Equation (3.11).

Table 3.3: Table of parameters chosen for Figure 3.6.

Species	$n$ ( $\text{cm}^{-3}$ )		$T_{\parallel}$ (eV)	$A = T_{\perp}/T_{\parallel} - 1$	$\kappa$
	case 3	case 4			
$n_{\text{H}^+,c}$	8	8	10	0	3
$n_{\text{He}^+,c}$	1.5	1.5	10	0	3
$n_{\text{O}^+,c}$	0.5	0.5	10	0	3
$n_{\text{H}^+,h}$	13.5	0.6	$10^4$	1	2
$n_{\text{He}^+,h}$	0.75	0.75	$10^4$	1	2
$n_{\text{O}^+,h}$	0.75	5.25	$10^4$	1	2
$n_e$	25	25	10	0	3

and 5% oxygen ions (case 6). These parameter choices correspond to the lines labelled “C” and “D” in Figure 3.4, respectively. The line labelled “C” represents case 5 with total proton and helium number density of  $0.5 n_i$  and  $0.45 n_i$ , respectively. The vertical line labelled “D” represents case 6 with a total proton and helium number density of  $0.85 n_i$  and  $0.1 n_i$ , respectively.

The top panel of Figure 3.7 illustrates the EMIC wave branches for case 5 (red lines) and case 6 (blue lines). For case 5 the proton branch is confined to the frequencies  $0.515 \Omega_{\text{H}^+} < \omega_r < \Omega_{\text{H}^+}$  while, for case 6 the frequency range is  $0.292 \Omega_{\text{H}^+} < \omega_r < \Omega_{\text{H}^+}$ . In case 5 the cutoff frequency (defining the lower boundary) is greater than  $\omega_{\text{H}^+}^* = 0.5 \Omega_{\text{H}^+}$ . Thus, the hot ring current protons are a source of damping along with all other ion species, since  $\omega_r > \omega_{\text{H}^+}^* > \omega_{\text{He}^+}^* > \omega_{\text{O}^+}^*$ . In case 6, there exists a range of frequencies which satisfy the condition  $\omega_r < \omega_{\text{H}^+}^* = 0.5 \Omega_{\text{H}^+}$ . Therefore, there is a range of frequencies for which the hot ring current protons will contribute positively to the growth rate of the proton branch.

In the bottom panel of Figure 3.7 it is clear that there is a range of wave numbers corresponding to the proton branch for case 6 for which  $\gamma > 0$ . This indicates that for this range of wave numbers, the positive contribution provided by the hot ring current protons is greater in magnitude than the magnitude of the negative contributions provided by the

other ion species. In case 5, however,  $\gamma < 0$  and the proton branch is damped for all wave numbers investigated, and the red line corresponding to this growth rate is absent in the lower panel. These results are consistent with the predictions of Figure 3.4. By comparing lines “C” and “D” in Figure 3.4, it is seen how an increase in the total number density of the protons (from  $0.5 n_i$  to  $0.85 n_i$ ) lowers the cutoff frequency of the proton branch so that there will be a range of  $\omega_r$  satisfying  $\omega_r < \omega_{\text{H}^+}^* = 0.5 \Omega_{\text{H}^+}$ , allowing the hot ring current protons to make a positive growth rate contribution to that branch.

In the helium branch both cases 5 and 6 have a range of frequencies,  $\omega_r$ , satisfying the condition  $\omega_r < \omega_{\text{H}^+}^* = 0.5 \Omega_{\text{H}^+}$  and, therefore, the hot ring current protons will always make a positive contribution to the growth rate of the helium branch for all frequencies investigated (see top panel of Figure 3.7). For the chosen set of parameters, both cases 5 and 6 have a range of frequencies which satisfy  $\omega_r < \omega_{\text{He}^+}^* = 0.125 \Omega_{\text{H}^+}$  and, therefore, in both instances, the ring current helium ions (along with the ring current protons) will contribute positively to the growth rate of the helium branch. In particular, we observe in the top panel of Figure 3.7 that the helium branch for case 5 satisfies  $\omega_r < \omega_{\text{He}^+}^*$  for  $0 \lesssim k\rho_{\text{H}^+,c} \lesssim 0.0043$ , while in case 6 this condition is satisfied over the range  $0 \lesssim k\rho_{\text{H}^+,c} \lesssim 0.0034$ . These results are consistent with those of Figure 3.4. In case 5 the helium branch has a cutoff at  $\omega = 0.068 \Omega_{\text{H}^+}$ , as predicted by “C” in Figure 3.4. In case 6 the helium branch has a cutoff at  $\omega = 0.069 \Omega_{\text{H}^+}$  as predicted by “D” in Figure 3.4. Although the helium branch is destabilised in both cases, we note in the bottom panel of Figure 3.7, that the growth rate is greater for case 6 than for case 5. This is due to the larger hot proton number density in case 6 and, therefore, the magnitude of the total positive contribution to the growth rate of the helium branch is greater.

The oxygen branch has no cutoff frequency and, therefore, satisfies  $\omega_r < \omega_{\text{O}^+}^* < \omega_{\text{He}^+}^* < \omega_{\text{H}^+}^*$  for case 5 as well as case 6. In both instances, all ring current ion components contribute positively to the growth rate of the oxygen branch. This gives rise to overall instability in both cases. However, the range of frequencies over which there is a resultant positive contribution to the growth rate ( $\gamma > 0$ ) is greater for case 5 and occurs over a larger range of wave numbers than that of case 6.

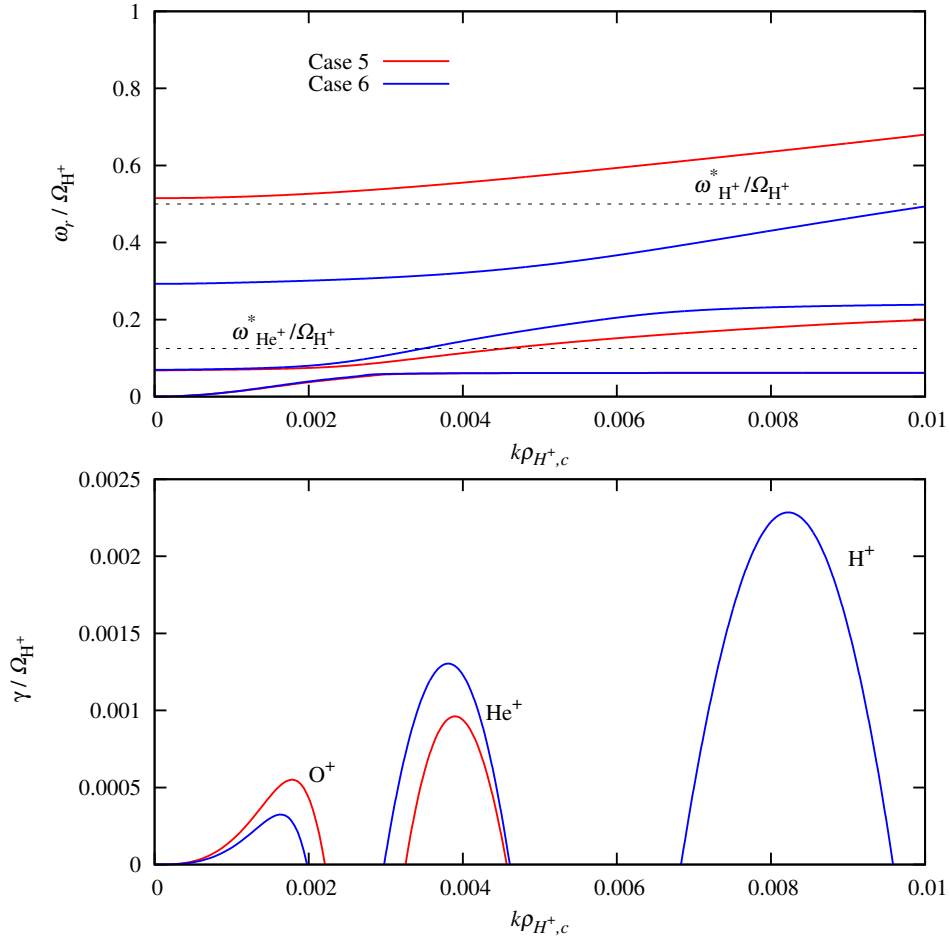


Figure 3.7: The EMIC waves branches (top panel) and their growth rates (bottom panel) shown for varying relative abundance of the ring current ions. The red lines denote the numerical solutions to Equation (3.5) with parameters for case 5. The blue lines denote solutions to the same equation but for case 6. For the full set of parameters refer to Table 3.4. The horizontal dashed lines represent  $\omega_{H^+}^* / \Omega_{H^+}$  and  $\omega_{He^+}^* / \Omega_{H^+}$  as calculated by Equation (3.11).

Table 3.4: Table of parameters chosen for Figure 3.7.

Species	$n$ ( $\text{cm}^{-3}$ )		$T_{\parallel}$ (eV)	$A = T_{\perp}/T_{\parallel} - 1$	$\kappa$
	case 5	case 6			
$n_{\text{H}^+,c}$	8	8	10	0	3
$n_{\text{He}^+,c}$	1.5	1.5	10	0	3
$n_{\text{O}^+,c}$	0.5	0.5	10	0	3
$n_{\text{H}^+,h}$	4.5	13.25	$10^4$	1	2
$n_{\text{He}^+,h}$	9.75	1	$10^4$	1	2
$n_{\text{O}^+,h}$	0.75	0.75	$10^4$	1	2
$n_e$	25	25	10	0	3

### 3.5 Discussion and conclusions

This chapter has presented the results from an investigation of how the electromagnetic ion cyclotron (EMIC) instability is affected by the relative abundance of both the cool ions (of plasmaspheric origin) as well as the hot, anisotropic ring current ions. The dispersion relation for parallel propagating EMIC instabilities in a multi-component kinetic plasma model, whose species have velocity distributions described by the bi-kappa distribution (Equation (3.5)), was solved numerically. This investigation was motivated by the work done by *Mace et al.* (2011). While the parameters used by *Mace et al.* (2011) were plausible, this chapter addresses how a more typical representation of the ion abundances, observed in the region of Earth's magnetosphere containing the ring current, could affect the EMIC instability.

We initially investigated how the cutoff frequencies of the proton and helium branches varied with the relative ion abundances of the proton, helium and oxygen ions. The position of the cutoff frequency of a wave branch relative to  $\omega_j^*$  determines whether there exists a range of frequencies for which species  $j$  contributes positively to the growth rate of the wave branch (*Mace et al.*, 2011). The position of the cutoff frequency of a wave branch is dependent on the total number density of the ion species. In our model, the cool ions as well as the electrons have anisotropies such that  $A = 0$ , and hence, by condition

(3.11), these species will be a source of cyclotron damping of all EMIC wave branches at all frequencies  $\omega_r > 0$ . The hot anisotropic ions, on the other hand, can be either a source of damping or a positive contributor to wave growth.

The proton branch cutoff frequency is dependent on the total number density of the protons (hot and cool). The larger the proton ion abundance, the lower the cutoff frequency of the proton branch. Therefore, for a given hot proton anisotropy,  $A_{H^+,h}$ , it is possible to select a proton ion abundance that ensures that the hot anisotropic protons will make a positive contribution to the growth rate of the proton branch. Depending on the magnitude of this contribution, this allows for that branch to be destabilised despite the negative contributions provided by the other ion species.

For our choice of anisotropies of the hot ring current ions,  $A = 1.0$ , there always exists a range of frequencies,  $\omega_r < \omega_{H^+}^*$ , for which the hot ring current protons will make a positive contribution to the growth rate of the helium branch. The hot oxygen ions will always be a source of cyclotron damping of the helium branch since  $\omega_r > \omega_{O^+}^*$ . The hot helium ions, however, can either contribute to the damping or destabilisation of the helium branch. This depends on where the cutoff frequency of the helium branch lies with respect to  $\omega_{He^+}^*$ . As long as the cutoff frequency lies below  $\omega_{He^+}^*$ , there will exist a range of frequencies for which the hot helium ions will contribute positively to the growth rate of the helium branch.

How the different wave branches of the EMIC instability are affected by a change in the plasmaspheric number density is illustrated in Figure 3.5. Here we compare case 1, with the cool ion abundance as used by *Mace et al.* (2011), to case 2, with typically observed cool ion abundances. It is evident from our investigation that while altering the ion abundances of the plasmaspheric ions does have an effect on the cutoff frequency of each branch, this effect is not as significant as expected. Even though there was a significant increase in the total number density of the protons from case 1 to case 2, the proton branch is still damped since the cutoff frequency remains above  $\omega_{H^+}^*$  for all wave numbers. The helium branch is also damped, despite the positive contribution from the hot protons. Since  $\omega_r > \omega_{He^+}^*$  in both cases, the hot helium ions contributed to the cyclotron damping

of the helium branch along with the hot oxygen ions and cool plasmaspheric ions. In both cases investigated, it is only the oxygen branch which is destabilised. This is because, in both cases, it is the only branch that satisfies the condition  $\omega_r < \omega_{O^+}^* < \omega_{He^+}^* < \omega_{H^+}^*$  and, therefore, all hot ion species make a positive contribution to the growth rate of the oxygen branch, which exceeds the cumulative damping of the cool isotropic ions.

The relative abundances of the hot ring current ions are highly variable and, therefore, four sets of parameters were used to investigate their influence on the dispersion curve and growth rate of each EMIC wave branch. We began with a comparison of the dispersion relations and growth rates for a ring current composed of 90% protons, 5% helium ions and 5% oxygen ions (case 3) and a ring current with 60% protons, 5% helium ions and 35% oxygen ions (case 4). These results are illustrated in Figure 3.6.

In case 3, all three branches were destabilised. It was found that for each of the EMIC branches there was in each case a finite range of  $\omega_r$  such that  $\omega_r < \omega_j^*$ . For the proton branch, the positive contribution from the anisotropic ring current protons was sufficient to destabilise it. The helium branch received a positive contribution to the growth rate from both the ring current protons and helium ions ( $\omega_r < \omega_{He^+}^* < \omega_{H^+}^*$  for some range of  $\omega_r$ ) resulting in its destabilisation. The oxygen branch has  $\omega_r < \omega_{O^+}^* < \omega_{He^+}^* < \omega_{H^+}^*$  and hence, all anisotropic ions make a positive contribution to the oxygen wave branch. In case 4, it is only the proton and oxygen branches that are destabilised, while the helium branch is cyclotron damped ( $\omega_r > \omega_{He^+}^*$ ).

While the proton branches of both case 3 and case 4 are destabilised, the magnitude of the growth rate is far greater for case 3 than that of case 4. This can be expected since case 3 has more energetic protons (90%) than that of case 4 (60%) and, in agreement with Figure 3.3, should therefore, have a lower cutoff frequency. The helium branch is destabilised for case 3 but cyclotron damped in case 4. This is because, as predicted by Figure 3.3, the inequality  $\omega_r < \omega_{He^+}^*$  only holds true for case 3 and, therefore, both the hot protons and helium ions contribute positively to the helium branch. This in turn results in a range of wave numbers where  $\gamma > 0$ . In case 4, the positive contribution provided by the hot protons is insufficient to overcome the negative contributions of the other ions

to the helium branch and it is, therefore, damped. In both cases the oxygen branch is destabilised as expected. However, the growth rate is greater in case 4 than in case 3 due to case 4 having more energetic ring current oxygen ions (see Table 3.2) that contribute positively to the growth rate of the oxygen branch.

The second investigation into the effects of the relative abundances of the hot ring current ions on the dispersion relation and growth rates of the EMIC wave branches is illustrated in Figure 3.7. How EMIC wave growth rate is affected by a ring current composed of 30% protons, 65% helium ions and 5% oxygen ions (case 5) was compared to that for a ring current with 88.3% protons, 6.7% helium ions and 5% oxygen ions (case 6). In case 5, it is only the helium and oxygen branches that are destabilised, while the proton branch is cyclotron damped. In case 6, all 3 branches were destabilised.

The proton branch is cyclotron damped for case 5 but destabilised for case 6. This is expected as case 6 has far more energetic ring current protons than case 5 (see Table 3.3). The cutoff frequency for case 6 is well below  $\omega_{H^+}^*$ , predicting growth, whereas for case 5 the cutoff lies above  $\omega_{H^+}^*$ , predicting damping. This is clearly evident by the vertical line labelled “D” in Figure 3.4. The lower cutoff frequency in case 6 allows for a range of frequencies for which the hot protons contribute positively to the growth rate of the proton branch. For case 5, the cutoff frequency is greater than  $\omega_{H^+}^*$ , resulting in the hot protons making a negative contribution to the growth rate of the proton branch for all frequencies. This negative contribution, along with the negative contributions provided by the other ion species, results in the proton branch being damped in case 5.

For both cases 5 and 6, the helium branch is destabilised. The helium branch cutoff frequency for both cases is below  $\omega_{He^+}^*$  and thus, both the hot protons and helium ions will make a positive contribution to the growth rate of the helium branch over some range of frequencies. This results in the helium branch being destabilised in both cases despite the damping effects of the hot oxygen ions and the other cool ion species. It is interesting to note that the growth rate of this branch for case 6 is greater than that for case 5 even though the cutoff frequency of case 5 is lower than in case 6. This lower cutoff frequency is due to case 5 having more energetic ring current helium ions than in case 6 as

Figure 3.4 predicts. The reason the growth rate of case 6 is greater than that of case 5 is most probably because case 6 has a larger hot proton number density and, therefore, the magnitude of the positive contribution by the hot protons to the growth rate is greater than for case 5. In both cases, the oxygen branch is destabilised; however, the contribution to the growth rate is greater in case 5 than case 6 even though the number densities of the oxygen ions are equal in both cases.

The results of this chapter have shown how EMIC instabilities are sensitive to the relative abundance of each ion species. This is especially true for the proton and helium branches. The contribution to the growth rate of each branch of the EMIC wave is dependent on the temperature anisotropy of each anisotropic ion species as well as the relative abundance of each ion species. Whether a wave branch experiences growth depends on both of these parameters, as they determine whether or not there exists a range of frequencies for which anisotropic ions can make a positive contribution to the growth rate, resulting in a range of wave numbers where  $\gamma > 0$ . The most significant effects were observed when we varied the relative ion abundance of the anisotropic ring current ions.

## Chapter 4

### General summary

In this chapter, a general overview of the thesis is presented. Detailed conclusions have been presented in the appropriate chapters, however, here we give a general summary of our results.

In this thesis we have performed a study of both the L and R mode waves. In Chapter 1, Sections 1.1 and 1.2, we discussed how these two modes are important as their interaction with energetic particles can transport energy from one region of the magnetosphere to another (*Tsurutani and Lakhina, 1997*). They also play an important role in the acceleration and pitch angle scattering of energetic particles (*Kennel and Petschek, 1966*). The interaction between these waves and particles is greatest when the particles' streaming velocity is such that the Doppler shifted wave frequency equals a harmonic of its gyrofrequency. This is known as the cyclotron resonance interaction between the particles and waves. Left hand circularly polarised waves (such as electromagnetic ion cyclotron waves) interact with positive ions and electrons interact with right hand circularly polarised waves (such as whistler waves), although anomalous interactions can occur (see Chapter 1, Section 1.2). Both the whistler and EMIC waves exist in a diverse range of plasma conditions, which reinforces the need to investigate their dispersive characteristics and growth rates for a variety of plasma parameters.

In Chapter 1, Section 1.3, we discussed how *in situ* measurements of space plasmas by spacecraft have shown mounting evidence that velocity space distributions are best described by the kappa distribution (*Pierrard and Lazar, 2010*). This is because of an overabundance (relative to the Maxwellian) of superthermal particles which are distributed in energy, or momentum, according to a power law (*Christon et al., 1988; Maksimovic et al., 1997a; Schippers et al., 2008; Dialynas et al., 2009; Arridge et al., 2009*). The kappa distribution provides a good fit to particle velocity distributions in space plasmas, as it has a power law superthermal tail that smoothly merges with a Gaussian core at smaller speeds.

*Schippers et al. (2008)* and *Arridge et al. (2009)* found that the dual kappa distribution model always provided the best fit to the electron velocity distribution in the Saturnian magnetosphere regardless of the region considered. In Chapter 2, the dispersion relation

for the parallel propagating whistler instability in the Saturnian magnetosphere driven by temperature anisotropy in both the hot and cool electron species, in a plasma where the velocity distribution for each plasma species is modelled by a bi-kappa distribution, was solved numerically. Using parameter values derived by *Schippers et al.* (2008) as a guide, a parameter survey of the dispersion relation for different anisotropies, temperatures and spectral indices of the two electron components was performed.

Whether the anisotropies of the two electron species are equal or not greatly affects the dispersive characteristics and growth rate. When they are equal there exists a single frequency and wave number at which all thermal effects and  $\kappa$  dependence vanish (*Mace and Sydora, 2010*). This point sets upper boundaries in frequency and wave number below which all wave growth is confined.

When the anisotropies are not equal, no such point exists. In such cases, we defined a wave number  $k^* \rho_h$ , corresponding to the point at which the growth rate is zero. This wave number is dependent on the spectral indices of both electron species. The dependence of  $k^* \rho_h$  on the spectral index of the hot electrons is non-monotonic at very low values of  $A_h$  ( $A_h = 0.1$ ). However, we see a monotonic increase in  $k^* \rho_h$  with an increase in spectral index of the hot electrons as  $A_h$  is increased. An increase in the spectral index of the cool electrons, on the other hand, resulted in a monotonic increase in  $k^* \rho_h$  for all anisotropies investigated.

The dependence of peak growth rates on  $\kappa$  of each electron species is strongly influenced by both the anisotropy and plasma parallel beta value,  $\beta_{\parallel h}$ , of the hot electrons. In most cases investigated, an increase in the spectral index of the hot electrons resulted in a monotonic decrease in peak growth rate at small anisotropies ( $A_h = 0.1$ ), with a reverse in this trend observed as the anisotropy is increased. The same trend is seen for a variation in the spectral index of the cool electrons. However, the critical value of the anisotropy at which the aforementioned trend is reversed is dependent on the value of  $\beta_{\parallel h}$ . For small  $\beta_{\parallel h}$  ( $\beta_{\parallel h} \ll 1$ ) we see a reverse in trend at larger anisotropies ( $A \geq 1.0$ ) than that for  $\beta_{\parallel h} \approx 1$ .

While our parameter survey has taken into account the variation of the spectral indices

and anisotropies of the two electron components, we have only looked at a variation in the temperature of the hot electron component. This variation in hot electron temperature resulted in a variation in the plasma parallel beta value of the hot electrons. As a suggestion for further work, an investigation into the effects of varying the plasma parallel beta value of the cool electrons is recommended. Additionally, as mentioned previously, the plasma parallel beta value of both species is also dependent on the number density and magnetic field strength. Investigating the effects of varying these parameters in future works is warranted and would account for the spatial variability of a dynamic magnetosphere such as Saturn.

In Chapter 3, we presented the results from a study of the behaviour of EMIC wave growth rate for a variety of relative abundances of the ion species. Following *Mace et al.* (2011), it was assumed that the hot ring current ions, cool ions of plasmaspheric origin, as well as the electrons, have particle velocity distributions modelled by the bi-kappa distribution. However, we addressed more completely the effects of varying the relative ion abundances and how this influences wave growth and damping.

Electromagnetic ion cyclotron (EMIC) waves in multi-ion species plasmas propagate in branches. Each branch is bound by a cutoff frequency at small wave numbers and a resonant frequency at large wave numbers. This is true for all branches except for the branch corresponding to the heaviest ion species. This branch has only a resonance at its gyrofrequency and is bound below by  $\omega = 0$ .

The gyrofrequency of an ion species,  $\Omega_j$ , determines the resonant frequency below which the wave branch of species  $j$  is confined at large wave numbers, which remains relatively constant for a given region of the magnetosphere. The cutoff frequency, defining the lower boundary of the wave branch, depends strongly on the number densities of the ion species (*Kozyra et al.*, 1984; *Mace et al.*, 2011) and can vary with prevailing conditions.

The condition for wave growth is determined by the thermal anisotropies of each ion species,  $j$ , which sets an upper bound,  $\omega_j^*$ , on the wave frequency below which that ion species contributes positively to the growth rate (*Mace et al.*, 2011). The relative positions of the cutoffs with respect to the critical frequencies  $\omega_j^*$  play a crucial role in determining

whether a particular wave branch will be unstable, as was pointed out by *Mace et al.* (2011).

We initially investigated how the cutoff frequencies of the proton and helium branches varied with the relative ion abundances of the proton, helium and oxygen ions, using cold plasma theory as a guide. This allowed us to find ion abundances that produced wave growth by lowering the cutoffs below the relevant  $\omega_j^*$  frequencies.

The plasmaspheric ion populations play a relatively minor role in governing the dispersive characteristics and growth rates of the branches of the EMIC instability. We found that the most significant effects in the dispersion curves and growth rates of each branch resulted from a variation in hot ring current ion abundances. When the ring current is composed predominantly of  $H^+$  ions, all branches of the EMIC wave are destabilised and the maximum growth rate corresponds to the proton branch. When the  $O^+$  ion abundance in the ring current is increased, a decrease in the growth rate of the proton branch and cyclotron damping of the helium branch are observed. The oxygen branch experiences an increase in the maximum growth rate with an increase in the  $O^+$  ion abundance. When the ring current is composed predominantly of  $He^+$  ions, only the helium and oxygen branches of the EMIC wave are destabilised and the maximum growth rate corresponds to the helium branch.

The results of Chapter 3 show how EMIC instabilities are sensitive to the relative abundance of each ion species. This is especially true for the proton and helium branches. The contribution to the growth rate of each branch of the EMIC wave is dependent on the temperature anisotropy of each anisotropic ion species as well as the relative abundance of each ion species. However, the EMIC instability exists in a diverse range of plasma conditions. Owing to this, further investigations into the effects of varying other plasma parameters such as the spectral indices of each ion species is warranted.



## Appendix A

# Dispersion relation for parallel propagating L and R mode waves in a plasma with an arbitrary velocity distribution

This appendix presents an outline of the derivation of the dispersion relation for parallel propagating L and R mode waves in a plasma with an arbitrary velocity distribution. This appendix follows closely the method employed by *Gurnett and Bhattacharjee* (2005, pp. 372-373).

Electromagnetic waves have both an electric and magnetic field and, therefore, we begin by seeking solutions to Maxwell's equations (ignoring external sources). A homogeneous system of equations can be obtained by taking the Fourier-Laplace transform of Faraday and Ampere's laws (*Gurnett and Bhattacharjee*, 2005, Eq. 4.2.7)

$$i\mathbf{k} \times \tilde{\mathbf{E}} = -(-i\omega)\tilde{\mathbf{B}}, \quad (\text{A.1})$$

and

$$i\mathbf{k} \times \tilde{\mathbf{B}} = \frac{-i\omega}{c^2} \overline{\mathbf{K}} \cdot \tilde{\mathbf{E}}, \quad (\text{A.2})$$

and eliminating the Fourier-Laplace transform of the magnetic field,  $\tilde{\mathbf{B}}$ . In Equations (A.1) and (A.2),  $\tilde{\mathbf{E}}$  is the Fourier-Laplace transform of the electric field,  $c$  is the speed of light and  $\mathbf{k}$  is the wave vector. The equivalent dielectric tensor,  $\overline{\mathbf{K}}$ , is given by  $\overline{\mathbf{K}} = \overline{\mathbf{I}} - \overline{\boldsymbol{\sigma}}/(i\omega\epsilon_0)$ , where  $\epsilon_0$  is the permittivity of free space,  $\overline{\mathbf{I}}$  is the unit tensor and  $\overline{\boldsymbol{\sigma}}$  is the conductivity tensor which is defined through the Fourier-Laplace transform of the current density,  $\tilde{\mathbf{J}}$ , such that (*Gurnett and Bhattacharjee*, 2005, Eq. 4.2.3)

$$\tilde{\mathbf{J}} = \overline{\boldsymbol{\sigma}} \cdot \tilde{\mathbf{E}}. \quad (\text{A.3})$$

The wave frequency,  $\omega$ , is complex with real part,  $\omega_r$ , where  $\omega_r > 0$  is always assumed, and an imaginary part,  $\gamma$ . We impose the condition  $\text{Im}(\omega) > 0$  to guarantee convergence of the Fourier-Laplace transforms. Solving Equation (A.1) for  $\tilde{\mathbf{B}}$  and substituting it into Equation (A.2), we arrive at a homogeneous equation for the electric field, (*Gurnett and Bhattacharjee*, 2005, Eq. 4.2.8),

$$\mathbf{k} \times (\mathbf{k} \times \tilde{\mathbf{E}}) + \frac{\omega^2}{c^2} \overline{\mathbf{K}} \cdot \tilde{\mathbf{E}} = 0. \quad (\text{A.4})$$

To analyse electromagnetic wave propagation in a dielectric medium, we seek non-trivial solutions to the homogeneous equation given by Equation (A.4). We can express Equation

(A.4) in terms of tensor elements such that (Gurnett and Bhattacharjee, 2005, Eq. 9.3.28)

$$\begin{pmatrix} K_{xx} - \frac{c^2 k^2}{\omega^2} \cos^2 \theta & K_{xy} & K_{xz} + \frac{c^2 k^2}{\omega^2} \sin \theta \cos \theta \\ K_{yx} & K_{yy} - \frac{c^2 k^2}{\omega^2} & K_{yz} \\ K_{zx} + \frac{c^2 k^2}{\omega^2} \sin \theta \cos \theta & K_{zy} & K_{zz} - \frac{c^2 k^2}{\omega^2} \sin^2 \theta \end{pmatrix} \begin{pmatrix} \tilde{E}_x \\ \tilde{E}_y \\ \tilde{E}_z \end{pmatrix} = 0, \quad (\text{A.5})$$

where  $\theta$  is the wave normal angle and  $k$  is the wave number. The derivation of each dielectric tensor element,  $K_{ij}$ , is presented in great detail in Chapter 9.3.1 of Gurnett and Bhattacharjee (2005, pp. 367 - 371). Each element is defined as follows (Gurnett and Bhattacharjee, 2005, Eqs. 9.3.19 - 9.3.27):

$$K_{xx} = 1 - \sum_j \frac{\omega_{pj}^2}{\omega} \sum_{n=-\infty}^{\infty} \int_{-\infty}^{\infty} \int_0^{\infty} \frac{n^2 J_n^2(z_j)}{z_j^2 (k_{\parallel} v_{\parallel} - \omega + n\Omega_j)} U_j 2\pi v_{\perp}^2 dv_{\perp} dv_{\parallel} \quad (\text{A.6})$$

$$K_{xy} = -i \sum_j \frac{\omega_{pj}^2}{\omega} \sum_{n=-\infty}^{\infty} \int_{-\infty}^{\infty} \int_0^{\infty} \frac{n J_n(z_j) J'_n(z_j)}{z_j (k_{\parallel} v_{\parallel} - \omega + n\Omega_j)} U_j 2\pi v_{\perp}^2 dv_{\perp} dv_{\parallel} \quad (\text{A.7})$$

$$K_{xz} = - \sum_j \frac{\omega_{pj}^2}{\omega} \sum_{n=-\infty}^{\infty} \int_{-\infty}^{\infty} \int_0^{\infty} \frac{n J_n^2(z_j)}{z_j (k_{\parallel} v_{\parallel} - \omega + n\Omega_j)} T_j 2\pi v_{\perp}^2 dv_{\perp} dv_{\parallel} \quad (\text{A.8})$$

$$K_{yx} = i \sum_j \frac{\omega_{pj}^2}{\omega} \sum_{n=-\infty}^{\infty} \int_{-\infty}^{\infty} \int_0^{\infty} \frac{n J_n(z_j) J'_n(z_j)}{z_j (k_{\parallel} v_{\parallel} - \omega + n\Omega_j)} U_j 2\pi v_{\perp}^2 dv_{\perp} dv_{\parallel} \quad (\text{A.9})$$

$$K_{yy} = 1 - \sum_j \frac{\omega_{pj}^2}{\omega} \sum_{n=-\infty}^{\infty} \int_{-\infty}^{\infty} \int_0^{\infty} \frac{J'_n(z_j) J'_n(z_j)}{(k_{\parallel} v_{\parallel} - \omega + n\Omega_j)} U_j 2\pi v_{\perp}^2 dv_{\perp} dv_{\parallel} \quad (\text{A.10})$$

$$K_{yz} = i \sum_j \frac{\omega_{pj}^2}{\omega} \sum_{n=-\infty}^{\infty} \int_{-\infty}^{\infty} \int_0^{\infty} \frac{J_n(z_j) J'_n(z_j)}{(k_{\parallel} v_{\parallel} - \omega + n\Omega_j)} T_j 2\pi v_{\perp}^2 dv_{\perp} dv_{\parallel} \quad (\text{A.11})$$

$$K_{zx} = - \sum_j \frac{\omega_{pj}^2}{\omega} \sum_{n=-\infty}^{\infty} \int_{-\infty}^{\infty} \int_0^{\infty} \frac{n J_n^2(z_j)}{z_j (k_{\parallel} v_{\parallel} - \omega + n\Omega_j)} U_j 2\pi v_{\perp} v_{\parallel} dv_{\perp} dv_{\parallel} \quad (\text{A.12})$$

$$K_{zy} = -i \sum_j \frac{\omega_{pj}^2}{\omega} \sum_{n=-\infty}^{\infty} \int_{-\infty}^{\infty} \int_0^{\infty} \frac{J_n(z_j) J'_n(z_j)}{(k_{\parallel} v_{\parallel} - \omega + n\Omega_j)} U_j 2\pi v_{\perp} v_{\parallel} dv_{\perp} dv_{\parallel} \quad (\text{A.13})$$

$$K_{zz} = 1 - \sum_j \frac{\omega_{pj}^2}{\omega} \sum_{n=-\infty}^{\infty} \int_{-\infty}^{\infty} \int_0^{\infty} \frac{J_n^2(z_j)}{(k_{\parallel} v_{\parallel} - \omega + n\Omega_j)} T_j 2\pi v_{\perp} v_{\parallel} dv_{\perp} dv_{\parallel}. \quad (\text{A.14})$$

In the above Equations (A.6) - (A.14), the signed gyrofrequency for the  $j$ th species is given by  $\Omega_j = q_j B_0 / m_j$  and is characterised by mass  $m_j$  and charge  $q_j$ . The plasma frequency,  $\omega_{pj}$ , for the  $j$ th species is given by  $\omega_{pj} = (n_{0j} q_j^2 / \epsilon_0 m_j)^{1/2}$  where  $n_{0j}$  is the number density. The parameters  $v_{\perp}$  and  $v_{\parallel}$  are the perpendicular and parallel components of the velocity, respectively. The components  $k_{\parallel}$  and  $k_{\perp}$ , are the parallel and perpendicular components, respectively, of the wave vector  $\mathbf{k}$ , with respect to the magnetic field. The parameter  $z_j$  is given by  $z_j = k_{\perp} v_{\perp} / \Omega_j$ . The function  $J_n(z_j)$  is the Bessel function of the first kind of order  $n$  and  $J'_n(z_j)$  denotes  $\frac{d}{dz_j} J_n(z_j)$ . We have defined  $U_j$  such that (*Gurnett and Bhattacharjee, 2005, Eq. 9.3.10*)

$$\begin{aligned} U_j &= \frac{\partial f_{j0}}{\partial v_{\perp}} + \frac{k_{\parallel}}{\omega} \left( v_{\perp} \frac{\partial f_{j0}}{\partial v_{\parallel}} - v_{\parallel} \frac{\partial f_{j0}}{\partial v_{\perp}} \right) \\ &= \left( 1 - \frac{k_{\parallel} v_{\parallel}}{\omega} \right) \frac{\partial f_{j0}}{\partial v_{\perp}} + \frac{k_{\parallel} v_{\perp}}{\omega} \frac{\partial f_{j0}}{\partial v_{\parallel}}, \end{aligned} \quad (\text{A.15})$$

and  $T_j$  such that (*Gurnett and Bhattacharjee, 2005, Eq. 9.3.14*)

$$T_j = \frac{\partial f_{j0}}{\partial v_{\parallel}} - \frac{n\Omega_j}{\omega v_{\perp}} \left( v_{\perp} \frac{\partial f_{j0}}{\partial v_{\parallel}} - v_{\parallel} \frac{\partial f_{j0}}{\partial v_{\perp}} \right), \quad (\text{A.16})$$

where the function  $f_{j0}$  is the zeroth-order velocity distribution function.

We confine our study to the case of parallel propagation and, therefore,  $k_{\perp} = 0$  and  $k = k_{\parallel}$ . Making this restriction implies that the wave vector is parallel to the magnetic field, i.e,  $\theta = 0$  and, therefore,  $\sin \theta = 0$  and  $\cos \theta = 1$ . The homogeneous equation, given by Equation (A.5), simplifies further since  $z_j = k_{\perp} v_{\perp} / \Omega_j = 0$  for parallel propagation. Owing to this, the Bessel function term  $n J_n^2(z_j) / z_j \rightarrow 0$  as  $z_j \rightarrow 0$  for all  $n$  and, therefore,  $K_{xz} = 0$  and  $K_{zx} = 0$ . A further simplification can be made since  $J_n(z_j) J'_n(z_j) \rightarrow 0$  as  $z_j \rightarrow 0$  for all  $n$  so that,  $K_{yz} = 0$  and  $K_{zy} = 0$ . Implementing the above simplifications, the homogeneous equation, Equation (A.5), becomes (*Gurnett and Bhattacharjee, 2005,*

Eq. 9.3.29)

$$\begin{pmatrix} K_{xx} - \frac{c^2 k_{\parallel}^2}{\omega^2} & K_{xy} & 0 \\ K_{yx} & K_{yy} - \frac{c^2 k_{\parallel}^2}{\omega^2} & 0 \\ 0 & 0 & K_{zz} \end{pmatrix} \begin{pmatrix} \tilde{E}_x \\ \tilde{E}_y \\ \tilde{E}_z \end{pmatrix} = 0, \quad (\text{A.17})$$

for parallel propagation. Equation (A.17) is of the form  $\mathbf{M} \cdot \tilde{\mathbf{E}} = 0$ . The condition for non-trivial solutions to Equation (A.17) is that the matrix,  $\mathbf{M}$ , be singular, i.e., be non-invertible. For this to be so we require that the determinant of  $\mathbf{M}$  be zero, which furnishes the dispersion relation. Evaluating the determinant of the matrix in Equation (A.17) and setting it to zero, we obtain (*Gurnett and Bhattacharjee, 2005, Eq. 9.3.30*),

$$D(k_{\parallel}, \omega) = \left[ \left( K_{xx} - \frac{c^2 k_{\parallel}^2}{\omega^2} \right) \left( K_{yy} - \frac{c^2 k_{\parallel}^2}{\omega^2} \right) - K_{xy} K_{yx} \right] K_{zz} = 0. \quad (\text{A.18})$$

By the definition of  $K_{xy}$ , Equation (A.7), and  $K_{yx}$ , Equation (A.9), it is clear that  $K_{xy} = -K_{yx}$ . Therefore, Equation (A.18) becomes

$$D(k_{\parallel}, \omega) = \left[ \left( K_{xx} - \frac{c^2 k_{\parallel}^2}{\omega^2} \right) \left( K_{yy} - \frac{c^2 k_{\parallel}^2}{\omega^2} \right) + K_{xy}^2 \right] K_{zz} = 0. \quad (\text{A.19})$$

Making use of the identity (*Harris, 1970, Eq. 3.44*)

$$J_{n+1}(z_j) + J_{n-1}(z_j) = \frac{2n}{z_j} J_n(z_j) \quad (\text{A.20})$$

it can be shown that

$$\begin{aligned} 4 \frac{n^2 J_n^2(z_j)}{z_j^2} &= (J_{n+1}(z_j) + J_{n-1}(z_j))^2 \\ &= J_{n+1}^2(z_j) + J_{n-1}^2(z_j) + 2J_{n+1}(z_j)J_{n-1}(z_j). \end{aligned} \quad (\text{A.21})$$

Taking the limit as  $z_j \rightarrow 0$  of Equation (A.21) and noting that  $\delta_{m,n}^2 = \delta_{m,n}$  yields,

$$\begin{aligned} \lim_{z_j \rightarrow 0} \frac{n^2 J_n^2(z_j)}{z_j^2} &= \frac{1}{4} \lim_{z_j \rightarrow 0} (J_{n+1}^2(z_j) + J_{n-1}^2(z_j) + 2J_{n+1}(z_j)J_{n-1}(z_j)) \\ &= \frac{1}{4} (\delta_{n+1,0} + \delta_{n-1,0} + 2\delta_{n+1,0}\delta_{n-1,0}). \end{aligned} \quad (\text{A.22})$$

We note that  $\delta_{n+1,0}\delta_{n-1,0} = 0$  for all  $n$ ,  $\delta_{n+1,0} = 1$  for  $n = -1$  and  $\delta_{n-1,0} = 1$  for  $n = 1$ . Therefore, the Bessel function term  $n^2 J_n^2(z_j)/z_j^2$  in  $K_{xx}$ , Equation (A.6), reduces to  $1/4$  for  $n = \pm 1$  and zero for all other values of  $n$ . It is also known that (*Abramowitz and Stegun*, 1964, Eq. 9.1.27)

$$J_{n-1}(z_j) - J_{n+1}(z_j) = 2J'_n(z_j). \quad (\text{A.23})$$

Using Equations (A.23), it can be shown that

$$\begin{aligned} \lim_{z_j \rightarrow 0} J'_n(z_j)J'_n(z_j) &= \frac{1}{4} \lim_{z_j \rightarrow 0} (J_{n-1}^2(z_j) + J_{n+1}^2(z_j) - 2J_{n+1}(z_j)J_{n-1}(z_j)) \\ &= \frac{1}{4} (\delta_{n+1,0} + \delta_{n-1,0} - 2\delta_{n+1,0}\delta_{n-1,0}), \end{aligned} \quad (\text{A.24})$$

and so the Bessel function term  $J'_n(z_j)J'_n(z_j)$  in  $K_{yy}$ , Equation (A.10), also reduces to  $1/4$  for  $n = \pm 1$  and zero for all other values of  $n$ . Since both  $K_{xx}$  and  $K_{yy}$  both reduce to  $1/4$  for  $n = \pm 1$  and zero for all other values of  $n$ , we can write  $K_{xx} = K_{yy}$  and Equation (A.19) becomes to

$$D(k_{\parallel}, w) = \left[ \left( K_{xx} - \frac{k_{\parallel}^2 c^2}{\omega^2} \right)^2 + K_{xy}^2 \right] K_{zz} = 0. \quad (\text{A.25})$$

Taking into account all of the above simplifications, the electromagnetic part of the dispersion relation comes from demanding that the term in square brackets of Equation (A.25) be zero such that (*Gurnett and Bhattacharjee*, 2005, Eq. 9.3.31)

$$\frac{k_{\parallel}^2 c^2}{\omega^2} = K_{xx} \pm iK_{xy}, \quad (\text{A.26})$$

whereas the solutions of  $K_{zz} = 0$  yields the usual electrostatic waves.

As previously shown (Equation (A.22)), in the limit  $z_j \rightarrow 0$ , the Bessel function term  $n^2 J_n^2(z_j)/z_j^2$  reduces to  $1/4$  for  $n = \pm 1$ . Therefore,  $K_{xx}$ , Equation (A.6), can be written

as

$$\begin{aligned}
K_{xx} &= 1 - \sum_j \frac{\omega_{pj}^2}{\omega} \left[ \int_{-\infty}^{\infty} \int_0^{\infty} \frac{1/4}{(k_{\parallel}v_{\parallel} - \omega - \Omega_j)} U_j 2\pi v_{\perp}^2 dv_{\perp} dv_{\parallel} \right. \\
&\quad \left. + \int_{-\infty}^{\infty} \int_0^{\infty} \frac{1/4}{(k_{\parallel}v_{\parallel} - \omega + \Omega_j)} U_j 2\pi v_{\perp}^2 dv_{\perp} dv_{\parallel} \right] \\
&= 1 - \sum_j \frac{\omega_{pj}^2}{\omega} \frac{1}{4} \int_{-\infty}^{\infty} \int_0^{\infty} \left[ \frac{1}{(k_{\parallel}v_{\parallel} - \omega - \Omega_j)} + \frac{1}{(k_{\parallel}v_{\parallel} - \omega + \Omega_j)} \right] U_j 2\pi v_{\perp}^2 dv_{\perp} dv_{\parallel} \\
&= 1 - \sum_j \frac{\omega_{pj}^2}{\omega} \frac{1}{4} \int_{-\infty}^{\infty} \int_0^{\infty} \left[ \frac{2(k_{\parallel}v_{\parallel} - \omega)}{(k_{\parallel}v_{\parallel} - \omega - \Omega_j)(k_{\parallel}v_{\parallel} - \omega + \Omega_j)} \right] U_j 2\pi v_{\perp}^2 dv_{\perp} dv_{\parallel} \\
&= 1 - \pi \sum_j \frac{\omega_{pj}^2}{\omega} \int_{-\infty}^{\infty} \int_0^{\infty} \frac{(k_{\parallel}v_{\parallel} - \omega) U_j v_{\perp}^2}{(k_{\parallel}v_{\parallel} - \omega - \Omega_j)(k_{\parallel}v_{\parallel} - \omega + \Omega_j)} dv_{\perp} dv_{\parallel}. \tag{A.27}
\end{aligned}$$

It can also be shown using Equations (A.20) and (A.23) that  $nJ_n(z_j) J'_n(z_j)/z_j$  reduces to  $1/4$  for  $n = 1$  and  $-1/4$  for  $n = -1$  (and zero for all other values of  $n$ ) as  $z_j \rightarrow 0$  so  $K_{xy}$ , Equation (A.7), can be written such that

$$\begin{aligned}
K_{xy} &= -i \sum_j \frac{\omega_{pj}^2}{\omega} \int_{-\infty}^{\infty} \int_0^{\infty} \left[ \frac{1/4}{(k_{\parallel}v_{\parallel} - \omega + \Omega_j)} + \frac{-1/4}{(k_{\parallel}v_{\parallel} - \omega - \Omega_j)} \right] U_j 2\pi v_{\perp}^2 dv_{\perp} dv_{\parallel} \\
&= -i\pi \sum_j \frac{\omega_{pj}^2}{\omega} \int_{-\infty}^{\infty} \int_0^{\infty} \left[ \frac{1}{(k_{\parallel}v_{\parallel} - \omega + \Omega_j)} + \frac{-1}{(k_{\parallel}v_{\parallel} - \omega - \Omega_j)} \right] U_j \frac{1}{2} v_{\perp}^2 dv_{\perp} dv_{\parallel} \\
&= i\pi \sum_j \frac{\omega_{pj}^2}{\omega} \int_{-\infty}^{\infty} \int_0^{\infty} \frac{\Omega_j U_j v_{\perp}^2}{(k_{\parallel}v_{\parallel} - \omega + \Omega_j)(k_{\parallel}v_{\parallel} - \omega - \Omega_j)} dv_{\perp} dv_{\parallel} \tag{A.28}
\end{aligned}$$

Substituting Equations (A.27) and (A.28) into Equation (A.26) yields

$$\begin{aligned}
\frac{k_{\parallel}^2 c^2}{\omega^2} &= \left[ 1 - \pi \sum_j \frac{\omega_{pj}^2}{\omega} \int_{-\infty}^{\infty} \int_0^{\infty} \frac{(k_{\parallel}v_{\parallel} - \omega) U_j v_{\perp}^2}{(k_{\parallel}v_{\parallel} - \omega - \Omega_j)(k_{\parallel}v_{\parallel} - \omega + \Omega_j)} dv_{\perp} dv_{\parallel} \right] \\
&\quad \pm i \left[ i\pi \sum_j \frac{\omega_{pj}^2}{\omega} \int_{-\infty}^{\infty} \int_0^{\infty} \frac{\Omega_j U_j v_{\perp}^2}{(k_{\parallel}v_{\parallel} - \omega + \Omega_j)(k_{\parallel}v_{\parallel} - \omega - \Omega_j)} dv_{\perp} dv_{\parallel} \right] \\
&= 1 - \pi \sum_j \frac{\omega_{pj}^2}{\omega} \int_{-\infty}^{\infty} dv_{\parallel} \int_0^{\infty} dv_{\perp} v_{\perp}^2 \left[ \frac{k_{\parallel}v_{\parallel} - \omega \pm \Omega_j}{(k_{\parallel}v_{\parallel} - \omega - \Omega_j)(k_{\parallel}v_{\parallel} - \omega + \Omega_j)} \right] U_j \tag{A.29}
\end{aligned}$$

If we choose “ $-\Omega_j$ ” in Equation (A.29), we arrive at the dispersion relation for parallel propagating L mode waves in a plasma with an arbitrary velocity distribution (*Mace et al.*,

2011),

$$\begin{aligned} \frac{k_{\parallel}^2 c^2}{\omega^2} = & 1 - \pi \sum_j \frac{\omega_{pj}^2}{\omega^2} \int_{-\infty}^{\infty} dv_{\parallel} \int_0^{\infty} dv_{\perp} v_{\perp}^2 \frac{1}{k_{\parallel} v_{\parallel} - \omega + \Omega_j} \\ & \cdot \left[ (\omega - k_{\parallel} v_{\parallel}) \frac{\partial f_{j0}}{\partial v_{\perp}} + k_{\parallel} v_{\perp} \frac{\partial f_{j0}}{\partial v_{\parallel}} \right] \quad \text{Im}(\omega) > 0. \end{aligned} \quad (\text{A.30})$$

This leaves the dispersion relation for parallel propagating R mode waves in a plasma with an arbitrary velocity distribution to be given by,

$$\begin{aligned} \frac{k_{\parallel}^2 c^2}{\omega^2} = & 1 - \pi \sum_j \frac{\omega_{pj}^2}{\omega^2} \int_{-\infty}^{\infty} dv_{\parallel} \int_0^{\infty} dv_{\perp} v_{\perp}^2 \frac{1}{k_{\parallel} v_{\parallel} - \omega - \Omega_j} \\ & \cdot \left[ (\omega - k_{\parallel} v_{\parallel}) \frac{\partial f_{j0}}{\partial v_{\perp}} + k_{\parallel} v_{\perp} \frac{\partial f_{j0}}{\partial v_{\parallel}} \right] \quad \text{Im}(\omega) > 0. \end{aligned} \quad (\text{A.31})$$

## Appendix B

Dispersion relation for parallel propagating L mode waves with an arbitrary number of kappa distributed plasma particle species

In this appendix the method used to derive the dispersion relation for parallel propagating L mode waves with an arbitrary number of kappa-distributed plasma particle species is outlined. We note that the same method can be used to derive the dispersion relation for parallel propagating R mode waves with an arbitrary number of kappa-distributed plasma particle species. The dispersion relation for parallel propagating L mode waves in a plasma with arbitrary distribution as derived in Appendix A, Equation (A.30), is

$$\frac{k_{\parallel}^2 c^2}{\omega^2} = 1 - \pi \sum_j \frac{\omega_{pj}^2}{\omega^2} \int_{-\infty}^{\infty} dv_{\parallel} \int_0^{\infty} dv_{\perp} v_{\perp}^2 \frac{1}{k_{\parallel} v_{\parallel} - \omega + \Omega_j} \left[ (\omega - k_{\parallel} v_{\parallel}) \frac{\partial f_{j0}}{\partial v_{\perp}} + k_{\parallel} v_{\perp} \frac{\partial f_{j0}}{\partial v_{\parallel}} \right] \quad \text{Im}(\omega) > 0. \quad (\text{B.1})$$

The notation in Equation (B.1) is the same as that described in Appendix A for Equation (A.30).

We assume that all particle species have unperturbed velocity distributions given by the bi-kappa distribution (*Summers and Thorne, 1991*),

$$f(v_{\perp}, v_{\parallel}) = \pi^{-3/2} \frac{1}{\theta_{\perp}^2 \theta_{\parallel}} \frac{\Gamma(\kappa + 1)}{\kappa^{3/2} \Gamma(\kappa - \frac{1}{2})} \left( 1 + \frac{v_{\perp}^2}{\kappa \theta_{\perp}^2} + \frac{v_{\parallel}^2}{\kappa \theta_{\parallel}^2} \right)^{-(\kappa+1)}, \quad (\text{B.2})$$

where  $\Gamma$  denotes the gamma function. The parameters  $\theta_{\perp}$  and  $\theta_{\parallel}$  are related to the kinetic temperatures,  $T_{\perp}$ ,  $T_{\parallel}$ , respectively perpendicular and parallel to  $\mathbf{B}_0$ , via (*Summers and Thorne, 1991*)

$$\begin{aligned} \theta_{\perp} &= \left[ 2 \left( \frac{\kappa - \frac{3}{2}}{\kappa} \right) \right]^{1/2} \left( \frac{T_{\perp}}{m} \right)^{1/2}, \\ \theta_{\parallel} &= \left[ 2 \left( \frac{\kappa - \frac{3}{2}}{\kappa} \right) \right]^{1/2} \left( \frac{T_{\parallel}}{m} \right)^{1/2}. \end{aligned} \quad (\text{B.3})$$

The parameters  $\theta_{\perp}$  and  $\theta_{\parallel}$  are commonly called generalised thermal speeds. In the isotropic case, however, they reduce to the most probable speed for a kappa distribution. We note going forward that we shall use  $\kappa = \kappa_j$ ,  $\theta_{\parallel} = \theta_{\parallel j}$  and  $\theta_{\perp} = \theta_{\perp j}$  with the subscript  $j$  being omitted for convenience.

From the bi-kappa distribution, Equation (B.2), we find the derivatives with respect to  $v_{\parallel}$  and  $v_{\perp}$  are

$$\frac{\partial f_{j0}}{\partial v_{\parallel}} = -\pi^{-3/2} \frac{2}{\theta_{\perp}^2 \theta_{\parallel}^3} \frac{\Gamma(\kappa + 2)}{\kappa^{5/2} \Gamma(\kappa - \frac{1}{2})} v_{\parallel} \left( 1 + \frac{v_{\perp}^2}{\kappa \theta_{\perp}^2} + \frac{v_{\parallel}^2}{\kappa \theta_{\parallel}^2} \right)^{-(\kappa+2)} \quad (\text{B.4})$$

and

$$\frac{\partial f_{j0}}{\partial v_{\perp}} = -\pi^{-3/2} \frac{2}{\theta_{\perp}^4 \theta_{\parallel}} \frac{\Gamma(\kappa + 2)}{\kappa^{5/2} \Gamma(\kappa - \frac{1}{2})} v_{\perp} \left( 1 + \frac{v_{\perp}^2}{\kappa \theta_{\perp}^2} + \frac{v_{\parallel}^2}{\kappa \theta_{\parallel}^2} \right)^{-(\kappa+2)}, \quad (\text{B.5})$$

respectively.

Substituting the above Equations (B.4) and (B.5) into Equation (B.1) yields,

$$\begin{aligned} \frac{k_{\parallel}^2 c^2}{\omega^2} &= 1 + \sum_j \pi^{-1/2} \frac{2}{\theta_{\perp}^2 \theta_{\parallel}} \frac{\Gamma(\kappa + 2)}{\kappa^{5/2} \Gamma(\kappa - \frac{1}{2})} \frac{\omega_{pj}^2}{\omega^2} \int_{-\infty}^{\infty} \frac{dv_{\parallel}}{k_{\parallel} v_{\parallel} - \omega + \Omega_j} \\ &\left[ \frac{\omega}{\theta_{\perp}^2} + \left( \frac{1}{\theta_{\parallel}^2} - \frac{1}{\theta_{\perp}^2} \right) k_{\parallel} v_{\parallel} \right] \int_0^{\infty} dv_{\perp} v_{\perp}^3 \left( 1 + \frac{v_{\perp}^2}{\kappa \theta_{\perp}^2} + \frac{v_{\parallel}^2}{\kappa \theta_{\parallel}^2} \right)^{-(\kappa+2)}. \end{aligned} \quad (\text{B.6})$$

We seek to evaluate the integral over  $v_{\perp}$ ,  $I_{\perp}$ ,

$$\begin{aligned} I_{\perp} &= \int_0^{\infty} dv_{\perp} v_{\perp}^3 \left( 1 + \frac{v_{\parallel}^2}{\kappa \theta_{\parallel}^2} + \frac{v_{\perp}^2}{\kappa \theta_{\perp}^2} \right)^{-(\kappa+2)} \\ &= \int_0^{\infty} v_{\perp}^3 (A + Bv_{\perp}^2)^{-C} dv_{\perp} \end{aligned}$$

where  $A = 1 + v_{\parallel}^2/\kappa\theta_{\parallel}^2$ ,  $B = 1/\kappa\theta_{\perp}^2$  and  $C = \kappa + 2$ . The above integral,  $I_{\perp}$ , is evaluated with the aid of the standard integral (*Gradshteyn and Ryzhik*, 2000, p. 322, ch.3.251, Eq. 11)

$$\int_0^{\infty} x^{\mu-1} (1 + \beta x^p)^{-\nu} dx = \frac{1}{p} \beta^{-\frac{\mu}{p}} B \left( \frac{\mu}{p}, \nu - \frac{\mu}{p} \right) \quad (\text{B.7})$$

$|\arg \beta| < \pi, p > 0, 0 < \text{Re } \mu < p \text{ Re } \nu.$

The Beta function,  $B(x, y)$ , has the identity (*Gradshteyn and Ryzhik*, 2000, p. 899, ch. 8.384, Eq. 1)

$$B(x, y) = \frac{\Gamma(x)\Gamma(y)}{\Gamma(x+y)},$$

so that

$$B \left( \frac{\mu}{p}, \nu - \frac{\mu}{p} \right) = \frac{\Gamma \left( \frac{\mu}{p} \right) \Gamma \left( \nu - \frac{\mu}{p} \right)}{\Gamma(\nu)}.$$

Using the identity given in Equation (B.7) to evaluate the integral  $I_{\perp}$  and noting that  $\Gamma(2) = 1$ , we find

$$I_{\perp} = \frac{1}{2} A^{-C} \left( \frac{B}{A} \right)^{-2} \frac{\Gamma(C-2)}{\Gamma(C)}$$

and, therefore,

$$I_{\perp} = \frac{1}{2} \frac{(\kappa \theta_{\perp}^2)^2}{(1 + v_{\parallel}^2 / \kappa \theta_{\parallel}^2)^{\kappa}} \frac{\Gamma(\kappa)}{\Gamma(\kappa + 2)}. \quad (\text{B.8})$$

Substituting Equation (B.8) into Equation (B.6), the dispersion relation then becomes

$$\frac{k_{\parallel}^2 c^2}{\omega^2} = 1 + \sum_j \frac{\omega_{pj}^2}{\omega^2} \frac{\pi^{-1/2} \kappa^{-1/2}}{\theta_{\parallel}} \frac{\Gamma(\kappa)}{\Gamma(\kappa - \frac{1}{2})} \int_{-\infty}^{\infty} (\omega + A_j k_{\parallel} v_{\parallel}) \frac{(1 + v_{\parallel}^2 / \kappa \theta_{\parallel}^2)^{-\kappa}}{k_{\parallel} v_{\parallel} - \omega + \Omega_j} dv_{\parallel} \quad (\text{B.9})$$

where,

$$A_j = \frac{\theta_{\perp}^2}{\theta_{\parallel}^2} - 1$$

is the temperature anisotropy of species  $j$ .

We seek to evaluate the integral over  $v_{\parallel}$ . Let  $I_{\parallel}$  be the integral over  $v_{\parallel}$  such that

$$I_{\parallel} = \frac{\pi^{-1/2} \kappa^{-1/2}}{\theta_{\parallel}} \frac{\Gamma(\kappa)}{\Gamma(\kappa - \frac{1}{2})} \int_{-\infty}^{\infty} \frac{(\omega + A_j k_{\parallel} v_{\parallel}) (1 + v_{\parallel}^2 / \kappa \theta_{\parallel}^2)^{-\kappa}}{k_{\parallel} v_{\parallel} - \omega + \Omega_j} dv_{\parallel}.$$

Let  $\mu = \omega / (A_j k_{\parallel})$ ,  $\beta = 1 / \kappa \theta_{\parallel}^2$  and  $\alpha = (\omega - \Omega_j) / k_{\parallel}$  so the above equation becomes

$$\begin{aligned} I_{\parallel} &= A_j \frac{\pi^{-1/2} \kappa^{-1/2}}{\theta_{\parallel}} \frac{\Gamma(\kappa)}{\Gamma(\kappa - \frac{1}{2})} \int_{-\infty}^{\infty} \frac{(\mu + v_{\parallel}) (1 + \beta v_{\parallel}^2)^{-\kappa}}{v_{\parallel} - \alpha} dv_{\parallel} \\ &= A_j \mu \frac{\pi^{-1/2} \kappa^{-1/2}}{\theta_{\parallel}} \frac{\Gamma(\kappa)}{\Gamma(\kappa - \frac{1}{2})} \int_{-\infty}^{\infty} \frac{(1 + \beta v_{\parallel}^2)^{-\kappa}}{(v_{\parallel} - \alpha)} dv_{\parallel} \\ &\quad + A_j \frac{\pi^{-1/2} \kappa^{-1/2}}{\theta_{\parallel}} \frac{\Gamma(\kappa)}{\Gamma(\kappa - \frac{1}{2})} \int_{-\infty}^{\infty} \frac{v_{\parallel} (1 + \beta v_{\parallel}^2)^{-\kappa}}{(v_{\parallel} - \alpha)} dv_{\parallel} \\ &= I_{\parallel 1} + I_{\parallel 2}. \end{aligned}$$

We look to evaluate the first integral over  $v_{\parallel}$ ,  $I_{\parallel 1}$ , which is given by

$$\begin{aligned} I_{\parallel 1} &= A_j \mu \frac{\pi^{-1/2} \kappa^{-1/2}}{\theta_{\parallel}} \frac{\Gamma(\kappa)}{\Gamma(\kappa - \frac{1}{2})} \int_{-\infty}^{\infty} \frac{(1 + \beta v_{\parallel}^2)^{-\kappa}}{(v_{\parallel} - \alpha)} dv_{\parallel} \\ &= \frac{\omega}{k_{\parallel} \theta_{\parallel}} \left( \pi^{-1/2} \kappa^{-1/2} \frac{\Gamma(\kappa)}{\Gamma(\kappa - \frac{1}{2})} \int_{-\infty}^{\infty} \frac{1}{(v_{\parallel} - \alpha)(1 + \beta v_{\parallel}^2)^{\kappa}} dv_{\parallel} \right). \quad (\text{B.10}) \end{aligned}$$

Letting  $s = v_{\parallel}/\theta_{\parallel}$  and  $\zeta = \alpha/\theta_{\parallel} = (\omega - \Omega_j)/(k_{\parallel}\theta_{\parallel})$  in Equation (B.10) it can be shown that

$$I_{\parallel 1} = \frac{\omega}{k_{\parallel}\theta_{\parallel}} \left( \pi^{-1/2} \kappa^{\kappa-1/2} \frac{\Gamma(\kappa)}{\Gamma(\kappa - \frac{1}{2})} \int_{-\infty}^{\infty} \frac{ds}{(s - \zeta)(\kappa + s^2)^{\kappa}} \right). \quad (\text{B.11})$$

Equation (B.11) can be compared directly to the function defined by *Mace and Hellberg* (2009, Equation 16)

$$U_{\kappa}(\zeta) = \pi^{-1/2} \kappa^{\kappa-1/2} \frac{\Gamma(\kappa)}{\Gamma(\kappa - \frac{1}{2})} \int_{-\infty}^{\infty} \frac{ds}{(s - \zeta)(\kappa + s^2)^{\kappa}} \quad \text{Im}(\zeta) > 0. \quad (\text{B.12})$$

Equation (B.11) requires  $\text{Im}(\omega) > 0$  (see Equation (B.1)). However, we also have the constraint  $\text{Im}(\zeta) > 0$  in Equation (B.12). By our definition of  $\zeta$ ,  $\text{Im}(\zeta) > 0$  only when  $k_{\parallel} > 0$ . This is not always the case and  $k_{\parallel} < 0$  must also be considered. To accommodate this we will have to proceed with our evaluation of Equation (B.11) for the two cases: (i)  $k_{\parallel} > 0$  and (ii)  $k_{\parallel} < 0$  separately.

For  $k_{\parallel} > 0$ , we set  $k_{\parallel} = |k_{\parallel}|$  and Equation (B.11) becomes

$$\begin{aligned} I_{\parallel 1} &= \frac{\omega}{|k_{\parallel}|\theta_{\parallel}} \left( \pi^{-1/2} \kappa^{\kappa-1/2} \frac{\Gamma(\kappa)}{\Gamma(\kappa - \frac{1}{2})} \int_{-\infty}^{\infty} \frac{ds}{(s - \zeta)(\kappa + s^2)^{\kappa}} \right) \\ &= \frac{\omega}{|k_{\parallel}|\theta_{\parallel}} U_{\kappa}(\zeta) \quad (k_{\parallel} > 0), \end{aligned} \quad (\text{B.13})$$

where we have redefined  $\zeta$  such that  $\zeta = (\omega - \Omega_j)/(|k_{\parallel}|\theta_{\parallel})$ .

For  $k_{\parallel} < 0$ , we set  $k_{\parallel} = -|k_{\parallel}|$  and substitute it into Equation (B.11) so that,

$$I_{\parallel 1} = \frac{\omega}{-|k_{\parallel}|\theta_{\parallel}} \left( \pi^{-1/2} \kappa^{\kappa-1/2} \frac{\Gamma(\kappa)}{\Gamma(\kappa - \frac{1}{2})} \int_{-\infty}^{\infty} \frac{1}{(s' + \zeta)(\kappa + s'^2)^{\kappa}} ds' \right). \quad (\text{B.14})$$

We proceed by making the change of variable  $s = -s'$ , therefore,

$$\begin{aligned} I_{\parallel 1} &= \frac{\omega}{-|k_{\parallel}|\theta_{\parallel}} \left( \pi^{-1/2} \kappa^{\kappa-1/2} \frac{\Gamma(\kappa)}{\Gamma(\kappa - \frac{1}{2})} \int_{\infty}^{-\infty} \frac{-1}{(-s + \zeta)(\kappa + s^2)^{\kappa}} ds \right) \\ &= \frac{\omega}{-|k_{\parallel}|\theta_{\parallel}} \left( \pi^{-1/2} \kappa^{\kappa-1/2} \frac{\Gamma(\kappa)}{\Gamma(\kappa - \frac{1}{2})} \int_{\infty}^{-\infty} \frac{1}{(s - \zeta)(\kappa + s^2)^{\kappa}} ds \right) \\ &= \frac{\omega}{|k_{\parallel}|\theta_{\parallel}} \left( \pi^{-1/2} \kappa^{\kappa-1/2} \frac{\Gamma(\kappa)}{\Gamma(\kappa - \frac{1}{2})} \int_{-\infty}^{\infty} \frac{1}{(s - \zeta)(\kappa + s^2)^{\kappa}} ds \right) \\ &= \frac{\omega}{|k_{\parallel}|\theta_{\parallel}} U_{\kappa}(\zeta) \quad (k_{\parallel} < 0). \end{aligned} \quad (\text{B.15})$$

The second integral over  $v_{\parallel}$ ,  $I_{\parallel 2}$ , where

$$I_{\parallel 2} = A_j \frac{\pi^{-1/2} \kappa^{-1/2}}{\theta_{\parallel}} \frac{\Gamma(\kappa)}{\Gamma(\kappa - \frac{1}{2})} \int_{-\infty}^{\infty} \frac{v_{\parallel}}{(v_{\parallel} - \alpha)(1 + \beta v_{\parallel}^2)^{\kappa}} dv_{\parallel} \quad (\text{B.16})$$

needs to be evaluated in the same way as,  $I_{\parallel 1}$ . For  $k_{\parallel} > 0$ , we set  $k_{\parallel} = |k_{\parallel}|$ . Making the change of variables  $s = v_{\parallel}/\theta_{\parallel}$  and  $\zeta = \alpha/\theta_{\parallel} = (\omega - \Omega_j)/(|k_{\parallel}|\theta_{\parallel})$ , Equation (B.16) becomes,

$$I_{\parallel 2} = A_j \pi^{-1/2} \kappa^{-1/2} \frac{\Gamma(\kappa)}{\Gamma(\kappa - \frac{1}{2})} \int_{-\infty}^{\infty} \frac{s}{(s - \zeta)(1 + s^2/\kappa)^{\kappa}} ds \quad (k_{\parallel} > 0). \quad (\text{B.17})$$

Using the definition of the function  $U_{\kappa}(\zeta)$  in Equation (B.12) it can be shown that,

$$\begin{aligned} I_{\parallel 2} &= A_j \pi^{-1/2} \kappa^{-1/2} \frac{\Gamma(\kappa)}{\Gamma(\kappa - \frac{1}{2})} \int_{-\infty}^{\infty} \frac{s}{(s - \zeta)(1 + s^2/\kappa)^{\kappa}} ds. \\ &= A_j \pi^{-1/2} \kappa^{-1/2} \frac{\Gamma(\kappa)}{\Gamma(\kappa - \frac{1}{2})} \left[ \int_{-\infty}^{\infty} \frac{1}{(1 + s^2/\kappa)^{\kappa}} ds + \kappa^{\kappa} \int_{-\infty}^{\infty} \frac{\zeta}{(s - \zeta)(\kappa + s^2)^{\kappa}} ds \right] \\ &= A_j \pi^{-1/2} \kappa^{-1/2} \frac{\Gamma(\kappa)}{\Gamma(\kappa - \frac{1}{2})} \left[ \int_{-\infty}^{\infty} \frac{1}{(1 + s^2/\kappa)^{\kappa}} ds \right] + A_j \zeta U_{\kappa}(\zeta) \quad (k_{\parallel} > 0). \end{aligned} \quad (\text{B.18})$$

Using the standard integral given by Equation (B.7), the remaining integral in Equation (B.18) can be evaluated such that

$$\int_{-\infty}^{\infty} \frac{1}{(1 + s^2/\kappa)^{\kappa}} du = \frac{\sqrt{\pi} \sqrt{\kappa} \Gamma(\kappa - \frac{1}{2})}{\Gamma(\kappa)}$$

and, therefore,

$$I_{\parallel 2} = A_j + A_j \zeta U_{\kappa}(\zeta) \quad (k_{\parallel} > 0). \quad (\text{B.19})$$

For  $k_{\parallel} < 0$ , we set  $k_{\parallel} = -|k_{\parallel}|$  and make the change of variables  $s' = v_{\parallel}/\theta_{\parallel}$  and  $\zeta = \alpha/\theta_{\parallel} = (\omega - \Omega_j)/(|k_{\parallel}|\theta_{\parallel})$ . Substituting these into Equation (B.16) yields,

$$I_{\parallel 2} = A_j \pi^{-1/2} \kappa^{-1/2} \frac{\Gamma(\kappa)}{\Gamma(\kappa - \frac{1}{2})} \int_{-\infty}^{\infty} \frac{s'}{(s' + \zeta)(1 + s'^2/\kappa)^{\kappa}} ds' \quad (k_{\parallel} < 0). \quad (\text{B.20})$$

Making the change of variable  $s = -s'$ , Equation (B.20) becomes

$$\begin{aligned} I_{\parallel 2} &= A_j \pi^{-1/2} \kappa^{-1/2} \frac{\Gamma(\kappa)}{\Gamma(\kappa - \frac{1}{2})} \int_{\infty}^{-\infty} \frac{-s}{(-s + \zeta)(1 + s^2/\kappa)^{\kappa}} (-ds) \\ &= A_j \pi^{-1/2} \kappa^{-1/2} \frac{\Gamma(\kappa)}{\Gamma(\kappa - \frac{1}{2})} \int_{\infty}^{-\infty} \frac{s}{(-s + \zeta)(1 + s^2/\kappa)^{\kappa}} ds \\ &= A_j \pi^{-1/2} \kappa^{-1/2} \frac{\Gamma(\kappa)}{\Gamma(\kappa - \frac{1}{2})} \int_{-\infty}^{\infty} \frac{s}{(s - \zeta)(1 + s^2/\kappa)^{\kappa}} ds \quad (k_{\parallel} < 0). \end{aligned} \quad (\text{B.21})$$

Equation (B.21) is in the exact same form as Equation (B.17) and is solved in the same way such that

$$I_{\parallel 2} = A_j + A_j \zeta U_\kappa(\zeta) \quad (k_{\parallel} < 0). \quad (\text{B.22})$$

We have now shown that

$$I_{\parallel 1} = \frac{\omega}{|k_{\parallel}| |\theta_{\parallel}|} U_\kappa \left( \frac{\omega - \Omega_j}{|k_{\parallel}| |\theta_{\parallel}|} \right) \quad (\text{B.23})$$

and

$$I_{\parallel 2} = A_j + A_j \left( \frac{\omega - \Omega_j}{|k_{\parallel}| |\theta_{\parallel}|} \right) U_\kappa \left( \frac{\omega - \Omega_j}{|k_{\parallel}| |\theta_{\parallel}|} \right) \quad (\text{B.24})$$

for both  $k_{\parallel} > 0$  and  $k_{\parallel} < 0$ . Substituting Equations (B.23) and (B.24) into Equation (B.9), we arrive at the dispersion relation for parallel propagating electromagnetic L mode waves in a plasma with bi-kappa distribution [cf. *Mace et al.* (2011)]

$$\frac{k^2 c^2}{\omega^2} = 1 + \sum_j \frac{\omega_{pj}^2}{\omega^2} \left\{ A_j + \left[ A_j \left( \frac{\omega - \Omega_j}{k \theta_{\parallel j}} \right) + \frac{\omega}{k \theta_{\parallel j}} \right] U_{\kappa_j} \left( \frac{\omega - \Omega_j}{k \theta_{\parallel j}} \right) \right\} \quad (\text{B.25})$$

where  $k = |k_{\parallel}|$ ,  $U_\kappa$  is the dispersion plasma function (*Mace and Hellberg*, 2009) defined in terms of the Gauss hypergeometric function  ${}_2F_1$  by

$$U_\kappa(\zeta) = i \frac{(\kappa - \frac{1}{2})}{\kappa^{3/2}} {}_2F_1 \left[ 1, 2\kappa; \kappa + 1; \frac{1}{2} \left( 1 - \frac{\zeta}{i \kappa^{1/2}} \right) \right]. \quad (\text{B.26})$$

The dispersion relation for parallel propagating electromagnetic R mode waves in a plasma with bi-kappa distribution is derived using the same method as that used to derive the L mode and is given by,

$$\frac{k^2 c^2}{\omega^2} = 1 + \sum_j \frac{\omega_{pj}^2}{\omega^2} \left\{ A_j + \left[ A_j \left( \frac{\omega + \Omega_j}{k \theta_{\parallel j}} \right) + \frac{\omega}{k \theta_{\parallel j}} \right] U_{\kappa_j} \left( \frac{\omega + \Omega_j}{k \theta_{\parallel j}} \right) \right\}. \quad (\text{B.27})$$



# Bibliography

- Abramowitz, M., and I. Stegun (1964), *Handbook of Mathematical Functions: With Formulas, Graphs, and Mathematical Tables*, Applied mathematics series, Dover Publications.
- Akalin, F., D. A. Gurnett, T. F. Averkamp, A. M. Persoon, O. Santolik, W. S. Kurth, and G. B. Hospodarsky (2006), First whistler observed in the magnetosphere of Saturn, *Geophysical Research Letters*, *33*(20), 2–6, doi:10.1029/2006GL027019.
- Albert, J. M., and J. Bortnik (2009), Nonlinear interaction of radiation belt electrons with electromagnetic ion cyclotron waves, *Geophysical Research Letters*, *36*, L12,110, doi:10.1029/2009GL038904.
- Anderson, B. J., R. E. Erlandson, and L. J. Zanetti (1992a), A Statistical Study of Pc 1-2 Magnetic Pulsations in the Equatorial Magnetosphere, 2. Wave Properties, *Journal of Geophysical Research*, *97*(A3), 3089–3101, doi:10.1029/91JA02697.
- Anderson, B. J., R. E. Erlandson, and L. J. Zanetti (1992b), A Statistical Study of Pc 1-2 Magnetic Pulsations in the Equatorial Magnetosphere, 1. Equatorial Occurrence Distributions, *Journal of Geophysical Research*, *97*(A3), 3075–3088, doi:10.1029/91JA02706.
- André, N., et al. (2008), Identification of Saturn’s magnetospheric regions and associated plasma processes: Synopsis of Cassini observations during orbit insertion, *Rev. Geophys.*, *46*, RG4008, doi:10.1029/2007RG000238.
- Arridge, C. S., et al. (2009), Plasma electrons in Saturn’s magnetotail: Structure, dis-

tribution and energisation, *Planetary and Space Science*, 57(14-15), 2032–2047, doi: 10.1016/j.pss.2009.09.007.

Baker, D. N., and I. A. Daglis (2001), Radiation belts and ring current, in *Space Weather - Physics and Effects*, Springer Praxis Books, chap. 6, pp. 173–202, Springer Berlin Heidelberg.

Baluku, T. K., M. A. Hellberg, and R. L. Mace (2011), Electron acoustic waves in double-kappa plasmas: Application to Saturn’s magnetosphere, *Journal of Geophysical Research*, 116(A04227), doi:10.1029/2010JA016112.

Baumjohann, W., and R. A. Treumann (1996), *Basic Space Plasma Physics*, Imperial College Press, London.

Chaston, C. C., Y. D. Hu, and B. J. Fraser (1997), Non-Maxwellian particle distributions and electromagnetic ion cyclotron instabilities in the near-Earth magnetotail, *Geophysical Research Letters*, 24(22), 2913–2916, doi:10.1029/97GL02972.

Christon, S. P., D. G. Mitchell, D. J. Williams, L. A. Frank, C. Y. Huang, and T. E. Eastman (1988), Energy spectra of plasma sheet ions and electrons from  $\sim 50\text{eV}/e$  to  $\sim 1\text{MeV}$  during plasma temperature transitions., *Journal of Geophysical Research*, 93(A4), 2562–2572, doi:10.1029/JA093iA04p02562.

Christon, S. P., D. J. Williams, D. G. Mitchell, L. A. Frank, and C. Y. Huang (1989), Spectral Characteristics of Plasma Sheet Ion and Electron Populations During Undisturbed Geomagnetic Conditions, *Journal of Geophysical Research*, 94(A10), 13,409–13,424, doi: 10.1029/JA094iA10p13409.

Christon, S. P., D. J. Williams, D. G. Mitchell, C. Y. Huang, and L. A. Frank (1991), Spectral Characteristics of Plasma Sheet Ion and Electron Populations during Disturbed Geomagnetic Conditions, *Journal of Geophysical Research*, 96(A1), 1–22, doi: 10.1029/90JA01633.

- Craven, P. D., D. L. Gallagher, and R. H. Comfort (1997), Relative concentration of  $\text{He}^+$  in the inner magnetosphere as observed by the DE 1 retarding ion mass spectrometer, *Journal of Geophysical Research*, *102*(A2), 2279–2289, doi:10.1029/96JA02176.
- Daglis, I. A., Y. Kamide, G. Kasotakis, C. Mouikis, B. Wilken, E. T. Sarris, and R. Nakamura (1998), Ion composition in the inner magnetosphere: Its importance and its potential role as a discriminator between storm-time substorms and non-storm substorms, in *Proceedings of the International Conference on Substorms 4, Lake Hamana, Japan, March 913*, Terra/Kluwer Publications, Tokyo, pp. 767–772.
- Daglis, I. A., R. M. Thorne, W. Baumjohann, and S. Orsini (1999), The terrestrial ring current: Origin, formation, and decay, *Reviews of Geophysics*, *37*(4), 407–438, doi:10.1029/1999RG900009.
- Dialynas, K., S. M. Krimigis, D. G. Mitchell, D. C. Hamilton, N. Krupp, and P. C. Brandt (2009), Energetic ion spectral characteristics in the Saturnian magnetosphere using Cassini/MIMI measurements, *Journal of Geophysical Research*, *114*, A01,212, doi:10.1029/2008JA013761.
- Du, J. L. (2006), Test of nonextensive statistical mechanics by solar sound speeds, *Europhys. Lett.*, *75*, 861–867, doi:10.1209/epl/i2006-10196-3.
- Ejiri, M. (1978), Trajectory Traces of Charged Particles in the Magnetosphere, *Journal of Geophysical Research*, *83*(A10), 4798–4810, doi:10.1029/JA083iA10p04798.
- Erlandson, R. E., and A. J. Ukhorskiy (2001), Observations of electromagnetic ion cyclotron waves during geomagnetic storms: Wave occurrence and pitch angle scattering, *Journal of Geophysical Research*, *106*(A3), 3883–3895, doi:10.1029/2000JA000083.
- Feldman, W. C., R. C. Anderson, J. R. Asbridge, S. J. Bame, J. T. Gosling, and R. D. Zwickl (1982), Plasma electron signature of magnetic connection to the Earth's bow shock: ISEE 3, *Journal of Geophysical Research*, *87*(A2), 632–642, doi:10.1029/JA087iA02p00632.

- Fraser, B. J., and T. S. Nguyen (2001), Is the plasmapause a preferred source region of electromagnetic ion cyclotron waves in the magnetosphere?, *Journal of Atmospheric and Solar-Terrestrial Physics*, *63*(11), 1225–1247, doi:10.1016/S1364-6826(00)00225-X.
- Fraser, B. J., T. M. Loto'aniu, and H. J. Singer (2006), Electromagnetic Ion Cyclotron Waves in the Magnetosphere, *Geophysical monograph*, *169*, 195 – 212, doi: 10.1029/169GM13.
- Fraser, B. J., R. S. Grew, S. K. Morley, J. C. Green, H. J. Singer, T. M. Loto'aniu, and M. F. Thomsen (2010), Storm time observations of electromagnetic ion cyclotron waves at geosynchronous orbit: GOES results, *Journal of Geophysical Research*, *115*(A5), A05,208, doi:10.1029/2009JA014516.
- Gary, S. P. (1981), Microinstabilities upstream of the Earth's bow shock: A brief review, *Journal of Geophysical Research*, *86*(A6), 4331–4336, doi:10.1029/JA086iA06p04331.
- Gary, S. P., and R. Sinha (1989), Electromagnetic waves and instabilities from cometary ion velocity shell distributions, *Journal of Geophysical Research*, *94*(A7), 9131–9138, doi:10.1029/JA094iA07p09131.
- Gary, S. P., and J. Wang (1996), Whistler instability: Electron anisotropy upper bound, *Journal of Geophysical Research*, *101*(A5), 10,749–10,754, doi:10.1029/96JA00323.
- Gary, S. P., and I. H. Cairns (1999), Electron temperature anisotropy instabilities: Whistler, electrostatic and z mode, *Journal of Geophysical Research*, *104*, 19835–19842, doi:10.1029/1999JA900296.
- Gary, S. P., K. Liu, and D. Winske (2011), Whistler anisotropy instability at low electron  $\beta$ : Particle-in-cell simulations, *Physics of Plasmas*, *18*(8), 082,902, doi:10.1063/1.3610378.
- Gary, S. P., K. Liu, R. E. Denton, and S. Wu (2012), Whistler anisotropy instability with a cold electron component: Linear theory, *Journal of Geophysical Research*, *117*(A7), A07,203, doi:10.1029/2012JA017631.

- Gombosi, T. I., and K. C. Hansen (2005), Saturn's variable magnetosphere, *Science*, *307*, 1224–1226.
- Gradshteyn, I. S., and I. M. Ryzhik (2000), *Table of Integrals, Series, and Products*, 6 ed., Academic Press, San Diego, edited by A. Jeffrey and D. Zwillinger.
- Gurnett, D. A., L. A. Frank, and R. P. Lepping (1976), Plasma waves in the distant magnetotail, *Journal of Geophysical Research*, *81*, 6059–6071, doi:10.1029/JA081i016p02765.
- Gurnett, D. A., R. R. Shaw, R. R. Anderson, W. S. Kurth, and F. L. Scarf (1979), Whistlers observed by Voyager 1: Detection of lightning on Jupiter, *Geophysical Research Letters*, *6*, 511–514, doi:10.1029/GL006i006p00511.
- Gurnett, D. A., W. S. Kurth, and F. L. Scarf (1981), Plasma Waves Near Saturn: Initial Results from Voyager 1, *Science*, *212*, 235–239.
- Gurnett, D. A., W. S. Kurth, I. H. Cairns, and L. J. Granroth (1990), Whistlers in Neptunes Magnetosphere: Evidence of Atmospheric Lightning, *Journal of Geophysical Research*, *95*, 20,967–20,976, doi:10.1029/JA095iA12p20967.
- Gurnett, D. A., et al. (2005), Radio and Plasma Wave Observations at Saturn from Cassini's approach and first orbit, *Science*, *307*, 1255–1259.
- Gurnett, D. A., and A. Bhattacharjee (2005), *Introduction to Plasma Physics With Space and Laboratory Applications*, 372–373 pp., Cambridge University Press, Cambridge, UK.
- Harris, E. G. (1970), *Physics of Hot Plasmas: Scottish Universities' Summer School 1968*, Oliver and Boyd, Edinburgh, UK.
- Hasegawa, A., K. Mima, and M. Duong-van (1985), Plasma Distribution Function in a Superthermal Radiation Field, *Physical Review Letters*, *54*(24), 2608–2610, doi:10.1103/PhysRevLett.54.2608.
- Hellberg, M. A., and R. L. Mace (2002), Generalized plasma dispersion function for a plasma with a kappa-Maxwellian velocity distribution, *Physics of Plasmas*, *9*(5), 1495–1504, doi:10.1063/1.1462636.

- Helliwell, R. A. (1969), Low-frequency waves in the magnetosphere, *Reviews of Geophysics*, 7(1, 2), 281–303, doi:10.1029/RG007i001p00281.
- Henning, F. D., R. L. Mace, and S. R. Pillay (2011), Electrostatic Bernstein waves in plasmas whose electrons have a dual kappa distribution: Applications to the Saturnian magnetosphere, *Journal of Geophysical Research*, 116(A12), A12,203, doi:10.1029/2011JA016965.
- Hill, T. W. (2006), Effect of the acceleration current on the centrifugal interchange instability, *J. Geophys. Res.*, 111, A03,214, doi:10.1029/2005JA011338.
- Horne, R. B., and R. M. Thorne (1998), Potential waves for relativistic electron scattering and stochastic acceleration during magnetic storms, *Geophysical Research Letters*, 25(15), 3011–3014, doi:10.1029/98GL01002.
- Ipavich, F. M., and M. Scholer (1983), Thermal and Suprathermal Protons and Alpha Particles in the Earths Plasma Sheet, *Journal of Geophysical Research*, 88(A1), 150–160, doi:10.1029/JA088iA01p00150.
- Ipavich, F. M., A. B. Galvin, M. Scholer, G. Gloeckler, D. Hovestadt, and B. Klecker (1985), Suprathermal O<sup>+</sup> and H<sup>+</sup> Ion Behavior During the March 22, 1979 (CDAW 6), Substorms, *Journal of Geophysical Research*, 90(A2), 1263–1272, doi:10.1029/JA090iA02p01263.
- Jordanova, V. K., C. J. Farrugia, R. M. Thorne, G. V. Khazanov, G. D. Reeves, and M. F. Thomsen (2001), Modeling ring current proton precipitation by electromagnetic ion cyclotron waves during the May 14-16, 1997, storm, *Journal of Geophysical Research*, 106(A1), 7–22, doi:10.1029/2000JA002008.
- Jordanova, V. K., L. M. Kistler, M. F. Thomsen, and C. Mouikis (2003), Effects of plasma sheet variability on the fast initial ring current decay, *Geophysical Research Letters*, 30(6), 1311, doi:10.1029/2002GL016576.

- Jurac, S., and J. D. Richardson (2005), A self-consistent model of plasma and neutrals at Saturn: Neutral cloud morphology, *J. Geophys. Res.*, *110*, A09,220, doi: 10.1029/2004JA010635.
- Kavanagh, L. D., Jr., J. W. Freeman Jr., and A. J. Chen (1968), Plasma Flow in the Magnetosphere, *Journal of Geophysical Research*, *73*(17), 5511–5519, doi: 10.1029/JA073i017p05511.
- Kennel, C. F., and H. E. Petschek (1966), Limit on stably trapped particle fluxes, *Journal of Geophysical Research*, *71*(1), 1–28, doi:10.1029/JZ071i001p00001.
- Kennel, C. F., F. V. Coroniti, and F. L. Scarf (1986), Plasma waves in magnetotail flux ropes, *Journal of Geophysical Research*, *91*(A2), 1424–1438, doi: 10.1029/JA091iA02p01424.
- Kozyra, J. U., T. E. Cravens, A. F. Nagy, E. G. Fontheim, and R. S. B. Ong (1984), Effects of Energetic Heavy Ions on Electromagnetic Ion Cyclotron Wave Generation in the Plasmopause Region, *Journal of Geophysical Research*, *89*(A4), 2217–2233, doi: 10.1029/JA089iA04p02217.
- Krall, N. A., and A. W. Trivelpiece (1986), *Principles of Plasma Physics*, San Francisco Press, California.
- Krimigis, S. M., J. F. Carbary, E. P. Keath, T. P. Armstrong, L. J. Lanzerotti, and G. Gloeckler (1983), General characteristics of hot plasma and energetic particles in the Saturnian magnetosphere: Results from the Voyager spacecraft, *Journal of Geophysical Research*, *88*(A11), 8871–8892, doi:10.1029/JA088iA11p08871.
- Kurth, W. S., B. D. Strayer, D. A. Gurnett, and F. L. Scarf (1985), A Summary of Whistlers Observed by Voyager 1 at Jupiter, *Icarus*, *61*, 497–507.
- Landau, L. (1946), On the vibration of the electronic plasma, *Journal of Physics*, *10*(25).

- Lavraud, B., and V. K. Jordanova (2007), Modeling the effects of cold-dense and hot-tenuous plasma sheet on proton ring current energy and peak location, *Geophysical Research Letters*, *34*, L02,102, doi:10.1029/2006GL027566.
- Lazar, M., S. Poedts, and M. J. Michno (2013), Electromagnetic electron whistler-cyclotron instability in bi-Kappa distributed plasmas, *Astronomy & Astrophysics*, *554*, A64, doi:10.1051/0004-6361/201220550.
- Leubner, M. P. (2002), A nonextensive entropy approach to kappa-distributions, *Astrophysics and Space Science*, *282*, 573–579, doi:10.1023/A:1020990413487.
- Leubner, M. P. (2004), Fundamental issues on kappa-distributions in space plasmas and interplanetary proton distributions, *Phys. Plasmas*, *11*, 1308, doi:10.1063/1.1667501.
- Leubner, M. P., and Z. Voros (2005), A nonextensive entropy approach to solar wind intermittency, *Astrophys. J.*, *618*, 547–555, doi:10.1086/425893.
- Liu, L. Y., and J. L. Du (2008), Energy fluctuation and correlation in Tsallis statistics, *Physica A*, *387*, 231–241.
- Livadiotis, G., and D. J. McComas (2009), Beyond kappa distributions: Exploiting Tsallis statistical mechanics in space plasmas, *Journal of Geophysical Research*, *114*(A11), A11,105, doi:10.1029/2009JA014352.
- Lyons, L. R., and D. J. Williams (1984), *Quantitative Aspects of Magnetospheric Physics*, Springer Science & Business Media.
- Mace, R. L., and M. A. Hellberg (1995), A dispersion function for plasmas containing superthermal particles, *Physics of Plasmas*, *2*(6), 2098–2109, doi:10.1063/1.871296.
- Mace, R. L. (1998), Whistler instability enhanced by suprathermal electrons within the Earth's foreshock, *Journal of Geophysical Research*, *103*(A7), 14,643–14,654, doi:10.1029/98JA00616.
- Mace, R. L. (2004), Generalized electron Bernstein modes in a plasma with a kappa velocity distribution, *Physics of Plasmas*, *11*(2), 507–522, doi:10.1063/1.1635824.

- Mace, R. L., and M. A. Hellberg (2009), A new formulation and simplified derivation of the dispersion function for a plasma with a kappa velocity distribution, *Physics of Plasmas*, *16*(7), 072,113, doi:10.1063/1.3179807.
- Mace, R. L., and R. D. Sydora (2010), Parallel whistler instability in a plasma with an anisotropic bi-kappa distribution, *Journal of Geophysical Research*, *115*, A07,206, doi:10.1029/2009JA015064.
- Mace, R. L., R. D. Sydora, and I. Silin (2011), Effects of superthermal ring current ion tails on the electromagnetic ion cyclotron instability in multi-ion magnetospheric plasmas, *Journal of Geophysical Research*, *116*(A5), A05,206, doi:10.1029/2010JA016393.
- Maksimovic, M., V. Pierrard, and P. Riley (1997a), Ulysses electron distributions fitted with Kappa functions, *Geophysical Research Letters*, *24*(9), 1151–1154, doi:10.1029/97GL00992.
- Maksimovic, M., V. Pierrard, and J. F. Lemaire (1997b), A kinetic model of the solar wind with Kappa distribution functions in the corona, *Astronomy and Astrophysics*, *324*, 725–734.
- Meredith, N. P., R. M. Thorne, R. B. Horne, D. Summers, B. J. Fraser, and R. R. Anderson (2003), Statistical analysis of relativistic electron energies for cyclotron resonance with EMIC waves observed on CRRES, *Journal of Geophysical Research*, *108*(A6), 1250, doi:10.1029/2002JA009700.
- Nosé, M., S. Taguchi, K. Hosokawa, S. P. Christon, R. W. McEntire, T. E. Moore, and M. R. Collier (2005), Overwhelming O<sup>+</sup> contribution to the plasma sheet energy density during the October 2003 superstorm: Geotail/EPIC and IMAGE/LENA observations, *Journal of Geophysical Research*, *110*, A09S24, doi:10.1029/2004JA010930.
- Pierrard, V., and M. Lazar (2010), Kappa Distributions: Theory and Applications in Space Plasmas, *Solar Physics*, *267*(1), 153–174, doi:10.1007/s11207-010-9640-2.

- Quan-Ming, L., W. Lian-Qi, Z. Yan, and W. Shui (2004), Electromagnetic Instabilities Excited by Electron Temperature Anisotropy, *Chinese Physics Letters*, *21*(1), 129–132, doi:10.1088/0256-307X/21/1/039.
- Roux, A., S. Perraut, J. L. Rauch, C. de Villedary, G. Kremser, A. Korth, and D. T. Young (1982), Wave-Particle Interactions Near  $\Omega_{\text{He}^+}$  Observed on Board GEOS 1 and 2, 2. Generation of Ion Cyclotron Waves and Heating of  $\text{He}^+$  Ions, *Journal of Geophysical Research*, *87*(A10), 8174–8190, doi:10.1029/JA087iA10p08174.
- Russell, C. T. (1993), Planetary magnetospheres, *Rep. Prog. Phys.*, *56*, 687–732, doi:10.1088/0034-4885/56/6/001.
- Rymer, A. M., et al. (2007), Electron sources in Saturn’s magnetosphere, *J. Geophys. Res.*, *112*, A02,201, doi:10.1029/2006JA012017.
- Scarf, F. L., and C. T. Russell (1976), Magnetospheric dynamics and wave-particle interactions, in *Astrophysics and Space Science Library, Astrophysics and Space Science Library*, vol. 57, edited by K. Knott and B. Battrock, pp. 261–279.
- Scarf, F. L., D. A. Gurnett, and W. S. Kurth (1979), Jupiter Plasma Wave Observations: An Initial Voyager 1 Overview, *Science*, *204*, 991–995.
- Scarf, F. L., D. A. Gurnett, W. S. Kurth, and R. L. Poynter (1982), Voyager 2 Plasma Wave Observations at Saturn, *Science*, *215*(4532), 587–594.
- Scarf, F. L., F. V. Coroniti, C. F. Kennel, R. W. Fredricks, D. A. Gurnett, and E. J. Smith (1984), ISEE3 wave measurements in the distant geomagnetic tail and boundary layer, *Geophysical Research Letters*, *11*, 335–338, doi:10.1029/GL011i004p00335.
- Schippers, P., et al. (2008), Multi-instrument analysis of electron populations in Saturn’s magnetosphere, *Journal of Geophysical Research*, *113*(A7), A07,208, doi:10.1029/2008JA013098.
- Shprits, Y. Y., R. M. Thorne, R. B. Horne, S. A. Glauert, M. Cartwright, C. T. Russell, D. N. Baker, and S. G. Kanekal (2006), Acceleration mechanism responsible for the

- formation of the new radiation belt during the 2003 Halloween solar storm, *Geophysical Research Letters*, *33*(5), L05,104, doi:10.1029/2005GL024256.
- Singhal, R. P., and A. K. Tripathi (2006), Study of whistler mode instability in Saturn's magnetosphere, *Annales Geophysicae*, *24*(6), 1705–1712, doi:10.5194/angeo-24-1705-2006.
- Sittler, E. C. J., K. W. Ogilvie, and J. Scudder (1983), Survey of low energy plasma electrons in Saturn's magnetosphere: Voyagers 1 and 2, *J. Geophys. Res.*, *88*, 8847–8870, doi:10.1029/JA088iA11p8847.
- Stix, T. (1992), *Waves in Plasmas*, American Inst. of Physics.
- Storey, L. R. O. (1953), An Investigation of Whistling Atmospheric, *Philosophical Transactions of the Royal Society A: Mathematical, Physical and Engineering Sciences*, *246*(908), 113–141, doi:10.1098/rsta.1953.0011.
- Summers, D., and R. M. Thorne (1991), The modified plasma dispersion function, *Physics of Fluids B: Plasma Physics*, *3*(8), 1835–1847, doi:10.1063/1.859653.
- Summers, D., and R. M. Thorne (2003), Relativistic electron pitch-angle scattering by electromagnetic ion cyclotron waves during geomagnetic storms, *Journal of Geophysical Research*, *108*(A4), 1143, doi:10.1029/2002JA009489.
- Swanson, D. G. (2003), *Plasma Waves*, 2 ed., Academic Press, San Diego.
- Thorne, R. M., and R. B. Horne (1997), Modulation of electromagnetic ion cyclotron instability due to interaction with ring current O<sup>+</sup> during magnetic storms, *Journal of Geophysical Research*, *102*(A7), 14,155–14,163, doi:10.1029/96JA04019.
- Thorne, R. M. (2010), Radiation belt dynamics: The importance of wave-particle interactions, *Geophysical Research Letters*, *37*(22), L22,107, doi:10.1029/2010GL044990.
- Tripathi, A., and R. Singhal (2008), Whistler-mode instability in magnetospheres of Uranus and Neptune, *Planetary and Space Science*, *56*(3-4), 310–319, doi:10.1016/j.pss.2007.09.003.

- Tsallis, C. (1988), Possible Generalization of Boltzmann-Gibbs Statistics, *Journal of Statistical Physics*, *52*, 479–487, doi:10.1007/BF01016429.
- Tsurutani, B. T., and G. S. Lakhina (1997), Some basic concepts of wave-particle interactions in collisionless plasmas, *Reviews of Geophysics*, *35*(4), 491–501, doi:10.1029/97RG02200.
- Vasyliunas, V. M. (1968), A Survey of Low-Energy Electrons in the Evening Sector of the Magnetosphere with OGO 1 and OGO 3, *Journal of Geophysical Research*, *73*(9), 2839–2884, doi:10.1029/JA073i009p02839.
- Vega, P., L. Palma, and R. Elgueta (1998), The L mode in electromagnetic proton-cyclotron waves in plasmas modelled by a Lorentzian distribution function, *Journal of Plasma Physics*, *60*(1), 29–48, doi:10.1017/S0022377898006382.
- Wentworth, R. C. (1964), Enhancement of hydromagnetic emissions after geomagnetic storms, *Journal of Geophysical Research*, *69*(11), 2291–2298, doi:10.1029/JZ069i011p02291.
- Williams, D. J. (1983), The Earth's ring current: Causes, generation, and decay, *Space Science Reviews*, *34*(3), 223–234, doi:10.1007/BF00175279.
- Wolf, R. A., J. Freeman, J. W., B. A. Hausman, R. W. Spiro, R. V. Hilmer, and R. L. Lambour (1998), Modeling convection effects in magnetic storms, *GEOPHYSICAL MONOGRAPH SERIES*, *98*, 161–172.
- Xiao, F., Q. Zhou, H. He, and L. Tang (2006a), Instability of whistler-mode waves by a relativistic kappa-loss-cone distribution in space plasmas, *Plasma Physics and Controlled Fusion*, *48*(9), 1437–1445, doi:10.1088/0741-3335/48/9/012.
- Xiao, F., Q. Zhou, H. Zheng, and S. Wang (2006b), Whistler instability threshold condition of energetic electrons by kappa distribution in space plasmas, *Journal of Geophysical Research*, *111*(A8), A08,208, doi:10.1029/2006JA011612.

- Xiao, F., Q. Zhou, H. He, H. Zheng, and S. Wang (2007), Electromagnetic ion cyclotron waves instability threshold condition of suprathermal protons by kappa distribution, *Journal of Geophysical Research*, *112*, A07,219, doi:10.1029/2006JA012050.
- Xiao, F., Z. Su, H. Zheng, and S. Wang (2009), Modeling of outer radiation belt electrons by multidimensional diffusion process, *Journal of Geophysical Research*, *114*(A3), A03,201, doi:10.1029/2008JA013580.
- Xiao, F., L. Chen, Y. He, Z. Su, and H. Zheng (2011), Modeling for precipitation loss of ring current protons by electromagnetic ion cyclotron waves, *Journal of Atmospheric and Solar-Terrestrial Physics*, *73*, 106–111, doi:10.1016/j.jastp.2010.01.007.
- Xiao, F., C. Yang, Q. Zhou, Z. He, Y. He, X. Zhou, and L. Tang (2012), Nonstorm time scattering of ring current protons by electromagnetic ion cyclotron waves, *Journal of Geophysical Research*, *117*, A08,204, doi:10.1029/2012JA017922.
- Xiao, F., Q. Zong, Z. Su, C. Yang, Z. He, Y. Wang, and Z. Gao (2013), Determining the mechanism of cusp proton aurora., *Scientific reports*, *3*, 1654, doi:10.1038/srep01654.
- Xue, S., R. M. Thome, and D. Summers (1996a), Growth and damping of oblique electromagnetic ion cyclotron waves in the Earth's magnetosphere, *Journal of Geophysical Research*, *101*(A7), 15,457–15,466, doi:10.1029/96JA01088.
- Xue, S., R. M. Thome, and D. Summers (1996b), Parametric study of electromagnetic ion cyclotron instability in the Earth's magnetosphere, *Journal of Geophysical Research*, *101*(A7), 15,467–15,474, doi:10.1029/96JA01087.
- Young, D. T., J. Geiss, H. Balsiger, P. Eberhardt, A. Ghielmetti, and H. Rosenbauer (1977), Discovery of He<sup>2+</sup> and O<sup>2+</sup> ions of terrestrial origin in the outer magnetosphere, *Geophysical Research Letters*, *4*(12), 561–564, doi:10.1029/GL004i012p00561.
- Young, D. T., et al. (2005), Composition and dynamics of plasma in Saturn's magnetosphere, *Science*, *307*, 1262–1266.

Zhou, Q., F. Xiao, J. Shi, C. Yang, Y. He, and L. Tang (2013a), Excitation of electromagnetic ion cyclotron waves under different geomagnetic activities: THEMIS observation and modeling, *Journal of Geophysical Research: Space Physics*, *118*(1), 340–349, doi: 10.1029/2012JA018325.

Zhou, Q., F. Xiao, J. Shi, C. Yang, Y. He, and L. Tang (2013b), Observation and modeling of magnetospheric cold electron heating by electromagnetic ion cyclotron waves, *Journal of Geophysical Research: Space Physics*, *118*(11), 6907–6914, doi: 10.1029/2012JA018325.